

A framework for personalized modeling and predictive simulation to study gait in children with cerebral palsy

Antoine FALISSE

Examination committee:

Prof. dr. I. Jonkers, supervisor
Prof. dr. ir. F. De Groot, co-supervisor
Prof. dr. W. Helsen, chair
Prof. dr. K. Desloovere
Prof. dr. ir. G. Pipeleers
Prof. dr. ir. J. De Schutter
Prof. dr. A. Ijspeert
(EPFL)

Dissertation presented in partial fulfillment of the requirements for the degree of Doctor of Biomedical Sciences (PhD)

© 2019 KU Leuven – Faculty of Movement and Rehabilitation Sciences
Uitgegeven in eigen beheer, Antoine Falisse, Tervuursevest 101 box 1501, B-3001 Leuven (Belgium)

Alle rechten voorbehouden. Niets uit deze uitgave mag worden vermenigvuldigd en/of openbaar gemaakt worden door middel van druk, fotokopie, microfilm, elektronisch of op welke andere wijze ook zonder voorafgaande schriftelijke toestemming van de uitgever.

All rights reserved. No part of the publication may be reproduced in any form by print, photoprint, microfilm, electronic or any other means without written permission from the publisher.

Cover image: Simulation of human walking designed with OpenSim 4.0. Courtesy of Antoine Falisse.

Abstract

Physics-based simulations of human movement have the potential to predict the functional outcome of treatments, thereby allowing clinicians to personalize and optimize clinical decision-making. These predictive simulations would be particularly valuable for treatments with modest and unpredictable outcomes, such as orthopedic surgeries aiming to improve walking abilities of children with cerebral palsy (CP). Yet computational and modeling challenges still limit the applicability of such simulations in clinical practice. This dissertation aimed to address some of these limitations by improving model-based predictions of walking in children with CP, paving the way for treatment outcome predictions.

The central hypothesis of this dissertation was that predictive simulations can be exploited to explore the differential effects of motor control and mechanical deficits on the walking abilities of children with CP. We carried out five studies addressing three objectives to investigate this hypothesis.

The first objective was to develop methods and models to characterize the mechanical and motor control deficits of children with CP. Mechanical deficits include altered muscle-tendon properties represented through Hill-type muscle-tendon parameters, whereas motor control deficits include muscle spasticity described as exaggerated muscle reflex activity.

In study 1, we proposed a computationally efficient approach based on optimal control and musculoskeletal modeling to estimate subject-specific Hill-type muscle-tendon parameters. The approach identifies parameters that minimize the difference between experimental and model-based joint torques during functional movements. We applied this optimization procedure to estimate optimal fiber lengths and tendon slack lengths of several knee actuators of healthy adults. In addition, we evaluated which functional movements

contained sufficient information to provide valid (i.e., representative of the subjects) parameter estimates. We showed that our estimation procedure identified subject-specific parameters that improved the accuracy of joint torque simulations as compared to generic parameters. Further, we found that only specific functional movements contained enough information for a valid estimation, underlining the importance of the experimental data selection.

In study 2, we developed and compared three models of spasticity based on delayed sensory feedback from muscle states. The models relied on feedback from muscle length and velocity, feedback from muscle length, velocity, and acceleration, and feedback from muscle force and force rate, respectively. It is thought that the muscle spindle proprioceptive receptors encode information about muscle length and velocity changes. Yet recent experimental findings suggest that spindle firing might be more directly related to muscle force and force rate. Hence, we hypothesized that the force-based model would better explain spastic activity than the length-based models. We developed an optimal control formulation to identify feedback gains that minimized the difference between feedback and measured muscle activity during passive muscle stretches eliciting spastic responses. We found that the force-based model better explained spastic activity than the length-based models, confirming our hypothesis. In addition, we showed that only the force-based model was able to predict muscle activity in agreement with pathological activity measured during gait, opening perspectives for studying the controversial influence of spasticity during gait.

The second objective was to develop methods to generate computationally efficient predictive simulations of human movement. We formulated predictive simulations as optimal control problems. Solving such problems is, however, challenging. On the one hand, the equations describing the dynamics of the musculoskeletal system are stiff and nonlinear. On the other hand, using complex musculoskeletal models results in large and computationally expensive problems.

In study 3, we developed a framework to generate computationally efficient predictive simulations with complex three-dimensional musculoskeletal models. Key to this efficiency is the combination of direct collocation methods, implicit differential equations, and algorithmic differentiation. We evaluated the computational benefits of using algorithmic differentiation against finite differences to compute derivatives when generating predictive simulations of walking. As expected, algorithmic differentiation drastically reduced the computational time as compared to finite differences. The proposed simulation framework allows overcoming computational roadblocks that have long limited the use of optimal control simulations for biomechanical applications.

The third objective was to exploit predictive simulations to i) evaluate candidate walking control strategies in healthy and impaired individuals and ii) explore the differential effects of motor control and mechanical deficits on the walking pattern of a child with CP. In predictive simulations formulated as optimal control problems, the performance criterion determines the control strategy of the motor task. Yet it remains unclear what such criterion would be for human gait. Further, it is unknown whether the same performance criterion can explain the range of gaits adopted by humans in different contexts.

In study 4, we identified a multi-objective performance criterion combining energy and effort considerations that produces physiologically realistic predictive simulations of walking based on a three-dimensional musculoskeletal model. We then showed that the same criterion predicts the walk-to-run transition and clinical gait deficiencies caused by muscle weakness and prosthesis use, suggesting that diverse gaits can emerge from the same control strategy. This finding is in line with prior experimental and simulation studies based on two-dimensional models. The ability to predict the mechanics and energetics of diverse gaits suggests that our neuro-musculoskeletal model and simulation framework are generalizable enough for studying healthy and pathological gaits.

In study 5, we tested the ability of our simulations to identify the main treatment targets for a child with CP. We generated predictive simulations of walking with a medical imaging based three-dimensional neuro-musculoskeletal model of a child with CP and explored the influence of altered muscle-tendon properties, reduced neuromuscular control complexity, and spasticity on walking performance. We modeled altered muscle-tendon properties through personalized Hill-type muscle-tendon parameters, reduced neuromuscular control complexity through muscle synergies, and spasticity through delayed muscle force and force rate feedback. We found that, in the presence of aberrant musculoskeletal geometries, altered muscle-tendon properties were the primary driver of the crouch gait pattern observed for this child, which is in line with the clinical examination. This suggests that muscle-tendon properties should be the primary target of treatments aiming to restore a more upright gait pattern for this child, which is in accordance with the orthopedic intervention that was performed.

The ability of our framework for personalized modeling and predictive simulation to distinguish the contribution of different impairments on walking performance opens the door for modeling the effect of treatments, with the aim of designing optimal and personalized interventions for neuro-musculoskeletal disorders.

Samenvatting

Simulaties van menselijke bewegingen op basis van een fysisch model hebben het potentieel om het resultaat van behandelingen op het bewegingspatroon te voorspellen. Hierdoor kunnen dergelijke simulaties helpen om de klinische besluitvorming te personaliseren en te optimaliseren. Deze voorspellende simulaties zouden vooral waardevol zijn voor behandelingen met beperkte en onvoorspelbare resultaten, zoals orthopedische operaties met als doel het wandelpatroon van kinderen met cerebrale parese (CP) te verbeteren. Maar de nauwkeurigheid van de modellen en de hoge rekentijd beperken nog steeds de toepasbaarheid van dergelijke simulaties in de klinische praktijk. Het doel van deze thesis was om model-gebaseerde voorspellingen van wandelen bij kinderen met CP te verbeteren en zo mee te bouwen aan de weg naar model-gebaseerde voorspelling van behandelresultaten.

De centrale hypothese van deze thesis is dat voorspellende simulaties kunnen worden gebruikt om de effecten van verschillende motorische en musculoskeletale beperkingen op het wandelpatroon van kinderen met CP te onderscheiden. Om deze hypothese te onderzoeken hebben we vijf studies uitgevoerd kaderend binnen drie doelstellingen.

De eerste doelstelling was het ontwikkelen van methodes en modellen om de musculoskeletale en motorische beperkingen van kinderen met CP te beschrijven. Musculoskeletale beperkingen omvatten veranderde eigenschappen van spieren en pezen, die worden beschreven door de parameters in het Hill-model, terwijl motorische beperkingen spasticiteit, omschreven als overdreven spier-reflexactiviteit, omvatten.

In studie 1 ontwikkelden we een numeriek efficiënte methode voor het schatten van de spier-pees-parameters van het Hill-model op basis van

optimale controle en musculoskeletaal modelleren. Deze methode schat parameters door het verschil tussen experimenteel opgemeten en gesimuleerde gewichtsmomenten tijdens functionele bewegingen te minimaliseren. We hebben deze optimalisatieprocedure toegepast om de optimale vezellengte en peeslengte van verschillende spieren die de knie actueren in gezonde volwassenen te schatten. Daarnaast hebben we geëvalueerd welke functionele bewegingen voldoende informatie bevatten om geldige (d.w.z. representatief voor de eigenschappen van de spieren van de testpersoon) parameterschattingen te geven. We toonden aan dat de gepersonaliseerde parameters de nauwkeurigheid van de gesimuleerde gewichtskoppels verbeteren ten opzichte van generische parameters. Verder hebben we vastgesteld dat alleen specifieke functionele bewegingen voldoende informatie bevatten voor een geldige schatting, wat aantoont dat het belangrijk is om de experimentele bewegingen zorgvuldig te selecteren.

In studie 2 hebben we drie modellen van spasticiteit, allen op basis van vertraagde sensorische feedback van de toestand van de spier, ontwikkeld en vergeleken. De modellen waren gebaseerd of feedback van spiervezellengte en -snelheid; feedback van spiervezellengte, -snelheid en -versnelling; of feedback van spierkracht en de tijdsafgeleide van spierkracht. Traditioneel wordt gedacht dat spierspoeltjes informatie over veranderingen in spiervezellengte en -snelheid coderen maar recente experimentele bevindingen suggereren dat het zenuwsignaal van spierspoeltjes gerelateerd is aan spierkracht en de tijdsafgeleide van spierkracht. Daarom was onze hypothese dat het model op basis van feedback van kracht-gerelateerde variabelen de opgemeten spastische activiteit beter zou verklaren dan de modellen op basis van lengte-gerelateerde variabelen. We hebben de feedback-parameters bepaald door het verschil tussen de opgemeten en gesimuleerde spieractiviteit tijdens passief rekken van de spieren te minimaliseren aan de hand van optimale controle. We vonden dat feedback van kracht-gerelateerde variabelen de opgemeten spieractiviteit het best verklaarde, wat onze hypothese bevestigt. Bovendien kon alleen feedback van kracht-gerelateerde variabelen de pathologische spieractiviteit opgemeten tijdens wandelen verklaren. Dit nieuwe model op basis van feedback van spierkracht en de tijdsafgeleide van spierkracht opent perspectieven om de controversiële invloed van spasticiteit tijdens het wandelen verder te onderzoeken.

De tweede doelstelling was om numeriek efficiënte methodes te ontwikkelen voor het voorspellend simuleren van menselijke bewegingen. We hebben voorspellende simulaties geformuleerd als optimale controleproblemen. Het oplossen van dergelijke problemen is echter een uitdaging. Enerzijds zijn de vergelijkingen die de dynamica van het musculoskeletaal systeem beschrijven stijf en niet-lineair, anderzijds leidt het gebruik van complexe musculoskeletale modellen tot grote

en dus numeriek dure problemen.

In studie 3 hebben we een framework ontwikkeld om numeriek efficiënte voorspellende simulaties te genereren met complexe driedimensionale musculoskeletale modellen. De sleutel tot deze efficiëntie is de combinatie van directe collocatie, impliciete differentiaalvergelijkingen en algoritmische differentiatie. We hebben geëvalueerd wat de reductie in rekentijd is door het gebruik van algoritmische differentiatie in plaats van eindige differenties om afgeleide-informatie te berekenen bij het genereren van voorspellende simulaties van wandelen. Zoals verwacht, was de rekentijd aanzienlijk lager bij het gebruik van algoritmische differentiatie in plaats van eindige differenties. Met deze reductie van de rekentijd hebben we een belangrijke barrière voor het gebruik van simulaties voor biomechanische toepassingen verwijderd.

De derde doelstelling was om voorspellende simulaties te gebruiken i) om kandidaat-controlestrategieën voor gaan te evalueren bij gezonde personen en personen met een beperking en ii) om de effecten van verschillende motorische en musculoskeletale beperkingen op het wandelpatroon van een kind met CP te onderzoeken. In voorspellende simulaties geformuleerd als optimalisatieproblemen beschrijft het optimalisatiecriterium de onderliggende strategie om een motorische taak uit te voeren. Toch blijft het onduidelijk wat een dergelijk criterium zou zijn voor het menselijk gaan. Verder is het onbekend of hetzelfde criterium het gamma van gangpatronen dat mensen hanteren in verschillende contexten kan beschrijven.

In studie 4 hebben we een multi-objectief criterium geïdentificeerd dat fysiologisch realistische voorspellende simulaties van wandelen produceert op basis van een driedimensionaal musculoskeletaal model. Dit criterium bevat zowel minimalisatie van energie als van inspanning. We hebben vervolgens aangetoond dat hetzelfde criterium de wandel-naar-loop-overgang en afwijkingen in het wandelpatroon veroorzaakt door spierzwakte en prothesengebruik voorspelt, wat suggereert dat eenzelfde controlestrategie kan leiden tot verschillende gangpatronen. Deze bevinding is in overeenstemming met eerder experimenteel onderzoek en simulaties op basis van tweedimensionale modellen. Het vermogen om de mechanica en energetica van verschillende gangpatronen te voorspellen suggereert dat ons neuro-musculoskeletaal model en simulatieframework voldoende veralgemeenbaar zijn voor het bestuderen van gezonde en pathologische gangpatronen.

In studie 5 hebben we getest of onze simulaties de belangrijkste behandelingsdelen voor een kind met CP kunnen identificeren. We genereerden voorspellende simulaties van wandelen met een op medische beeldvorming gebaseerd driedimensionaal musculoskeletaal model van een kind met CP en onderzochten de invloed van veranderde spier-pees eigenschappen, verminderde complexiteit van de motorische controle en spasticiteit op het wandelpatroon. We hebben de afwijkende spier-pees eigenschappen gemodelleerd door gepersonaliseerde Hill-type spier-pees parameters, verminderde complexiteit van de motorische controle door spiersynergieën, en spasticiteit door vertraagde feedback van spierkracht en de tijdsafgeleide van spierkracht. We vonden dat, in aanwezigheid van afwijkende musculoskeletale geometrie, veranderde spier-pees eigenschappen de primaire oorzaak waren van het voor het kind waargenomen wandelpatroon met overdreven flexie in de knie en heup. Dit is in overeenstemming met het klinisch onderzoek en suggereert dat spier-pees eigenschappen het primaire doelwit zouden moeten zijn van behandelingen die gericht zijn op het herstellen van een meer rechtop wandelpatroon voor dit kind, hetgeen in overeenstemming is met de orthopedische interventie die werd uitgevoerd.

Het vermogen van ons framework voor gepersonaliseerd modelleren en voorspellend simuleren om de bijdrage van verschillende beperkingen aan het afwijkende wandelpatroon te onderscheiden, opent de deur voor het modelleren van het effect van behandelingen met als doel optimale en gepersonaliseerde interventies voor neuro-musculoskeletale aandoeningen te ontwerpen.

Contents

Abstract	i
Samenvatting	v
Contents	ix
1 General introduction	1
2 General methodology	17
3 Study 1: EMG-driven optimal estimation of subject-specific Hill model muscle-tendon parameters of the knee joint actuators	43
4 Study 2: A spasticity model based on feedback from muscle force explains muscle activity during passive stretches and gait in children with cerebral palsy	67
5 Study 3: Algorithmic differentiation improves the computational efficiency of OpenSim-based trajectory optimization of human movement	91
6 Study 4: Rapid predictive simulations with complex musculoskeletal models suggest that diverse healthy and pathological human gaits can emerge from similar control strategies	117

7 Study 5: Physics-based predictive simulations to explore the differential effects of motor control and musculoskeletal deficits on gait dysfunction in cerebral palsy: a retrospective case study	137
8 General discussion	165
A Study 1: supplementary material	185
B Study 2: supplementary material	197
C Study 4: supplementary material	205
D Study 5: supplementary material	223
E OpenSim versus Human Body Model: A comparison study for the lower limbs during gait	231
Acknowledgments	259
Scientific acknowledgments, personal contribution, conflict of interest statement, and appositions	261
Curriculum vitae	263
Bibliography	267

Chapter 1

General introduction

What if clinicians could predict the functional outcome of treatments for specific patients? This thought might have seemed far-fetched a few decades ago but the dawn of digital age has disrupted traditional practices, marking start of a new era for medicine. This era integrates digital technology as part of the diagnosis and treatment of disease. But more is to come. The recent increase in computational performance enables rapid and accurate computer modeling and simulation, making achievable *in silico* predictions of treatment outcome. These predictions would be particularly valuable for treatments with modest and unpredictable outcomes, such as orthopedic surgeries aiming to improve walking abilities of children with cerebral palsy (CP).

CP is the most common cause of motor disability amongst children, affecting 2 to 3 per 1000 live births in Europe [1]. CP is caused by a non-progressive lesion in the immature brain that may induce inabilities to selectively control muscles, spasticity, and weakness. These impairments undermine walking performance and progressively lead to secondary impairments, such as bony deformities and muscle contractures, that further deteriorate walking abilities [2].

Numerous treatments target impairments of children with CP, with the aim of improving walking performance. Among them are botulinum toxin-A injections [3] and selective dorsal rhizotomy [4] to reduce spasticity, and orthopedic surgeries, including tendon transfer, muscle-tendon lengthening, and bony derotation osteotomies, to correct musculoskeletal deformities. Multiple surgeries are often performed in a single intervention—single-event multi-level surgeries (SEMLS)—to have only one hospital admission and rehabilitation

period [5]. The clinical decision for selecting the treatment typically rests on a clinical assessment, an integrated three-dimensional (3D) gait analysis, and the experience of the clinicians. Yet it remains a particularly difficult decision to take as walking involves complex interactions between the musculoskeletal and motor control systems, which are both impaired in CP. Hence, the treatment outcome does not only depend on the success of the intervention but also on the remaining motor control [6] and muscle function of the patient. For example, SEMLS have been reported to improve walking performance in only 25 to 43% of the patients [7, 8] and to lead to a clinically meaningful improvement over natural progression in only 37% of the limbs [9]. Overall, treatment outcome has stagnated over the last two decades [10].

Computer models that can predict the outcome of treatments on walking performance have the potential to improve the success rate of treatments in children with CP by allowing clinicians to personalize and optimize the clinical decision-making process. Yet computational and modeling challenges still limit the applicability of such models in clinical practice. This dissertation aims to address some of these limitations by improving model-based predictions of walking in children with CP, paving the way for model-based predictions of treatment outcomes.

Model-based simulations of walking: general perspective

The neuro-musculoskeletal model

A neuro-musculoskeletal model is a mathematical description of how the neural and musculoskeletal systems interact to generate a movement (Figure 1.1).

Within the neural system, different structures interact to generate and control human locomotion, namely the supra-spinal structures, the spinal structures, and the sensory feedback pathways. The supra-spinal structures include the motor cortex, brain stem, cerebellum, and basal ganglia, and are involved in initiating and regulating human locomotion. Different subsystems can be distinguished. First, descending pathways from the brain stem are thought to initiate walking and control its speed. For instance, it has been shown that electrically stimulating the mesencephalic locomotor region of the brain stem initiates walking in decerebrate animals and that gait speed increases with the stimulation intensity [11]. Second, descending pathways from the motor cortex

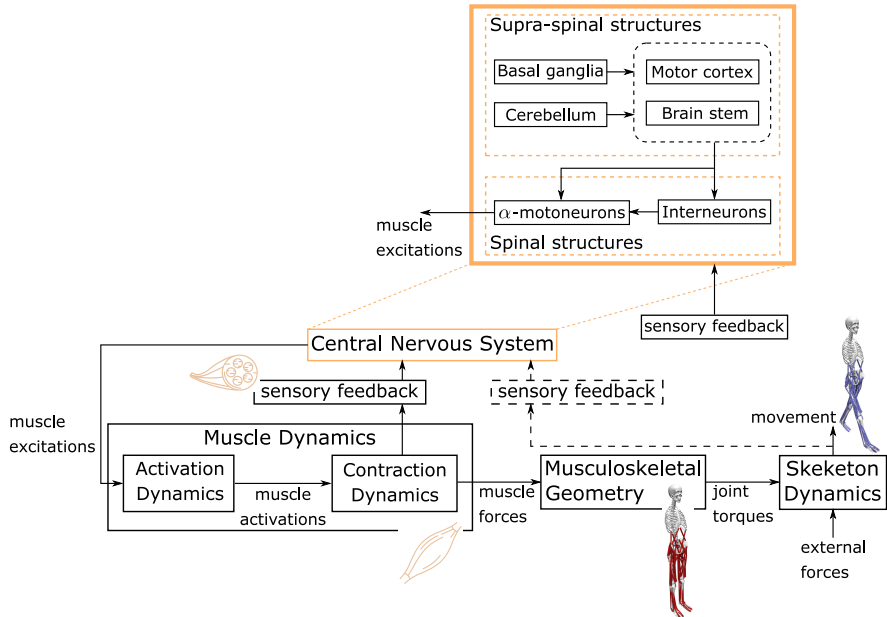


Figure 1.1: The neuro-musculoskeletal model describes how the central nervous system (CNS) generates muscle excitations, theoretically resulting from interactions between supra-spinal and spinal structures, how these excitations are transformed into muscle activations (muscle activation dynamics) and muscle forces (muscle contraction dynamics), how these forces are applied to the skeleton to generate joint torques (musculoskeletal geometry), how the skeleton moves under the influence of joint torques and external forces (skeleton dynamics), and how sensory feedback pathways interact with the CNS. The model used in this dissertation does not distinctly describe the neural structures of the CNS. Instead, it assumes that outcome muscle excitations optimize a performance criterion during walking. Further, the model we used is limited to sensory feedback from muscle states but ignores other types of sensory feedback (dashed lines).

are believed to be involved in the visuomotor coordination of human locomotion. Third, the cerebellum is thought to act as a movement controller that compares actual and intended movements, and accordingly regulates the activity of other supra-spinal structures such as regions of the motor cortex and brain stem. Finally, the basal ganglia are believed to filter out undesired movements and to contribute to the initiation of voluntary movements. The spinal structures consist of α -motoneurons whose axons innervate muscles and of interneurons that form the primary source of synaptic junctions with α -motoneurons. These interneurons are under influence of descending pathways from supra-spinal structures and sensory feedback. Spinal interneurons are thought to form neuronal spinal networks able to generate rhythmic activity without rhythmic input and named central pattern generators (CPGs). The role of CPGs in the control of vertebrate locomotion has been demonstrated through experiments in isolated spinal cords and deafferented animals (i.e., with no sensory feedback) in which activity patterns generated through electrical or chemical stimulation were similar to those recorded during intact locomotion [12]. Nevertheless, the contribution of CPGs to the control of human locomotion remains unclear [13]. For instance, spinal cord lesions affecting descending pathways often prevent injured patients to walk, suggesting an increased dependence of spinal interneurons on descending pathways in humans. Sensory feedback pathways are believed to contribute to shaping the rhythmic patterns of activity generated by the spinal interneurons, thereby maintaining the neural activity coordinated with the body movements. Different sensory feedback pathways exist, such as the stretch reflex that generates feedback activity upon passive muscle stretch. The stretch reflex originates in the muscle spindles and is under the influence of descending pathways [14, 15, 16, 17].

Different approaches have been proposed to model the neural system when simulating human walking. An approach is to assume that muscle excitations resulting from the aforementioned neural structures optimize a performance criterion. This assumption results in a very simple description of the neural system and does not require directly modeling the different neural structures. On the other hand, this approach necessitates finding a performance criterion that describes human walking. Although knowledge about such optimality criterion is still limited, numerous experimental studies have described how humans (e.g., [18, 19, 20, 21]) and animals (e.g., [22]) select gait features (e.g., speed, step frequency, walk-to-run transition) that minimize metabolic energy expenditure, suggesting that this criterion may capture the result from the distributed pathways within the neural system. Another approach for modeling the neural system is to directly describe several of the neural structures interacting to generate and control human walking. For example, Geyer and Song proposed a model based on spinal reflexes and supra-spinal modulations, but without

CPGs, that could reproduce diverse behaviors of human locomotion [23, 24, 25]. Interestingly, Dzeladini *et al.* extended this reflex-based model with a CPG component to also allow for gait speed modulation [26]. In this dissertation, we rely on a model of the neural system primarily based on the first approach, meaning that we do not model the supra-spinal and spinal structures thought to be involved in the control of human locomotion (except when modeling spasticity based on sensory feedback). The rest of this introduction is therefore framed on that control model.

The musculoskeletal system describes how muscles and skeleton interact to generate a movement given muscle excitations and external forces. In our model of this system, muscle activation dynamics first relate muscle excitations (i.e., firing of motor units) to activations (i.e., concentration of calcium ions within the muscle) [27, 28, 29, 30]. These activations then produce muscle forces through the muscle contraction dynamics, typically described by a Hill-type muscle-tendon model [27]. Since muscles actuate the joints of the skeleton, muscle forces then generate joint torques according to the geometry of the musculoskeletal system. Finally, the skeleton dynamics describe the skeletal movement as a function of the joint torques and external forces following the equations of motion of a rigid multibody model.

Dynamic simulation of walking

Combining this neuro-musculoskeletal model with dynamic simulation is a powerful approach to study the mechanisms underlying human movement. Two main types of model-based simulations can be distinguished. Inverse simulations identify controls (e.g., muscle excitations) underlying a given movement, whereas forward simulations generate the movement based on the controls. The inverse approach has been extensively used to analyze biomechanical variables, such as muscle and joint contact forces [31, 32], that are difficult to measure experimentally. Yet inverse simulations require the measured movement as input, which does not allow for predictive analyses such as treatment outcome predictions. By contrast, this type of analyses is possible through forward simulations that allow the generation of new movements without relying on measured movement data.

Forward simulations are commonly combined with numerical optimization techniques to compute optimal control trajectories. In such optimal control problems, an objective function is minimized subject to constraints describing the muscle and skeleton dynamics. Researchers have used forward simulations

in data-tracking and predictive problems. In tracking problems, the objective function is typically the difference between a variable's measured and simulated value, whereas in predictive problems, the objective function represents the goal of the motor task. Predictive simulations have the potential to reveal cause-effect relationships that cannot be explored through inverse or tracking simulations. Nevertheless, generating predictive simulations is challenging. First, the nonlinearity and stiffness of the equations describing the musculoskeletal dynamics cause the underlying optimal control problems to be difficult to solve. For example, small changes in controls can cause large changes in kinematics and hence a foot to penetrate into the ground, drastically increasing ground reaction forces. Second, the problem size increases with model complexity, making the generation of predictive simulations with complex 3D neuromusculoskeletal models computationally expensive. Yet such complexity is necessary in clinical practice, since the model should sufficiently describe the musculoskeletal structures and motor control processes that may be affected by treatment. An orthopedic surgeon considering a femoral osteotomy in a patient with CP will not be able to accurately predict the effect of the surgery on the walking pattern of the patient using a simple two-dimensional (2D) model driven by few muscles. Third, predictive simulations assuming optimal performance rely on a certain performance criterion that is modeled through the objective function. As introduced earlier, minimal metabolic energy expenditure has been suggested to underlie walking. Yet it remains unclear whether such criterion comprehensively captures human locomotion.

Following experimental observations suggesting that energy considerations might govern human locomotion [18, 19], numerous simulation studies have used energy-based performance criteria to predict human walking and running [33, 34, 35, 36, 25, 37]. Predictive simulations based on conceptual models (i.e., models, such as the inverted pendulum, that only describe the most prominent features of the musculoskeletal system [38]) also showed that a sole energy-based criterion produced walking at low speeds and running at high speeds [33, 34]. However, criteria centered on muscle activity, used as surrogates for muscle effort and fatigue, have also been suggested to underlie gait [39, 36, 25]. Simulation studies based on 2D musculoskeletal models found that using a performance criterion based on muscle activity better predicted the preferred walking speed in elderly [40] and resulted in more accurate kinematics during running [41] as compared to using an energy-based performance criterion. Yet it remains unclear whether these observations hold for simulations based on 3D musculoskeletal models. Further, gait might be governed by multiple performance criteria [41, 42] but the effect of combining different criteria on the predicted gait pattern has not been widely explored with complex 3D models, likely due to the associated computational costs.

These computational and modeling challenges have caused the biomechanics community to study human locomotion using primarily inverse and tracking [43, 44, 45, 46] simulations with complex 3D models, and predictive simulations with 2D or simple 3D models [39, 41, 47, 48, 49, 25, 50, 40, 51]. The few studies predicting gait with complex 3D models required high computational times (between 13 and 10,000 hours [35, 36, 37]) and reported only few gait patterns. In addition, they sometimes addressed the computational cost issue by using simplified muscle models [36, 37], which might not be physiologically realistic. Further, they often used measured data to create initial guesses [36, 37] or used fixed initial conditions [35], which might influence the final solution. Finally, no predictive study has yet explored whether different gaits can emerge from the same underlying control strategy when using complex 3D musculoskeletal models. It remains, therefore, uncertain whether the same control strategy can be used for predicting gaits in different conditions, such as in healthy individuals and in children with CP who have altered musculoskeletal properties.

Overall, although predicting human gait is not a new problem, no approach has yet been established to generate rapid and physiologically realistic predictive simulations of gaits encountered by humans in different contexts using complex 3D musculoskeletal models and without tracking experimental data. Nevertheless, over the last decade, progress has been made by using efficient numerical methods and formulations to solve the optimal control problems underlying predictive simulations. These numerical tools include direct collocation methods [52, 39, 53, 54, 46, 37], implicit differential equations [52, 55, 53], and algorithmic differentiation [56] that we present in more detail in the general methodology.

Impairments in children with CP

Children with CP suffer from mechanical and neural impairments that undermine their walking abilities. Accurate simulations of CP gait thus require taking these impairments into account. The mechanical impairments include bony deformities and altered muscle force generating capacities such as muscle weakness and contracture, whereas the neural impairments include spasticity and a reduced complexity of the neuromuscular control (i.e., an inability to selectively control muscles). Spasticity affects about 85% of the children with CP [57, 1] and is generally defined as a velocity-dependent increase in tonic stretch reflexes resulting from hyper-excitability of the stretch reflex [58]. The inability to

selectively control muscles is commonly described through muscle synergies [59], which are independent groups of muscles that are activated in a fixed ratio by a single input signal [60]. Children with CP have been shown to use fewer synergies (i.e., a simpler control strategy) than typically developing (TD) individuals during walking [61] as well as to use synergies exhibiting a greater stride-to-stride variability [62].

Model-based simulations of CP gait

The CP impairments result in abnormal walking patterns and cause children to adopt strategies to compensate for their impairments. By relying on detailed neuro-musculoskeletal models incorporating neural and mechanical deficits, predictive simulations have the potential to produce these abnormal patterns and to let emerge these compensation strategies. In other words, predictive simulations can let us explore the differential effects of motor control and mechanical deficits on the walking pattern and, therefore, predict the effect of treating certain deficits, for example through virtual orthopedic surgeries. Nevertheless, incorporating these deficits in the neuro-musculoskeletal models is not trivial. On the one hand, the mechanisms underlying CP impairments are not always fully understood, making the development of comprehensive models that accurately capture their impact on the neuro-musculoskeletal system difficult. On the other hand, CP impairments are often subject-specific, which prevents the use of generic models for accurate simulations. In addition, as previously introduced, generating predictive simulations with complex neuro-musculoskeletal models is challenging.

These reasons have caused the field to primarily rely on generic models and inverse simulations to study CP gait, where generic indicates that musculoskeletal geometry and muscle-tendon properties are linearly-scaled, based on the subjects' anthropometry, from a reference model derived from cadaver studies [63]. Nevertheless, such models have provided valuable insights into relationships between impaired gait and musculoskeletal functions. Crouch and stiff knee gaits are typical CP gait patterns that have been the focus of numerous modeling and simulation studies. They are characterized by excessive knee flexion during stance and by reduced knee flexion during swing, respectively. Hicks *et al.* [64, 65] showed that both external tibial torsion and crouch gait posture reduce the capacity of several major muscles to extend the knee. Steele *et al.* [66] found that required knee extensor strength increased with crouch gait severity, but required hip abductor and ankle plantarflexor strength were reduced in mild crouch gait. Arnold *et al.* [67] compared hamstrings length and velocity pre- and post-treatment of crouch gait and showed that subjects

were less likely to exhibit improved knee extension after hamstrings lengthening when they did not have short or slow hamstrings pre-treatment. Researchers have also used simulation to help unravel the role of the rectus femoris in limiting knee flexion in stiff knee gait [68, 69]. Finally, other simulation studies have, for example, shed light on the contribution of muscle weakness to gait impairments, showing that weakness of the plantarflexors, hip abductors, and hip flexors affect gait the most [70], that weakness of stance limb muscles has an influence on the swing leg behavior [71], and that weakness of one muscle is likely compensated by multiple muscles rather than by a single muscle [72].

These simulation studies greatly contributed to our understanding of CP gait. However, the use of models with subject-specific musculoskeletal geometry and muscle-tendon properties has the potential to improve the simulation accuracy, unraveling mechanisms at play for specific subjects.

Subject-specific modeling: mechanical system

The mechanical system consists of muscles actuating the skeleton, both of which are impaired in CP. To account for bony deformities and resultant altered muscle path trajectories, researchers have used musculoskeletal models with subject-specific geometry based on Magnetic Resonance Imaging (MRI) [73, 74, 75]. Such models have been shown to improve the accuracy of moment arm estimation [76] and allow relating bony deformities and altered muscle-tendon functions. For example, Bosmans *et al.* [77] showed the effect of combined bony deformities and aberrant gait kinematics on the potential of muscles to accelerate joints. However, MRI-based models often still assume generic muscle-tendon parameters, whereas muscle-tendon properties are known to vary with age, gender, and activity level [78, 79]. Furthermore, these properties have been shown to be altered in children with CP [80]. Barber *et al.* [81, 82, 83] found smaller volume and shorter lengths in medial gastrocnemius of individuals with CP as compared to TD individuals as well as longer Achilles tendon. This is consistent with the systematic review of Barrett *et al.* [84] reporting reduced muscle belly length, muscle volume, cross-sectional area, and muscle thickness in individuals with CP. These studies suggest a need for methods providing non-invasive subject-specific estimates of muscle-tendon parameters.

Different methods have been developed for estimating subject-specific muscle-tendon parameters. Among them are methods relying on anthropometric dimensions [85, 86] or on experimental angle-torque relationships from dynamometry experiments [87, 88, 89] or functional movements [90, 91].

Methods based on anthropometric dimensions are the most common. They only require simple measurements such as lengths and masses and are computationally efficient. Yet muscle properties are known to vary with age, gender, and activity level [92, 79] and are altered in children with CP. Muscle-tendon parameters cannot thus be truly estimated based on anthropometric dimensions. Dynamometry is also subject to several limitations, including difficulties to obtain a comprehensive set of measurements and to reach maximal muscle contraction during the experiments [87, 88, 93]. Methods relying on information from functional trials are more appropriate for estimating muscle-tendon parameters of children with CP. On the one hand, data can be easily collected from functional trials using standard motion capture equipment. On the other hand, the resulting dataset contains information about muscle actions. A typical approach for estimating subject-specific muscle-tendon parameters based on a functional approach is to identify the parameters that minimize the difference between experimental joint torques and joint torques derived from musculoskeletal models driven by electromyography (EMG), where EMG is assimilated to muscle excitations [90, 91]. Yet since the muscle-tendon parameter dependent relationship between muscle excitations and joint torques is dynamic (Figure 1.1), solving such optimization problem corresponds to solving an optimal control problem, which might be computationally expensive. To date, no computationally efficient approach has been proposed for estimating muscle-tendon parameters based on a functional approach. Note also that a careful selection of the functional movements is required to ensure a valid estimation. When the dataset contains insufficient information, the experimental data can be fitted with high precision while the estimated parameters are inaccurate and hence result in unreliable simulations for movements not included in the dataset, a phenomenon named overfitting.

Subject-specific modeling: neural system

Due to the complex interplay between motor control and mechanics, a successful intervention targeting mechanical impairments, such as an orthopedic surgery, might still result in a poor outcome because of remaining motor control impairments. In particular since altered motor control has been shown to only minimally change after treatment [94]. Predictive simulations aiming to predict treatment outcomes should, therefore, incorporate subject-specific neuromuscular control models [44]. Here, we distinguish two control impairments: spasticity and non-selective motor control. Note that we refer to spasticity as only the neural phenomenon as described below. We separately consider the secondary alterations in the intrinsic mechanical properties of the muscle and tendon [95]. These altered mechanical properties can be captured

through personalizing the muscle-tendon parameters.

Spasticity, described as an increased muscle reflex activity in response to muscle spindle firing, undoubtedly manifests during passive muscle stretches. However, its influence on walking performance remains subject to debate, with conflicting experimental findings from the literature (see [95] for a review). Modeling and simulation are useful tools for exploring whether spasticity affects gait but only few studies have exploited them for such purpose. Bar-On *et al.* [96] related muscle-tendon lengthening velocity during passive stretches of spastic hamstrings and gastrocnemii with muscle-tendon velocities during the swing phase of gait. They reported that the peak muscle-tendon velocity during swing exceeded the stretch reflex threshold for the hamstrings but not for the gastrocnemii, suggesting potential spastic hamstrings activity during swing. That study, however, only compared thresholds expressed in terms of muscle-tendon lengthening velocity and did not evaluate other muscle variables that have been related to muscle spindle firing and that may, therefore, drive spasticity (e.g., muscle fiber length and velocity [97, 98], and muscle force [99]). In addition, there was no attempt to model the spastic response to passive stretches and to evaluate how such model would apply to gait. More recently, Van der Krogte *et al.* [100] proposed a model of spasticity based on feedback from muscle fiber velocity. That model could capture the salient features of EMG responses measured during fast passive stretches of spastic hamstrings but could neither reproduce the oscillations observed in the measured EMG, nor the sustained muscle activity following the stretch. Furthermore, this model was not applied to gait, providing no information about the influence of spasticity during gait. This underlines the need for a more comprehensive model of spasticity that can be applied in simulation to help unravel the role of spasticity during gait.

As already introduced, the reduced complexity of the neuromuscular control characterizing children with CP can be modeled through muscle synergies; the lower the number of synergies the simpler the neuromuscular control. Forward simulations have successfully produced walking patterns using a synergy-based control [101, 102] and, therefore, provide an ideal approach for dissociating the influence of motor control and mechanical deficits on walking performance. Mehrabi *et al.* [103] recently showed that a 2D musculoskeletal model could reproduce an unimpaired walking pattern when using five synergies but deviated from that pattern when using two synergies similar to those seen after neurological injury, suggesting that impaired control affects walking performance. However, that study relied on a simple 2D model, neglecting control mechanisms in the frontal plane, and used a tracking optimal control approach that limits the emergence of compensation strategies by including

a tracking term (e.g., minimal deviation from measured kinematics) in the performance criterion. Overall, no study has yet explored the differential effects of motor control and mechanical impairments on the walking pattern of children with CP through predictive simulations with 3D musculoskeletal models.

Thesis overview

Summary of the gaps

- Altered muscle-tendon properties in children with CP require the use of subject-specific muscle-tendon parameters for accurate simulations. However, no computationally efficient method based on functional movements has yet been proposed to provide such subject-specific estimates.
- Spasticity manifests during passive stretches but its influence during gait remains debated. Modeling and simulations have the potential to test whether spasticity affects gait performance. However, no comprehensive model, which can capture the distinct features of the spastic response observed during passive stretches, has yet been developed and exploited for such purpose.
- Predictive simulations have the potential to reveal cause-effect relationships that cannot be explored through inverse or tracking simulations. However, computational challenges prevent the generation of rapid predictive simulations with complex 3D musculoskeletal models, limiting the applicability of such simulations in clinical contexts.
- Due to limited knowledge about gait control, it is unclear whether different gaits, for example healthy and pathological walking, can emerge from optimizing the same control strategy. Predictive simulations offer a platform for testing such hypothesis but have been rarely exploited for such purpose in combination with complex 3D musculoskeletal models.
- No predictive analyses based on complex 3D musculoskeletal models have yet been performed to explore the differential effects of motor control and mechanical impairments (e.g., spasticity, reduced neuromuscular complexity, and altered muscle-tendon properties) on the gait pattern of children with CP.

Objectives

The central hypothesis of this dissertation is that predictive simulations can be exploited to explore the differential effects of motor control and mechanical deficits on the walking abilities of children with CP. We formulated three objectives to investigate this hypothesis (Figure 1.2).

1. The first objective was to develop methods and models to characterize the mechanical and motor control deficits of children with CP.
2. The second objective was to develop methods to generate computationally efficient predictive simulations of movement.
3. The third objective was to exploit predictive simulations to i) evaluate candidate walking control strategies in healthy and impaired individuals and ii) explore the differential effects of motor control and mechanical deficits on the walking pattern of a child with CP.

Objective 1

Develop methods and models to characterize mechanical and motor control deficits of children with CP.

Study 1

Develop a computationally efficient method to estimate subject-specific muscle-tendon parameters.

Study 2

→ Develop and evaluate models of spasticity based on delayed sensory feedback.

Objective 2

Develop methods to generate computationally efficient predictive simulations of movement.

Study 3

Explore the computational benefits of algorithmic differentiation against finite differences in optimal control simulations of human movement.

Objective 3

Exploit predictive simulations to:

- i) evaluate candidate control strategies in healthy and impaired individuals.
- ii) explore the differential effects of motor control and mechanical deficits on the walking pattern of a child with CP.

Study 4

Identify a performance criterion that can predict healthy human walking.

Explore whether diverse healthy and pathological gaits can emerge from optimizing that criterion.

Study 5

→ Explore the differential effects of altered muscle-tendon properties, spasticity, and

impaired selective motor control on the walking pattern of child with CP.

Figure 1.2: Overview of the objectives and studies. Arrows indicate when outcomes (e.g., methods or models) of a study are used in another study. For example, the spasticity model of study 2 was used in study 5.

Objective 1: Develop methods and models to characterize the mechanical and motor control deficits of children with CP.

Alterations in muscle-tendon properties can be represented through the parameters of the Hill-type muscle-tendon model that determine the force

generating capacities of the muscle-tendon units. Previous research reported that these force generating capacities are most sensitive to the optimal muscle fiber lengths and tendon slack lengths [104, 105, 106, 107]. Different methods have been developed to provide subject-specific estimates of these parameters. Among them are methods based on experimental angle-torque relationships from functional movements that account for muscle actions and may hence be appropriate for reflecting the altered muscle-tendon properties of children with CP. Yet published methods proved to be computationally expensive [90, 108]. Further, no existing study investigated which experimental data was necessary to estimate valid muscle-tendon parameters and prevent overfitting.

In study 1, we aimed to develop a computationally efficient approach to provide subject-specific estimates of optimal fiber lengths and tendon slack lengths. The approach relied on optimal control and EMG-driven musculoskeletal modeling, and was applied for estimating parameters of the knee actuators in eight healthy adults. To ensure that the estimated parameters were valid (i.e., representative of the subjects), we also performed an identifiability analysis providing information about which experimental data was necessary to obtain valid estimates of parameters and prevent overfitting.

Hypothesis study 1: A computationally efficient approach based on optimal control can identify subject-specific muscle-tendon parameters that improve the accuracy of motion simulations as compared to generic (i.e., linearly-scaled from anthropometric dimensions) parameters.

Spasticity can be described as an exaggerated muscle reflex activity in response to muscle spindle firing. It is widely thought that the spindle proprioceptive receptors encode information about muscle length and velocity changes [97, 98], which supports modeling spasticity based on feedback from muscle length and velocity [100]. Yet recent experimental findings suggest that spindle firing might be more directly related to muscle force and its first time derivative (i.e., force rate) rather than to muscle length and velocity [99].

In study 2, we aimed to develop and evaluate three models of spasticity based on delayed sensory feedback from muscle states. The first model relied on feedback from muscle length and velocity, the second model relied on feedback from muscle length, velocity, and acceleration, and the third model relied on feedback from muscle force and force rate. The models were calibrated by optimizing feedback gains to reproduce the response of spastic hamstrings and gastrocnemii of six children with CP to fast passive stretches. The calibrated models were

then used to predict the spastic response during gait.

Hypothesis study 2: A spasticity model based on feedback from muscle force and force rate better explains the spastic response of hamstrings and gastrocnemii during passive stretches and gait than models based on feedback from muscle length, velocity, and acceleration.

Objective 2: Develop methods to generate computationally efficient predictive simulations of movement.

Predictive simulations can be formulated as optimal control problems in which an objective function is minimized subject to constraints describing the musculoskeletal dynamics. Yet these problems are challenging to solve because of the stiffness and nonlinearity of the equations describing muscle and skeleton dynamics. Further, combining predictive simulations with complex musculoskeletal models results in large and computationally expensive problems.

In study 3, we aimed to develop a framework to generate computationally efficient predictive simulations of movement with complex 3D musculoskeletal models. The framework combined different numerical methods including direct collocation, implicit formulations of the muscle and skeleton dynamics, and algorithmic differentiation. In particular, in study 3, we evaluated the computational benefits of using algorithmic differentiation over traditional finite differences when performing optimal control simulations of human movement including predictive and tracking simulations of walking.

Hypothesis study 3: Algorithmic differentiation improves the computational efficiency of optimal control simulations of human movement as compared to finite differences.

Objective 3: Exploit predictive simulations to i) evaluate candidate walking control strategies in healthy and impaired individuals and ii) explore the differential effects of motor control and mechanical deficits on the walking pattern of a child with CP.

In predictive simulations assuming optimal performance, the performance criterion (i.e., objective function) describes the high-level control strategy of the motor task. Yet it remains unclear whether a single task-level performance criterion can explain the range of gaits adopted by healthy and impaired

individuals in different contexts and what such criterion would be. The ability to generalize simulations and models to different contexts is, nevertheless, a prerequisite to using these tools for optimal treatment design.

In study 4, we first aimed to identify a performance criterion that could accurately predict healthy human walking by exploring a wide range of walking-related performance criteria using complex 3D musculoskeletal models. We then aimed to evaluate whether the identified criterion could predict the mechanics and energetics of a broad range of gaits encountered under different conditions, namely at different speeds, with muscle strength deficits, and with a passive transtibial prosthesis.

Hypothesis study 4: A broad range of healthy and pathological human gaits can emerge from optimizing the same control strategy.

Another prerequisite to using simulations for optimal treatment design is to demonstrate their ability to identify the main treatment targets for specific patients. In particular, for children with CP, simulations should allow distinguishing the contributions of neural and mechanical impairments on walking performance to inform clinicians about their treatment selection.

In study 5, we aimed to demonstrate the ability of our simulations to differentiate the contributions of altered muscle-tendon properties, reduced neuromuscular control complexity, and spasticity on the impaired walking pattern of a specific child with CP. The child's clinical examination reported a crouch gait pattern, close to normal range of motion at the hip and ankle but bilateral knee extension deficits, bilateral spasticity, and good muscle strength and selective control. Hence, we expected our simulations to produce a crouch gait pattern when incorporating the subject's impairments into the neuro-musculoskeletal model. Further, we expected altered muscle-tendon properties and spasticity rather than reduced neuromuscular control complexity to be the main drivers of the crouch gait pattern.

Hypothesis study 5: Accounting for altered muscle-tendon properties and spasticity produces a crouch gait pattern resembling the observed pattern of the child.

Chapter 2

General methodology

This dissertation includes five studies that relied on optimal control to explore the differential effects of motor control and mechanical deficits on the walking abilities of children with CP (Figure 2.1). The first two studies relied on experimental data to develop methods and models characterizing impairments in children with CP. The last three studies relied on predictive simulations to explore computational methods, control strategies, and the sensitivity of walking predictions to impairments in children with CP.

Experimental data

All studies were approved by the Ethics Committee at KU/UZ Leuven (Belgium). Data from studies 1 and 3-4 (same data) was collected from healthy adults in the Motion and Posture Analysis Laboratory Leuven (MALL, KU Leuven), whereas data from studies 2 and 5 was collected from children with CP at the University Hospital Pellenberg (UZ Leuven). In studies 1 and 3-4, the subjects gave informed consent to participate in the studies, whereas in studies 2 and 5, children older than 11 years gave informed assent and all parents signed an informed consent form. In all studies, the subjects were instrumented with retro-reflective skin mounted markers whose 3D trajectories were recorded (100 Hz) using a motion capture system (Vicon, Oxford, UK, 10 and 8-15 cameras at KU and UZ Leuven, respectively). Ground reaction forces (GRFs) were recorded (1000 Hz) using force plates (AMTI, Watertown, USA) and low-pass filtered (6-10 Hz) using a second-order dual-pass Butterworth filter. A brief description of the data collection specific to each study is given below.

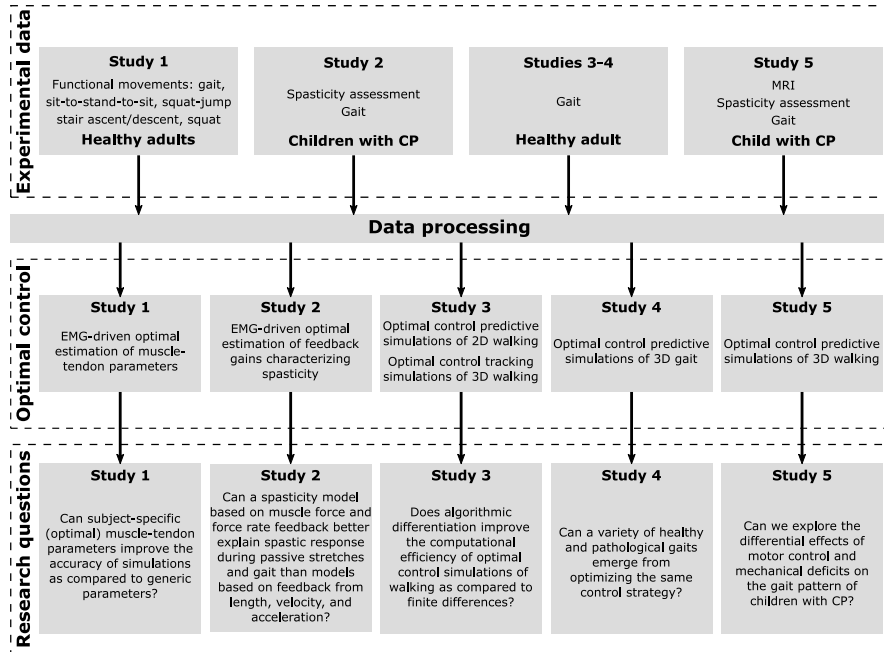


Figure 2.1: Overview of the methods.

Study 1

We collected experimental data (3D-marker trajectories, GRFs, and EMG) from eight healthy adults (four males and four females; age 29.8 ± 3.9 years; height 176 ± 6.6 cm; mass 69.6 ± 6.0 kg) during six functional movements: gait, squat, stair descent, stair ascent, sit-to-stand-to-sit, and squat jump. EMG was recorded (1000 Hz) using wireless EMG acquisition systems (ZeroWire EMG Aurion, Milano, Italy) from six muscles of each leg (hamstrings lateralis and medialis, gastrocnemius lateralis, rectus femoris, and vastus lateralis and medialis) and was processed by band-pass filtering (20-400 Hz), full-wave rectification, and low-pass filtering (10 Hz) using a second-order dual-pass Butterworth filter. EMG was also collected during maximum voluntary contraction trials and processed using the same protocol.

Study 2

We collected experimental data from legs with spastic involvement of six children with CP (four with unilateral and two with bilateral involvement). As part of their treatment, three children (two with unilateral and one with bilateral involvement) received a botulinum toxin-A (BTX) injection to reduce spasticity and we collected data before and six to 14 weeks after treatment, resulting in 12 included legs. We analyzed hamstrings and gastrocnemii. Due to poor EMG quality, data from the hamstrings of four legs was not included. This resulted in data from 20 muscle groups (eight hamstrings and 12 gastrocnemii, Table 2.1).

	Hamstrings (n = 8)	Gastrocnemii (n = 12)
Gender (male/female)	3/2	3/3
Age in years (mean ± std)	12.4 ± 2.6	11.7 ± 2.9
Involvement (unilateral/bilateral)	4/1	4/2
BTX-treatment (unilateral/bilateral)	2/0	2/1

Table 2.1: Demographic information study 2.

We collected experimental data (3D-marker trajectories, GRFs, and EMG) from walking trials. EMG was recorded (2000 Hz) using a telemetric Zerowire system (Cometa, Milan, Italy) from eight muscles of each leg (rectus femoris, vastus lateralis, biceps femoris short head, semitendinosus, tibialis anterior, gastrocnemius lateralis, soleus, and gluteus medius) and processed using the same protocol as in study 1. On the same day as the gait analysis, spasticity of the medial hamstrings and gastrocnemii was assessed using an instrumented passive spasticity assessment (IPSA, detailed by Bar-On *et al.* [109]). During IPSA, hamstrings and gastrocnemii were stretched by moving knee and ankle, respectively, one at a time from a predefined position throughout the full range of motion. The stretches were performed at slow, medium, and fast velocities. EMG was collected from four muscles (semitendinosus, gastrocnemius lateralis, rectus femoris, and tibialis anterior) using the same system and electrode placement as for the gait analysis. EMG processing was comparable to Bar-On *et al.* [109], namely high-pass filtering (20 Hz), stop-pass filtering (49.5–50.5 Hz) to remove a line frequency interference, full-wave rectification, and low pass filtering (10 Hz) using a sixth-order dual-pass Butterworth filter. The motion of the distal limb segment with respect to the proximal fixed segment was tracked using two inertial measurement units (Analog Devices, ADIS16354). The forces applied to the segment were measured using a hand-held six degrees of freedom (DOFs) load-cell (ATI Industrial Motion, mini45). The position of the load-cell relative to the joint axis was manually measured by the examiner.

Studies 3-4

We collected experimental data (3D-marker trajectories, GRFs, and EMG) from one healthy adult (female; age: 35 years; height: 170 cm; mass: 62 kg) during walking trials at steady-state speed and running trials on a treadmill at 10 km h⁻¹. EMG was recorded (1000 Hz) using a wireless EMG acquisition system (Cometa Mini Wave, Milano, Italy) from 14 muscles of each leg (peroneus brevis and longus, tibialis anterior, gastrocnemius lateralis and medialis, soleus, vastus lateralis and medialis, adductor longus, rectus femoris, tensor fascia latae, gluteus medius, hamstrings lateralis and medialis) and processed using the same protocol as in study 1.

Study 5

We collected experimental data (3D-marker trajectories, GRFs, and EMG) from one child with diplegic CP (male; age: 15 years; height: 143 cm; mass: 33.1 kg) during walking trials at self-selected speed. EMG was recorded (2000 Hz) using a telemetric Zerowire system (Cometa, Milan, Italy) from eight muscles of each leg (rectus femoris, vastus lateralis, biceps femoris short head, semitendinosus, tibialis anterior, gastrocnemius lateralis, soleus, and gluteus medius) and processed using the same protocol as in study 1. Spasticity of the right medial hamstrings and gastrocnemii was assessed using IPSA. Muscle strength, selectivity, and range of motion were evaluated through a standardized clinical examination protocol [110]. Finally, MRI images were collected for the hip region (i.e., pelvis and femur according to the protocol described by Bosmans *et al.* [111]).

Data processing

The experimental data was processed in OpenSim 3.3 [112] using musculoskeletal models scaled to the subjects' anthropometry with OpenSim's Scale tool based on marker information from standing calibration trials. The musculoskeletal models used in the different studies were primarily derived from the gait2392 model [63] although with some variations (Table 2.2). The gait2392 model consists of 20 segments, 23 DOFs (six between pelvis and ground; three at each hip joint; one at each knee, ankle, subtalar, and metatarsophalangeal (MTP) joint; three at the lumbar joint between trunk and pelvis), and 92 muscles (43 per leg and six for the lumbar joint).

	Musculoskeletal model(s)
Study 1	gait2392 with functional knee flexion axis [113] and locked subtalar and MTP joints
Study 2	gait2392 with locked subtalar and MTP joints
Study 3	gait2392 with locked MTP and with arms (four DOFs) from the Full Body Running Model [114] gait1018 [112]
Study 4	gait2392 with locked MTP and with arms (four DOFs) from the Full Body Running Model [114]
Study 5	MRI-based model [75]: similar to gait2392 with locked MTP and no muscles at the lumbar joint

Table 2.2: **Musculoskeletal models used for data processing across studies.**

We applied inverse analyses to process the experimental data. Typically, joint kinematics were calculated based on marker trajectories by applying a Kalman smoothing algorithm [115] or through OpenSim’s Inverse Kinematics tool. Joint kinetics were calculated based on joint kinematics and GRFs using OpenSim’s Inverse Dynamics tool. Muscle-tendon lengths and moment arms were calculated based on joint kinematics using OpenSim’s Muscle Analysis tool.

Optimal control

All studies involved solving optimal control problems with various levels of complexity. A basic formulation of an optimal control problem is:

$$\begin{aligned} & \underset{\boldsymbol{u}, \boldsymbol{p}}{\text{minimize}} \quad \int_{t_0}^{t_f} J(\boldsymbol{x}(t), \boldsymbol{u}(t), \boldsymbol{p}) dt, \\ & \text{subject to} \quad \dot{\boldsymbol{x}}(t) = f(\boldsymbol{x}(t), \boldsymbol{u}(t), \boldsymbol{p}), \\ & \qquad \qquad \qquad g_{\min} \leq g(\boldsymbol{x}(t), \boldsymbol{u}(t), \boldsymbol{p}) \leq g_{\max}, \end{aligned} \tag{2.1}$$

where $\boldsymbol{x}(t)$ is the vector of differentiable states, $\boldsymbol{u}(t)$ is the vector of controls, \boldsymbol{p} is the vector of time-independent parameters, t_0 and t_f are initial and final times, t is time, $J(\cdot)$ is the cost functional, $f(\cdot)$ is the set of dynamic constraints, and $g(\cdot)$ is the set of path constraints.

Numerical methods

Different approaches exist to solve this problem, including direct single shooting, direct multiple shooting, and direct collocation methods. Direct single shooting methods parametrize the controls and solve for control parameters that optimize the cost function. The dynamic constraints are then satisfied by integrating the differential equations using a time-marching approach. The main drawback of single shooting is that numerical difficulties arise due to instabilities in the dynamics when applying time-marching over a long time interval [116, 53]. Direct multiple shooting methods overcome this issue by dividing the time horizon into subintervals or meshes. Single shooting is then applied over each subinterval while continuity conditions enforce that the states at the end of a subinterval are equal to those at the beginning of the next subinterval. Multiple shooting results in larger problems since the states at the beginning of each subinterval become optimization variables. Nevertheless, the instabilities are reduced because of the smaller time intervals over which time-marching is applied [116]. Direct collocation methods can be observed as an extreme case of multiple shooting, where the time horizon is divided into many more meshes and both states and controls are parametrized at each mesh point. The differential equations are then discretized and the discretized equations are solved while optimizing the cost function, resulting in a nonlinear programming problem (NLP) that is generally large but sparse and thus tractable [116, 53]. Since direct collocation does not rely on time-marching for integration, it reduces dynamic instabilities observed, for example, in single shooting.

In all studies of this dissertation, we used direct collocation methods to solve the different optimal control problems. We relied on a certain type of methods called orthogonal direct collocation methods in which the state of each mesh interval is approximated by a linear combination of Lagrange polynomials. The degree of the Lagrange polynomial is determined by the number of Gaussian quadrature collocation points where the collocation is performed. The location of these points depends on the degree of the approximating polynomial and the employed collocation scheme (e.g., Legendre or Radau). At these collocation points, the Lagrange polynomials provide an exact expression of the state derivative that is used to enforce the dynamic constraints [116]. Gaussian quadrature methods present the main advantage over fixed order methods (e.g., Hermite-Simpson or backward Euler) that accuracy can be improved by adjusting the number of mesh intervals and their width but also by adjusting the degree of the approximating polynomials. Another important property of Gaussian quadrature methods is their ability to achieve exponential convergence if the underlying function is sufficiently smooth [116, 117].

Explicit and implicit formulations

The differential equations describing the dynamic constraints can be formulated explicitly or implicitly. Both approaches are equivalent but result in different problem formulations. With an explicit formulation, the differential equations generally have the form:

$$\dot{\boldsymbol{x}} = f_{\text{explicit}}(\boldsymbol{x}, \boldsymbol{u}). \quad (2.2)$$

With an implicit formulation, additional controls \boldsymbol{u}_{dx} can be introduced for the time derivatives of the states, which allows imposing the differential equations as path constraints in their implicit rather than explicit form:

$$\dot{\boldsymbol{x}} = \boldsymbol{u}_{dx}, \quad (2.3)$$

$$0 = f_{\text{implicit}}(\boldsymbol{x}, \boldsymbol{u}_{dx}, \boldsymbol{u}). \quad (2.4)$$

In our optimal control problems, implicit formulations improve the numerical conditioning of the NLP by, for example, removing the need to divide by small muscle activations in the contraction dynamics [53] or invert a mass matrix that is near-singular due to segments with large range of masses and moments of inertia in the skeleton dynamics [55].

These implicit formulations result in linear dynamic equations and nonlinear path constraints (2.4). If these path constraints are imposed at the mesh points but not at the collocation points (i.e., points in between the mesh points when using an orthogonal collocation method), then the use of any numerical method to integrate the dynamic equations in between the mesh points should be of similar numerical efficiency (since the dynamics are linear). There might thus be less benefits in using an orthogonal collocation method with such formulation as compared to a formulation in which the path constraints would be imposed at the mesh points as well as at the collocation points. Further, imposing the path constraints at both mesh and collocation points would likely allow reducing the mesh density. We only imposed the path constraints at the mesh points when formulating our predictive optimal control simulations and, therefore, recommend considering to impose them at both mesh and collocation points in future research.

Differentiation

Solving an optimal control problem, discretized as a NLP, involves computing derivatives. In more detail, the NLP solver requires evaluations of the cost function gradient (i.e., first order derivatives of the cost function with respect to the optimization variables), constraint Jacobian (i.e., first order derivatives of the constraints with respect to the optimization variables), and Hessian of the Lagrangian (i.e., second order derivatives of the cost function and constraints with respect to the optimization variables). The standard approach to compute derivatives is by using finite differences (FD), such as backward, central, or forward differences.

Automatic or algorithmic differentiation (AD) is an alternative to FD that can be used to evaluate derivatives of functions represented by computer programs [118]. These evaluations are obtained free of truncation errors, in contrast with FD, and for a computational cost of the same order of magnitude as the cost of evaluating the original function. AD relies on the observation that any function can be broken down into a sequence of elementary operations, forming an expression graph. AD then relies on the chain rule of calculus that describes how to calculate the derivative of a composition of functions [118]. By traversing a function's expression graph while applying the chain rule, AD allows computing the function derivatives. AD allows traversing the expression graph in two directions or modes: from the inputs to the outputs in its forward mode, and from the outputs to the inputs in its reverse mode. Depending on the dimensions and the sparsity pattern of the function, the use of the forward or reverse mode is advantageous. Typically, the reverse mode is computationally more efficient (i.e., it requires fewer function evaluations) than the forward mode when the function has many more inputs than outputs, whereas the opposite holds when the function has many more outputs than inputs. AD has been underused in biomechanics, likely because open-source software packages for musculoskeletal modeling and dynamic simulation, such as OpenSim and OpenSim's dynamics engine Simbody [119], do not leverage tools for AD.

Two main approaches exist for adding AD to existing software. In the operator overloading approach, the AD algorithms (i.e., forward and reverse modes) are applied after the evaluation of the original function using concrete numerical inputs. This is typically performed by introducing a new numerical type that stores information about partial derivatives as calculations proceed (e.g., through operator overloading in C++) [120, 118]. In the source code transformation approach, the AD tool analyzes a given function's source code and outputs

a new function that computes the forward or reverse mode of that function. Source code transformation is inherently faster than operator overloading, but may not be readily available for all features of a programming language.

Software packages

Numerous software packages have been developed to formulate and solve optimal control problems. In studies 1-2, we used the optimal control software package GPOPS-II, which is a closed-source MATLAB (The Mathworks Inc., USA) program that transcribes an optimal control problem into a NLP using a Gaussian quadrature collocation method [121]. GPOPS-II provides different collocation schemes (e.g., Legendre, Gauss, Legendre-Gauss-Radau) and can be interfaced with the open-source source code transformation AD software package ADiGator. In studies 3-5, we used the open-source software package CasADi, which is a modern and actively developed tool for nonlinear optimization and AD [56]. In contrast with GPOPS-II, CasADi does not perform the transcription of the optimal control problem for the end-users but provides all the building blocks necessary for such purpose. CasADi hence requires more inputs from the end-users but also provides a larger modeling flexibility. CasADi is written in C++ but has a MATLAB API. Both GPOPS-II and CasADi can interface with NLP solvers that are able to handle large and sparse NLPs such as IPOPT [122].

In all studies, we used IPOPT as NLP solver. IPOPT is an interior-point optimizer and relies on a linear solver when computing the Newton step direction during an optimization [123]. GPOPS-II provides an interface with several linear solvers, including mumps [124] and linear solvers from the HSL collection [125]. Mumps freely comes with CasADi but linear solvers from the HSL collection, which are only free to academics, must be compiled by end-users for use with CasADi. In studies 1-2, we used the linear solver ma57 from the HSL collection, whereas in studies 3-5, we primarily used mumps. As part of study 3, we compared the efficiency of mumps against linear solvers from the HSL collection when solving different optimal control problems.

As already introduced, OpenSim and Simbody are open-source software packages for musculoskeletal modeling and dynamic simulation but do not support AD. In study 3, we describe how we addressed this limitation. We enabled the use of AD through the open-source operator overloading tool ADOL-C [126] but also developed a custom open-source source code transformation tool that we named Recorder. We compared both approaches and found that Recorder was more

efficient. Therefore, in studies 4-5, we relied on Recorder to compute derivatives when generating predictive simulations.

Neuro-musculoskeletal models

We solved two main types of optimal control problems across the studies. The problems either identified optimal controls that underlay a given movement (studies 1-2) or that generated a new movement (studies 3-5) (Figure 2.2). Both types of problems involved optimizing a certain optimality criterion subject to constraints enforcing the muscle and/or skeleton dynamics.

When the movement is given, inverse approaches can be used to compute muscle-tendon lengths, moment arms, and joint torques. These variables can serve as inputs for optimal control problems that include the muscle dynamics and/or sensory feedback but that do not include the skeleton dynamics. When EMG is also given, it can be assimilated to muscle excitations to drive musculoskeletal models (i.e., EMG-driven models). In study 1, we used an optimal control formulation to identify muscle-tendon parameters that minimized the difference between joint torques calculated from inverse dynamics during functional movements and joint torques computed from muscle dynamics with EMG-driven models (Figure 2.2). In study 2, we used an optimal control formulation to identify sensory feedback parameters that minimized the difference between EMG from passive muscle stretches and muscle excitations from sensory feedback (Figure 2.2).

When the movement is generated and under the assumption that optimal performance drives human movement, the problem consists in identifying the optimal controls that minimize a performance criterion representing the control strategy and subject to constraints enforcing muscle and skeleton dynamics. Further, in order to simulate gait patterns, we added constraints imposing a predefined average gait speed (defined as the distance traveled by the pelvis divided by the gait cycle duration) as well as symmetry or periodicity of the gait pattern. A symmetric gait pattern assumes that states and controls from pairs of opposite joints and muscles are equal when phase-shifted by half a gait cycle (e.g., the right and left soleus activities are equal at right and left heel strikes, respectively), whereas a periodic gait pattern assumes that states and controls are equal when phase-shifted by a full gait cycle. Imposing symmetry allows optimizing for only half a gait cycle, with the full gait cycle being reconstructed in a post-processing phase. Imposing periodicity necessitates optimizing for a full

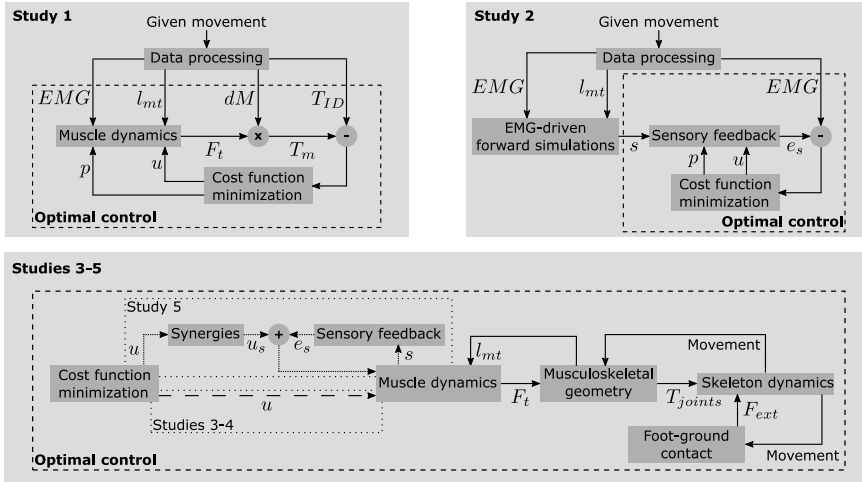


Figure 2.2: Flowcharts describing the optimal control problems solved in the different studies. In **study 1**, we identified the optimal controls u and muscle-tendon parameters p that minimized the difference between joint torques from inverse dynamics T_{ID} and muscle torques T_m resulting from the product between muscle-tendon forces F_t from muscle dynamics and experimental moment arms dM . The muscle dynamics are driven by EMG and take as inputs experimental muscle-tendon lengths l_{mt} . In **study 2**, we identified the optimal controls u and feedback parameters p that minimized the difference between EMG and feedback muscle excitations e_s . The sensory feedback takes as input sensory information s generated from EMG -driven forward simulations in a pre-processing phase. In **studies 3-5**, we identified the optimal controls u that produced a movement following a control strategy modeled through the cost function. The muscle dynamics relate controls (muscle excitations) and muscle-tendon forces F_t , the musculoskeletal geometry converts muscle-tendon forces into joint torques T_{joints} , and the skeleton dynamics produce the movement resulting from the applied joint torques and external forces F_{ext} . In **study 5**, the motor control selectivity is reduced through muscle synergies and sensory feedback, representing spasticity, is incorporated into the control scheme. These flowcharts omit and simplify certain components on purpose to facilitate the reading.

gait cycle. In studies 3-5, we used optimal control formulations to identify control trajectories that optimized a gait-related performance criterion and produced a gait pattern. In study 5, we also explored the effect of impaired control mechanisms modeled through exaggerated sensory feedback and synergistic muscle activations (Figure 2.2). We imposed symmetry and periodic constraints when simulating healthy and pathological gait patterns, respectively.

The five studies were designed with different goals in mind but relied on similar dynamic models and formulations that are described in the following sections.

Muscle dynamics

The muscle dynamics include activation and contraction dynamics that describe how muscle excitations are successively transformed into muscle activations and forces.

Activation dynamics

Activation dynamics relate excitations e to activations a , typically through a nonlinear first order differential equation [28, 29, 30]. This relation can be formulated explicitly or implicitly. We relied on both formulations across the studies of this dissertation. In study 1, we used an explicit formulation with controls e and states a based on Winters' model [28, 30]. This model is not twice continuously differentiable and thus not suitable for use with gradient-based optimization algorithms, such as IPOPT. To overcome this limitation, we performed a smooth approximation using a hyperbolic tangent (\tanh) function [53]:

$$f = 0.5 \tanh(b_a(e - a)), \quad (2.5)$$

$$\frac{da}{dt} = \left[\frac{1}{\tau_a(0.5 + 1.5a)} (f + 0.5) + \frac{0.5 + 1.5a}{\tau_d} (-f + 0.5) \right] (e - a), \quad (2.6)$$

where $\tau_a = 15$ ms is activation time constant, $\tau_d = 60$ ms is deactivation time constant, and $b_a = 0.1$ is a parameter that determines the smoothness of the \tanh transition. In study 1, the musculoskeletal model was driven by EMG that provides an estimate of muscle excitations.

In the other studies, we used an implicit formulation based on Raasch's model [29, 52]. Such formulation eliminates muscle excitations from the problem

and is, therefore, not suitable for EMG-driven models as in study 1. Yet the advantage of the implicit formulation is the elimination of the computationally expensive tanh function from the problem formulation. To implicitly formulate activation dynamics, we first introduced additional controls u_{da} that are the time derivatives of the states a :

$$\frac{da}{dt} = s_a u_{da}, \quad (2.7)$$

where $s_a = 100$ is a scale factor. We then imposed the differential equations describing activation dynamics as path constraints:

$$0 \leq s_a u_{da} + \frac{a}{\tau_d}, \quad (2.8)$$

$$s_a u_{da} + \frac{a}{\tau_a} \leq \frac{1}{\tau_a}. \quad (2.9)$$

Although muscle excitations are eliminated from the implicit problem formulation, they can be computed post-processing [52]:

$$e = \begin{cases} \tau_d u_{da} + a & u_{da} \leq 0, \\ \frac{ac_1 - c_2 + \sqrt{D}}{2c_1} & u_{da} > 0, \end{cases} \quad (2.10)$$

where $c_1 = (1/\tau_a - 1/\tau_d)$, $c_2 = 1/\tau_d$, and $D = (c_1 a + c_2)^2 + 4c_1 u_{da}$.

Contraction dynamics

We used a Hill-type muscle-tendon model (Figure 2.3) to relate muscle activations and tendon forces F_t [27]. This model describes the muscle-tendon unit of length l_{mt} as a tendon of length l_t in series with a muscle of length l_m and pennation angle α . The dimensionless relationships of this model (detailed by De Groote *et al.* [53]) describe the force generating capacity of the muscle-tendon unit and can be scaled to a specific unit through five muscle-tendon parameters: the maximal isometric force F_m^{\max} , the optimal fiber length l_m^{opt} , the tendon slack length l_t^s , the optimal pennation angle α_m^{opt} , and the maximal fiber contraction velocity v_m^{\max} .

The tendon was modeled as a nonlinear spring:

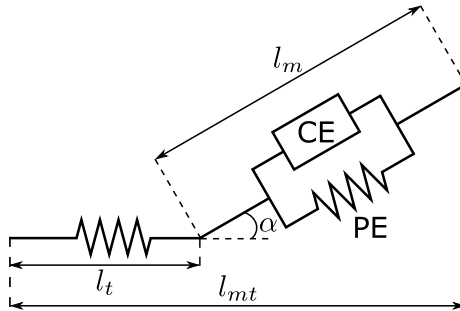


Figure 2.3: **Schematic representation of the Hill-type muscle-tendon model [27].** The muscle-tendon unit, of length l_{mt} , comprises a tendon in series with a pennate muscle. The tendon is modeled as a nonlinear spring of length l_t . The muscle, of length l_m , consists of a contractile element (CE) parallel to a passive element (PE). The pennation angle α is the angle between the orientation of the muscle fibers and the tendon.

$$F_t = F_m^{\max} f_t(\tilde{l}_t), \quad (2.11)$$

where $\tilde{l}_t = l_t/l_t^s$ is normalized tendon length and $f_t(\cdot)$ describes the tendon force-length relationship. The muscle was modeled as a contractile element in parallel with a passive element:

$$F_m = F_m^{\max} [a f_{act}(\tilde{l}_m) f_v(\tilde{v}_m) + f_{pas}(\tilde{l}_m) + d\tilde{v}_m], \quad (2.12)$$

where F_m is muscle force, $\tilde{l}_m = l_m/l_m^{\text{opt}}$ is normalized fiber length, $\tilde{v}_m = v_m/v_m^{\max}$ is normalized fiber velocity, $f_{act}(\cdot)$, $f_v(\cdot)$, and $f_{pas}(\cdot)$ describe the active muscle force-length, active muscle force-velocity, and passive muscle force-length relationships, respectively, and $d = 0.01$ is a damping factor. The muscle-tendon interaction was described by:

$$l_{mt} = l_t + l_m \cos \alpha, \quad (2.13)$$

$$l_m \sin \alpha = l_m^{\text{opt}} \sin \alpha_m^{\text{opt}}, \quad (2.14)$$

$$F_t = F_m \cos \alpha. \quad (2.15)$$

Equations 2.11-2.15 determine the relation between the model inputs (a and l_{mt}) and unknowns (F_t , F_m , l_t , l_m , and α). This relation is dynamic due to its

dependence on fiber velocity.

In all studies, we used implicit formulations of this dynamic model [53]. Since algebraic equations relate fiber length and tendon force (equations 2.13-2.15), it is equivalent to use either normalized fiber length or normalized tendon force as state. With normalized fiber length as state, the dynamic equation becomes:

$$\frac{d\tilde{l}_m}{dt} = s_{d\tilde{l}_m} u_{d\tilde{l}_m}, \quad (2.16)$$

where $u_{d\tilde{l}_m} = \tilde{v}_m$ is introduced as a new control and $s_{d\tilde{l}_m} = v_m^{\max}/l_m^{\text{opt}}$ is a scale factor that converts $u_{d\tilde{l}_m}$ into the time derivative of \tilde{l}_m . The equations describing the contraction dynamics $f_{\tilde{l}_m}(\cdot)$ are then imposed as path constraints:

$$0 = f_{\tilde{l}_m}(a, \tilde{l}_m, u_{d\tilde{l}_m}). \quad (2.17)$$

Similarly, with normalized tendon force as state, the dynamic equation becomes:

$$\frac{d\tilde{F}_t}{dt} = s_{d\tilde{F}_t} u_{d\tilde{F}_t}, \quad (2.18)$$

where $u_{d\tilde{F}_t}$ is introduced as a new control and $s_{d\tilde{F}_t}$ is a scale factor. The equations describing the contraction dynamics $f_{\tilde{F}_t}(\cdot)$ are then imposed as path constraints:

$$0 = f_{\tilde{F}_t}(a, \tilde{F}_t, u_{d\tilde{F}_t}). \quad (2.19)$$

We have used normalized fiber lengths as states in study 1 and normalized tendon forces as states in the remaining studies. Yet we could have opted for the other state option in each study, since both formulations are equivalent.

In problems where the movement is given, muscle-tendon lengths and moment arms can be computed from known joint kinematics in a pre-processing step. Muscle-tendon lengths can be used as inputs to the muscle contraction dynamics (equations 2.11-2.15), whereas moment arms dM can be multiplied with tendon forces (equation 2.15) to provide muscle torques:

$$T_m = F_t dM. \quad (2.20)$$

The sum of muscle torques should equate joint torques when no other structures generating torques around the joints, such as ligaments, are considered.

Trunk and arm dynamics

In our studies, we used musculoskeletal models with different levels of complexity. In some cases, the models comprised a lumbar joint in the trunk as well as elbow and shoulder joints in the arms that were actuated by ideal torque actuators. To limit the rate of torque developed by the ideal torque actuators, we used a dynamic model relating trunk/arms excitations $e_{\text{trunk/arms}}$ to trunk/arms activations $a_{\text{trunk/arms}}$ through a differential equation corresponding to the first order approximation of a time delay:

$$\frac{da_{\text{trunk/arms}}}{dt} = \frac{e_{\text{trunk/arms}} - a_{\text{trunk/arms}}}{\tau_{\text{trunk/arms}}}, \quad (2.21)$$

where $\tau_{\text{trunk/arms}} = 35$ ms. We used $e_{\text{trunk/arms}}$ as controls and $a_{\text{trunk/arms}}$ as states that were bounded between 0 and 1. We then related $a_{\text{trunk/arms}}$ to trunk/arms torques as follows:

$$T_{\text{trunk/arms}} = s_{\text{trunk/arms}} a_{\text{trunk/arms}}, \quad (2.22)$$

where $s_{\text{trunk/arms}} = 150$ is a scale factor.

Skeleton dynamics

The skeleton dynamics describe how the skeleton moves under the influence of joint torques and external forces.

Joint torques

Joint torques result from applying muscle-tendon forces to the skeleton and depend on the musculoskeletal geometry that determines the muscle-tendon lengths, velocities, and moment arms of the muscles actuating the joints. In studies 1-2, the movements were given and these variables could, therefore, be calculated using an inverse approach. In studies 3-5, new movements were generated, which required the computation of these variables during the optimization process. Such estimation might be computational expensive. Therefore, to increase computational speed, we defined muscle-tendon lengths,

velocities, and moment arms as a polynomial function of joint positions q and velocities \dot{q} [127]. For example, the second order polynomial approximation of the muscle-tendon length of a bi-articular muscle is:

$$l_{mt,\text{approx}} = c_1 + c_2 q_1 + c_3 q_2 + c_4 q_1 q_2 + c_5 q_1^2 + c_6 q_2^2, \quad (2.23)$$

where q_{1-2} are the positions of the two joints spanned by the muscle and c_{1-6} are polynomial coefficients. The general definition of a moment arm is [128]:

$$dM = -\frac{\partial l_{mt}}{\partial q}. \quad (2.24)$$

Equations 2.23 and 2.24 thus provide expressions for the second order polynomial approximation of the moment arms of the muscle:

$$dM_{q1,\text{approx}} = -(c_2 + c_4 q_2 + 2c_5 q_1), \quad (2.25)$$

$$dM_{q2,\text{approx}} = -(c_3 + c_4 q_1 + 2c_6 q_2), \quad (2.26)$$

where $dM_{q1-2,\text{approx}}$ are the approximated moment arms with respect to the two joints spanned by the muscle. Muscle-tendon velocities are defined as:

$$v_{mt} = \frac{dl_{mt}}{dt} = \frac{\partial l_{mt}}{\partial q} \frac{\partial q}{\partial t} = -dM\dot{q}, \quad (2.27)$$

which implies the following expression for the polynomial approximation of the muscle:

$$v_{mt,\text{approx}} = -dM_{q1,\text{approx}}\dot{q}_1 - dM_{q2,\text{approx}}\dot{q}_2. \quad (2.28)$$

In studies 3-5, we optimized the polynomial coefficients to fit muscle-tendon lengths and moment arms (maximal root mean square deviation: 3 mm; maximal order: ninth) obtained from OpenSim using a wide range of joint positions.

External forces

Our studies dealt with gait simulations, in which external forces only consisted of forces resulting from interactions between the feet and the ground. We modeled

these interactions using compliant Hunt-Crossley contact [119] between spheres attached to the feet and a plane representing the ground. We used a smooth approximation of the Hunt-Crossley contact model for use with gradient-based optimization algorithms. This model includes normal restoring force, dissipation force, and friction force. The normal restoring force was described by:

$$f_{\text{norm}} = \frac{4}{3}k\sqrt{rk} \left(\sqrt{p_d^2 + c_f} \right)^{3/2}, \quad (2.29)$$

where $k = 0.5E^{2/3}$ is a stiffness coefficient related to the material's plain strain modulus E , r is the radius of the contact sphere, p_d is the penetration depth, and $c_f = 10^{-5}$ is a constant that enforces a small contact force even when there is no contact between the sphere and the plane to ensure non-null derivatives. We used a tanh function to have a smooth transition between time periods with (positive penetration depth) and without (negative penetration depth) foot-ground contact:

$$f_{\text{norm},s} = f_{\text{norm}}(0.5 + 0.5 \tanh(b_{\text{norm}} p_d)), \quad (2.30)$$

where $b_{\text{norm}} = 300$ determines the smoothness of the tanh transition. The dissipation force was combined with the normal restoring force to form the Hunt-Crossley force:

$$f_{hc} = f_{\text{norm},s}(1 + 1.5c\dot{p}_d), \quad (2.31)$$

where $c = 2$ is a dissipation coefficient and \dot{p}_d is the penetration depth rate. We used a tanh function to have a smooth transition between null and positive Hunt-Crossley force:

$$f_{hc,s} = f_{hc} \left[0.5 + 0.5 \tanh \left(b_{hc} \left(\dot{p}_d + \frac{2}{3c} \right) \right) \right], \quad (2.32)$$

where $b_{hc} = 50$ determines the smoothness of the tanh transition. The friction force was defined by:

$$f_f = f_{hc,s} \left[\min(v_s/v_t, 1) \left(u_d + \frac{2(u_s - u_d)}{1 + (v_s/v_t)^2} \right) + u_v v_s \right], \quad (2.33)$$

where v_s is the slip velocity defined as the norm of the tangential velocity v_{tang} , $v_t = 0.2$ is the transition velocity, and $u_s = 0.8$, $u_d = 0.8$, and $u_v = 0.5$ are

coefficients of static, dynamic, and viscous friction, respectively. Finally, the contact force was described as:

$$f = f_{hc,s} d_{\text{norm}} + \frac{f_f v_{\tan}}{v_s}, \quad (2.34)$$

where d_{norm} is a vector defining the direction of the normal to the contact plane.

The number of contact spheres varied as a function of the model we used in our simulations (between two and six for 2D and 3D models, respectively) as did their locations in the feet and their radii. In studies 3-5, we optimized these locations and radii as part of gait simulations.

Skeleton movement

The skeleton dynamics were defined by the equations of motion:

$$M(q)\ddot{q} + C(q, \dot{q}) + G(q) + F_{\text{ext}} = T, \quad (2.35)$$

where M is the system mass matrix, \ddot{q} are joint accelerations, C is the vector of Coriolis and centrifugal forces, G is the vector of gravitational force, F_{ext} is the vector of external forces, and T is the vector of joint torques. To facilitate the reading, we will distinguish torques at the pelvis T_{pelvis} (pelvis residuals) from torques at the other joints T_{joints} . A dynamically consistent movement has null pelvis residuals.

In our simulations, we used an implicit formulation of the skeleton dynamics with joint positions and velocities as states, and introducing new controls $u_{d\dot{q}}$ for the time derivatives of the joint velocities, namely the joint accelerations ($u_{d\dot{q}} = \ddot{q}$). With such formulation, the dynamic equations become:

$$\frac{dq}{dt} = \dot{q}, \quad (2.36)$$

$$\frac{d\dot{q}}{dt} = u_{d\dot{q}}, \quad (2.37)$$

and the joint torques from the skeleton dynamics (equation 2.35) are imposed to equal those from muscles and, potentially, passive structures. In studies 3-5, we

added passive joint torques to our models that mimic the role of the ligaments and other passive structures. These torques were modeled by [35]:

$$T_p = k_1 e^{k_2(q-\theta_1)} + k_3 e^{k_4(q-\theta_2)} - d_p \dot{q}, \quad (2.38)$$

where k_{1-4} are coefficients, θ_{1-2} are reference joint angles, and d_p is a damping factor. Passive torques are generated in extreme positions (i.e., when joint angles exceed the reference joint angles). Using such torques result in the following equilibrium:

$$T_{\text{joints}}(q, \dot{q}, \ddot{q}) = T_m(\tilde{F}_t) + T_p(q, \dot{q}). \quad (2.39)$$

Note that T_m should be replaced by $T_{\text{trunk/arms}}$ in case the joint is not driven by muscles but by ideal torque actuators, as was modeled for the arm joints and, in some cases, for the lumbar joint in our studies.

Neural system

The neural system generates muscle excitations that drive the musculoskeletal system following a certain control strategy. Under the assumption of optimal performance, this strategy is modeled through a performance criterion. The neural system also includes sensory feedback pathways that generate muscle excitations based on delayed feedback from sensory information. In children with CP, these feedback pathways may be dysregulated due to spasticity [95]. In addition, CP may induce a lack of selective motor control, typically modeled through muscle synergies [61].

Performance criterion

The performance criterion is modeled through the cost function of the optimal control problem. In studies 3-5, we used multi-objective cost functions combining physiologically-relevant walking-related performance criteria. We used different cost functions depending on the complexity of the model (2D versus 3D) and the type of problem (tracking versus predictive). In tracking problems, the kinematics and external forces are known, and the cost function should mainly allow solving the muscle redundancy (i.e., the fact that each movement can be achieved by an infinite number of possible muscle recruitment strategies due to overactuation of the musculoskeletal system). In predictive problems, the cost function should capture the high-level control strategy underlying the

intended task, and allow solving both kinematic and muscle redundancies (the kinematic redundancy being the fact that a given task can be achieved by an infinite number of possible movement patterns). Since the redundancies increase with the complexity of the musculoskeletal model, a cost function that captures human walking with a 2D model might not perform as well for a 3D model. We designed our multi-objective cost functions as weighted sums of different terms, each term representing a performance criterion, and selected criteria whose omission from the cost function deteriorated the human representativeness of our simulations. We followed heuristic approaches to select the weight factors.

In study 3, we generated predictive simulations of walking with a 2D model and tracking simulations of walking with a 3D model. For the 2D predictive simulations, we used a cost functional that combined muscle fatigue (i.e., muscle activations at the third power [39]), joint accelerations, and excitations of ideal trunk actuators:

$$J_{\text{pred2D}} = \int_{t_0}^{t_f} \frac{1}{d} \left(\underbrace{w_1 \|a\|_3^3}_{\text{Muscle fatigue}} + \underbrace{w_2 \|u_{dq}\|_2^2}_{\text{Joint accelerations}} + \underbrace{w_3 \|e_{\text{trunk}}\|_2^2}_{\text{Trunk excitations}} \right) dt, \quad (2.40)$$

where d is distance traveled by the pelvis in the forward direction and w_{1-3} are weight factors. To avoid singular arcs, situations for which controls appear only linearly in the constraints and, therefore, are not uniquely defined by the optimality conditions [129], we appended a penalty function with the remaining controls to the cost functional:

$$J_{\text{pred2D},p} = \int_{t_0}^{t_f} \frac{w_u}{d} \left(\|u_{da}\|_2^2 + \|u_{d\tilde{F}_t}\|_2^2 \right) dt, \quad (2.41)$$

where $w_u = 0.001$ weights the penalty function against the other terms in the cost functional. For the 3D tracking simulations, we used a cost functional that combined muscle effort (i.e., squared muscle activations [39]) and the difference between simulated and measured joint positions, GRFs, ground reaction torques (GRTs), and joint torques:

$$J_{\text{track3D}} = \int_{t_0}^{t_f} \left(\underbrace{w_1 \|a\|_2^2}_{\text{Muscle effort}} + \underbrace{w_2 \|q - \hat{q}\|_2^2}_{\text{Joint positions}} + \underbrace{w_3 \|GRF - G\hat{R}F\|_2^2}_{\text{Ground reaction forces}} \right. \\ \left. + \underbrace{w_4 \|GRT - G\hat{R}T\|_2^2}_{\text{Ground reaction torques}} + \underbrace{w_5 \|T_{\text{joints}} - \hat{T}_{\text{joints}}\|_2^2}_{\text{Joint torques}} \right) dt, \quad (2.42)$$

where w_{1-5} are weight factors and hats indicate measured data. We appended a penalty function with the remaining controls to the cost functional:

$$J_{\text{track3D},p} = \int_{t_0}^{t_f} w_u (\|u_{da}\|_2^2 + \|u_{d\tilde{F}_t}\|_2^2 + \|u_{d\dot{q}}\|_2^2) dt. \quad (2.43)$$

In study 4, we generated predictive simulations of walking with a 3D model and used a cost functional that combined metabolic energy rate, muscle effort, joint accelerations, passive joint torques, and excitations of ideal arm actuators:

$$J_{\text{pred3D}} = \int_{t_0}^{t_f} \frac{1}{d} \left(\underbrace{w_1 \|\dot{E}\|_2^2}_{\text{Metabolic energy rate}} + \underbrace{w_2 \|a\|_2^2}_{\text{Muscle effort}} + \underbrace{w_3 \|u_{d\dot{q},\text{ll-trunk}}\|_2^2}_{\text{Joint accelerations}} \right. \\ \left. + \underbrace{w_4 \|T_p\|_2^2}_{\text{Passive torques}} + \underbrace{w_5 \|e_{\text{arms}}\|_2^2}_{\text{Arm excitations}} \right) dt, \quad (2.44)$$

where \dot{E} is metabolic energy rate, w_{1-5} are weight factors, and $u_{d\dot{q},\text{ll-trunk}}$ are joint accelerations of the lower limb and trunk DOFs. We appended a penalty function with the remaining controls to the cost functional:

$$J_{\text{pred3D},p} = \int_{t_0}^{t_f} \frac{w_u}{d} \left(\|u_{da}\|_2^2 + \|u_{d\bar{F}_t}\|_2^2 + \|u_{d\dot{q},\text{arms}}\|_2^2 \right) dt, \quad (2.45)$$

where $u_{d\dot{q},\text{arms}}$ are joint accelerations of the arm DOFs. We modeled metabolic energy rate using a smooth approximation of the phenomenological model described by Bhargava *et al.* [130]. This metabolic model requires parameters for fiber type composition and muscle specific tension, which we obtained from the literature [131]. We performed the smooth approximation using tanh functions.

In study 5, we used a similar cost functional as in study 4 (equations 2.44-2.45) but also considered sensory feedback and synergistic muscle activations.

Sensory feedback

The sensory feedback describes how muscle excitations are generated based on delayed feedback from sensory information. We primarily used such feedback pathway to model spasticity (studies 2 and 5). Spasticity can be described as an exaggerated muscle activity in response to muscle spindle firing. Therefore, we modeled such phenomenon as exaggerated feedback muscle excitations e_s from delayed sensory information s (i.e., muscle states). We tested different sources of sensory information as feedback drivers, namely fiber length, velocity, acceleration, tendon force, and the first time-derivative of tendon force (i.e., force rate). We described the dynamics of the feedback model through a smooth first order differential equation relating controls s and states e_s in an explicit way:

$$f = 0.5 \tanh(b_s(s - T_s)), \quad (2.46)$$

$$\frac{de_s}{dt} = -\frac{e_s}{\tau_s} + \frac{g_s s (f + 0.5)}{\tau_s}, \quad (2.47)$$

where T_s is a feedback threshold, g_s is a feedback gain, $\tau_s = 30$ ms is the time delay, and $b_s = 100$ determines the smoothness of the tanh transition.

In study 2, we optimized the feedback gains that minimized the difference between feedback muscle excitations and EMG. In a pre-processing phase, we first used EMG-driven forward simulations to generate the sensory information

(source of feedback). We then determined the feedback thresholds for fiber length, velocity, and tendon force as the values 20 ms before the EMG onset that we identified according to the method of Staude and Wolf [132]. We used zero thresholds for fiber acceleration and force rate feedback (i.e. there is feedback when the signal is positive). In study 5, we determined the feedback thresholds and identified the feedback gains following the same process. We then incorporated the feedback model dynamics as part of the optimal control problem. Finally, the feedback commands were combined with the feedforward commands and served as inputs to the muscle dynamics. Since, we used an implicit formulation of activations dynamics, muscle excitations were eliminated from the problem formulation and we considered the feedback signals to be muscle activations rather than muscle excitations.

Muscle synergies

Muscle synergies describe how groups of muscles are activated in a fixed ratio by a single input signal [60]. Synergies can be formulated through two matrices: a $N_{\text{syn}} \times N_f$ matrix H , where N_{syn} is the number of synergies and N_f is the number of frames (e.g., 100 frames for a gait cycle means one frame per percent), containing synergy activation profiles and a $N_m \times N_{\text{syn}}$ matrix W , where N_m is the number of muscles, containing weight factors that determine the contribution of each muscle in each synergy. Muscle activations are then composed as:

$$a_{\text{syn}} = W \times H, \quad (2.48)$$

where a_{syn} has dimensions $N_m \times N_f$.

In study 5, we imposed synergistic muscle activations. We formulated the synergy activation dynamics in a similar way as the implicit muscle activation dynamics (equations 2.7-2.9). Specifically, we used H as states and introduced controls that are the derivatives of the states u_H :

$$\frac{dH}{dt} = s_a u_{dH}. \quad (2.49)$$

where $s_a = 100$ is the same as in the muscle activation dynamics (equation 2.7). We then imposed the differential equations describing synergy activation dynamics as path constraints:

$$0 \leq s_a u_{dH} + \frac{H}{\tau_d}, \quad (2.50)$$

$$s_a u_{dH} + \frac{H}{\tau_a} \leq \frac{1}{\tau_a}, \quad (2.51)$$

where $\tau_a = 15$ ms and $\tau_d = 60$ ms are the same time constants as in the muscle activation dynamics (equations 2.8-2.9). Finally, we composed muscle activations from synergy activations following equation (2.48) where synergy weights were time-independent parameters (optimization variables). The resultant muscle activations were inputs to the muscle contraction dynamics. This formulation reduces the neuromuscular control complexity by decreasing the number of optimization variables (there are as many controls and states for activation dynamics as there are synergies rather than muscles).

Chapter 3

Study 1: EMG-driven optimal estimation of subject-specific Hill model muscle-tendon parameters of the knee joint actuators

Published as:

Falisse A., Van Rossum S., Jonkers I., De Groot F. *EMG-driven optimal estimation of subject-specific Hill model muscle-tendon parameters of the knee joint actuators*, (2017). IEEE Transactions on Biomedical Engineering, **64**(9): 2253-2262.

Abstract

Objective: the purpose of this paper is to propose an optimal control problem formulation to estimate subject-specific Hill model muscle-tendon (MT-) parameters of the knee joint actuators by optimizing the fit between experimental and model-based knee moments. Additionally, this paper aims at determining which sets of functional motions contain the necessary information to identify the MT-parameters. **Methods:** the optimal control and parameter estimation problem underlying the MT-parameter estimation is solved for subject-specific MT-parameters via direct collocation using an electromyography-driven musculoskeletal model. The sets of motions containing sufficient information to identify the MT-parameters are determined by evaluating knee moments simulated based on subject-specific MT-parameters against experimental moments. **Results:** the MT-parameter estimation problem was solved in about 30 CPU minutes. MT-parameters could be identified from only seven of the 62 investigated sets of motions, underlining the importance of the experimental protocol. Using subject-specific MT-parameters instead of more common linearly scaled MT-parameters improved the fit between inverse dynamics moments and simulated moments by about 30% in terms of the coefficient of determination (from 0.57 ± 0.20 to 0.74 ± 0.14) and by about 26% in terms of the root mean square error (from 15.98 ± 6.85 to 11.85 ± 4.12 N·m). In particular, subject-specific MT-parameters of the knee flexors were very different from linearly scaled MT-parameters. **Conclusion:** we introduced a computationally efficient optimal control problem formulation and provided guidelines for designing an experimental protocol to estimate subject-specific MT-parameters improving the accuracy of motion simulations. **Significance:** the proposed formulation opens new perspectives for subject-specific musculoskeletal modeling, which might be beneficial for simulating and understanding pathological motions.

Introduction

Human motions can be simulated using musculoskeletal models that reproduce the muscle-tendon (MT-) force distribution and translate it into skeletal motions. The MT-force distribution is calculated from the MT-dynamics that comprise activation and contraction dynamics describing the nonlinear relations between muscle excitation and muscle activation and between muscle activation and MT-force, respectively. The contraction dynamics can be represented by the Hill model [27] that defines the force generating capacity of a MT-actuator based on five MT-parameters: the maximal isometric muscle force F_m^{\max} , the optimal

muscle fiber length l_m^{opt} , the tendon slack length l_t^s , the maximal muscle fiber velocity v_m^{max} , and the optimal pennation angle α^{opt} . The MT-parameters are difficult to estimate from *in vivo* measurements and are mostly compiled from cadaver studies [63, 133, 134]. Different methods then exist to scale these generic parameters based on the subject's anthropometry. Although linear scaling is common, scaling methods that preserve the muscle operating range, such as proposed by Winby *et al.* [85] and recently generalized by Modenese *et al.* [86], have been shown to be more accurate. Yet the MT-properties are known to vary with age, gender, and activity level [78, 79]. They are hence subject-specific and cannot be truly estimated based on anthropometrical dimensions only. In this study, we therefore rely on a functional approach (i.e., based on experimental angle-moment relationships) to estimate subject-specific MT-parameters. In particular, we focus on the estimation of l_t^s and l_m^{opt} as joint moment simulations are most sensitive to those two MT-parameters [104, 105, 106, 107].

The overall approach to estimate subject-specific parameters based on a functional approach is to minimize the difference between experimental and model-based joint moments by optimizing the parameters. Such an approach was used to determine subject-specific torque-angle-angular velocity relationships [135] and subject-specific MT-parameters. In the second case, we can distinguish approaches based on maximal and submaximal muscle contraction that rely on angle-moment relationships measured during isometric dynamometry [87, 136, 89], and functional motions [90, 108], respectively. Isometric dynamometry, however, has several limitations, restricting its use for estimating MT-parameters. First, a complete and large set of measurements is difficult to obtain, since it requires many maximal voluntary contractions leading to a lengthy protocol and requiring substantial effort from the test subject which may cause fatigue [136, 89]. Second, maximal muscle contraction is practically never reached [93], limiting the applicability of such approaches as illustrated by Wesseling *et al.* [137]. For these reasons, we selected a submaximal contraction-based approach to estimate subject-specific MT-parameters. Such an approach allows the collection of a rich experimental dataset with standard motion capture equipment. Although muscle excitation is *a priori* unknown in submaximal contraction-based approaches, electromyography (EMG) provides a muscle excitation estimate that can drive musculoskeletal models to simulate joint moments during functional motions (e.g., EMG-driven models (EDMs) of the knee [90, 138]). In this study, we use an EDM to estimate MT-parameters by optimizing the fit between experimental and model-based joint moments. Since the MT-parameter dependent relationship between EMG and joint moments is dynamic, solving the corresponding optimization problem requires the transcription of an infinite dimensional problem into a finite-dimensional approximation. Estimating the MT-parameters using this approach therefore

corresponds to solving an optimal control and parameter estimation problem, also referred to as an optimal estimation problem [139].

The formulation of the MT-parameter estimation problem influences the convergence and efficiency of the numerical optimization. Numerically efficient formulations of the MT-parameter estimation problem were introduced [136, 89], but only for methods based on maximal contraction-based approaches that do not include the MT-dynamics. When considering the MT-dynamics for consistency with muscle physiology, the problem becomes challenging to solve due to the nonlinearity and stiffness of the dynamic equations. A suitable numerical method is therefore required to solve the underlying complex system of differential equations. Direct collocation methods have recently become increasingly popular for the numerical solution of optimal control problems and were used in several human motion simulation studies [39, 140, 53]. A direct collocation method implicitly takes the system dynamics into account by parameterizing both controls and states, defining a sparse and thus tractable nonlinear programming problem (NLP). Collocation methods are often more computationally efficient than, for example, shooting methods that rely on explicit integration of the dynamic equations [90, 108, 35]. The first aim of this study is to use, for the first time, a direct collocation method to estimate subject-specific MT-parameters, relying on a robust and computationally efficient formulation of the optimal estimation problem [53].

In particular, this study seeks to estimate subject-specific MT-parameters that represent the subject's MT-properties rather than optimize the fit with the experimental data for a set of motions. This is an important requirement when using the subject-specific models in predictive *what if* scenarios that differ from the experimental conditions. Since the information in the experimental dataset determines whether the MT-parameters can be accurately estimated, a careful selection of the experimental dataset is required. When the dataset contains insufficient information, the experimental data can be fitted with high precision while the estimated parameters are inaccurate and hence result in unreliable predictions for motions that were not included in the dataset. This phenomenon is known as overfitting [91]. We thus want to select experimental datasets that can identify the MT-parameters and hence provide valid MT-parameter estimates. The second aim of this study is therefore to investigate the identifiability of the MT-parameters based on different sets of motions. To this end, the accuracy of knee moment simulations based on subject-specific MT-parameters estimated from various sets of motions was evaluated. In this study, novelty is twofold. First, an optimal estimation problem is formulated to efficiently estimate subject-specific MT-parameters of the knee actuators

based on an EDM. Second, the identifiability of the MT-parameters based on different sets of motions is studied to provide valuable information regarding the experimental datasets needed for their estimation.

Methods

A. Experimental data

Eight healthy volunteers (four males and four females, age 29.8 ± 3.9 years, height 176 ± 6.6 cm, and weight 69.6 ± 6.0 kg) gave informed consent to participate in the study approved by the Ethics Committee at UZ Leuven (Belgium). Each subject was instrumented with 65 retro-reflective skin-mounted markers, corresponding to an extended plug-in-gait marker set, whose 3-D locations were recorded (100 Hz) using a ten-camera motion capture system (Vicon, Oxford, UK) during six functional motions: gait, squat, stair descent, stair ascent, sit-to-stand-to-sit, and squat jump. The motions were chosen as they:

1. encompass a wide range of contractile conditions;
2. require large knee moments (up to ~ 100 N·m);
3. require a large range of knee angles ($\sim 2^\circ$ to 100° knee flexion);
4. reflect various MT-force distributions; and
5. are easily achievable in practice.

In particular, the squat jump motion was included as it requires higher muscle activation. The wide variety of motions was intended to provide a dataset with sufficient information to estimate MT-parameters that truly represent the subject's MT-properties rather than only reproduce the experimental data. Ground reaction forces (GRF) and EMG data were recorded (1000 Hz) using force plates (AMTI, Watertown, USA) and wireless EMG acquisition systems (ZeroWire EMG Aurion, Milano, Italy), respectively. GRF were low-pass filtered (10 Hz) using a fourth-order Butterworth filter. EMG data were collected from six muscle groups of each leg (see Table 3.1) and were processed by band-bass filtering (20-400 Hz), full-wave rectification, and low-pass filtering (10 Hz) using a fourth-order Butterworth filter. EMG data were also collected during maximum voluntary contraction (MVC) trials and processed using the same protocol. To robustly determine the maximal EMG values, a centered moving

average with a 50 ms time window was applied to the processed EMG data of both functional motions and MVC trials. The resulting peak values were then used to normalize the EMG envelopes [141]. Based on the quality of the normalized EMG envelopes, 11 experimental datasets (seven left and four right legs) were selected.

Experimental EMG envelopes	Model's knee actuators
Hamstring lateralis	Biceps femoris long head (BFLH) Biceps femoris short head (BFSH)
Gastrocnemius lateralis	Gastrocnemius lateralis (GL) Gastrocnemius medialis (GM)
Hamstring medialis	Semimembranosus (SM) Semitendinosus (ST) Sartorius (SA) Gracilis (GR)
Rectus femoris	Rectus femoris (RF)
Average (vastus lateralis, vastus medialis)	Vastus intermedius (VI)
Vastus lateralis	Vastus lateralis (VL)
Vastus medialis	Vastus medialis (VM)

Table 3.1: Assignment of EMG envelopes to the model's knee actuators.

B. Musculoskeletal model and data processing

The experimental data were processed in OpenSim 3.2 [112] based on the gait2392 musculoskeletal model containing 20 segments and 23 degrees of freedom (DOFs) [63]. The marker-based knee axis of this model was replaced by a functional axis, estimated based on knee flexion-extension measurements [113]. Each knee joint was actuated by 12 MT-actuators ($N = 12$): eight flexors (biceps femoris long head (BFLH), biceps femoris short head (BFSH), sartorius (SA), gastrocnemius lateralis (GL), gastrocnemius medialis (GM), semimembranosus (SM), semitendinosus (ST), and gracilis (GR)) and four extensors (rectus femoris (RF), vastus intermedius (VI), vastus lateralis (VL), and vastus medialis (VM)). The musculoskeletal model was scaled to the subject's anthropometry using OpenSim's scale tool based on marker information collected during a static trial. This process included linear scaling of l_t^s and l_m^{opt} using a scale factor computed as the ratio of the corresponding MT-actuator's length before and after scaling. This approach therefore preserves the ratio l_m^{opt} to l_t^s . For each functional motion, joint kinematics and moments were calculated based on marker trajectories and GRF by successively applying a Kalman smoothing algorithm for inverse kinematics [115] and an inverse dynamics (ID) analysis via OpenSim. Only knee flexion-extension moments were further considered. MT-lengths and moment

arms were computed as a function of the joint kinematics using OpenSim's muscle analysis tool. The EMG envelopes were assigned to the model's knee actuators as described in Table 3.1. Hamstring lateralis EMG drove both BFLH and BFSH. Hamstring medialis EMG drove SM and ST [108] as well as SA and GR. GL EMG drove both GM and GL, whilst the input of VI was estimated as the average of VL and VM EMG [90, 108]. An electromechanical delay of 40 ms was introduced by time-shifting the EMG envelopes [91]. The MT-dynamics, comprising activation and contraction dynamics, were described by two nonlinear first-order differential equations relating the control, muscle excitation, to the states, neural excitation and normalized muscle fiber length. Activation dynamics were defined based on Thelen [30, 28]:

$$r = f_a(e), \quad (3.1)$$

where f_a describes the transformation from muscle excitation e to neural excitation r . This equation was augmented with the EMG-to-activation relationship [90, 91] relating neural excitation r to muscle activation a :

$$a = \frac{e^{Ar} - 1}{e^A - 1}, \quad (3.2)$$

where A is a nonlinear shape factor. Contraction dynamics were described by the Hill model [27] that defines the MT-actuator as a tendon in series with a pennate muscle. The tendon is modeled as a nonlinear spring of length l_t and the muscle, of length l_m with pennation angle α , consists of a contractile element (CE) in parallel with a passive element (PE) (see Figure 3.1). The MT-force F_{mt} was given by:

$$F_{mt} = F_t(\tilde{l}_t) = F_m(a, \tilde{l}_m, \tilde{v}_m) \cos \alpha, \quad (3.3)$$

where F_t is tendon force, which is a function of the normalized tendon length $\tilde{l}_t = l_t/l_t^s$, and F_m is muscle force, which is a function of muscle activation a , normalized muscle fiber length $\tilde{l}_m = l_m/l_m^{\text{opt}}$ and normalized muscle fiber velocity $\tilde{v}_m = v_m/v_m^{\text{max}}$ (see Appendix A for more details).

C. Optimal estimation of subject-specific MT-parameters

The overall process to solve the optimal estimation problem for subject-specific MT-parameters is outlined in Figure 3.2(a).

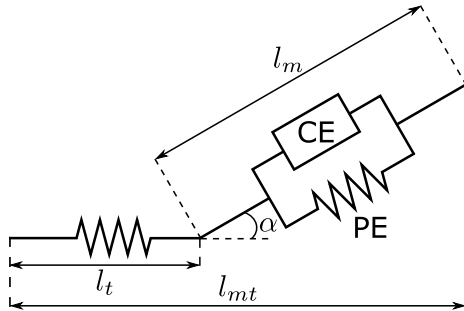


Figure 3.1: **Schematic representation of the Hill model [27].** The MT-actuator, of length l_{mt} , comprises a tendon in series with a pennate muscle. The tendon is modeled as a nonlinear spring of length l_t . The muscle, of length l_m , consists of a contractile element (CE) parallel to a passive element (PE). The pennation angle α is the angle between the orientation of the muscle fibers and the tendon.

1) Multiple-phase optimal estimation problem

The subject-specific MT-parameters were estimated based on different sets of motions, later referred to as calibration sets. Each calibration set represents a possible combination amongst the six motions. There exist thus 63 ($\sum_{i=1}^6 6! / i!(6-i)!$) possible calibration sets. For each of these sets, a multiple-phase optimal estimation problem with each phase corresponding to a motion was solved for subject-specific MT-parameters. For example, the calibration set consisting of gait and squat results in a two-phase optimal estimation problem (phase 1: gait and phase 2: squat) which is solved for the corresponding subject-specific MT-parameters. Solving the optimal estimation problem consisted in determining the controls, states and static parameters (defined in section C2) satisfying the constraints imposing the MT-dynamics (C3), the boundary conditions (C4), and the path constraints (C5), while optimizing a cost functional (C6).

2) Static parameters

l_t^s and l_m^{opt} of eight ($J = 8$) knee actuators (four flexors: BFLH, GL, GM, SM and four extensors: RF, VI, VL, VM) were estimated based on a sensitivity analysis [106]. Values from the linearly scaled models were assigned to the other MT-parameters.

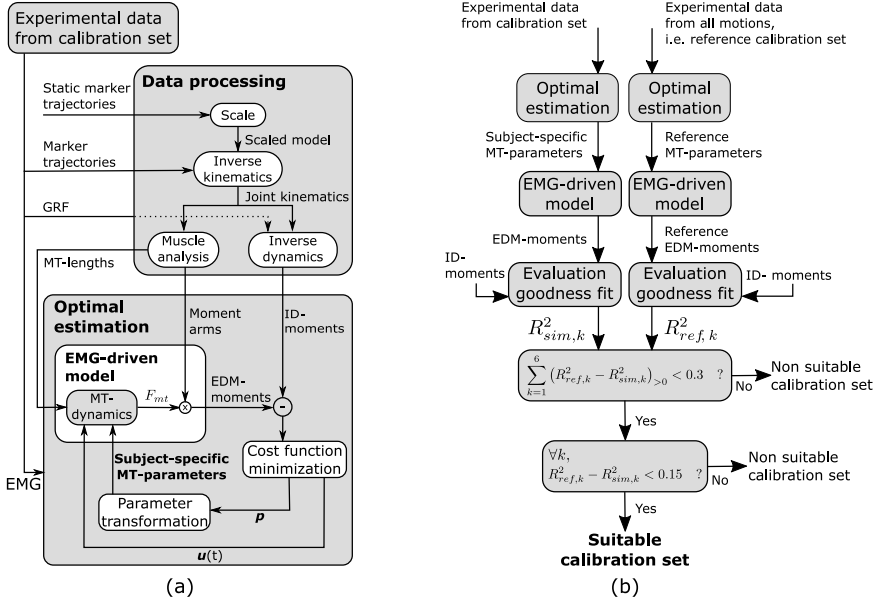


Figure 3.2: (a) Flowchart illustrating the process used to estimate the subject-specific MT-parameters. The optimal estimation problem underlying the MT-parameter estimation is solved for the states $x(t)$ (defining the MT-force F_{mt}), controls $u(t)$, and static parameters p that minimize the difference between ID- and EDM-moments. A parameter transformation is applied to extract the subject-specific MT-parameters from the static parameters. (b) Flowchart illustrating the process used to select the calibration sets that are suitable (i.e., contain sufficient information) to identify the MT-parameters. $k = 1, \dots, 6$ represents the functional motions.

For each knee actuator j ($j = 1, \dots, J$), physiologically feasible combinations $[l_{m,j}^{\text{opt}}, l_{t,j}^s]$ were defined to constrain the search space of the optimal estimation problem as described by Van Campen *et al.* [89]. Furthermore, to improve the numerical condition of the problem, the ratio $l_{t,j}^s/l_{m,j}^{\text{opt}}$ and a parameter δ_j were used as static parameters instead of $l_{t,j}^s$ and $l_{m,j}^{\text{opt}}$. The parameter δ_j determines the deviation from the first-order regression of the physiologically feasible combinations $[1/l_{m,j}^{\text{opt}}, l_{t,j}^s/l_{m,j}^{\text{opt}}]$ defined by:

$$\frac{1}{l_{m,j}^{\text{opt}}} - C_{1,j} \frac{l_{t,j}^s}{l_{m,j}^{\text{opt}}} - C_{2,j} = \delta_j, \quad (3.4)$$

where $C_{1,j}$ and $C_{2,j}$ are the regression coefficients [89] (see Appendix A for more details).

A single nonlinear shape factor A (3.2) for all muscles was added to the set of static parameters.

3) Constraints imposing the MT-dynamics

The MT-dynamics were formulated as described by De Groote *et al.* [53]. Activation dynamics were imposed using muscle excitation e and neural excitation r as respectively control and state. Contraction dynamics were imposed using normalized muscle fiber length \tilde{l}_m as state and introducing u_v , the scaled time derivative of \tilde{l}_m , as a new control simplifying the dynamic equations:

$$\frac{d\tilde{l}_m}{dt} = \frac{v_m^{\max}}{l_m^{\text{opt}}} u_v, \quad (3.5)$$

where $v_m^{\max}/l_m^{\text{opt}}$ is a scaling factor that converts u_v into \tilde{v}_m . The nonlinear equations describing the contraction dynamics were then imposed as algebraic constraints in their implicit form, simplifying their evaluation. Efficiency and robustness of this implicit formulation of the contraction dynamics were previously demonstrated [53].

4) Boundary conditions

States $\mathbf{x}(t) = [r_j, \tilde{l}_{m,j}]$, controls $\mathbf{u}(t) = [e_j, u_{v,j}]$ and static parameters $\mathbf{p} = [l_{t,j}^s/l_m^{\text{opt}}, \delta_j, A]$ were bounded by:

$$0 \leq r_j, e_j \leq 1, \quad (3.6)$$

$$0.4 \leq \tilde{l}_{m,j} \leq 1.6, \quad (3.7)$$

$$-1 \leq u_{v,j} \leq 1, \quad (3.8)$$

$$\left(\frac{l_{t,j}^s}{l_{m,j}^{\text{opt}}} \right)^{\min} \leq \frac{l_{t,j}^s}{l_{m,j}^{\text{opt}}} \leq \left(\frac{l_{t,j}^s}{l_{m,j}^{\text{opt}}} \right)^{\max}, \quad (3.9)$$

$$\delta_j^{\min} \leq \delta_j \leq \delta_j^{\max}, \quad (3.10)$$

$$-3 < A < 0. \quad (3.11)$$

Constraints (3.6-3.8) were based on the definition of the Hill model [27], (3.9) and (3.10) followed from the definition of the physiologically feasible combinations and (3.11) was imposed to limit the variation of the nonlinear shape factor A in the EMG-to-activation relationship [90, 91].

5) Path constraints

Additional path constraints were introduced:

$$-0.01 < e_j - EMG_j < 0.01, \quad (3.12)$$

$$-0.9 < \frac{l_{m,VI}^{\text{opt}}}{l_{m,VL}^{\text{opt}}}, \frac{l_{m,VI}^{\text{opt}}}{l_{m,VM}^{\text{opt}}}, \frac{l_{m,VL}^{\text{opt}}}{l_{m,VM}^{\text{opt}}} < 1.1, \quad (3.13)$$

$$-0.9 < \frac{l_{m,GL}^{\text{opt}}}{l_{m,GL}^{\text{opt}}} < 1.1. \quad (3.14)$$

Nonzero bounds were chosen in (3.12) to allow for small deviations from the measured EMG signals in order to compensate for measurement errors. Only small deviations were permitted to limit the redundancy (a better fit between simulated and ID-moments can be obtained by optimizing either muscle excitation or MT-parameters). Constraints (3.13) and (3.14) were anatomically-informed and, respectively, enforced that optimal muscle fiber lengths of the three vasti and both gastrocnemii were in the same range [89].

6) Cost functional

The multiple-phase optimal estimation problem was solved by determining, in each phase, the controls $\mathbf{u}(t)$, states $\mathbf{x}(t)$ and phase-independent static parameters \mathbf{p} that minimize the cost functional:

$$L = \int_{t_i}^{t_f} (M_{\text{ID}}(t) - M_{\text{EDM}}(\mathbf{u}(t), \mathbf{x}(t), \mathbf{p}))^2 dt, \quad (3.15)$$

where t is the time, t_i and t_f are the initial and final times, M_{ID} represents the ID-moments, and M_{EDM} represents the EDM-moments given by:

$$M_{\text{EDM}} = \sum_{j=1}^J d_j(t) F_{t,j}(\mathbf{u}(t), \mathbf{x}(t), \mathbf{p}) + f, \quad (3.16)$$

where d_j is the moment arm of knee actuator j . The contribution to the knee moments of the four ($B = 4$) knee actuators whose MT-parameters were not estimated was precomputed:

$$f = \sum_{b=1}^B d_b(t) F_{t,b}(\text{EMG}(t)), \quad (3.17)$$

where $F_{t,b}$ was obtained by forward integration of the MT-dynamic equations using the EMG envelope as control.

Finally, to penalize deviation of muscle excitation from the EMG envelope, a penalty function ϕ was appended to the cost functional:

$$\phi = w \int_{t_i}^{t_f} \sum_{j=1}^J (e_j - \text{EMG}_j)^2 dt, \quad (3.18)$$

where $w = 1000$ is a parameter that weights the penalty function against the other term in the cost functional.

7) Computational solution

The optimal estimation problem was solved numerically via direct collocation using GPOPS-II optimal control software [121]. The problem was solved on

a mesh of 100 intervals per motion using third-order Legendre-Gauss-Radau collocation. The interior point solver IPOPT [122] was used to solve the resulting NLP using second order derivative information. The derivatives required by the NLP solver were provided by the open-source automatic differentiation software ADiGator [142].

8) Initial guess

To decrease the probability of finding local optima as a consequence of using a gradient-based method, the optimal estimation problem was solved using two initial guesses of static parameters. The first initial guess was based on a precomputed hot start whereas the second initial guess was arbitrary (see Appendix A for more details). The solution resulting in the smallest value of the cost functional was then selected.

D. MT-parameter identification

MT-parameters were estimated from each calibration set resulting in 63 estimates of subject-specific MT-parameters per dataset. The motions belonging to the calibration sets will be referred to as calibration motions and the remaining motions as validation motions. For example, when MT-parameters are estimated based on experimental data from gait and squat, the calibration motions are gait and squat and the validation motions are stair ascent, stair descent, sit-to-stand-to-sit, and squat jump.

Knee moments (EDM-moments) were computed via forward integration of the MT-dynamic equations using the EMG envelopes as controls for all motions and for the 63 MT-parameter estimates. Two metrics were used to evaluate the goodness of fit between ID- and EDM-moments: the coefficient of determination (R^2) and the root mean square error (RMSE).

The calibration set containing all six motions was chosen as reference calibration set and we refer to the corresponding MT-parameter estimate and EDM-moments as, respectively, reference MT-parameters and reference EDM-moments. The reference MT-parameters minimize the difference between ID and EDM-moments over all motions, resulting in the best overall fit but not in the best fit for each individual motion.

The identifiability of the MT-parameters from different calibration sets was assessed by comparing the coefficients of determination calculated between ID- and EDM-moments (R^2_{sim}) to the ones calculated between ID- and reference EDM-moments (R^2_{ref}). Calibration sets for which R^2_{sim} were similar to R^2_{ref} for all motions were considered suitable to identify the MT-parameters. The process for selecting the calibration sets that were suitable to identify the MT-parameters is outlined in Figure 3.2(b). The similarity between R^2_{sim} and R^2_{ref} was evaluated based on two criteria: 1) the sum of the positive deviations (i.e., if $R^2_{ref} - R^2_{sim} > 0$) over all motions was limited to 0.3; and 2) a deviation ($R^2_{ref} - R^2_{sim}$) larger than 0.15 was not allowed for any individual motion. These criteria were chosen to limit the overall deviation from reference EDM-moments as well as the deviation for each individual motion. This second criterion was especially important to prevent overfitting characterized by a good fit for the calibration motions but large deviations for validation motions. In total, subject-specific MT-parameters estimated from 62 calibration sets were investigated and compared to the reference MT-parameters. Calibration sets that were suitable across all 11 datasets were selected. The other calibration sets did not result in valid MT-parameter estimates as they failed to reproduce the joint moments for the validation motions. The subject-specific MT-parameters were then compared to 1) the reference MT-parameters; 2) the linearly scaled MT-parameters obtained from OpenSim's scale tool; and 3) the nonlinearly scaled MT-parameters computed using an anthropometric algorithm recently proposed by Modenese *et al.* [86] (see Appendix A for more details regarding the implementation of the algorithm).

Results

Seven of the 62 investigated calibration sets satisfied both criteria across all 11 datasets and were thus suitable to identify the MT-parameters (calibration sets A-G in Table 3.2). Gait and sit-to-stand-to-sit were part of all (7/7) suitable calibration sets followed by squat jump (6/7), squat and stair ascent (4/7), and stair descent (3/7).

EMG-driven simulations based on subject-specific MT-parameters yielded more accurate knee moment predictions than simulations based on anthropometry-based scaled MT-parameters (see Table 3.3). The fits between ID- and EDM-moments improved from 0.57 ± 0.20 to 0.74 ± 0.14 in terms of R^2 and 15.98 ± 6.85 to 11.85 ± 4.12 N·m in terms of RMSE using subject-specific MT-parameters rather than linearly scaled MT-parameters. These results are averaged over all six motions, 11 datasets and, for subject-specific MT-parameters, seven suitable

Calibration sets	Gait	Squat	Calibration motions				CPU time (mean)
			Stair descent	Stair ascent	Sit-to-stand-to-sit	Squat jump	
A	x				x	x	17 min
B	x	x			x	x	26 min
C	x			x	x	x	22 min
D	x	x	x	x	x		34 min
E	x	x	x		x	x	41 min
F	x	x		x	x	x	37 min
G	x		x	x	x	x	31 min
Reference	x	x	x	x	x	x	53 min

Table 3.2: **Suitable calibration sets for identifying the MT-parameters.** Calibration sets A-G satisfied both criteria to identify the MT-parameters of the knee actuators for all 11 datasets. The CPU time, averaged over all 11 datasets, required to solve the optimal estimation problem from both initial guesses of static parameters is given for the different suitable calibration sets.

calibration sets. Similar observations hold when comparing to the nonlinearly scaled MT-parameters for which the fits were 0.57 ± 0.21 in terms of R^2 and 15.99 ± 6.94 N·m in terms of RMSE when averaged over all six motions and 11 datasets.

Although the subject-specific MT-parameters estimated from the seven suitable calibration sets were not identical, they closely resembled the reference MT-parameters estimated from all motions. For l_t^s and l_m^{opt} , the largest averaged deviations were observed for BFLH (4.5%) and RF (6.3%), respectively. Compared to linearly scaled MT-parameters, subject-specific l_t^s of the flexors were smaller (averaged ratio $82.1 \pm 10.2\%$), subject-specific l_m^{opt} of the flexors were larger (averaged ratio $143.0 \pm 25.8\%$) and subject-specific l_t^s and l_m^{opt} of the extensors were relatively comparable. Linearly scaled MT-parameters were thus comparable to subject-specific MT-parameters for the extensors, in particular the vasti, but not for the flexors. Similar observations hold when comparing subject-specific MT-parameters to nonlinearly scaled MT-parameters. All ratios are averaged over all seven suitable calibration sets and 11 datasets. Detailed numbers of those analyses are presented in Appendix A (Tables A.4-A.5).

Between 17 and 41 computation (CPU) minutes were required to solve the optimal estimation problem from both initial guesses for the suitable calibration sets (see Table 3.2).

MT-parameters	Metric	Gait	Squat	Stair descent	Stair ascent	Sit-to-stand	Squat jump
Subject-specific	Cal. R^2	0.66 ± 0.10	0.80 ± 0.13	0.71 ± 0.17	0.79 ± 0.08	0.79 ± 0.08	0.65 ± 0.13
	set A RMSE	11.64 ± 2.64	11.12 ± 4.17	12.38 ± 3.96	11.17 ± 2.42	9.03 ± 1.89	16.70 ± 4.62
	Cal. R^2	0.66 ± 0.11	0.83 ± 0.12	0.73 ± 0.18	0.76 ± 0.10	0.77 ± 0.09	0.66 ± 0.12
	set B RMSE	11.60 ± 2.72	10.33 ± 4.23	11.84 ± 3.89	11.78 ± 2.72	9.53 ± 2.21	16.55 ± 4.82
	Cal. R^2	0.66 ± 0.12	0.80 ± 0.13	0.73 ± 0.17	0.81 ± 0.08	0.80 ± 0.08	0.65 ± 0.13
	set C RMSE	11.64 ± 2.85	11.15 ± 4.29	12.00 ± 3.92	10.69 ± 2.48	8.97 ± 1.86	16.70 ± 4.60
	Cal. R^2	0.67 ± 0.11	0.82 ± 0.10	0.73 ± 0.20	0.83 ± 0.07	0.80 ± 0.08	0.59 ± 0.16
	set D RMSE	11.57 ± 2.64	10.52 ± 3.52	11.71 ± 3.92	10.12 ± 2.35	8.82 ± 2.07	18.09 ± 5.55
	Cal. R^2	0.66 ± 0.11	0.82 ± 0.13	0.75 ± 0.18	0.78 ± 0.09	0.78 ± 0.08	0.66 ± 0.12
	set E RMSE	11.67 ± 2.82	10.49 ± 4.38	11.29 ± 3.582	11.46 ± 2.83	9.34 ± 2.09	16.49 ± 4.73
Reference	Cal. R^2	0.67 ± 0.11	0.82 ± 0.11	0.70 ± 0.21	0.81 ± 0.08	0.79 ± 0.08	0.65 ± 0.14
	set F RMSE	11.47 ± 2.77	10.50 ± 3.76	12.38 ± 4.19	10.75 ± 2.50	9.22 ± 2.13	16.85 ± 4.81
	Cal. R^2	0.66 ± 0.12	0.80 ± 0.13	0.77 ± 0.14	0.81 ± 0.08	0.80 ± 0.09	0.65 ± 0.13
	set G RMSE	11.70 ± 2.82	11.30 ± 4.10	11.14 ± 3.26	10.52 ± 2.25	8.90 ± 1.76	16.72 ± 4.70
Linearly scaled	Cal. R^2	0.66 ± 0.12	0.82 ± 0.13	0.74 ± 0.20	0.81 ± 0.08	0.79 ± 0.08	0.65 ± 0.13
	RMSE	11.65 ± 2.78	10.63 ± 4.26	11.59 ± 3.91	10.76 ± 2.44	9.08 ± 1.86	16.76 ± 4.79
	Cal. R^2	0.54 ± 0.11	0.47 ± 0.28	0.71 ± 0.12	0.68 ± 0.12	0.60 ± 0.16	0.40 ± 0.22
	RMSE	13.72 ± 3.11	19.96 ± 9.70	12.86 ± 3.31	14.02 ± 3.83	12.92 ± 4.61	22.41 ± 7.77
Nonlinearly scaled	Cal. R^2	0.54 ± 0.11	0.46 ± 0.28	0.71 ± 0.12	0.68 ± 0.12	0.60 ± 0.16	0.41 ± 0.22
	RMSE	13.66 ± 3.10	20.12 ± 9.86	12.82 ± 3.31	13.98 ± 3.84	12.98 ± 4.65	22.41 ± 7.97

Table 3.3: **Summary of R^2 and RMSE (N·m) between ID- and EDM-moments.** A larger R^2 /smaller RMSE value represents a better fit. EDM-moments are simulated based on subject-specific MT-parameters estimated from the suitable calibration (cal) sets A-G (see Table 3.2), reference MT-parameters, linearly scaled MT-parameters, and nonlinearly scaled MT-parameters. Distinction is made between calibration motions and validation motions (in bold). Results are averaged over all 11 datasets (mean ± standard deviation)

Discussion

First, we presented an optimal control problem formulation to estimate subject-specific MT-parameters of the knee actuators based on an EMG-driven model (EDM). Second, we identified several datasets containing the necessary information to estimate MT-parameters of the knee actuators.

The use of subject-specific MT-parameters rather than anthropometry-based scaled parameters improved the fit between ID- and EDM-moments for all motions (see Table 3.3 and example Figure 3.3). This suggests that the experimental approach developed in this study results in more accurate MT-parameter estimates than its anthropometric counterparts, underlining its importance for human motion simulation studies where subject-specificity is required.

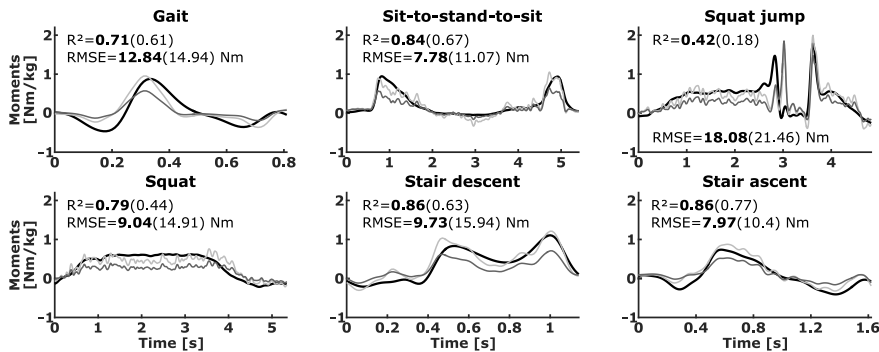


Figure 3.3: Comparison between ID- (thick black) and EDM-moments simulated based on subject-specific MT-parameters (light gray) and linearly scaled MT-parameters (dark gray). This representative example from one dataset shows how the use of subject-specific MT-parameters, estimated from a suitable calibration set (top, calibration motions: gait, sit-to-stand-to-sit, squat jump), improves moment predictions for validation motions: squat, stair descent, stair ascent (bottom). Using subject-specific MT-parameters (in bold) instead of linearly scaled MT-parameters (between brackets) results in larger R^2 and smaller RMSE for all motions.

The optimal estimation problem was solved via direct collocation in about 30 CPU minutes (see Table 3.2). Direct comparison with the literature is difficult, since the CPU time largely depends on the number of optimization parameters and is often not reported. Using direct collocation methods nevertheless typically

results in shorter CPU times than other approaches such as direct shooting or genetic algorithms. Sartori *et al.* [108], for example, needed more than 20 CPU hours to estimate parameters of 34 muscles using a shooting approach with a simulated annealing algorithm.

To test the robustness of our results against the initial guess, we performed all computations using two different sets of initial static parameters: a precomputed hot start and an arbitrary guess. The most optimal solution was then selected. The two initial guesses were very different (see Table A.1 in Appendix A for details). Nevertheless, optimal cost function values were very similar (average ratio hot start to arbitrary guess $101.12 \pm 5.45\%$), indicating that the hot start did not outperform the arbitrary guess. The influence of the initial guess on the MT-parameter estimates was also, on average, limited although larger variabilities were observed for the tendon slack length of the BFLH and the optimal muscle fiber lengths (see Table A.3 in Appendix A for details). These differences underline the need for multiple initial guesses. Future work may consider the use of a second arbitrary guess instead of the hot start to avoid the associated computational costs.

The variability of subject-specific tendon slack length estimates of the BFLH and subject-specific optimal muscle fiber length estimates of the RF among the seven suitable calibration sets was rather high. Further analysis nonetheless showed that these parameters had a relatively low effect on the knee moments. Therefore, we consider to keep those parameters constant in future work. Overall, subject-specific MT-parameters were comparable to anthropometry-based scaled MT-parameters for the extensors, in particular the vasti, but not for the flexors (see Figure 3.4). Further analysis showed that anthropometry-based scaled MT-parameters of the flexors, in particular the gastrocnemii and the SM, were often outside the range of physiologically feasible combinations of MT-parameters, which might provide insight in why anthropometry-based scaled MT-parameters resulted in worse moment simulations. Two explanations may explain why these MT-parameters are outside this range. First, the physiologically feasible combinations may be inappropriately defined. Their definition relied on the assumption that muscles can actively generate force at maximal and minimal MT-lengths encountered across the functional motions. These MT-lengths may however correspond to positions where the muscle cannot actively produce force, invalidating the approach. Second, an anthropometry-based scaling of the MT-parameters may not be suitable for some muscles. Delp and Zajac [143] reported that muscle forces developed by ankle plantarflexors, such as the gastrocnemii, are extremely sensitive to changes in tendon length. Scaling the MT-parameters of the gastrocnemii based on the subject's anthropometry might therefore have

a large effect on muscle forces and corresponding muscle fiber lengths, which would exclude them from the physiologically feasible combinations. The second explanation is more likely than the first one based on the increased accuracy of moment simulations obtained with subject-specific versus anthropometry-based scaled MT-parameters. Future work will further investigate both explanations.

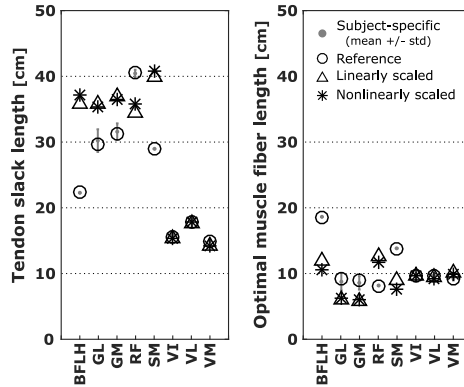


Figure 3.4: Comparison between subject-specific MT-parameters averaged over the seven suitable calibration sets (gray), reference MT-parameters (circles), linearly scaled MT-parameters (triangles), and nonlinearly scaled MT-parameters (stars). This example is given for one representative dataset (subject's height, 175 cm) (see Figure A.3 in Appendix A for other datasets).

Studying the identifiability of the MT-parameters based on different sets of motions allowed us to determine which sets of motions contain the necessary information to identify the MT-parameters. This identifiability study was essential to ensure the estimation of parameters that describe the subject's MT-properties and could therefore be used in *what if* studies where novel motions are predicted or to calculate MT-force distributions. The subject-specific MT-parameters were estimated and validated using a rich dataset, including a wide variety of functional motions. In particular, a validation was performed by extrapolating to novel motions (i.e., motions not used in the estimation). The estimated subject-specific MT-parameters are thus expected to be valid for a wide variety of motions, including motions that were not included in this study. Without such a validation, the use of MT-parameters estimated based on functional motions should not be extrapolated to other motions and the computed MT-force distributions should be interpreted with care. We identified seven sets of motions that were suitable to identify the MT-parameters over all datasets (see Table 3.2). Information from gait and sit-to-stand-to-sit was essential as those motions were part of all suitable calibration sets. Their

sole combination was however not sufficient for four out of eleven datasets. Combining as few as three motions (calibration set A: gait, sit-to-stand-to-sit, squat jump) was sufficient for all datasets. Performing a squat jump may however be difficult in a clinical context (e.g., patients with cerebral palsy). In that case, calibration set D, containing all motions but squat jump, is a good alternative. All other suitable sets of motions were extensions of calibration set A. Although adding additional motions to calibration set A resulted in a slight increase in accuracy ($\tilde{1}\%$) based on R^2 and RMSE, their use required on average three times higher CPU times and additional time-consuming measurements. These findings provide guidelines about which measurements to perform and combine to estimate the MT-parameters of the knee actuators. A choice can be made based on the subject's functional abilities and the available equipment. Future research should extend this study to other motions that are more easily achievable in a clinical context and that require no or little equipment.

The selection of optimization parameters was driven by the need to balance accuracy of the model and available experimental information. Based on existing sensitivity studies [106, 89, 90], only a limited number of MT-parameters were optimized. These studies, however, only considered a range of parameter values from control subjects. Deviations from this range in the presence of musculoskeletal disorders may require the inclusion of additional parameters. In patients with muscle weakness it may, for example, be necessary to adjust F_m^{\max} whereas this is not the case for healthy controls. Estimating a different set of parameters necessitates an analysis similar to the one presented in this study to determine whether the available experimental data contain enough information. A single optimization parameter for all muscles was used in the EMG-to-activation relationship. It is expected that including muscle-specific shape factors may result in better moment simulations [90] as it may better reflect the muscle physiology [144]. This would, however, considerably increase the number of optimization parameters and thus the risk of overfitting. Similarly, a fixed electromechanical delay (40 ms) was introduced whereas muscle- and motion-specific electromechanical delays are anticipated to result in better moment simulations.

The use of more physiologically correct models is expected to result in better moment simulations [90] and may therefore increase the MT-parameter estimation accuracy. Future research may therefore consider the inclusion of additional muscle features such as multiple muscle fiber types to better represent the motor unit recruitment strategies [145]. Muscle fatigue [146] and history-dependence [147] may also be considered. A balance between model complexity and numerical aspects is, however, needed to maintain a high computational

efficiency. The model outcomes also depend on the quality of the EMG signals and the number of muscle groups from which EMG signals are extracted. On the one hand, the quality of the EMG signals is deteriorated by noise from cross-talk or movement artifacts and is affected by the envelope extraction procedure [148]. On the other hand, the collection of EMG signals from more muscle groups is expected to better represent the individual muscle contributions to the joint moments. In this study, the assignment of EMG envelopes to the model's knee actuators mainly followed common practice from the literature [90, 108]. The GL EMG was further assumed to drive the GM whereas the hamstring medialis EMG was assumed to drive the SA and GR. The first assumption was supported by the fact that the gastrocnemii share the same tendon and have a common knee flexion function. Experimental data are thus expected to contain information about their common function and not about their individual muscle contributions to the knee moments. The MT-parameters of those muscles will thus be estimated to provide the expected knee flexion moments. Inaccuracies in the EMG envelopes are therefore anticipated to have a small influence on this estimation. Regarding the second assumption, the SA and GR have the smallest cross-sectional areas among the hip and knee muscles [108] and inaccuracies in their EMG envelopes are hence expected to have a very limited impact on the knee moment predictions. Furthermore, the MT-parameters of the SA and GR were not estimated due to their low sensitivity [106]. For those different reasons, we did not consider the use of other approaches, such as hybrid EMG-informed models [108, 148], to estimate the EMG of those three muscles. Overall, we were able to estimate subject-specific MT-parameters based on surface EMG signals from six muscle groups that improved the accuracy of knee moment predictions for novel motions. Therefore, EDMs are useful even in the absence of EMG data from presumably agonistic and smaller muscles.

Sartori *et al.* [108] investigated the limitations associated with the use of EDMs that constrain MT-actuators to satisfy joint moments with respect to a single DOF. They reported discrepancies in the MT-force distribution of several biarticular muscles (GR, ST, SA, RF and both gastrocnemii) when simulated from different single-DOF EDMs. Their findings, however, do not affect the validity of our results. First, in this study, the GR, ST, and SA were not included in the calibration process because of the low sensitivity of knee moments to MT-parameters of those muscles [89]. Second, the variations in the MT-force distribution of the RF when estimated from knee- versus hip-based EDMs in the study of Sartori *et al.* [108] might be caused by omitting active contributions of psoas and illiacus whose electrical activity could not be measured via surface EMG. This omission impacts the MT-force distribution of other hip actuators, such as the RF, when simulated using hip-based EDMs and may explain the differences with the MT-force distribution obtained using knee-

based EDMs. Third, as stated above, the gastrocnemii have a common knee flexion function and experimental data are thus expected to contain information about their common function, preventing independent estimation of their MT-parameters. Note that, for this reason, an additional constraint was imposed in the optimal estimation problem (3.14). Discrepancies in MT-force distribution are therefore expected for these two muscles when simulated from ankle- versus knee-based EDMs while the combined MT-force distribution is anticipated to be similar. Overall, using a model that considers a sole DOF is suitable if the MT-parameters are selected so that the information needed for their estimation is available in the experimental dataset.

This study has several limitations. First, a sole DOF was considered, limiting the number of muscles included in the analysis. Extending this research to other DOFs is necessary to consider muscles spanning other joints. This nevertheless would require an identifiability study to assess whether the available experimental data contain enough information to estimate the additional parameters. Second, a limited number of functional motions were used to estimate and validate the MT-parameters. Motions not considered in the current study might provide more information. In particular, the inclusion of maximal isometric contraction trials may be beneficial although, as mentioned in the introduction, several limitations arise when using isometric dynamometry. Overall, combinations of the considered motions were suitable to obtain valid estimates of MT-parameters. Third, only sagittal plane motions were included in this study. While we could provide valid MT-parameters for these motions, extrapolation to motions in the other planes should be performed with care. Fourth, the approach for computing the moment arms is an approximation for biarticular muscles as contact forces between joint and muscles are ignored [128]. This may therefore affect the results. In the future, the use of via-point wrapping and wrapping system [149] will be considered. Finally, no passive motions were included in the experimental datasets. Therefore, passive MT-properties cannot be estimated based on the proposed dataset.

Conclusion

This study proposed a new and computationally efficient optimal control problem formulation to estimate subject-specific Hill model MT-parameters of the knee actuators based on an EMG-driven model. In addition, an identifiability study was performed and underlined the importance of the selection of experimental data to provide valid estimates of MT-parameters and to prevent overfitting. Our results demonstrated the need to use subject-specific MT-parameters to obtain

accurate knee moment simulations and highlighted the limitations associated with the use of anthropometric approaches to scale the MT-parameters of the knee flexors. In the future, we will extend this research to patients (e.g., children with cerebral palsy), considering their various neuromuscular impairments and their diminished abilities to perform certain motions.

Acknowledgments

This work was supported by the IWT-TBM grant SimCP (140184). AF also received a PhD grant (1S35416N) from the Research Foundation Flanders (FWO).

Chapter 4

Study 2: A spasticity model based on feedback from muscle force explains muscle activity during passive stretches and gait in children with cerebral palsy

Published as:

Falisse A., Bar-On L., Desloovere K., Jonkers I., De Groote F. *A spasticity model based on feedback from muscle force explains muscle activity during passive stretches and gait in children with cerebral palsy*, (2018). PLoS ONE, **13**(12): e0208811.

Abstract

Muscle spasticity is characterized by exaggerated stretch reflexes and affects about 85% of the children with cerebral palsy. However, the mechanisms underlying spasticity and its influence on gait are not well understood. Here, we first aimed to model the response of spastic hamstrings and gastrocnemii in children with cerebral palsy to fast passive stretches. Then, we evaluated how the model applied to gait. We developed three models based on exaggerated proprioceptive feedback. The first model relied on feedback from muscle fiber length and velocity (velocity-related model), the second model relied on feedback from muscle fiber length, velocity, and acceleration (acceleration-related model), and the third model relied on feedback from muscle force and its first time derivative (force-related model). The force-related model better reproduced measured hamstrings and gastrocnemii activity during fast passive stretches (coefficients of determination (R^2): 0.73 ± 0.10 and 0.60 ± 0.13 , respectively, and root mean square errors (RMSE): 0.034 ± 0.031 and 0.009 ± 0.007 , respectively) than the velocity-related model (R^2 : 0.46 ± 0.15 and 0.07 ± 0.13 , and RMSE: 0.053 ± 0.051 and 0.015 ± 0.009), and the acceleration-related model (R^2 : 0.47 ± 0.15 and 0.09 ± 0.14 , and RMSE: 0.052 ± 0.050 and 0.015 ± 0.008). Additionally, the force-related model predicted hamstrings and gastrocnemii activity that better correlated with measured activity during gait (cross correlations: 0.82 ± 0.09 and 0.85 ± 0.06 , respectively) than the activity predicted by the velocity-related model (cross correlations: 0.49 ± 0.17 and 0.71 ± 0.22) and the acceleration-related model (cross correlations: 0.51 ± 0.16 and 0.67 ± 0.20). Our results therefore suggest that force encoding in muscle spindles in combination with altered feedback gains and thresholds underlie activity of spastic muscles during passive stretches and gait. Our model of spasticity opens new perspectives for studying movement impairments due to spasticity through simulation.

Introduction

Cerebral palsy (CP) is the most common cause of physical disability in children. It is described as a group of permanent disorders that are attributed to lesions occurring in the developing brain. These disorders are accompanied by secondary musculoskeletal problems including muscle spasticity that affects about 85% of the children with CP [57, 1]. Spasticity is commonly defined by a velocity-dependent increase in tonic stretch reflexes resulting from hyper-excitability of the stretch reflex [58]. The most common clinical diagnoses of spasticity are exaggerated tendon tap reflexes and hypertonia that induce a velocity-dependent

resistance of spastic muscles to stretch [95]. Yet, despite the vast amount of research, the mechanisms underlying spasticity and the influence of spasticity on functional motions such as gait are not well understood. In this study, we use a simulation-based approach to model the spastic response to muscle stretch and we evaluate how this model applies to gait.

Spasticity is qualitatively assessed by passively moving a joint while grading the resistance, typically using the Modified Ashworth Scale (MAS) [150] or the Modified Tardieu Scale (MTS) [151]. To further quantify the level of spastic involvement, Bar-On *et al.* [109] developed instrumented tests that yield better accuracy and reliability than the MAS and MTS. During these tests, later referred to as instrumented passive spasticity assessments (IPSAs), passive muscles are stretched at different velocities while collecting biomechanical (joint moments, angular positions and velocities) and electrophysiological (electromyography (EMG)) data that quantify the resistance to the imposed motion. These tests therefore provide valuable information to comprehensively describe spasticity.

Spasticity is believed to emerge from exaggerated reflex activity in response to muscle spindle firing. In unaffected muscles, fast conducting group Ia nerve fibers mediate the activity of short-latency reflexes from the spindles to the spinal cord [95]. The central motor lesions accompanying CP are thought to affect the strength and sensitivity of this reflex loop [95, 152], inducing exaggerated reflexes upon muscle stretch, i.e. spasticity.

Models of spasticity explain the increase in muscle activity following lengthening through exaggerated proprioceptive feedback from the spindles. Since it is widely thought that the spindle proprioceptive receptors encode information about muscle length and velocity changes [97, 98], spasticity has been modeled based on muscle length and velocity feedback [153, 154, 155]. In particular, van der Krog et al. [100] proposed a spasticity model based on velocity feedback. This model captured the salient features of the spastic response observed during fast passive stretches of the hamstrings in CP children but did not reproduce the oscillations in the measured muscle activity (EMG), that were not reflected in fiber velocity, and the sustained muscle activity following the stretch.

Recent findings suggest that muscle spindle firing might be more directly related to muscle force than to muscle length and velocity. In particular, Blum *et al.* [99] showed that history-dependent transients of spindle firing are not uniquely related to muscle fiber lengths and velocities. Further, they demonstrated that

muscle spindle firing can be explained based on encoding of fiber force and its first time derivative across a wide range of stretch conditions, whereas length- and velocity-related variables cannot explain spindle firing during history-dependent conditions such as short-range stiffness. Their results therefore suggest that spindle proprioceptive receptors encode information about muscle force rather than length. This is in accordance with existing spindle models that describe spindle firing based on the stretch in a spring element representing the sensory zone, which is proportional to the intrafusal muscle fiber force [156, 157, 158], and with older *in vitro* studies relating peaks in muscle spindle firing rates to muscle force transients at stretch onset [159, 160]. Since spasticity is believed to result from an exaggerated response to spindle firing, a model of spasticity based on feedback from muscle force and its first time derivative should be considered. To the authors' knowledge, such model of spasticity has never been proposed.

While spasticity manifests during passive muscle stretches, its influence during functional motions such as gait remains subject to debate. In their review, Dietz and Sinkjaer [95] reported that the clinical signs of spasticity, i.e. exaggerated tendon tap reflexes and muscle hypertonia, are little related to the functional spastic motion disorders. They further argued that exaggerated reflexes have a minor role in spastic motion disorders whereas secondary changes in mechanical muscle fiber properties have a major role. These conclusions are in line with several studies that reported a lack of correlation between spasticity as diagnosed during passive motions and determinants of gait. Ada *et al.* [161] showed that tonic stretch reflexes in the gastrocnemii, provoked in conditions that simulated gait, were of similar magnitude in stroke patients and controls. This suggested no influence of spasticity on gait whereas most stroke patients exhibited exaggerated resting tonic stretch reflexes indicating spasticity in a relaxed state. Marsden *et al.* [162] reported no correlation between the degree of knee flexion during walking and spasticity of the knee extensors as assessed during passive stretches in people with hereditary and sporadic spastic paraparesis. Willerslev *et al.* [163] showed that the contribution of sensory feedback to soleus activity during swing was not larger in CP children than in typically developing children and that soleus activity was observed to the same extent during swing in both groups. They therefore concluded that spasticity was unlikely to contribute to altered ankle kinematics. In contrast, other studies could relate measures of spasticity to determinants of gait suggesting that spasticity affects walking. Damiano *et al.* [164] showed that CP children who exhibited increased stretch reflexes in the hamstrings and quadriceps during passive stretches had lower knee angular velocities during the swing phase of gait. Tuzson *et al.* [165] reported similar results as well as a correlation between the spastic threshold velocity, expressed in terms of knee angular velocity, and the peak knee angular velocity during fast

walking in CP children. Further, spasticity is often assumed to affect walking performance. For example, it is thought that rectus femoris spasticity leads to abnormal activity during early swing, limiting knee flexion during that phase [166, 167]. In summary, the relation between spasticity measures and gait as well as the influence of spasticity on walking performance are still under debate.

Musculoskeletal modeling and simulations have been used to investigate whether spasticity, as assessed during passive motions, e.g. with IPSA, affects gait. These tools can provide information about the muscle-tendon units, e.g. muscle fiber length, velocity, force, that might contribute to our understanding of the mechanisms underlying spasticity. Bar-On *et al.* [96] have used modeling to relate muscle-tendon lengthening velocity during passive stretches of the gastrocnemii and hamstrings of CP children and muscle-tendon velocities during the swing phase of gait. They reported that the peak muscle-tendon velocity during swing exceeded the stretch reflex thresholds, i.e. the muscle-tendon velocity at reflex onset, for the hamstrings but not for the gastrocnemii. Additionally, they could relate stretch reflex thresholds with peak muscle-tendon velocity during gait for both muscle groups at specific walking speeds. Finally, they reported no correlation between EMG measured during passive stretches and peak muscle-tendon lengthening velocity during gait. That study however only compared thresholds expressed in terms of muscle-tendon lengthening velocity and did not evaluate other muscle variables that have been related to muscle spindle firing such as muscle fiber length, velocity or force. Additionally, there was no attempt to model the spastic response to passive stretches and to evaluate how that model would apply to gait.

The contribution of this study is twofold. First, we developed three spasticity models and compared their ability to explain measured reflex muscle activity during passive muscle stretches in CP children. All three models described reflexes through proprioceptive feedback. The velocity-related model relied on muscle fiber length and velocity feedback. The acceleration-related model relied on muscle fiber length, velocity, and acceleration feedback. The force-related model relied on feedback from muscle force and its first time derivative (dF/dt). We hypothesized, based on the aforementioned findings from Blum *et al.* [99], that the force-related model would better reproduce the measured muscle activity than the velocity- and acceleration-related models. Second, we evaluated how well muscle activity predicted by the three models correlated with measured muscle activity from CP children during gait. We found that the force-related model could explain muscle activity during passive stretches and gait whereas the velocity- and acceleration-related models could not.

Methods

Experimental Data

We collected experimental data from six CP children (four with unilateral and two with bilateral spastic involvement) (Table 4.1). As part of their treatment, three children (two with unilateral and one with bilateral spastic involvement) received a botulinum toxin-A (BTX) injection to reduce spasticity and we collected data before and six to 14 weeks after treatment. We considered that the spasticity models should be able to describe different levels of spastic involvement and therefore should be valid pre- and post-BTX injection. We analyzed two muscle groups: hamstrings and gastrocnemii. In all cases, the MAS score of the hamstrings and gastrocnemii was between one and two indicating mild hyper-resistance [150]. The data were collected as part of another study and the ethical committee of the UZ / KU Leuven (Belgium) approved the protocol (s060799). All children older than 11 years and all parents signed an informed consent form.

	Hamstrings (n = 8)	Gastrocnemii (n = 12)
Gender (male/female)	3/2	3/3
Age in years (mean ± std)	12.4 ± 2.6	11.7 ± 2.9
Involvement (unilateral/bilateral)	4/1	4/2
BTX-treatment (unilateral/bilateral)	2/0	2/1
Modified Ashworth Scale score (1:5)	1: 1 1+: 4 2: 3	1+: 5 2: 7
Modified Tardieu Scale Angle in degrees (mean ± std)	-81.4 ± 3.8	-9.2 ± 9.8

Table 4.1: Demographic information.

First, the children's gait was assessed using 3D motion analysis. Each child was instrumented with retro-reflexive markers, corresponding to the lower limb plug-in-gait marker set, whose 3D locations were recorded (100 Hz) using an eight- to 15-camera motion capture system (Vicon, Oxford, UK) during walking trials. Data from three to 10 walking trials with valid force plate contact were selected per subject. Ground reaction forces (GRFs) (1000 Hz) and surface EMG (2000 Hz) were recorded using force plates (AMTI, Watertown, USA) and a telemetric Zerowire system (Cometa, Milan, Italy), respectively. GRFs were low-pass filtered (6 Hz) with a second-order dual-pass Butterworth filter. EMG was collected from eight muscles: rectus femoris, vastus lateralis, biceps

femoris short head, semitendinosus, tibialis anterior, gastrocnemius lateralis, soleus, and gluteus medius. EMG was processed by band-pass filtering (20-400 Hz), full-wave rectification, and low pass filtering (10 Hz) using a second-order dual pass Butterworth filter.

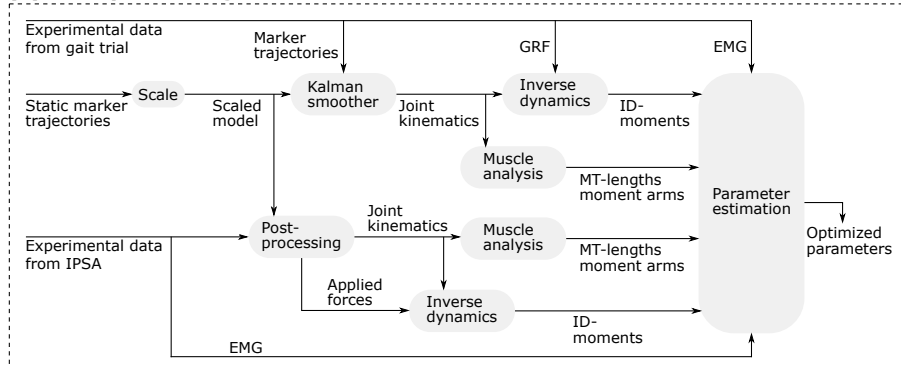
On the same day as the gait analysis, spasticity of the medial hamstrings and gastrocnemii was assessed using IPSA (described in detail by Bar-On *et al.* [109]). During IPSA, hamstrings and gastrocnemii were stretched by moving knee and ankle, respectively, one at a time from a predefined position throughout the full range of motion. The stretches were performed at slow (about 15 and 10 degrees/s for testing the hamstrings and gastrocnemii, respectively), medium (about 75 and 55 degrees/s, respectively) and fast (about 200 and 100 degrees/s, respectively) velocities. Surface EMG was collected from the semitendinosus and gastrocnemius lateralis as well as from their antagonists (rectus femoris and tibialis anterior, respectively) using the same system as used for gait analysis. The electrodes remained in place between both analyses. EMG processing was comparable to Bar-On *et al.* [109], namely high-pass filtering (20 Hz), stop-pass filtering (49.5-50.5 Hz) to remove the observed line frequency interference, full-wave rectification, and low pass filtering (10 Hz) using a sixth-order dual pass Butterworth filter. Due to poor EMG quality, data from the hamstrings were not included for the child with bilateral involvement who received BTX treatment. This resulted in data from 20 individual muscle groups (eight hamstrings and 12 gastrocnemii) included for further analysis. The motion of the distal limb segment with respect to the proximal fixed segment was tracked using two inertial measurement units (Analog Devices, ADIS16354). The forces applied to the segment were measured using a hand-held six degrees of freedom (DOFs) load-cell (ATI Industrial Motion, mini45). The position of the load-cell relative to the joint axis was manually measured by the examiner.

Musculoskeletal modeling and data processing

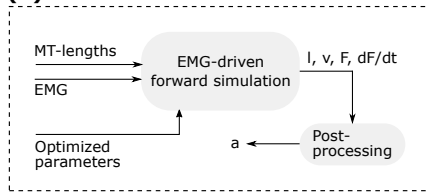
In this section, we detail the data processing steps that preceded the development and evaluation of the spasticity models (Figure 4.1a).

We processed the experimental data from IPSA and gait trials in OpenSim 3.3 [112] using the gait2392 musculoskeletal model containing 20 segments, 23 DOFs, and 43 Hill-type muscle-tendon actuators per leg [63] (Figure 4.1a). The musculoskeletal model was scaled to the subjects' anthropometry using OpenSim's Scale tool based on marker information collected during a static trial performed during the gait analysis. The maximal isometric muscle forces were

(a) Data processing



(b) EMG-driven forward simulation



(c) Feedback gain estimation

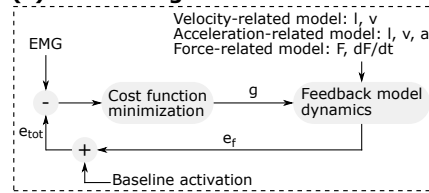


Figure 4.1: Flowcharts illustrating data processing (a), EMG-driven forward simulation (b), and feedback gain estimation (c). (a) Experimental data from gait trials and IPSA at slow velocities are processed using musculoskeletal modeling to obtain muscle-tendon (MT) lengths, moment arms, and inverse dynamic (ID) joint moments that are input to the EMG-driven muscle-tendon parameter estimation. (b) Sensory information (l : muscle fiber length, v : muscle fiber velocity, F : muscle force, dF/dt : first time derivative of muscle force, a : muscle fiber acceleration) is obtained through EMG-driven forward simulations using MT-lengths, EMG, and optimized muscle-tendon parameters as input. EMG-driven forward simulations are performed for passive stretches at medium and fast velocities and for walking trials. (c) Feedback gains g are estimated by minimizing the difference between EMG and simulated excitation e_{tot} , which is the sum of baseline activation and muscle excitation resulting from proprioceptive feedback e_f . The feedback gain estimation is performed using experimental data from three fast passive stretches.

scaled to the subjects' mass. For each gait trial, joint kinematics were calculated from the measured marker trajectories using a Kalman smoothing algorithm [115]. Inverse dynamic joint moments were calculated from joint kinematics and measured GRFs using OpenSim's Inverse Dynamics tool. For each passive motion (IPSA), experimental joint angles and forces applied by the examiner,

pre-processed using custom-made software [109], were imported in OpenSim and inverse dynamic joint moments were calculated using the Inverse Dynamics tool. Muscle-tendon lengths and moment arms were computed for joint kinematics during gait and passive motions using OpenSim's Muscle Analysis tool.

We normalized EMG based on estimated muscle excitation. We computed muscle excitation that reproduced the inverse dynamic moments during gait by minimizing muscle excitation squared while accounting for Hill's muscle-tendon dynamics (including a compliant tendon) [53]. For each gait trial and muscle, we determined the normalizing factor as the ratio between peak EMG and peak estimated muscle excitation. For the passive motions, we normalized the EMG envelopes using the individuals' largest normalizing factor from the gait trials (within-subject differences between normalizing factors for different gait trials were small, within-subject standard deviation of normalizing factors averaged over all subjects: 0.05 ± 0.05).

To account for inter-subject differences in muscle-tendon properties, we estimated subject-specific tendon slack lengths and optimal muscle fiber lengths of eight knee muscles (four knee extensors: biceps femoris long head, gastrocnemius lateralis and medialis, semimembranosus and four knee extensors: rectus femoris, vastus intermedius, lateralis, and medialis) by optimizing the fit between inverse dynamic and simulated joint moments (Figure 4.1a). Joint moments were simulated using an EMG-driven approach [168]. We used experimental data from three gait trials and from slow passive motions to optimize the parameters using the parameter estimation approach described by Falisse *et al.* [168]. Passive motions at medium and fast velocities were not used for the parameter estimation since only few EMG channels were available during these trials. For slow passive motions, we could assume low activity for muscles without EMG channels. However, this assumption does not necessarily hold for faster speeds, which motivated the exclusion of trials at faster speeds from the parameter estimation.

Models of spasticity

We developed three spasticity models based on proprioceptive feedback. The first model relied on feedback from muscle fiber length and velocity, and is referred to as velocity-related model. The second model relied on feedback from muscle fiber length, velocity, and acceleration, and is referred to as acceleration-related model. The third model relied on feedback from muscle force and dF/dt , and is referred to as force-related model. Each feedback component, e_s , is

described by first order dynamics to model the time delay, $\tau = 30$ ms [100]. The feedback is characterized by a threshold, T_s , and a gain factor, g_s :

$$\tau \frac{de_s}{dt} = \begin{cases} -e_s, & s \leq T_s \\ -e_s + g_s(s - T_s), & s > T_s \end{cases} \quad (4.1)$$

where s refers to the sensory information, i.e. muscle fiber length, velocity, acceleration, muscle force, or dF/dt . For numerical reasons, we implemented a continuously differentiable approximation of equation (4.1) using a hyperbolic tangent function to smoothly transition between feedback contributions above and below the threshold. We determined the thresholds for muscle fiber length, velocity, and muscle force as the values 20 ms before the EMG onset that we identified according to the method of Staude and Wolf [132]. We manually corrected the EMG onsets that were misidentified, likely due to filtering. This delay of 20 ms differs from the time delay $\tau = 30$ ms because we used a first order approximation in the formulation of the feedback dynamics (equation 4.1). We used zero thresholds for acceleration and dF/dt feedback, i.e. there is only feedback when the signal is positive.

We estimated the sensory information, i.e. muscle fiber length, velocity, acceleration, muscle force, and dF/dt , that is input to the spasticity models during passive motions at medium and fast velocities (for both hamstrings and gastrocnemii) by performing EMG-driven forward simulations of Hill's muscle-tendon model dynamics (Figure 4.1b). Muscle fiber length, velocity, muscle force, and dF/dt follow directly from forward integration of the muscle-tendon dynamics (Hill's model with personalized parameters) using the muscle's EMG and muscle-tendon length trajectories as input. We used semitendinosus EMG to drive biceps femoris long head, semimembranosus, and semitendinosus. Similarly, we used gastrocnemius lateralis EMG to drive both gastrocnemius lateralis and medialis. We estimated muscle fiber acceleration through a spline approximation of the muscle fiber velocity that was low pass filtered (second-order dual pass Butterworth filter with cut-off frequency of 10Hz).

For the three spasticity models, we optimized the feedback gains of the spastic muscles by minimizing the difference between experimental EMG and modeled muscle excitation, e_{tot} , over three fast passive motions, later referred to as calibration motions (Figure 4.1c):

$$\min \sum_{k=1}^3 \int_{t_i}^{t_f} (e_{\text{tot}}(t) - EMG(t))^2 dt, \quad (4.2)$$

where k is calibration motion index, t is time, and t_i and t_f define the time interval. Only fast motions were used for calibrating the feedback gains since stretches at other velocities did not consistently provoke spastic responses. Note that we could not use gait trials to determine the feedback gains, since not all muscle activity during walking is due to sensory feedback. We assumed that muscle activity during passive motions consisted of a constant baseline activation and the different feedback components. The baseline activation was the minimal EMG value during the 0.5 s preceding stretch onset. The values of t_i and t_f were manually selected such that the optimization time window was centered around the increase in EMG corresponding to the spastic response (average optimization time window: 0.7 ± 0.2 s and 0.9 ± 0.5 s for the hamstrings and gastrocnemii, respectively).

The optimization problems were solved numerically via direct collocation using GPOPS-II optimal control software [121] on a mesh of 300 equally spaced intervals per second using third order Legendre-Gauss-Radau collocation. The interior point solver IPOPT [122] was used to solve the resulting nonlinear programming problems (NLP) using second-order derivative information. The automatic differentiation software ADiGator [142] was used to provide the derivatives required by the NLP solver.

We then used the spasticity models with optimized feedback gains to compute the muscle excitation of the spastic muscles during the entire duration of the passive motions at fast velocities, i.e. calibration motions, and medium velocities. The passive motions at medium velocities were used for validation only and will be referred to as validation motions. For the validation motions, we used, for each subject, as feedback thresholds the smallest thresholds from the three calibration motions (differences between thresholds for each subject were small, within-subject standard deviation of thresholds averaged over all subjects: 0.01 ± 0.01 , 0.02 ± 0.03 , and 0.02 ± 0.01 for the normalized muscle force, muscle fiber length, and muscle fiber velocity, respectively). To simulate the excitation of the spastic muscles, we performed forward integration of the feedback model dynamics, i.e. spasticity models (equation 4.1), using the ode45 solver in MATLAB (The Mathworks Inc., Natick, USA).

Spastic contribution during gait

We then used the spasticity models with optimized feedback gains to simulate muscle excitation due to spindle reflexes during the gait trials. To this aim, we first estimated sensory information during gait trials for the spastic muscles by

performing EMG-driven forward simulations of Hill's muscle-tendon dynamics (Figure 4.1b). We then performed forward integration of the spasticity models (equation 4.1) to simulate muscle excitation due to spindle reflexes. We used, for each subject, the smallest thresholds from the three calibration motions as feedback thresholds. Both steps were performed in a similar way as described above for the passive stretches.

Code developed to optimize the muscle-tendon parameters, implement the spasticity models, optimize the feedback gains, and simulate the spastic contributions during passive motions and gait trials are available at <https://simtk.org/home/simcspasticity>.

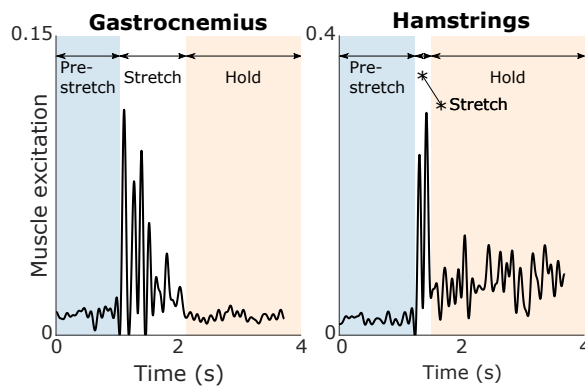


Figure 4.2: Examples of measured muscle activity (EMG) during fast passive stretches of gastrocnemii (left) and hamstrings (right). Typically, each stretch consists of a pre-stretch phase with low muscle activity corresponding to the baseline activation, a stretch phase with increased muscle activity corresponding to the spastic response, and a hold-phase with sustained muscle activity for the hamstrings and low muscle activity for the gastrocnemii.

Outcome measures

We first compared the ability of the spasticity models to explain EMG during IPSAs. We then evaluated how muscle excitation predicted by the spasticity models during gait correlated with measured EMG. During gait, we expect the muscle excitation resulting from the spasticity models to lie within the EMG envelope when a spastic contribution is expected but not to fully explain the EMG, motivating the selection of a correlation analysis rather than an analysis

of the quality of fit.

For the IPSAs, we computed the root mean square error (RMSE) and the coefficient of determination (R^2) between the EMG and the simulated muscle excitation over the entire duration of each calibration motion (average duration: 2.7 ± 0.7 s and 3.9 ± 1.0 s for the hamstrings and gastrocnemii, respectively) and validation motion (average duration: 2.7 ± 0.6 s and 2.6 ± 0.8 s for the hamstrings and gastrocnemii, respectively). Each motion included a pre-stretch phase, a stretch phase, and a hold phase (Figure 4.2). The duration of the pre-stretch and hold phases varied across trials, explaining why a passive motion at fast velocity may be longer than a passive motion at medium velocity. Typically, we observed low muscle activity, corresponding to the baseline activation, during the pre-stretch phase, an increased muscle activity, corresponding to the spastic response, during the stretch-phase, and a low or sustained muscle activity for the gastrocnemii or hamstrings, respectively, during the hold phase. We included all three phases when comparing the fits between models to evaluate the ability of the models to capture the entire muscle activity patterns. For the gait trials, we correlated the EMG and the simulated muscle excitation using a cross-correlation with zero-lag.

We then compared RMSE and R^2 for IPSAs, and cross-correlations for gait trials between the three spasticity models using paired t-tests with a 0.05 significance level. We tested the IPSA movements used for calibration (fast velocity) and validation (medium velocity) separately. The samples included eight and 12 values for the hamstrings and gastrocnemii, respectively.

Results

The force-related spasticity model better explained the experimental EMG during the passive stretch motions at fast velocities than the velocity- and acceleration-related models (Figure 4.3). R^2 values between EMG and simulated muscle excitation were higher using the force-related model (average 0.73 ± 0.10 and 0.60 ± 0.13 for the hamstrings and gastrocnemii, respectively) compared to the velocity-related model (average 0.46 ± 0.15 and 0.07 ± 0.13) and the acceleration-related model (average 0.47 ± 0.15 and 0.09 ± 0.14). RMSE were smaller using the force-related model (average 0.034 ± 0.031 and 0.009 ± 0.007 for the hamstrings and gastrocnemii, respectively) compared to the velocity-related model (average 0.053 ± 0.051 and 0.015 ± 0.009) and the acceleration-related model (average 0.052 ± 0.050 and 0.015 ± 0.008). The

differences between the force-related model and the two other models were statistically significant ($p < 0.05$) for all muscles in terms of R^2 and for the semimembranosus, gastrocnemius medialis, and gastrocnemius lateralis in terms of RMSE. The differences were also statistically significant between the velocity- and acceleration-models for the gastrocnemius medialis in terms of RMSE. For the passive stretches at medium velocities, the force-related model also outperformed the two other models (Figure B.1 in Appendix B). However, the fits between EMG and simulated muscle excitation were worse (smaller R^2) than for the passive stretches at fast velocities.

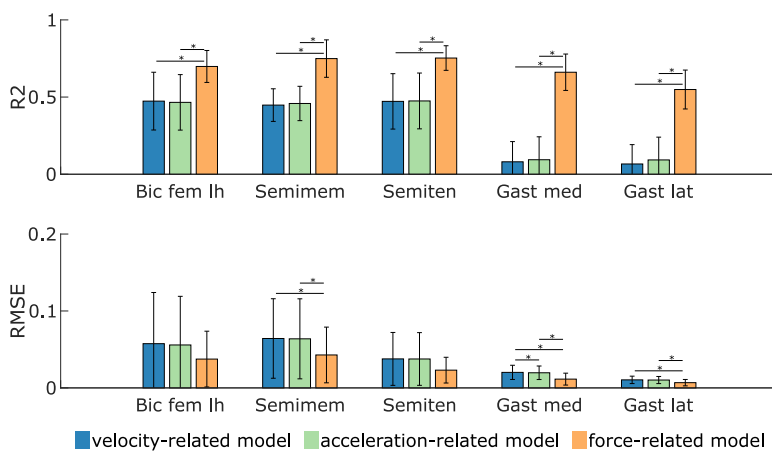


Figure 4.3: Fits (R^2 and RMSE) between EMG and simulated muscle excitation during fast passive stretches. Muscle excitation is estimated based on the three spasticity models (velocity-, acceleration-, and force-related). A larger R^2 /smaller RMSE value represents a better fit. The statistical significance level was set to 0.05 and statistical differences between models are indicated using a horizontal bar. Results are averaged over eight and 12 values for the hamstrings (biceps femoris long head (Bic fem Ih), semimembranosus (Semimem), and semitendinosus (Semiten)) and gastrocnemii (gastrocnemius medialis (Gast med) and lateralis (Gast lat)), respectively.

Only the force-related model accurately described the oscillations in the measured EMG of both hamstrings and gastrocnemii. During fast passive stretches of the hamstrings, all three models could capture the salient features of the EMG (peak during stretch and sustained activity in hold phase) (example in Figure 4.4, top; other cases in Figure B.2 in Appendix B) but only the force-related model could reproduce the distinct features of the signal (Figure

4.4, top-right). In all cases (example in Figure 4.5, right), we observed that delayed feedback from dF/dt explained the peaks in muscle activity during the stretch and the rapid changes (oscillations) in muscle activity throughout the response, whereas feedback from muscle force mainly contributed to the sustained baseline muscle activity after the stretch. Feedback from fiber velocity reproduced the increase in muscle activity upon stretch but the single peak of the simulated activity did not match the peaks in EMG. Feedback from fiber length contributed to the sustained baseline muscle activity after the stretch (Figure 4.4, top-left and top-middle, and Figure B.2 in Appendix B). In three out of eight cases, feedback from fiber acceleration reproduced the rapid changes (oscillations) in muscle activity, although to a lesser extent than feedback from dF/dt (Figure 4.4, top-middle, and Figure B.2 in Appendix B). In the other cases, estimated fiber acceleration feedback gains were very small.

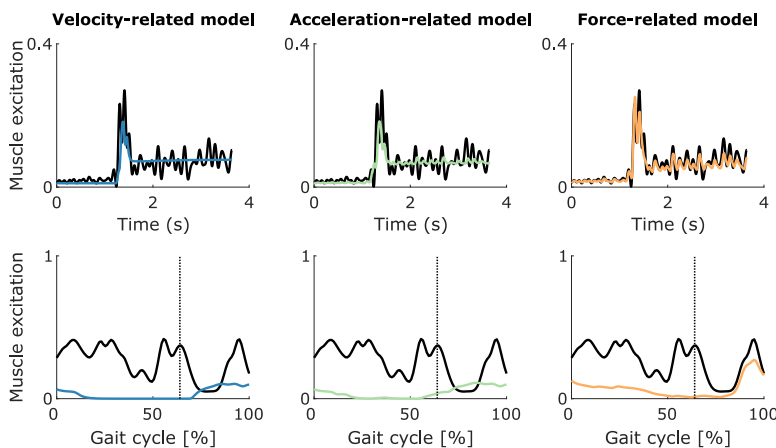


Figure 4.4: EMG compared to sensory feedback of the semimembranosus (hamstrings). The EMG (thick black lines) and sensory feedback (colored lines) are shown for one trial of a fast passive stretch motion (top) and a gait motion (bottom) for the semimembranosus (hamstrings) of one CP child. The velocity-related model combines muscle fiber length and velocity feedback. The acceleration-related model combines muscle fiber length, velocity, and acceleration feedback. The force-related model combines muscle force and dF/dt feedback. The three models also include a baseline activation during the fast passive stretch motion (top). The vertical lines indicate the transition from stance to swing (bottom). Other cases are shown in Figure B.2 in Appendix B.

During fast passive stretch motions of the gastrocnemii, the force-related model

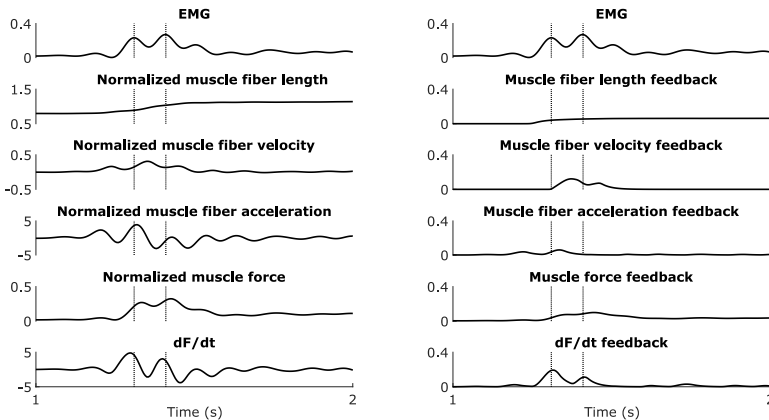


Figure 4.5: EMG, sensory information, and sensory feedback of the semimembranosus (hamstrings) during a fast passive stretch motion. The EMG (top), normalized sensory information (left), and corresponding sensory feedback (right) are shown for one trial of a fast passive stretch motion for the semimembranosus (hamstrings) of one CP child (corresponding to Figure 4.4 (zoom between 1 and 2 s)). The vertical lines indicate the first two EMG peaks. Normalized muscle fiber acceleration is the first time derivative of normalized muscle fiber velocity. dF/dt is the first time derivative of normalized muscle force.

could reproduce the EMG whereas the two other models could not even capture the overall shape of the signal (example in Figure 4.6, top; other cases in Figures B.3-B.4 in Appendix B). In all cases (example in Figure 4.7, right), delayed feedback from dF/dt reproduced the large peaks in muscle activity during the stretch and the smaller oscillations in muscle activity during the pre-stretch and hold phases, whereas muscle force feedback contributed to the low/sustained muscle activity after the stretch. In five out of twelve cases, fiber velocity feedback resulted in a single peak in muscle activity that was out of phase with the EMG and had a lower amplitude than the peak EMG. Estimated velocity feedback gains were very small in the other cases. In all cases, fiber length feedback mainly contributed to the low/sustained muscle activity after the stretch (Figure 4.6, top-left and top-middle, and Figures B.3-B.4 in Appendix B). In six out of twelve cases, fiber acceleration feedback reproduced the oscillations in EMG during the stretch to some extent, although the amplitude of the simulated muscle activity was a lot smaller than the amplitude of the EMG, whereas estimated acceleration feedback gains were very small in the other cases (Figure 4.6, top-middle, and Figures B.3-B.4 in

Appendix B).

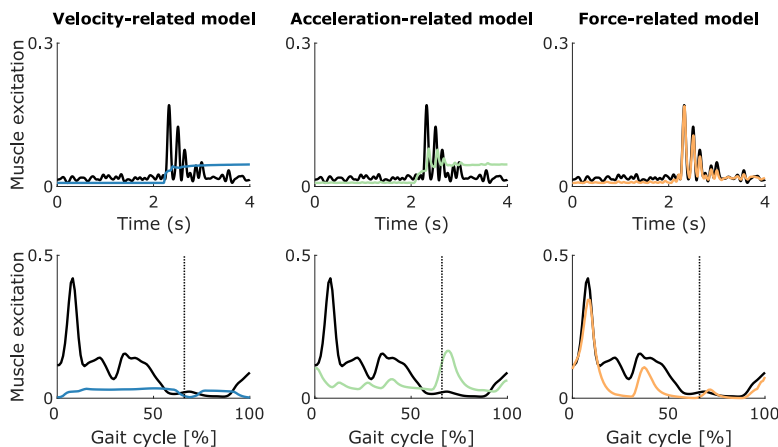


Figure 4.6: EMG compared to sensory feedback of the gastrocnemius medialis (gastrocnemii). The EMG (thick black lines) and sensory feedback (colored lines) are shown for one trial of a fast passive stretch motion (top) and a gait motion (bottom) for the gastrocnemius medialis (gastrocnemii) of one CP child. The velocity-related model combines muscle fiber length and velocity feedback. The acceleration-related model combines muscle fiber length, velocity, and acceleration feedback. The force-related model combines muscle force and dF/dt feedback. The three models also include a baseline activation during the fast passive stretch motion (top). The vertical lines indicate the transition from stance to swing (bottom). Other cases are shown in Figures B.3-B.4 in Appendix B.

Muscle activity predicted by the force-related spasticity model during gait was consistent with measured EMG whereas this was not the case for the velocity- and acceleration-related models (see Figures 4.4 and 4.6 for examples; other cases in Figures B.2-B.4 in Appendix B). The agreement between predicted feedback muscle activity and measured EMG is reflected in the cross-correlations (Figure 4.8). The cross-correlations between EMG and predicted muscle activity were larger using the force-related model (average 0.82 ± 0.09 and 0.85 ± 0.06 for the hamstrings and gastrocnemii, respectively) compared to the velocity-related model (average 0.49 ± 0.17 and 0.71 ± 0.22) and the acceleration-related model (average 0.51 ± 0.16 and 0.67 ± 0.20). The differences between the force-related model and the two other models were statistically significant ($p < 0.05$) for all

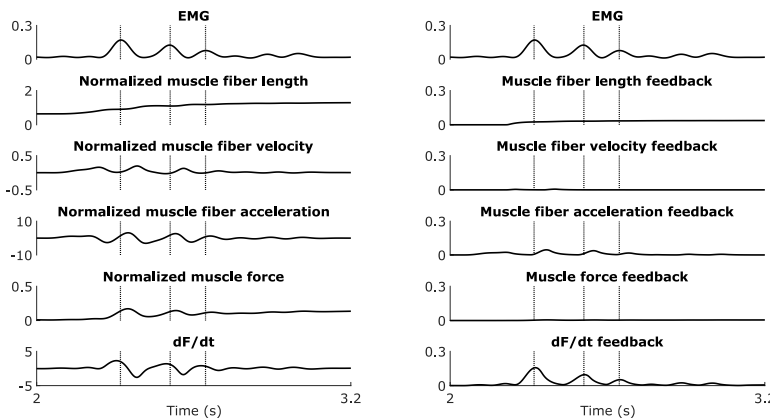


Figure 4.7: **EMG, sensory information, and sensory feedback of the gastrocnemius medialis (gastrocnemii) during a fast passive stretch motion.** The EMG (top), normalized sensory information (left), and corresponding sensory feedback (right) are shown for one trial of a fast passive stretch motion for the gastrocnemius medialis (gastrocnemii) of one CP child (corresponding to Figure 4.6 (zoom between 2 and 3.2 s)). The vertical lines indicate the first three EMG peaks. Normalized muscle fiber acceleration is the first time derivative of normalized muscle fiber velocity. dF/dt is the first time derivative of normalized muscle force.

muscles.

During gait, only the force-related spasticity model predicted muscle activity that lay within the EMG envelope for the hamstrings (example in Figure 4.4, bottom; other cases in Figure B.2 in Appendix B). The force-related model predicted high muscle activity at the end of swing that resembled measured EMG and lower feedback muscle activity during stance that lay within the EMG envelope (in one out of eight cases, the predicted muscle activity exceeded the EMG at the end of swing) (Figure 4.4, bottom-right, and Figure B.2 in Appendix B). In all cases, the velocity- and acceleration-related models predicted muscle activity during mid-swing that was not consistent with EMG (Figure 4.4, bottom-left and bottom-middle, and Figure B.2 in Appendix B), i.e. the predicted muscle activity occurred when no EMG was measured. Sensory information and corresponding feedback contributions of the example in Figure 4.4 are in Appendix B (Figure B.5).

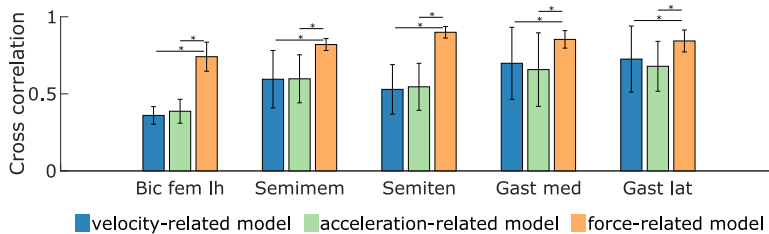


Figure 4.8: Cross-correlations between EMG and simulated muscle excitation during gait. Muscle excitation is estimated based on the three spasticity models (velocity-, acceleration-, and force-related). The statistical significance level was set to 0.05 and statistical differences between models are indicated using a horizontal bar. Results are averaged over eight and 12 values for the hamstrings (biceps femoris long head (Bic fem lh), semimembranosus (Semimem), and semitendinosus (Semiten)) and gastrocnemii (gastrocnemius medialis (Gast med) and lateralis (Gast lat)), respectively.

During gait, only the force-related model predicted activity of the gastrocnemii that lay within the EMG envelope and captured the abnormal peak in activity at initial contact that we observed in a subgroup of the subjects. A first group of subjects landed on their heel at initial contact (four out of twelve cases) whereas a second group of subjects landed on their forefoot instead of their heel at initial contact (eight out of twelve cases). In this second group, increased muscle activity, which is not observed in healthy individuals during walking, was measured at the beginning of stance (example in Figure 4.6, bottom; other cases in Figure B.4 in Appendix B). In the first group, the force-related model predicted muscle activity during both stance and swing that lay within the EMG envelope whereas the two other models predicted low muscle activity (Figure B.3 in Appendix B). In the second group, the force-related model predicted the abnormal increase in EMG during initial stance as well as muscle activity during mid-stance and at the end of swing that lay within the EMG envelope (Figure 4.6, bottom-right, and Figure B.4 in Appendix B). The other two models predicted either low levels of muscle activity or muscle activity that lay outside the EMG envelope (Figure 4.6, bottom-left and bottom-middle, and Figure B.4 in Appendix B). Sensory information and corresponding feedback contributions of the example in Figure 4.6 are in Appendix B (Figure B.6).

Discussion

We showed that a spasticity model combining delayed feedback from muscle force and its first time derivative (dF/dt) (force-related model) could explain muscle activity measured during fast passive stretches of the hamstrings and gastrocnemii of children with spastic CP. Although spasticity has been defined as a velocity-dependent increase in stretch reflexes, our models combining feedback from muscle fiber length, velocity, and acceleration (velocity- and acceleration-related models) could not explain the measured muscle activity during passive stretches. In addition, we showed that the force-related model predicted muscle excitation during gait that was consistent with the muscle activity measured in the hamstrings and gastrocnemii of the CP children. Specifically, the force-related model predicted the abnormal peak in gastrocnemii activity in early stance that was observed in the subset of children that landed on their forefoot instead of on their heel. Our force-related model of spasticity may therefore be useful in quantifying gait impairments resulting from spasticity on a patient-specific basis.

Our results suggest that spastic muscle activity can be described by exaggerated feedback from muscle force and its first time derivative, and are therefore in agreement with a recent experimental study [99] that shows that muscle spindles encode muscle force and force rate. Spindle firing is traditionally thought to encode information about muscle fiber length and velocity. Fiber length and velocity are related to muscle force through the muscle's force-length-velocity properties. During a stretch, the increased fiber velocity results in an increase in (eccentric) muscle force and, if the muscle is working on the ascending part of the force-length curve, the increased fiber length also results in an increase in muscle force. However, this relation is not linear and Blum *et al.* [99] demonstrated that spindle firing, measured *in vitro* during stretch of passive muscles, is uniquely related to muscle fiber force and its first time derivative but not to length and velocity. This observation is in line with older *in vitro* studies that related peaks in muscle spindle firing rates to muscle force transients at stretch onset [159, 160]. Furthermore, our model is in agreement with existing physiology-inspired models of spindle firing that describe the sensory region of the spindle as a spring in series with the intrafusal muscle fibers, thereby modeling spindle firing as proportional to spring elongation, which is in turn proportional to muscle force [156, 157, 158]. Finally, our model is based on delayed sensory feedback and therefore the peak in dF/dt that mainly explains the peak in EMG (Figures 4.5 and 4.7) cannot solely be a response of altered muscle activity. Instead, the muscle's state is altered by the imposed stretch and this is reflected in the EMG with a delay. Further delays are also introduced

by muscle activation and contraction dynamics. However, there is a need for additional studies documenting force encoding in muscle spindles.

Our predictions of reflex muscle activity during gait based on feedback from force-related variables suggest that spasticity contributes to gait impairments in CP. Several studies argued that spasticity of the hamstrings might contribute to crouch gait, a typical pathological gait pattern in CP children [169], by restricting knee extension at terminal swing [165, 169, 170, 171, 172]. Our simulation results demonstrate that exaggerated proprioceptive feedback from muscle force and dF/dt may indeed contribute to hamstrings activity at the end of swing (see example simulation of a subject with crouch gait in Figure 4.4). Landing on the forefoot instead of the heel during initial contact is another common pathological deviation from normal walking seen in CP children. This gait deviation has been correlated to abnormally large stretch responses in the gastrocnemii [164]. In these cases, there is a large peak in gastrocnemius activity at about 8% of the gait cycle whereas the peak muscle activity in typical walking is expected at about 40% of the gait cycle [173]. Our results demonstrate that exaggerated feedback from dF/dt may cause the peak in gastrocnemius activity during early stance. Hence, modeling spasticity based on force-related variables allowed us to directly relate measures of spasticity in passive muscles to muscle activity during walking, providing further support for the role of spasticity in impeding gait performance in CP. We could explain measured muscle activity during passive stretches and gait based on the same feedback model parameters (reflex thresholds and gains), which is in agreement with a lack of or decrease in reflex modulation reported for patients with spasticity [95, 174, 175, 176]. In healthy individuals, reflex modulation has been shown to be context-dependent whereas it has been suggested that supraspinal input is dysregulated in patients with CP [175, 177, 178, 179, 180]. As examples, Faist *et al.* [175] reported less quadriceps reflex depression and modulation in patients with spasticity due to cerebral lesions during gait as compared to healthy subjects and Sinkjaer *et al.* [176] reported less soleus stretch reflex modulation during gait in patients with spasticity due to multiple sclerosis. Furthermore, Nielsen *et al.* [181] provided a reasoning that supports our approach of using the same spasticity model in passive motions and gait. On the one hand, stretch reflex activity is larger in active contractions than in passive conditions due to depression of the inhibitory mechanisms in healthy subjects in active conditions. On the other hand, inhibitory mechanisms are already depressed in passive conditions in spastic individuals. Thus, these mechanisms cannot be depressed further during active contractions in spastic individuals leading to similar reflexes during passive and active conditions.

It is likely that not all reflex muscle activity predicted by the spasticity model during gait is pathological. In particular, the hamstrings are active at the end of swing in normal walking to modulate the rate of knee extension and prepare the leg for stance [173] and this activity has been attributed to stretch reflexes [182]. It is therefore hard to dissociate normal and pathological muscle activity. It is possible that the feedback pathways used to model spasticity in this study are part of the neural circuitry responsible for normal gait that is inhibited in passive conditions and modulated throughout the gait cycle in typically developed individuals. However, our spasticity model that was calibrated based on muscle activity during passive motions that has been attributed to spasticity, also predicted muscle activity during gait that matched experimental EMG of CP children but is not observed in healthy individuals, e.g. burst in gastrocnemius activity at the beginning of stance.

Our spasticity models do not differentiate between hypersensitivity of the muscle spindles, i.e. increased muscle spindle firing rates, and hyperexcitability of the motoneuron pool. Instead, muscle spindle firing and motoneuron excitability are lumped in our simple models that describe muscle spindle reflexes by delayed sensory feedback. Our results suggest that force encoding in muscle spindles underlies spastic muscle activity but should not be interpreted as spasticity being primarily due to changes in muscle spindle sensitivity rather than spinal cord and supraspinal dysregulation. Previous studies that separately modeled the muscle spindle and neuromotor pool suggested that alterations in motoneuron excitability and not muscle spindle hypersensitivity is the primary cause of spasticity [183, 184].

Fits between EMG and simulated muscle excitation were relatively low for the gastrocnemii for the passive motions at medium velocity that were not used for calibration, although the force-related model still outperformed the other models (average R^2 and RMSE: 0.24 ± 0.21 and 0.014 ± 0.013 , respectively). This is partly explained by the fact that, in several cases, the clinical tests did not reveal any spastic involvement at medium velocities, i.e. no EMG onsets were identified, which was poorly reproduced by the models and explains the large variability in the results. In the future, we might therefore need to refine our model and our approach to determine the feedback thresholds. Other methods have been proposed in the literature. For example, instead of modeling reflex thresholds for each feedback component, Safavynia and Ting [185] reconstructed EMG signals based on linear feedback of the state variables by adding all feedback components and then half-wave rectifying the total signal. Such an approach might result in better fits by including information from negative signals. Overall, also for the stretches at medium velocity the

force-related model outperformed the other models and captured the distinct features of the spastic response in most cases.

We made several assumptions when developing the spasticity models. First, we used muscle-tendon force feedback whereas spindles presumably sense active muscle force [99]. Muscle-tendon force is nevertheless a good surrogate for active muscle force if passive force and pennation angle are small, as in our case. Yet, future work should consider using active muscle force rather than muscle-tendon force. Second, we used a fixed delay of 30 ms for all feedback pathways. Using larger delays could have increased the quality of the fit between EMG and muscle excitation resulting from the velocity feedback for the gastrocnemii. However, having the peak velocity feedback matching the peak EMG would have required delays exceeding reported values [186]. Third, there was no attempt to model the influence of gamma drive on the spindle sensitivity. Nielsen *et al.* [181] reported that the increased gamma-motor activity should not play a role in spasticity. Fourth, we did not explicitly constrain feedback muscle activity to muscle lengthening, which could be a valid assumption since spasticity models aim to simulate exaggerated muscle activity resulting from hyper-excited stretch reflexes. However, we verified that this would have had little influence on the main conclusions. In the example of Figure 4.4, the only noticeable difference would have been an inhibition of the feedback contributions observed in the stance phase for the hamstrings since the latter are shortening during that phase (Figure B.5 in Appendix B). The influence on the gastrocnemii would have been minor. Constraining feedback muscle activity to phases where the muscle is lengthening would therefore not change our conclusions. Fifth, the EMG processing workflow might influence the results. However, we verified that increasing the low-pass cut-off frequency had little influence on the main conclusions. Finally, we did not model the increased muscle stiffness that is known to contribute to muscle hyper-resistance in CP children [100]. However, we estimated subject-specific muscle-tendon parameters to reproduce inverse dynamic moments during slow passive stretches and gait. Since inverse dynamic moments and moments simulated using the optimized parameters were in good agreement for the slow passive stretches, there was no need to further model the increased passive stiffness.

Conclusion

In this study, we proposed a spasticity model based on delayed feedback from muscle force and its first time derivative that could explain muscle activity from instrumented passive spasticity assessments. Additionally, the model could

predict hamstrings and gastrocnemii activity during gait in spastic CP children that was consistent with measured muscle activity. Using personalized models of spasticity may be important to advance our understanding of movement impairments due to spasticity. Moreover, inclusion of spasticity models in predictive simulations of walking may result in more accurate simulations of walking kinematics that can eventually be used to predict treatment outcome in children with CP.

Acknowledgments

The authors would like to thank Prof. J. Duysens and Prof. L. Ting for the insightful discussions when interpreting the findings of this study. All authors were supported by the IWT-TBM grant SimCP (140184). AF also received a PhD grant (1S35416N) from the Research Foundation Flanders (FWO). LB also received a postdoctoral grant (12R4215N) from the Research Foundation Flanders (FWO) and a grant (016.186.144) from the Netherlands Organisation for Scientific Research (NWO). KD also received a grant (DBOF/12/058) from the Doctoral Scholarships Committee for International Collaboration with non EER-countries (DBOF) of the KU Leuven (Belgium).

Data availability

The data and scripts required for reproducing the results are available at <https://simtk.org/home/simcpspasticity>.

Chapter 5

Study 3: Algorithmic differentiation improves the computational efficiency of OpenSim-based trajectory optimization of human movement

Published as:

Falisse A., Serrancolí G., Dembia C.L., Gillis J., De Groote F. *Algorithmic differentiation improves the computational efficiency of OpenSim-based trajectory optimization of human movement*, (2019). PLoS ONE, **14**(10): e0217730.

Abstract

Algorithmic differentiation (AD) is an alternative to finite differences (FD) for evaluating function derivatives. The primary aim of this study was to demonstrate the computational benefits of using AD instead of FD in OpenSim-based trajectory optimization of human movement. The secondary aim was to evaluate computational choices including different AD tools, different linear solvers, and the use of first- or second-order derivatives. First, we enabled the use of AD in OpenSim through a custom source code transformation tool and through the operator overloading tool ADOL-C. Second, we developed an interface between OpenSim and CasADI to solve trajectory optimization problems. Third, we evaluated computational choices through simulations of perturbed balance, two-dimensional predictive simulations of walking, and three-dimensional tracking simulations of walking. We performed all simulations using direct collocation and implicit differential equations. Using AD through our custom tool was between 1.8 ± 0.1 and 17.8 ± 4.9 times faster than using FD, and between 3.6 ± 0.3 and 12.3 ± 1.3 times faster than using AD through ADOL-C. The linear solver efficiency was problem-dependent and no solver was consistently more efficient. Using second-order derivatives was more efficient for balance simulations but less efficient for walking simulations. The walking simulations were physiologically realistic. These results highlight how the use of AD drastically decreases computational time of trajectory optimization problems as compared to more common FD. Overall, combining AD with direct collocation and implicit differential equations decreases the computational burden of trajectory optimization of human movement, which will facilitate their use for biomechanical applications requiring the use of detailed models of the musculoskeletal system.

Introduction

Combining musculoskeletal modeling and dynamic simulation is a powerful approach to study the mechanisms underlying human movement. In the last decades, researchers have primarily used inverse dynamic simulations to identify biomechanical variables (e.g., muscle forces and joint loads) underlying observed movements. Yet dynamic simulations can also be applied to generate novel movements. Such predictive simulations have the potential to reveal cause-effect relationships that cannot be explored based on inverse dynamic simulations that require movement kinematics as input. Novel movements can be generated by solving trajectory optimization problems. Generally, trajectory optimization consists of identifying a trajectory that optimizes an

objective function subject to a set of dynamic and path constraints [117]. In the biomechanical field, researchers have used trajectory optimization for solving two main types of problems. In tracking problems, the objective function is the difference between a variable's measured and simulated value [43, 44, 46], whereas in predictive problems, the objective function represents a movement related performance criterion (e.g., minimizing muscle fatigue) [35, 39, 25, 37]. However, the nonlinearity and stiffness of the dynamic equations characterizing the musculoskeletal system cause the underlying optimal control problems to be challenging to solve and computationally expensive [35, 25, 37]. For example, small changes in controls can cause large changes in kinematics and hence a foot to penetrate into the ground, drastically increasing ground reaction forces. These challenges have caused the biomechanics community to primarily perform studies based on inverse dynamic analyses of observed movements rather than trajectory optimization of novel movements.

Over the last decade, the increase in computer performance and the use of efficient numerical methods have equipped researchers with more efficient tools for solving trajectory optimization problems. In particular, direct collocation methods [46, 39, 37, 52, 53, 54] and implicit formulations of the musculoskeletal dynamics [53, 55] have become popular. Direct collocation reduces the sensitivity of the objective function to the optimization variables, compared to other methods such as direct shooting [35], by reducing the time horizon of the integration. Direct collocation converts optimal control problems into large sparse nonlinear programming problems (NLPs) that readily available NLP solvers (e.g., IPOPT [122]) can solve efficiently. Implicit formulations of the musculoskeletal dynamics improve the numerical conditioning of the NLP over explicit formulations by, for example, removing the need to divide by small muscle activations [53] or invert a mass matrix that is near-singular due to body segments with a large range of masses and moments of inertia [55]. In implicit formulations, additional controls are typically introduced for the time derivative of the states, which allows imposing the nonlinear dynamic equations as algebraic constraints in their implicit rather than explicit form (i.e., $\dot{y} = u$, $0 = f_i(y, u)$ instead of $\dot{y} = f_e(y)$).

Algorithmic differentiation (AD) is another numerical tool that can improve the efficiency of trajectory optimization [187, 118]. AD is a technique for evaluating derivatives of functions represented by computer programs. It is, therefore, an alternative to finite differences (FD) for evaluating the derivative matrices required by the NLP solver, namely the objective function gradient, the constraint Jacobian, and the Hessian of the Lagrangian (henceforth referred to as simply Hessian). These evaluations are obtained free of truncation errors, in

contrast with FD, and for a computational cost of the same order of magnitude as the cost of evaluating the original function. AD relies on the observation that any function can be broken down into a sequence of elementary operations, forming an expression graph (example in Figure 5.1). AD then relies on the chain rule of calculus that describes how to calculate the derivative of a composition of functions [118]. By traversing a function's expression graph while applying the chain rule, AD allows computing the function derivatives. Note that, like FD, AD can exploit the sparsity of the aforementioned derivative matrices resulting, for example, from applying direct collocation [188].

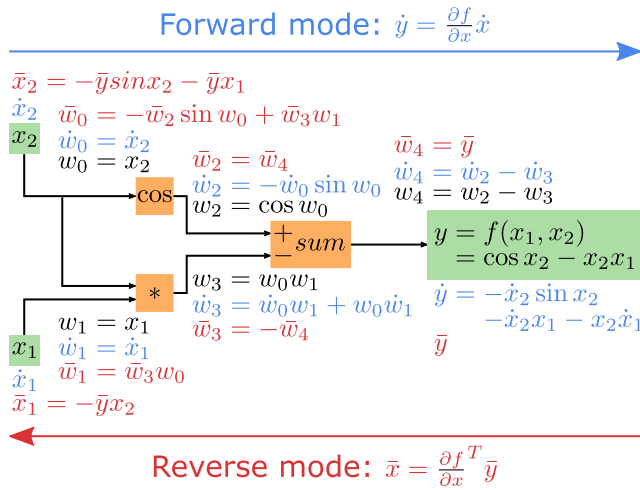


Figure 5.1: **Example of AD forward and reverse modes.** A function $y = f(x_1, x_2) = \cos x_2 - x_2 x_1$ is broken down into a sequence of elementary operations, forming an expression graph. In the forward mode, the forward seeds \dot{x}_1 and \dot{x}_2 are propagated from the inputs to the output, and the Jacobian $J = \partial f / \partial \mathbf{x}$ relates \dot{x}_1 and \dot{x}_2 and forward sensitivities \dot{y} . In the reverse mode, the reverse seed \bar{y} is propagated from the output to the inputs, and the transposed Jacobian J^T relates \bar{y} and reverse sensitivities \bar{x}_1 and \bar{x}_2 .

AD allows traversing the expression graph in two directions or modes: from the inputs to the outputs in its forward mode and from the outputs to the inputs in its reverse mode. This permits the evaluation of two types of directional derivatives: Jacobian-times-vector product and Jacobian-transposed-times-vector product in the forward and reverse mode, respectively. The computational efficiency of the AD mode depends on the problem dimensions. Consider the function $G : \mathbb{R}^n \rightarrow \mathbb{R}^m : y = G(x)$ describing the m NLP constraints y as a function of the n optimization variables x . The constraint Jacobian $J = \frac{\partial y}{\partial x}$ is a matrix

with size $m \times n$. In the forward mode, J relates forward seeds \dot{x} to forward sensitivities \dot{y} : $\dot{y} = J\dot{x}$ (example in Figure 5.1). In the reverse mode, J^T relates reverse seeds \bar{y} to reverse sensitivities \bar{x} : $\bar{x} = J^T\bar{y}$ (example in Figure 5.1). In the forward mode, the cost of evaluating J is proportional to n times the cost of evaluating G . In the reverse mode, the cost of evaluating J^T is proportional to m times the cost of evaluating G . If there are many more inputs n than outputs m , the reverse mode may drastically decrease the number of function evaluations required to evaluate J and highly reduce the computational time (CPU time) as compared to the forward mode [118, 120].

Two main approaches exist for adding AD to existing software, namely operator overloading and source code transformation. Source code transformation is inherently faster than operator overloading but may not be readily available for all features of a programming language. In the operator overloading approach, AD's algorithms are applied after the evaluation of the original function using concrete numerical inputs. This is typically performed by introducing a new numerical type that stores information about partial derivatives as calculations proceed (e.g., through operator overloading in C++) [118, 120]. Examples of AD tools using operator overloading in C++ are ADOL-C [126] and CppAD [189]. In the source code transformation approach, the AD tool analyzes a given function's source code and outputs a new function that computes the forward or reverse mode of that function. Examples of AD tools using source code transformation are ADiGator for MATLAB [142] and CasADi that is available for C++, Python, and MATLAB [56]. CasADi is a modern actively developed tool for nonlinear optimization and AD that has many additional features (e.g., code generation) and interfaces with NLP solvers designed to handle large and sparse NLPs (e.g., IPOPT). CasADi provides a high-level, symbolic, way to construct an expression graph, on which source code transformation is applied. The resultant expression graph can be code-generated to achieve the computational efficiency of pure source code transformation.

AD has a long history [187] but has rarely been applied in biomechanics, likely because AD is relatively unknown in the field and is not integrated as part of widely used biomechanical software packages. In previous work, we solved muscle redundancy problems while exploiting AD [53, 168]. For this purpose, we used GPOPS-II [121], a MATLAB software for solving optimal control problems with direct collocation, in combination with ADiGator. However, these problems were limited to models implemented in MATLAB, enabling the use of ADiGator. Generating simulations of human movement requires expanding these problems to account for the multi-body dynamics. OpenSim [112][190] and its dynamics engine Simbody [119] are widely used open-source

software packages for musculoskeletal modeling and biomechanical dynamic simulation. These packages provide multi-body dynamics models and have been used for trajectory optimization of human gait [44, 46, 37, 54]. Yet they currently do not leverage tools for AD. Moreover, they are written in C++, which would prevent the use of ADiGator.

AD is increasingly used for trajectory optimization in related fields such as rigid body dynamics for robotic applications and several software packages leverage AD tools [191]. RobCoGen is a modeling tool for rigid body dynamics that supports AD through source code transformation. Giftthaler *et al.* showed that trajectory optimization of gait for a quadrupedal robot modeled with RobCoGen was five times faster with AD than with FD [191]. Other packages for robotic applications with modules supporting AD include Drake [192], Robotran [193], MBSlib [194], and Pinocchio [195]. Drake is a collection of tools that relies on Eigen [196] for linear algebra. Eigen has a module supporting AD's forward mode using operator overloading. Robotran is a symbolic software to model multibody systems that can be interfaced with CasADi to solve optimal control problems. MBSlib is a multibody system library supporting AD through ADOL-C. Finally, Pinocchio is a software platform implementing algorithms for rigid body dynamics that can be interfaced with ADOL-C, CppAD, and CasADi. Note that AD is not exclusively used for trajectory optimization and is also applied in other related fields including deep learning with libraries such as TensorFlow [197] and Theano [198], and applications for robotic gait optimization (e.g., [199]).

The contribution of this study is threefold. First, we enabled the use of AD in OpenSim and Simbody (henceforth referred to as OpenSim). We compared two approaches: we incorporated the operator overloading AD tool ADOL-C and we developed our own AD tool Recorder that uses operator overloading to construct an expression graph on which source code transformation is applied using CasADi. Second, we interfaced OpenSim with CasADi, enabling trajectory optimization using OpenSim's multi-body dynamics models while benefiting from CasADi's efficient interface with NLP solvers. Third, we evaluated the efficiency of different computational choices based on trajectory optimization problems of varying complexity solved with IPOPT. We compared three different derivative scenarios: AD with ADOL-C, AD with Recorder, and FD. In addition, we compared different linear solvers and different Hessian calculation schemes within IPOPT, to aid users in choosing the most efficient solver settings. Primal-dual interior point methods such as IPOPT rely on linear solvers to solve the primal-dual system, which involves the Hessian, when computing the Newton step direction during the optimization [123]. The Hessian can be exact (i.e.,

based on second-order derivative information) or approximated with a limited-memory quasi-Newton method (L-BFGS) that only requires first-order derivative information. We found that using AD through Recorder was more efficient than using FD or AD through ADOL-C, whereas the efficiency of the linear solver and Hessian calculation scheme was problem-dependent.

Methods

Tools to enable the use of AD in OpenSim

We first incorporated the operator overloading AD tool ADOL-C in OpenSim. ADOL-C relies on the concept of active variables, which are variables that may be considered as differentiable quantities at some time during the execution of a computer program [126]. To distinguish these variables and store information about their partial derivatives, ADOL-C introduced the augmented scalar type `adouble` whose real part is of standard type `double`. All active variables should be of type `adouble`. To differentiate OpenSim functions using ADOL-C, we modified OpenSim's source code by replacing the type of potential active variables to `adouble` (example for `SimTK::square()` in Figure 5.2). We maintained a layer of indirection so that OpenSim could be compiled to use either `double` or `adouble` as the scalar type. We excluded parts of the code, such as numerical optimizers, that were not relevant to this study.

The limited computational benefits of using AD through ADOL-C led us to seek alternative AD strategies (see discussion for more detail). We developed our own tool, Recorder, which combines the versatility of operator overloading and the speed of source code transformation. Recorder is a C++ scalar type for which all operators are overloaded to generate an expression graph. When evaluating an OpenSim function numerically at a nominal point, Recorder generates the function's expression graph as MATLAB source code in a format that CasADI's AD algorithms can transform into C-code. Note that this workflow is currently only practical when the branches (if-tests) encountered at the nominal point remain valid for all evaluations encountered during the optimization.

To use Recorder with OpenSim, we relied on the code we had modified for incorporating ADOL-C but replaced `adouble` with the Recorder scalar type (example for `SimTK::square()` in Figure 5.2). This change required minimal effort but enabled Recorder to identify all differentiable variables when constructing the expression graphs.

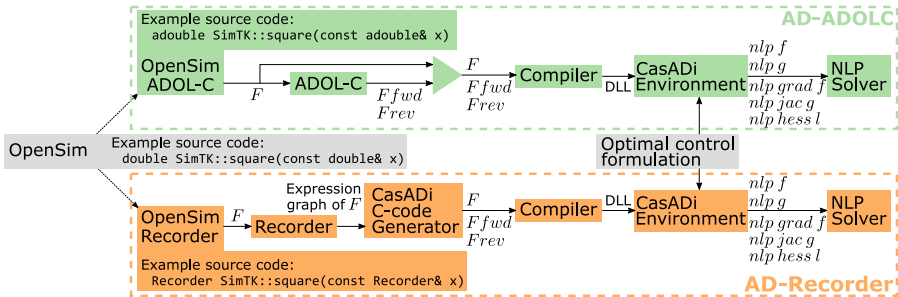


Figure 5.2: **Flowchart depicting the optimal control framework.** We developed two approaches (AD-ADOLC and AD-Recorder) to make an OpenSim function F and its forward (F_{fwd}) and reverse (F_{rev}) directional derivatives available within the CasADI environment for use by the NLP solver during the optimization. In the AD-ADOLC approach (top), ADOL-C’s algorithms are used in a C++ code to provide F_{fwd} and F_{rev} . In the AD-Recorder approach (bottom), Recorder provides the expression graph of F as MATLAB source code from which CasADI’s C-code generator generates C-code containing F , F_{fwd} , and F_{rev} . The AD-Recorder approach combines operator overloading, when generating the expression graph, and source code transformation, when processing the expression graph to generate C-code for F , F_{fwd} , and F_{rev} . In both approaches, the code comprising F , F_{fwd} , and F_{rev} is compiled as a Dynamic-link Library (DLL), which is imported as an external function within the CasADI environment. In our application, F represents the multi-body dynamics and is called when formulating the optimal control problem. The latter is then composed into a differentiable optimal control transcription using CasADI. During the optimization, CasADI provides the NLP solver with evaluations of the NLP objective function ($nlp\ f$), constraints ($nlp\ g$), objective function gradient ($nlp\ grad\ f$), constraint Jacobian ($nlp\ jac\ g$), and Hessian of the Lagrangian ($nlp\ hess\ l$). CasADI efficiently queries F_{fwd} and F_{rev} to construct the full derivative matrices.

Interface between OpenSim and CasADi

We enabled the use of OpenSim functions within the CasADi environment by compiling the functions and their derivatives as Dynamic-link Libraries that are then imported as external functions for use by CasADi (Figure 5.2). The function derivatives can be computed through ADOL-C (AD-ADOLC in Figure 5.2) or through Recorder (AD-Recorder in Figure 5.2).

Trajectory optimization problems to evaluate computational choices

We designed three example trajectory optimization problems to evaluate different computational choices (see Tables 5.1-5.3 for detailed formulations). The general formulation of the optimal control problems consists of computing the controls $\mathbf{u}(t)$, states $\mathbf{x}(t)$, and time-independent parameters \mathbf{p} minimizing an objective functional:

$$\int_{t_i}^{t_f} L(\mathbf{x}(t), \mathbf{u}(t), \mathbf{p}) dt, \quad (5.1)$$

where t_i and t_f are initial and final times, and t is time. This objective functional is subject to dynamic constraints:

$$\dot{\mathbf{x}}(t) = f(\mathbf{x}(t), \mathbf{u}(t), \mathbf{p}), \quad (5.2)$$

and to algebraic path constraints:

$$g_{\min} \leq g(\mathbf{x}(t), \mathbf{u}(t), \mathbf{p}) \leq g_{\max}, \quad (5.3)$$

which are equality constraints if $g_{\min} = g_{\max}$. The optimization variables are typically bounded as follows:

$$x_{\min} \leq \mathbf{x}(t) \leq x_{\max}, \quad (5.4)$$

$$u_{\min} \leq \mathbf{u}(t) \leq u_{\max}, \quad (5.5)$$

$$p_{\min} \leq \mathbf{p} \leq p_{\max}. \quad (5.6)$$

Example 1: Pendulum simulations			
Number of optimization variables	States $x(t)$	Controls $u(t)$	Derivatives of v (accelerations): u_{dv} Joint torques u_T
2 degree of freedom pendulum: 504	Joint positions q and velocities v	$s_q = 3; \tilde{q} = q/s_q$	2 degree of freedom pendulum: 458
3 degree of freedom pendulum: 756		$\tilde{q}_{lb} = q_{lb}/s_q; \tilde{q}_{ub} = q_{ub}/s_q$	3 degree of freedom pendulum: 687
4 degree of freedom pendulum: 1008		$s_t = 0.2; \tilde{v} = v/(s_q/s_t)$	4 degree of freedom pendulum: 916
5 degree of freedom pendulum: 1260		$\tilde{v}_{lb} = v_{lb}/(s_q/s_t); \tilde{v}_{ub} = v_{ub}/(s_q/s_t)$	5 degree of freedom pendulum: 1145
6 degree of freedom pendulum: 1512		$\tilde{u}_{dv,lb} = u_{dv,lb}/(s_q/s_t^2); \tilde{u}_{dv,ub} = u_{dv,ub}/(s_q/s_t^2)$	6 degree of freedom pendulum: 1374
7 degree of freedom pendulum: 3514		$\tilde{s}_T = 500; \tilde{u}_T = u_T/s_T; \tilde{u}_{T,lb} = u_{T,lb}/s_T$	7 degree of freedom pendulum: 3178
8 degree of freedom pendulum: 4016		$\tilde{u}_{T,ub} = u_{T,ub}/s_T$	8 degree of freedom pendulum: 3632
9 degree of freedom pendulum: 4518		$(dq/dt)/s_q = v/s_q$	9 degree of freedom pendulum: 4086
10 degree of freedom pendulum: 10020		$(dv/dt)/(s_q/s_t) = u_{dv}/(s_q/s_t)$	10 degree of freedom pendulum: 9040
Bounds	Scaling		
$-\pi/2 = q_{lb} \leq q \leq q_{ub} = \pi/2$		$\tilde{q}_{lb} = q_{lb}/s_q; \tilde{q}_{ub} = q_{ub}/s_q$	
$-20 = v_{lb} \leq v \leq v_{ub} = 20$		$s_t = 0.2; \tilde{v} = v/(s_q/s_t)$	
$-500 = u_{dv,lb} \leq u_{dv} \leq u_{ub} = 500$		$\tilde{v}_{lb} = v_{lb}/(s_q/s_t); \tilde{v}_{ub} = v_{ub}/(s_q/s_t)$	
$-1000 = u_{T,lb} \leq u_T \leq u_{ub} = 1000$		$\tilde{u}_{dv,lb} = u_{dv,lb}/(s_q/s_t^2); \tilde{u}_{dv,ub} = u_{dv,ub}/(s_q/s_t^2)$	
Objective function	Dynamic constraints		
$L = \ \tilde{u}_T\ _2^2 + L_p$	$T = f_s(q, v, u_{dv})$	$\tilde{u}_{T,ub} = u_{T,ub}/s_T$	
$L_p = 0.1 \ \tilde{u}_{dv}\ _2^2$	$T/s_T = \tilde{u}_T$	$(dq/dt)/s_q = v/s_q$	
Path constraints			$\tilde{q}(0) = \tilde{q}(1) = \tilde{v}(0) = \tilde{v}(1) = 0$

Table 5.1: **Formulation example 1.** **Controls:** we introduced accelerations (time derivative of velocities) as controls (implicit formulations) in addition to joint torques. **Bounds:** lb and ub are for lower and upper bounds, respectively. **Scaling:** we used time scaling for the joint states and controls. **Objective function:** to avoid singular arcs, situations for which controls are not uniquely defined by the optimality conditions [129], we appended a penalty function L_p with the remaining controls to the objective function L . **Dynamic constraints** are scaled using the same scale factors as used for the states [129]. We used implicit formulations. **Path constraints:** $f_s(\cdot)$ computes net joint torques T according to the skeleton dynamics.

Example 2: 2D predictive simulations of walking						
Number of optimization variables	13807	Number of constraints	12857 equality constraints 1800 inequality constraints			
States $x(t)$	Muscle activations a and tendon forces F_t Joint positions q and velocities v Trunk activations $a_{t,\text{trunk}}$	Controls $u(t)$	Derivatives of a : u_{da} and F_t ; u_dF_t Derivatives of v (accelerations): u_{dv} Trunk excitations $e_{t,\text{trunk}}$			
Parameters p	Half gait cycle duration t_f $0 \leq a \leq 1; 0 \leq F_t \leq F_{t,ub} = 5$ $-\tau_d/100 \leq u_{da} \leq \tau_a/100$ $\tau_d = 60 \text{ ms}; \tau_a = 15 \text{ ms}$ $-1 \leq u_dF_t, a_{t,\text{trunk}}, e_{t,\text{trunk}} \leq 1$ $q_{lb,\text{man}} = q_{lb} \leq q \leq q_{ub} = q_{ub,\text{man}}$ $v_{lb,\text{man}} = v_{lb} \leq v \leq v_{ub} = v_{ub,\text{man}}$ $u_{dv,lb,\text{man}} = u_{dv,lb} \leq u_{dv}$ $u_{dv} \leq u_{dv,ub,\text{man}} = u_{dv,ub,\text{man}}$ $0.1 \leq t_t \leq 1$	$s_q = \max(\abs(q_{lb}), \abs(q_{ub}))$ $\tilde{q} = q/s_q; \tilde{q}_{lb} = q_{lb}/s_q; \tilde{q}_{ub} = q_{ub}/s_q$ $s_v = \max(\abs(v_{lb}), \abs(v_{ub}))$ $\tilde{v} = v/s_v; \tilde{v}_{lb} = v_{lb}/s_v; \tilde{v}_{ub} = v_{ub}/s_v$ $s_{u_{dv}} = \max(\abs(u_{dv,lb}), \abs(u_{dv,ub}))$ $\tilde{u}_{dv} = u_{dv}/s_{u_{dv}}$ $\tilde{u}_{dv,lb} = u_{dv,lb}/s_{u_{dv}}$ $\tilde{u}_{dv,ub} = u_{dv,ub}/s_{u_{dv}}$ $s_{dF_t} = s_dF_t = 100$ $s_{F_t} = F_t/F_t = 1/F_t$ $\tilde{F}_{t,ub} = F_{t,ub}/s_{F_t}$	Scaling			
Bounds	$L = \frac{(w_1 \ a\ _3^3 + w_2 \ e_{t,\text{trunk}}\ _2^2 + w_3 \ \tilde{u}_{dv}\ _2^2 + L_p)}{d}$ $L_p = 0.001 (\ u_{da}\ _2^2 + \ u_dF_t\ _2^2)$	Dynamic constraints	$\frac{da}{dt} = s_{da} u_{da}$ $(dF_t/dt)/s_{F_t} = (s_dF_t/u_dF_t)/s_{F_t}$ $(dq/dt)/s_q = v/s_q; (dv/dt)/s_v = u_{dv}/s_v$ $d_{a,\text{trunk}}/dt = (e_{t,\text{trunk}} - a_{t,\text{trunk}})/\tau$	$T_{\text{ll}} = \sum_{m=1}^M M A_m F_{t,m}$ $T_{\text{trunk}}/s_{\text{trunk}} = a_{t,\text{trunk}}$ $\bar{x}(t_f) = \bar{x}(0)$ $(q_{\text{pelvis},\text{for}}(t_f) - q_{\text{pelvis},\text{for}}(0))/t_f = 1.33 \text{ ms}$		
Objective function	$0 \leq s_{da} u_{da} + a/\tau_d; s_{da} u_{da} + a/\tau_a \leq 1/\tau_a$ $f_c(a, F_t, u_dF_t) = 0$ $T = f_s(q, v, u_{dv})$ $T_{\text{pelvis}} = 0$					
Path constraints						

Table 5.2: **Formulation example 2.** Controls are introduced for state derivatives. **Bounds** are manually (man) set for joint states and controls; lb and ub are lower and upper bounds. **Scaling:** joint states and controls, and tendon forces are scaled such that bounds are between -1 and 1. **Objective function** L is normalized by distance traveled d . To avoid singular arcs [129], a penalty function L_p with the remaining controls is appended to L . **Dynamic constraints** are scaled using state scale factors [129]. **Path constraints:** $f_s(\cdot)$ computes net joint torques T according to the skeleton dynamics, $f_c(\cdot)$ describes the muscle contraction dynamics [53], MA_m is moment arm of muscle m , $\bar{x}(\cdot)$ contains all states except the pelvis forward position $q_{\text{pelvis},\text{for}}$ (symmetry), and 1.33 m s^{-1} is the prescribed gait speed.

Example 3: 3D tracking simulations of walking			
Number of optimization variables	61318	Number of constraints	56050 equality constraints 9200 inequality constraints
States $x(t)$	Muscle activations a and tendon forces F_t Joint positions q and velocities v Arm activations a_{arm}	Controls $u(t)$	Derivatives of a : u_{da} and F_t : u_{dF_t} Derivatives of v (accelerations): u_{dv} Arm excitations e_{arm}
Parameters p	Contact sphere transversal plane locations p_{cl} Contact sphere radii p_{cr}		
Bounds	$0 \leq a \leq 1; 0 \leq F_t \leq F_{t,ub} = 5$ $-\tau_d/100 \leq u_{da} \leq \tau_a/100$ $\tau_d = 60 \text{ ms}; \tau_a = 15 \text{ ms}$ $-1 \leq u_{dF_t}, a_{\text{arm}}, e_{\text{arm}} \leq 1$ $\hat{q}_{\min} - \hat{q}_r = q_{lb} \leq q \leq q_{ub} = \hat{q}_{\max} + \hat{q}_r$ $\hat{v}_{\min} - \hat{v}_r = v_{lb} \leq v \leq v_{ub} = \hat{v}_{\max} + \hat{v}_r$ $\hat{u}_{dv,\min} - \hat{u}_{dv,r} = u_{dv,lb} \leq u_{dv}$ $u_{dv} \leq u_{dv,ub} = \hat{u}_{dv,\max} + \hat{u}_{dv,r}$ $\hat{p}_{cl} - 0.025 = p_{cl,lb} \leq p_{cl}$ $p_{cl} \leq p_{cl,ub} = \hat{p}_{cl} + 0.025$ $\hat{p}_{cr} - 0.5\hat{p}_{cr} = p_{cr,lb} \leq p_{cr}$ $p_{cr} \leq p_{cr,ub} = \hat{p}_{cr} + 0.5\hat{p}_{cr}$	Scaling	$s_q = \max(\abs(q_{lb}), \abs(q_{ub})); \tilde{q} = q/s_q$ $\tilde{q}_{lb} = q_{lb}/s_q; \tilde{q}_{ub} = q_{ub}/s_q$ $\tilde{v} = v/s_v; \tilde{v}_{lb} = v_{lb}/s_v; \tilde{v}_{ub} = v_{ub}/s_v$ $s_{u_{dv}} = \max(\abs(u_{dv,lb}), \abs(u_{dv,ub}))$ $\tilde{u}_{dv} = u_{dv}/s_{u_{dv}}; \tilde{u}_{dv,lb} = u_{dv,lb}/s_{u_{dv}}$ $\tilde{u}_{dv,ub} = u_{dv,ub}/s_{u_{dv}}$ $s_{da} = s_{dF_t} = 100; s_T = s_{\text{arms}} = 150$ $s_{dF_t} = F_{t,ub}; \tilde{F}_t = F_t/s_{F_t}; \tilde{F}_{t,ub} = F_{t,ub}/s_{F_t}$ $\tilde{p}_{cl,cr}, v = 1 / (p_{cl,cr}, b - p_{cl,cr}, b)$ $\tilde{p}_{cl,r} = 0.5 - p_{cl,ub} / (p_{cl,ub} - p_{cl,b})$ $\tilde{p}_{cr,r} = 0.5 - p_{cr,ub} / (p_{cr,ub} - p_{cr,b})$ $\tilde{p}_{cl,lb} = \tilde{p}_{cr,lb} = -0.5; \tilde{p}_{cl,ub} = \tilde{p}_{cr,ub} = 0.5$ $da/dt = s_{da} u_{da}$ $(dF_t/dt)/s_{F_t} = (s_d u_{dF_t} u_{dF_t})/s_{F_t}$ $(dq/dt)/s_q = v/s_q; (dv/dt)/s_v = u_{dv}/s_v$ $da_{\text{arms}}/dt = (e_{\text{arms}} - a_{\text{arms}})/\tau; \tau = 35 \text{ ms}$
Path constraints	$L = w_1 \ a\ _2^2 + w_2 \ v\ _2^2 + w_3 \ GRF - \hat{GRF}\ _2^2 + w_4 \ GRT - \hat{GRT}\ _2^2 + L_p$ $L_p = 0.001 (\ u_{da}\ _2^2 + \ u_{dF_t}\ _2^2 + \ u_{dv}\ _2^2)$ $0 \leq s_{da} u_{da} + a/\tau_d; s_{da} u_{da} + a/\tau_a \leq 1/\tau_a$ $f_c(a, F_t, u_{dF_t}) = 0$ $T = f_s(q, v, u_{dv})$	Dynamic constraints	$T_{\text{pelvis}}/s_T = \tilde{T}_{\text{pelvis}}/s_T$ $T_{\text{trunk}} = \sum_{m=1}^M M A_m F_{t,m} + T_p$ $T_{\text{arms}}/s_{\text{arms}} = a_{\text{arms}}$

Table 5.3: **Formulation example 3.** **Controls** are introduced for state derivatives. **Bounds** of joint states and controls are based on measured data ($\hat{q}, \dot{u}, \ddot{u}_{dv}$); r is range of motion; lb and ub are lower and upper bounds; bounds of contact parameters ($\hat{p}_{cl}, \hat{p}_{cr}$) are based on [46]. **Scaling:** joint states and controls, and tendon forces are scaled such that bounds are between -1 and 1; contact parameters are scaled such that lower and upper bounds are -0.5 and 0.5. **Objective function** L tracks experimental joint positions (\hat{q}), ground reaction forces (\hat{GRF}) and torques (\hat{GRT}), and joint torques of the lower limbs, trunk, and arms ($\hat{T}_{\text{l,trunk,arms}}$). A penalty function L_p is appended to L . **Dynamic constraints** are scaled using state scale factors [129]. **Path constraints:** $f_s(\cdot)$ computes net joint torques T , $f_c(\cdot)$ describes muscle contraction dynamics [53], $M A_m$ is moment arm of muscle m , and T_p are passive joint torques [35].

In the first example, we perturbed the balance of nine inverted pendulums, with between two and 10 degrees of freedom, by applying a backward translation to their base of support. The optimal control problem identified the joint torques necessary to restore the pendulums' upright posture within one second while minimizing the actuator effort (i.e., squared joint torques) and satisfying the pendulum dynamics.

In the second example, we performed predictive simulations of walking with a two-dimensional (2D) musculoskeletal model (10 degrees of freedom, 18 muscles actuating the lower limbs, one ideal torque actuator at the trunk, and two contact spheres per foot [112]). We identified muscle excitations and half walking cycle duration that minimized a weighted sum of muscle fatigue (i.e., muscle activations at the third power [39]) and joint accelerations subject to constraints describing the musculoskeletal dynamics, imposing left-right symmetry, and prescribing gait speed (i.e., distance traveled by the pelvis divided by gait cycle duration). Imposing left-right symmetry allowed us to only optimize for half a gait cycle.

In the third example, we performed tracking simulations of walking with a three-dimensional (3D) musculoskeletal model (29 degrees of freedom, 92 muscles actuating the lower limbs and trunk, eight ideal torque actuators at the arms, and six contact spheres per foot [35, 112, 114]) while calibrating the foot-ground contact model. We identified muscle excitations and contact sphere parameters (locations and radii) that minimized a weighted sum of muscle effort (i.e., squared muscle activations) and the difference between measured and simulated variables (joint angles and torques, and ground reaction forces and torques) while satisfying the musculoskeletal dynamics. Data collection was approved by the Ethics Committee at UZ / KU Leuven (Belgium).

In these examples, we modeled pendulum/skeletal movement with Newtonian rigid body dynamics and, for the walking simulations, compliant Hunt-Crossley foot-ground contact [112, 119]. We created a continuous approximation of a contact model from Simbody to provide twice continuously differentiable contact forces, which are required when using second-order gradient-based optimization algorithms [51]. We performed the approximations of conditional if-tests using hyperbolic tangent functions. For the muscle-driven walking simulations, we described muscle activation and contraction dynamics using Raasch's model [52, 29] and a Hill-type muscle model [53, 27], respectively. We defined muscle-tendon lengths, velocities, and moment arms as a function of joint positions and velocities using polynomial functions [127]. We optimized the polynomial coefficients to fit muscle-tendon lengths and moment arms (maximal root mean

square deviation: 3 mm; maximal order: ninth) obtained from OpenSim for a wide range of joint positions.

We transcribed each optimal control problem into a NLP using a third order Radau quadrature collocation scheme. We formulated each problem in MATLAB using CasADi and IPOPT. We imposed an NLP relative error tolerance of 1×10^{-6} and used an adaptive barrier parameter update strategy. We selected a number of mesh intervals for each problem such that the results were qualitatively similar when using a mesh twice as fine. We used 10 and three initial guesses for the pendulum and walking simulations, respectively. We ran all simulations on a single core of a standard laptop computer with a 2.9 GHz Intel Core i7 processor.

Results analysis

We compared CPU time and number of iterations required to solve the problems using the different computational choices. First, we compared AD, using the Recorder approach, with FD. Second, we compared the AD approaches, namely AD-Recorder and AD-ADOLC. We performed these two comparisons using the linear solver mumps [124], which CasADi provides, and an approximated Hessian. Third, we compared different linear solvers, namely mumps with the collection of solvers from HSL (ma27, ma57, ma77, ma86, and ma97) [125], while using AD-Recorder and an approximated Hessian. Finally, we compared the use of approximated and exact Hessians. For this last comparison, we used AD-Recorder and tested all linear solvers. In all cases, we ran simulations from different initial guesses and compared results from simulations that started from the same initial guess and converged to similar optimal solutions. Table 5.4 distinguishes the numerical tools used in our analyses.

NLP solver	Linear solvers	AD approaches	
IPOPT	HSL collection	mumps	
		ma27	
		ma57	
		ma77	
		ma86	
		ma97	
		Operator overloading (ADOL-C)	
		Source code transformation (Recorder)	

Table 5.4: Numerical tools.

Results

Using AD-Recorder was computationally more efficient than using FD or AD-ADOLC (Figure 5.3). The CPU time decreased when using AD-Recorder as compared to FD (between 1.8 ± 0.1 and 17.8 ± 4.9 times faster with AD-Recorder) and AD-ADOLC (between 3.6 ± 0.3 and 12.3 ± 1.3 times faster with AD-Recorder). CPU time spent in evaluating the objective function gradient accounted for $95 \pm 10\%$ (average \pm standard deviation) of the difference in CPU time between AD-Recorder and FD. The difference in CPU time spent in evaluating the constraint Jacobian accounted for $89 \pm 6\%$ of the difference in CPU time between AD-Recorder and AD-ADOLC. The number of iterations was similar when using AD-Recorder, FD, and AD-ADOLC. For the 2D predictive and 3D tracking simulations, one and two cases, respectively, out of nine (three derivative scenarios and three initial guesses) were excluded from the comparison as they converged to different solutions.

The solvers from the HSL collection were on average more efficient (faster with a similar number of iterations) than mumps for the pendulum simulations, but the efficiency varied for the 2D predictive and 3D tracking simulations (Table 5.5). The solver ma27 was on average faster than mumps in all cases although ma27 required more iterations for the 2D predictive simulations. The other solvers from the HSL collection were on average slower than mumps for the 2D predictive simulations. For the 3D tracking simulations, the solvers ma77 and ma86 were faster and slower, respectively, than mumps. The solvers ma57 and ma97 failed to solve the 3D tracking simulations due to memory issues. For all simulations, the solvers from the HSL collection except ma86 (and ma77 for the 2D predictive simulations) required less CPU time per iteration than mumps. For the 2D predictive and 3D tracking simulations, one case out of 18 (six solvers and three initial guesses) and four cases out of 12 (four solvers and three initial guesses), respectively, were excluded from the comparison as they converged to different solutions.

Using an exact Hessian was more efficient than using an approximated Hessian for the pendulum simulations but not for the 2D predictive simulations (Figure 5.4). The exact Hessian required less CPU time and fewer iterations than the approximated Hessian for the pendulum simulations (average 2.4 ± 1.2 times faster and 2.5 ± 0.9 times fewer iterations). By contrast, the exact Hessian required more CPU time and iterations than the approximated Hessian for the 2D predictive simulations (average 6.0 ± 0.8 times slower and 2.1 ± 0.2 times more iterations). For the pendulum simulations, 27 cases out of 540 (nine pendulums, six solvers, and 10 initial guesses) were excluded from the

Solver * vs mumps	Pendulum simulations			2D predictive simulations			3D tracking simulations		
	CPU time	Iteration Number	CPU time per iteration	CPU time	Iteration Number	CPU time per iteration	CPU time	Iteration Number	CPU time per iteration
*ma27	0.6 ± 0.1	1.0 ± 0.0	0.6 ± 0.1	1.0 ± 0.3	1.4 ± 0.3	0.7 ± 0.1	0.7 ± 0.2	0.9 ± 0.3	0.7 ± 0.0
*ma57	0.6 ± 0.0	1.0 ± 0.0	0.6 ± 0.0	2.4 ± 2.5	2.8 ± 2.8	0.8 ± 0.0	/	/	/
*ma77	0.9 ± 0.1	1.0 ± 0.0	0.9 ± 0.0	1.3 ± 0.0	1.2 ± 0.0	1.1 ± 0.0	0.5 ± 0.2	0.7 ± 0.3	0.7 ± 0.0
*ma86	1.1 ± 0.1	1.0 ± 0.0	1.1 ± 0.1	2.1 ± 0.5	1.1 ± 0.1	1.8 ± 0.3	2.3 ± 0.0	1.9 ± 0.0	1.2 ± 0.0
*ma97	0.7 ± 0.0	1.0 ± 0.0	0.7 ± 0.0	1.2 ± 0.3	1.2 ± 0.1	1.0 ± 0.2	/	/	/

Table 5.5: Comparison of computational time, number of iterations, and computational time per iteration between linear solvers. The comparisons are expressed as ratios (mean ± one standard deviation; results obtained with solver from the HSL collection over results obtained with mumps, * indicates ma27, ma57, ma77, ma86, or ma97). The ratios are averaged over results from different initial guesses. Ratios larger than one indicate faster convergence, fewer iterations, or less time per iteration with mumps. The use of the solvers ma57 and ma97 led to memory issues for the 3D tracking simulations and these cases were therefore excluded from the analysis. The simulations were run using AD-Recorder and an approximated Hessian.

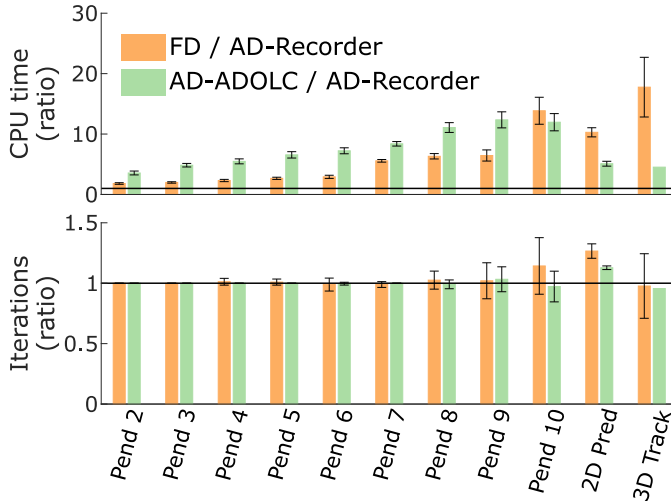


Figure 5.3: Comparison of computational time (top) and number of iterations (bottom) between FD, AD-ADOLC, and AD-Recorder. The comparisons are expressed as ratios and averaged over results from different initial guesses (error bars represent \pm one standard deviation). The horizontal lines indicate 1:1 ratios. Ratios larger than one indicate slower convergence (top) and more iterations (bottom) with FD or AD-ADOLC as compared to AD-Recorder. Pend indicates pendulum simulations with the number being the number of degrees of freedom; Pred and Track indicate predictive and tracking simulations, respectively. The results were obtained using mumps and an approximated Hessian.

comparison as they converged to different solutions with the two Hessian settings. One case was also excluded as it had not converged after 3000 iterations with the exact Hessian but converged in 209 iterations with the approximated Hessian. For the 2D predictive simulations, only results obtained with the solvers ma86 and ma97 were included, since the use of the other solvers led to memory issues. Further, four cases out of six (two solvers and three initial guesses) were excluded from the comparison as they converged to different solutions with the two Hessian settings. Finally, the 3D tracking simulations were not included for this comparison as the large problem size induced memory issues with the exact Hessian.

In the different analyses, we examined the cases that we excluded from the comparison because of convergence to different solutions but we did not find

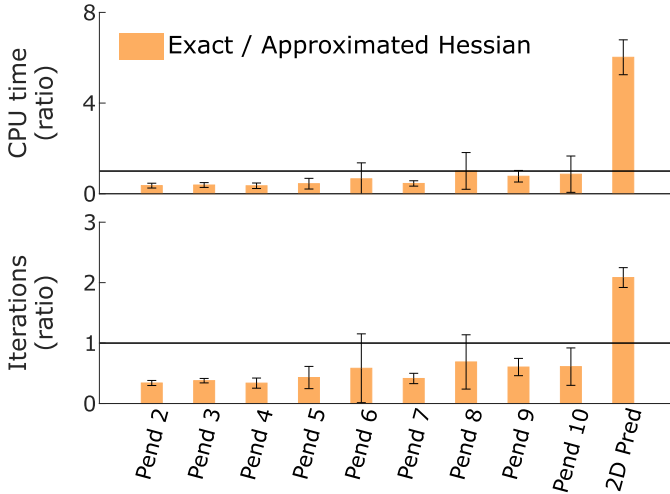


Figure 5.4: **Comparison of computational time (top) and number of iterations (bottom) between exact and approximated Hessian.** The comparisons are expressed as ratios and averaged over results from different initial guesses (error bars represent \pm one standard deviation). The horizontal lines indicate 1:1 ratios. Ratios larger than one indicate slower convergence (top) and more iterations (bottom) with an exact versus an approximated Hessian. Pend indicates pendulum simulations with the number being the number of degrees of freedom; Pred and Track indicate predictive and tracking simulations, respectively. The results were obtained using all solvers and AD-Recorder.

that one derivative scenario, solver, or initial guess consistency led to a local optimum with a lower cost.

The pendulum simulations required at most 21 s and 366 iterations to converge (results obtained with AD-Recorder, mumps, and an approximated Hessian); CPU time and number of iterations depended on the number of degrees of freedom (Movie 1).

The 2D predictive simulations reproduced salient features of human gait but deviated from experimental data in three noticeable ways (Figure 5.5; Movie 2). First, the predicted knee flexion during mid-stance was limited, resulting in small knee torques. Second, the simulations produced less ankle plantarflexion at push-off. Third, the vertical ground reaction forces exhibited a large peak at impact. The simulations converged in less than one CPU minute (average over

solutions starting from three initial guesses: 36 ± 17 s and 247 ± 143 iterations; results obtained with AD-Recorder, mumps, and an approximated Hessian).

The 3D tracking simulations accurately tracked the experimental walking data (average coefficient of determination R^2 : 0.95 ± 0.17 ; Figure 5.5; Movie 3). Simulated muscle activations also qualitatively resembled experimental electromyography data, even though electromyography was not tracked (Figure 5.5). The configuration of the contact spheres differed from the generic model after the calibration. The simulations converged in less than 20 CPU minutes (average over simulations starting from two initial guesses: 19 ± 7 minutes and 493 ± 151 iterations; results obtained with AD-Recorder, mumps, and an approximated Hessian).

Discussion

We showed that the use of AD over FD improved the computational efficiency of OpenSim-based trajectory optimization of human movement. Specifically, AD drastically decreased the CPU time spent in evaluating the objective function gradient. This time decrease results from AD's ability to evaluate a Jacobian-transposed-times-vector product through its reverse mode. The objective function gradient has many inputs (all optimization variables) but only one output. It can thus be evaluated in only one reverse sensitivity sweep; the computational cost is hence proportional to the cost of evaluating the objective function. By contrast, with FD, the computational cost is proportional to the number of optimization variables times the cost of evaluating the objective function. The efficiency benefit of AD also increased with the complexity of the problems. This is expected, since the number of optimization variables increases with problem size; FD thus requires more objective function evaluations, whereas AD still requires only one reverse sweep. In our problems, AD did not outperform FD when evaluating the constraint Jacobian. Yet we expect that AD will be more efficient than FD for trajectory optimization problems in which the number of optimization variables largely exceeds the number of constraints, thereby resulting in faster constraint Jacobian evaluations with AD's reverse mode.

The choice of the objective function influences CPU time. As an illustration, we added a term representing the metabolic energy rate [130] to the objective function of the 2D predictive simulations. Minimizing metabolic energy rate is common in predictive studies of walking [35, 25, 51]. Solving the resulting optimal control problem was about 60 times faster with AD-Recorder than with

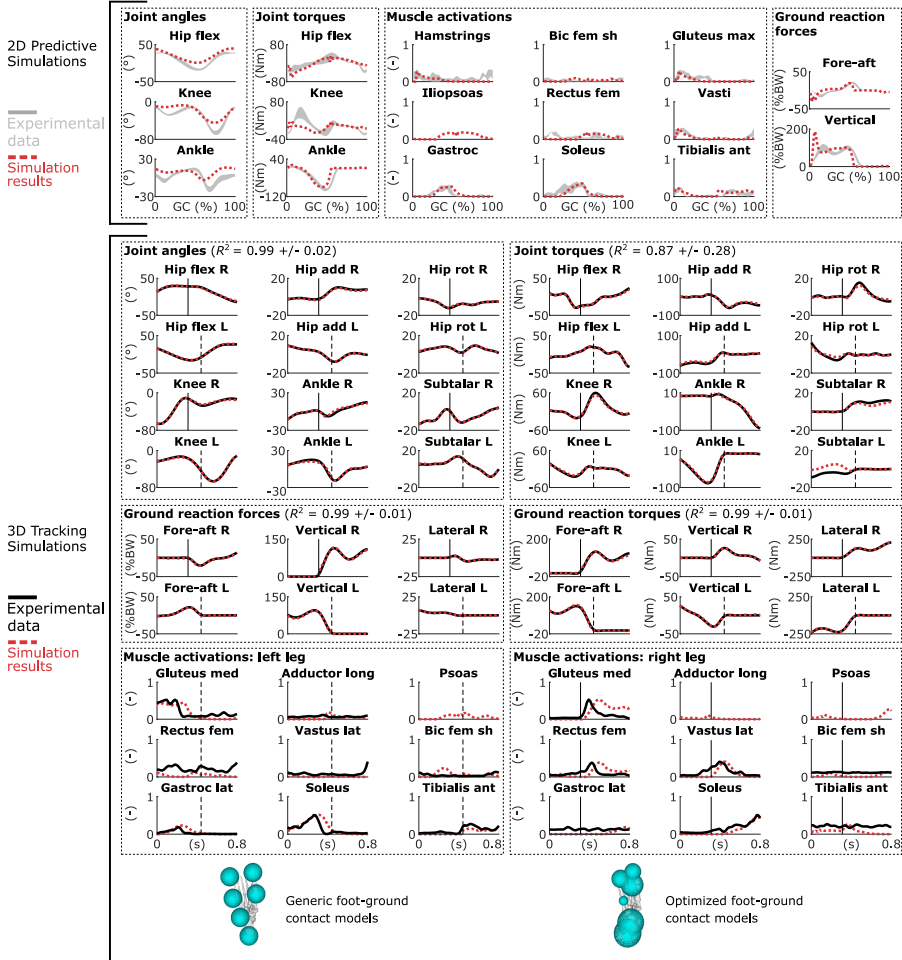


Figure 5.5: Results from trajectory optimization of walking. (Top) Results from 2D predictive simulations of walking (joint angles: flex is flexion, GC is gait cycle; muscle activations: bic is biceps, fem is femoris, sh is short head, max is maximus, gastroc is gastrocnemius, ant is anterior; ground reaction forces: BW is body weight). Experimental data are shown as mean \pm two standard deviations. (Bottom) Results from 3D tracking simulations of walking (joint angles: R is right, L is left, add is adduction, rot is rotation; muscle activations: med is medialis, long is longus, lat is lateralis). The vertical lines indicate right heel strike (solid) and left toe-off (dashed); only part of the gait cycle, with available experimental ground reaction forces, is tracked. Experimental electromyography data is normalized to peak muscle activations. The foot diagrams depict a down-up view of the contact sphere configuration of the right foot pre-calibration (left: generic) and post-calibration (right: optimized). The coefficient of determination R^2 is given for the tracked variables.

FD (although FD required fewer iterations), whereas AD-Recorder was only about 10 times faster than FD without incorporating the metabolic energy rate in the objective function. This increased time difference can be explained by our use of computationally expensive hyperbolic tangent functions to make the metabolic energy rate model twice continuously differentiable, as required when using second-order gradient-based optimization algorithms [51]. Overall, AD reduces the number of function evaluations, which has an even larger effect if these functions are expensive to compute.

The implementation of AD was computationally more efficient through Recorder than through ADOL-C. Specifically, Recorder decreased the CPU time by a factor 4-12 compared to ADOL-C. ADOL-C records all calculations involving differential variables on a sequential data set called a tape [18], which is then evaluated by ADOL-C's *virtual machine*. By contrast, Recorder generates plain C-code. The factor 4-12 is the difference between a *virtual machine* interpreting a list of instructions (ADOL-C) and machine code performing these instructions directly (Recorder).

The effort required to enable the use of AD through Recorder was minimal once OpenSim's source code had been modified for use with the ADOL-C libraries. Indeed, Recorder relies on operator overloading for constructing the expression graphs, which is similar to ADOL-C. The only required change was to replace the adouble scalar type (ADOL-C) by the Recorder scalar type. Recorder also facilitates the interface with CasADI, since it generates expression graphs in a format from which CasADI can directly generate C-code. This code can then be compiled as a Dynamic-link Library and imported in the CasADI environment without any scripting input required from the user (Figure 5.2). Using ADOL-C's AD algorithms with CasADI necessitates manually writing C++ code to provide forward and reverse directional derivatives using ADOL-C's drivers in a format recognized by CasADI, which might be prone to errors (Figure 5.2). Note that the manual effort required for using Recorder or ADOL-C is independent of problem complexity. Overall, using Recorder is more efficient but also simpler than using ADOL-C when solving trajectory optimization problems with CasADI.

The process of converting OpenSim's source code to code that compiles with the AD tools (ADOL-C and Recorder) was a considerable but one-time effort. OpenSim-based trajectory optimization problems can now be solved through the proposed framework while benefiting from AD and without any additional developments. We made our OpenSim-based AD framework available so that others can build upon our work. Importantly, using AD does not increase the

complexity for the end user as compared to using FD. Indeed, the simulation framework relies on CasADI that provides evaluations of function derivatives to the NLP solver. Hence, the user does not need to re-implement AD’s forward and reverse algorithms. It is also worth mentioning that, in this study, we used Recorder to enable the use of AD with OpenSim. However, Recorder is a general C++ class that could be applied to any other C++ code for use with CasADI. Compiling existing source code with Recorder would require replacing the scalar type of active variables (i.e., differentiable quantities) with the Recorder scalar type. Our study suggests that this programming effort might be particularly valuable when the goal is to solve complex trajectory optimization problems. Specifically, our results showed that the difference between AD and FD increased with problem size. Users might thus consider the programming effort only when the aim is to solve multiple complex problems and when they are not satisfied with the computational performance obtained with FD.

It is difficult to provide guidelines for the linear solver selection based on our results, as their efficiency was problem-dependent. In contrast with mumps, the solvers from the HSL collection do not freely come with CasADI and are only free to academics. Hence, our study does not support the extra effort to obtain them since they did not consistently outperform mumps in our applications. Yet an in-depth analysis of the solvers’ options and underlying mathematical details should be considered in future work.

The use of an exact Hessian, rather than an approximated Hessian, improved the computational efficiency for the pendulum simulations but not for the walking simulations. For the 2D walking simulations, using an exact Hessian required more CPU time but also more iterations. This might seem surprising, since an exact Hessian is expected to provide more accurate information and, therefore, lead to convergence in fewer iterations. However, IPOPT requires the Hessian to be positive definite when calculating a Newton step to guarantee that the step is in the descent direction. When this is not the case, the Hessian is approximated with a positive definite Hessian by adding the identity matrix multiplied by a regularization term to the Hessian [123]. We observed that for the 2D predictive simulations, the magnitude of the regularization term was much greater than for the pendulum simulations. Yet excessive regularization might degrade the performance of the algorithm, as regularization alters the second-order derivative information and causes IPOPT to behave more like a steepest-descent algorithm [200]. The approximated Hessian requires no regularization, which likely explains the difference in number of iterations. Overall, convexification of the currently non-convex optimal control problems is expected to further improve the computational efficiency [52].

Our comparison of derivative scenarios (AD-ADOLC, AD-Recorder, and FD), linear solvers (mumps and the HSL collection), and Hessian calculation schemes was based on several specific choices. First, we solved all problems using the NLP solver IPOPT, whereas other solvers compatible with CasADi, such as SNOPT [201] and KNITRO [202] (see [56] for detailed list), might behave differently. We selected IPOPT since it is open-source (SNOPT and KNITRO are commercial products), widely used, and well suited for large and very sparse NLPs [56]. Second, we transcribed the optimal control problems into NLPs using a third order Radau quadrature collocation scheme, whereas different orders, schemes (e.g., Legendre), and transcription methods (e.g., trapezoidal and Hermite-Simpson) might lead to different results. We selected quadrature collocation methods as they achieve exponential convergence if the underlying function is sufficiently smooth [117, 116]. Third, we used specific models of muscle activation dynamics, contraction dynamics, and compliant contacts, whereas other models might behave differently. We selected models that were continuously differentiable for use with gradient-based optimization algorithms. Finally, our focus was on solving trajectory optimization problems for biomechanical applications with OpenSim. We chose OpenSim as it is an open-source and widely used software package in biomechanics. The difference in computational performance between AD and FD might thus vary with other software packages and applications. Investigating all these other modeling and computational choices was out of the scope of this study but might be useful for helping users select the best settings for their applications. Overall, our study underlined the computational benefit of using AD over FD for trajectory optimization in biomechanics, which is in agreement with previous research in robotics (e.g., [191]).

The 2D predictive and 3D tracking simulations produced realistic movements although deviations remain between simulated and measured data. Modeling choices rather than local optima likely explain these deviations. These choices have a greater influence on the predictive simulations, since deviations from measured data are minimized in tracking simulations, whereas only the motor task goal is specified in the objective function of predictive simulations. Several modeling choices might explain the main deviations for the predictive simulations. First, we did not model stability requirements, which might explain the limited knee flexion during mid-stance [39, 51]. Instead, we included muscle activity in the cost function, which might explain why reducing knee torques and, therefore, knee extensor activity was optimal. Second, the model did not include a metatarsophalangeal joint, which might explain the limited ankle plantarflexion at push-off; similar ankle kinematics have indeed been observed

experimentally when limiting the range of motion of the metatarsophalangeal joint [203]. Third, the lack of knee flexion combined with the simple trunk model (i.e., one degree of freedom controlled by one ideal torque actuator) might explain the high vertical ground reaction forces at impact [39]. Finally, the goal of the motor task (i.e., minimizing muscle fatigue) likely does not fully explain the control strategies governing human walking. In this study, the focus was on evaluating different computational choices but future work should exploit the improved computational efficiency to explore how modeling choices affect the correspondence between simulated and measured quantities.

Our results indicate that AD is particularly beneficial with increasingly complex models. Hence, our OpenSim-based AD framework might allow researchers to rely on complex models, such as three-dimensional muscle-driven neuro-musculoskeletal models, in their studies. This model complexity might be highly desirable when studying, for instance, the impact of treatment on gait performance in patients with neuro-musculoskeletal disorders. Indeed, in such cases, the model should be complex enough to describe the musculoskeletal structures and motor control processes underlying gait that may be affected by treatment. Previous studies based on predictive models reported high computational times and were therefore limited to few predictions when relying on complex musculoskeletal models [35, 37, 36]. Using AD has the potential to drastically decrease the computational time of such predictive simulations, thereby extending their application.

Conclusion

In this study, we enabled the use of AD when performing OpenSim-based trajectory optimization of human movement. We showed that using AD drastically improved the computational efficiency of such simulations. This improved efficiency is highly desirable for researchers using complex models or aiming to implement such models in clinical practice where time constraints are typically more stringent than in research context. Overall, the combination of AD with other efficient numerical tools such as direct collocation and implicit differential equations allows overcoming the computational roadblocks that have long limited the use of trajectory optimization for biomechanical applications. In the future, we aim to exploit this computational efficiency to design optimal treatments for neuro-musculoskeletal disorders, such as cerebral palsy.

Acknowledgments

The authors would like to thank Michael Sherman for helpful technical discussions. This work was supported by the Research Foundation Flanders (FWO) under PhD grant (1S35416N) and travel grant (V441717N) to AF, and research project grant (G079216N) to FDG, and by the NIH under grant (P2C HD065690) to the National Center for Simulation in Rehabilitation Research (NCSRR). CLD received a Stanford Bio-X Graduate Fellowship. JG has benefited from KU Leuven-BOF PFV/10/002 Center of Excellence: Optimization in Engineering (OPTEC) and from Flanders Make ICON (DriveTrainCodesign).

Data availability

The data and scripts required for reproducing the results are available at <https://simtk.org/projects/algodiff>. The movies are available upon request.

Chapter 6

Study 4: Rapid predictive simulations with complex musculoskeletal models suggest that diverse healthy and pathological human gaits can emerge from similar control strategies

Published as:

Falisse A., Serrancolí G., Dembia C.L., Gillis J., Jonkers I., De Groote F. *Rapid predictive simulations with complex musculoskeletal models suggest that diverse healthy and pathological human gaits can emerge from similar control strategies*, (2019). Journal of the Royal Society Interface, **16**(157): 20190402.

Abstract

Physics-based predictive simulations of human movement have the potential to support personalized medicine, but large computational costs and difficulties to model control strategies have limited their use. We have developed a computationally efficient optimal control framework to predict human gaits based on optimization of a performance criterion without relying on experimental data. The framework generates three-dimensional muscle-driven simulations in 36 minutes on average—more than 20 times faster than existing simulations—by using direct collocation, implicit differential equations, and algorithmic differentiation. Using this framework, we identified a multi-objective performance criterion combining energy and effort considerations that produces physiologically realistic walking gaits. The same criterion also predicted the walk-to-run transition and clinical gait deficiencies caused by muscle weakness and prosthesis use, suggesting that diverse healthy and pathological gaits can emerge from the same control strategy. The ability to predict the mechanics and energetics of a broad range of gaits with complex three-dimensional musculoskeletal models will allow testing novel hypotheses about gait control and hasten the development of optimal treatments for neuro-musculoskeletal disorders.

Introduction

Scientists have long tried to decipher the principles underlying bipedal locomotion with the aim of improving human gait performance and treatment of neuro-musculoskeletal disorders. A powerful approach to this problem is the use of physics-based predictive simulations that generate *de novo* movements based on a mathematical description of the neuro-musculoskeletal system without relying on experimental data. Such simulations can explore diverse hypotheses about mechanisms underlying locomotion that are difficult to study through experiments. The high computational time of predictive simulations has favored the use of conceptual models that only describe the most prominent features of the musculoskeletal system. Predictive simulations based on conceptual models have contributed to our understanding of the mechanics [204, 205] and energetics [206, 207, 33, 34] of bipedal locomotion. However, such models provide limited support for personalized clinical decision-making, since they do not sufficiently describe the musculoskeletal structures and motor control processes underlying gait that may be affected by treatment. An orthopedic surgeon considering a rectus femoris transfer in a patient with cerebral palsy cannot predict the effect of the surgery on the walking pattern of the patient using conceptual

models. By contrast, complex musculoskeletal models that include the many degrees of freedom of the skeleton and the many muscles actuating the lower limbs have the potential to make such predictions. Yet these complex models are computationally expensive in predictive simulations [35, 36, 25, 37] and, therefore, the field has not explored their ability to predict the broad range of gaits encountered under different environments, pathologies, and augmentations. Such generalizability is a prerequisite for using predictive simulations to design optimal treatments.

Predictive simulations typically optimize a performance criterion that describes the high-level goal of the motor task without relying on experimental motion data. Yet it remains unclear what such criterion would be for human gait. Experimental studies suggest that humans select gait features, such as step frequency and length, that optimize the cost of transport (COT, defined as metabolic energy consumed per unit distance traveled) [18] and that they continuously optimize the COT during walking [19]. Similarly, energy considerations have been suggested to drive the walk-to-run transition as gait speed increases [21]. Following these experimental observations, numerous simulation studies have used energy-based performance criteria to predict human walking or running [33, 34, 35, 36, 25, 37]. Predictive simulations based on conceptual models also showed that the same energy-based criterion produced walking at low speeds and running at high speeds [33, 34]. However, criteria centered on muscle activity, used as surrogates for muscle effort and fatigue, have also been suggested to underlie gait [39, 41, 40]. Simulation studies based on two-dimensional (2D) musculoskeletal models reported that using a performance criterion based on muscle activity better predicted the preferred walking speed in elderly [40] and resulted in more accurate kinematics during running [41] as compared to using an energy-based performance criterion. Yet it is unclear whether these observations hold for simulations based on three-dimensional (3D) models. Further, gait might be governed by multiple performance criteria [41, 208] but the effect of combining different criteria on the predicted gait pattern has not been widely explored with complex 3D models, likely due to the associated computational costs.

Finally, it remains unclear whether a single task-level performance criterion can explain the range of gaits adopted by humans in different contexts. No simulation study has yet explored whether different gaits, such as healthy walking and running or pathological gaits, can emerge from the same underlying control strategy when using complex 3D models.

The purpose of our study was threefold. First, we developed a computationally

efficient optimal control framework to predict human gaits based on complex musculoskeletal models. To this aim, we combined direct collocation, implicit differential equations, and algorithmic differentiation. Second, we sought a performance criterion that could accurately predict human walking. To this aim, we explored a wide range of walking-related performance criteria and selected the criteria that best described walking at self-selected speed. Third, we tested whether our framework could predict healthy and pathological gaits when altering gait speed and musculoskeletal properties but without altering the control strategy (i.e., using the same performance criterion). To this aim, we simulated gait (i) at different speeds, (ii) with muscle strength deficits, and (iii) with a lower leg prosthesis and compared our simulation results to those from experiments. The computational efficiency of our framework (goal 1) allowed us to explore potential cost functions (goal 2) and to test the ability to predict the mechanics and energetics of a range of human gaits based on complex musculoskeletal models (goal 3).

Methods

Musculoskeletal model

We used an OpenSim musculoskeletal model with 29 degrees of freedom (six between pelvis and ground; respectively three, one, and two at each hip, knee, and ankle; three at the lumbar joint between trunk and pelvis, and four per arm), 92 muscles actuating the lower limbs and trunk (43 per leg and six actuating the lumbar joint), eight ideal torque actuators at the arms, and six contact spheres per foot [114, 112]. To increase computational speed, we fixed the moving knee flexion axis to its anatomical reference position; moving and fixed knee flexion axes give similar results for gait [209]. We added passive stiffness (exponential) and damping (linear) to the joints of the lower limbs and trunk to model ligaments and other passive structures [35].

We used Raasch's model [29, 52] to describe muscle excitation-activation coupling and a Hill-type muscle model [27, 53] to describe muscle-tendon interaction and the dependence of muscle force on fiber length and velocity. We modeled skeletal motion with Newtonian rigid body dynamics and compliant Hunt-Crossley foot-ground contacts [112, 119]. We used smooth approximations of the Hunt-Crossley model that were twice continuously differentiable as required with gradient-based optimization [51]. Conditional if statements were smoothed using hyperbolic tangent functions (example in Appendix C). To increase computational speed, we defined muscle-tendon lengths, velocities,

and moment arms as a polynomial function of joint positions and velocities [127]. We optimized the polynomial coefficients to fit muscle-tendon lengths and moment arms (maximal root mean square deviation: 3 mm; maximal order: ninth) obtained from OpenSim using a wide range of joint positions.

Experimental data

We used experimental data for comparison with simulation outcomes as well as to provide some of the bounds and initial guesses of the predictive simulations. Not all initial guesses were based on experimental data. We collected data (marker coordinates, ground reaction forces, and electromyography; recording details in Appendix C) from one healthy adult. The subject was instructed to walk over ground at a self-selected speed and to run on a treadmill at 10 km h^{-1} . The average walking speed, henceforth referred to as preferred walking speed, was $1.33 \pm 0.06 \text{ m s}^{-1}$. We processed the experimental data with OpenSim 3.3 [112]. The musculoskeletal model was scaled to the subject's anthropometry based on marker information from a standing calibration trial. Joint kinematics were calculated based on marker coordinates by applying a Kalman smoothing algorithm [115]. Joint kinetics were calculated based on joint kinematics and ground reaction forces.

Optimal control framework

We formulated predictive simulations of gait as optimal control problems. We identified muscle excitations and gait cycle duration that minimized a cost function subject to constraints describing muscle and skeleton dynamics, imposing left-right symmetry, and prescribing gait speed (defined as distance traveled by the pelvis divided by gait cycle duration).

This optimal control problem is challenging to solve because of the stiffness of the equations describing muscle and skeleton dynamics. Due to these stiff differential equations, a small change in muscle excitations can have a large impact on the simulated movement pattern and the cost function because of, for example, the high sensitivity of the ground reaction forces to the kinematics. To overcome this challenge, we used an optimal control method called direct collocation [39, 53]. Compared to others methods such as direct shooting [35], direct collocation reduces the sensitivity of the cost function to the optimization variables by reducing the time horizon of the integration. Applying direct collocation results in large sparse nonlinear programming problems (NLP) that

readily available NLP solvers can solve efficiently.

We formulated muscle and skeleton dynamics with implicit rather than explicit differential equations, which are more common [53, 55]. Using implicit formulations improves the numerical conditioning of the NLP by, for example, removing the need to divide by small muscle activations [53] or invert the mass matrix that is near-singular due to the large range of masses and moments of inertia of the body segments [55]. For the muscle contraction and skeleton dynamics, we introduced additional controls u_{dF_t} and u_{dv} that equal (dynamic constraints) the time derivatives of tendon forces F_t and joint velocities v , respectively, and we imposed the nonlinear dynamic equations describing muscle contraction and skeleton dynamics as algebraic constraints in their implicit rather than explicit form [53]. We used a slightly different approach for muscle activation dynamics [52]. We introduced additional controls u_{da} that equal the time derivatives of activations a and imposed activation dynamics by linear constraints on a and u_{da} . Hence, muscle excitations were eliminated from the problem but can be computed post-processing [52]. Activation dynamics of the ideal actuators driving the arms were described by a linear first order approximation of a time delay relating excitations e_{arms} to activations a_{arms} . This equation is linear and continuously differentiable and there was thus no computational rationale for using implicit formulations. Details of the problem formulation are in Appendix C.

We formulated our problems in MATLAB (The Mathworks Inc., USA) using CasADi [56], applied direct collocation using a third order Radau quadrature collocation scheme with 50 mesh intervals per half gait cycle, and solved the resulting NLP with the solver IPOPT [122]. We increased computational efficiency by applying algorithmic differentiation [56], which is an alternative to finite differences for computing function derivatives required by the NLP solver. In contrast with finite differences, algorithmic differentiation is free of truncation errors. Further, it permits the evaluation of derivatives through both forward and reverse algorithms (the forward algorithm is comparable to finite differences). Typically, the reverse algorithm requires fewer function evaluations than the forward algorithm when the function has many more inputs than outputs, whereas the opposite holds when the function has many more outputs than inputs. Hence, the reverse algorithm is more efficient for computing, for example, the cost function gradient, since the cost function is a single value (one output) that depends on many variables (many inputs). We created custom versions of OpenSim and its dynamics engine Simbody [119] to enable the use of algorithmic differentiation.

Performance criterion underlying healthy human walking

We first sought a performance criterion that could predict healthy human walking by generating simulations, at the subject's preferred walking speed (1.33 m s^{-1}), using multi-objective cost functions describing trade-offs between physiologically-relevant walking-related performance criteria. Our cost functions included metabolic energy rate, muscle activity, joint accelerations, passive joint torques, and arm excitations:

$$J = \frac{1}{d} \int_0^{t_f} \left(\underbrace{w_1 \|\dot{E}\|_2^2}_{\text{Metabolic energy rate}} + \underbrace{w_2 \|a\|_2^2}_{\text{Muscle activity}} + \underbrace{w_3 \|u_{dv,lt}\|_2^2}_{\text{Joint accelerations}} + \underbrace{w_4 \|T_p\|_2^2}_{\text{Passive torques}} + \underbrace{w_5 \|e_{\text{arms}}\|_2^2}_{\text{Arm excitations}} \right) dt, \quad (6.1)$$

where d is distance traveled by the pelvis in the forward direction, t_f is half gait cycle duration, $u_{dv,lt}$ are joint accelerations of the lower limbs and trunk, T_p are passive joint torques, t is time, and w_{1-5} are weight factors. We modeled metabolic energy rate \dot{E} using a smooth approximation of the phenomenological model described by Bhargava *et al.* [130]. We obtained the parameters for fiber type composition and muscle specific tension from the literature [131]. We did not include the length dependence of the model's maintenance heat rate. This function is very unsMOOTH, which is physiologically unlikely and numerically problematic. Further, muscles are working close to their optimal fiber lengths during gait and including length dependency is thus expected to have a minor effect. We smoothed the metabolic energy model in a similar way as the contact model. To avoid singular arcs, situations for which controls are not uniquely defined by the optimality conditions [129], we appended a penalty function J_p with the remaining controls to the cost function:

$$J_p = \frac{1}{d} \int_0^{t_f} w_u \left(\|u_{da}\|_2^2 + \|u_{dF_t}\|_2^2 + \|u_{dv,\text{arms}}\|_2^2 \right) dt, \quad (6.2)$$

where $w_u = 0.001$ and $u_{dv,\text{arms}}$ are joint accelerations of the arms. We explored many sets of weight factors, by manually tuning them, until we found a cost function that predicted human-like walking, henceforth referred to as nominal cost function. We started each optimization from two initial guesses (Table C.1 in Appendix C) and selected the result with the lowest optimal cost. Only one initial guess was based on experimental data.

We investigated the effect of different terms in the cost function by consecutively replacing the metabolic energy rate term by $2w_1 \sum_{m=1}^M \dot{E}_m$ where M is the number of muscles (i.e., not squaring metabolic energy rate), removing the metabolic energy rate term, removing the muscle activity term, lowering the weight on joint accelerations, and removing the passive torque term.

Predictive simulations under different conditions

We then tested whether the nominal cost function could predict healthy and pathological gaits when altering gait speed and musculoskeletal properties.

First, we generated predictive simulations at different gait speeds (from 0.73 to 2.73 m s⁻¹ by increments of 0.1 m s⁻¹). For each speed (except for the preferred walking speed), we used five initial guesses (Table C.1 in Appendix C). Our criterion to evaluate whether the model adopted a walking or running gait was potential and kinetic energy being out-of-phase or in-phase [210].

Second, we investigated the influence of weak hip muscles and ankle plantarflexors during walking. We generated predictive simulations, at the preferred walking speed, while successively decreasing the maximal isometric force of muscles in the corresponding muscle group by 50, 75, and 90%.

Third, we explored the influence of a transtibial passive prosthesis during walking. To model the prosthesis, we removed the ankle and subtalar muscles (including the gastrocnemii) of the right leg and modeled a passive prosthesis by describing ankle and subtalar torques as linear functions of joint angles q :

$$T = -kq, \quad (6.3)$$

where $k = 800$ N m rad⁻¹ is torsional stiffness [211]. We reduced the mass of the lower leg and foot segments by 35% and moment of inertia by 60% compared to the biological leg [211]. We did not alter the foot-ground contact model. To allow for gait asymmetry, we imposed periodicity of the states over a complete gait cycle (except for the pelvis forward position) instead of symmetry over half a gait cycle. We used 100 rather than 50 mesh intervals to account for the longer motion.

Sensitivity analyses

We evaluated the sensitivity of our simulations to different parameters. If not explicitly mentioned, these simulations minimized the nominal cost function at the preferred walking speed. First, we evaluated how using different metabolic energy models, namely the models proposed by Umberger *et al.* (2003) [146], Umberger (2010) [212], and Uchida *et al.* [131], influenced walking simulations. These models treat negative mechanical work, muscle lengthening heat rate, and motor unit recruitment differently (Table C.2 in Appendix C). Second, we tested the influence of increasing the lower bound on muscle activations to simulate co-contraction (using 0.1, 0.15, or 0.2 instead of 0.05). Third, we evaluated the sensitivity of the simulations to the foot-ground contact model parameters. We first calibrated a subset of the contact model parameters (transverse plane locations and radii of the contact spheres) by minimizing tracking errors with respect to the subject’s walking data (details in Appendix C). We then used the optimized contact models in predictive simulations. Fourth, we evaluated the sensitivity of the results to the number of mesh intervals by using 100 rather than 50 intervals. Finer meshes increase accuracy but also problem size and likely computational time. Finally, we evaluated the sensitivity of the walk-to-run transition speed to the model’s peak mechanical power. We increased muscle power by doubling the maximal muscle contraction velocities (from 10/s to 20/s) and generated predictive simulations at increasing gait speeds (from 1.33 to 2.23 m s⁻¹ by increment of 0.1 m s⁻¹).

Results

Our framework generated 3D muscle-driven simulations that converged in an average of 36 minutes of computational time (over 197 simulations; Table C.3 in Appendix C) on a single core of a standard laptop computer (2.9 GHz Intel Core i7 processor).

We found that metabolic energy rate, muscle activity, joint accelerations, and, to a lesser extent, passive joint torques—all terms squared—were important criteria to capture key features of human walking. We identified a set of weight factors that predicted joint kinematics, kinetics, ground reaction forces, and muscle activations resembling experimental data of the subject at the preferred walking speed ($w_1 = 5 \times 10^2 / 92$ /body mass, $w_2 = 2 \times 10^3 / 92$, $w_3 = 5 \times 10^4 / 21$, $w_4 = 1 \times 10^3 / 15$, $w_5 = 1 \times 10^6 / 8$; each weight factor is scaled by the number of elements in the vector from which we take the norm). Minimizing this nominal cost function required 23 minutes of computational time (Table C.3

in Appendix C) and resulted in a human-like walking gait (Figure 6.1; Movie 1). The COT from this simulation, $3.55 \text{ J kg}^{-1} \text{ m}^{-1}$, was in the range of experimental measurements ($3.35 \pm 0.25 \text{ J kg}^{-1} \text{ m}^{-1}$ [36]) (Figure 6.1). As opposed to previous studies [35, 36, 25, 37], we squared the metabolic energy rate term; minimizing energy rate without squaring resulted in exaggerated trunk sway (Figure 6.1; Movie 2).

Each term in the proposed nominal cost function was necessary for predicting the prominent features of walking. Removing the metabolic energy rate term resulted in increased trunk sway and step width, whereas removing the muscle activity term resulted in unrealistically high muscle activations for several muscles (Figure 6.1; Movie 2). The joint acceleration term was important for convergence of the optimization algorithm and smoothness of the motion, whereas the passive joint torque term limited knee overextension (Movie 3).

Our framework predicted a continuum of walking and running gaits as we varied the prescribed gait speed (Movie 4). Further, the predicted COT, stride frequency, and vertical ground reaction forces changed as a function of speed in agreement with reported data (Figure 6.2). A transition from walking to running occurred at 2.23 m s^{-1} (Figure C.1 in Appendix C). In agreement with the literature, we found quadratic (coefficient of determination $R^2 = 0.98$) and linear ($R^2 = 0.66$) relations between COT and speed for walking and running, respectively (Figure 6.2(A)) [210]; a linear relation ($R^2 = 0.99$) between stride frequency and walking speed (Figure 6.2(B)) [213]; and vertical ground reaction forces whose first peak increased and mid-stance magnitude decreased as walking speed increased (Figure 6.2(C)) [31].

Altering musculoskeletal properties led to gaits that accurately exhibited clinical gait deficiencies. Reduced hip muscle strength resulted in greater hip circumduction (i.e., conical movement of the legs) to reduce hip torques (Figure 6.3(A); Movie 5). This strategy, known as compensated Trendelenburg gait, may be observed in patients with neural injuries or myopathies affecting hip muscles [214]. Reduced ankle plantarflexor strength resulted in calcaneal gaits that reduced ankle torques (Figure 6.3(B); Movie 6). Such gaits may be observed in children with spastic diplegia who have a weak triceps surae, possibly due to an Achilles tendon lengthening surgery [215].

Our simulations produced ankle torques and COT that are typical of amputees with a transtibial passive prosthesis. In agreement with experiments [216], ankle plantarflexion torques of the affected leg were larger during early- and

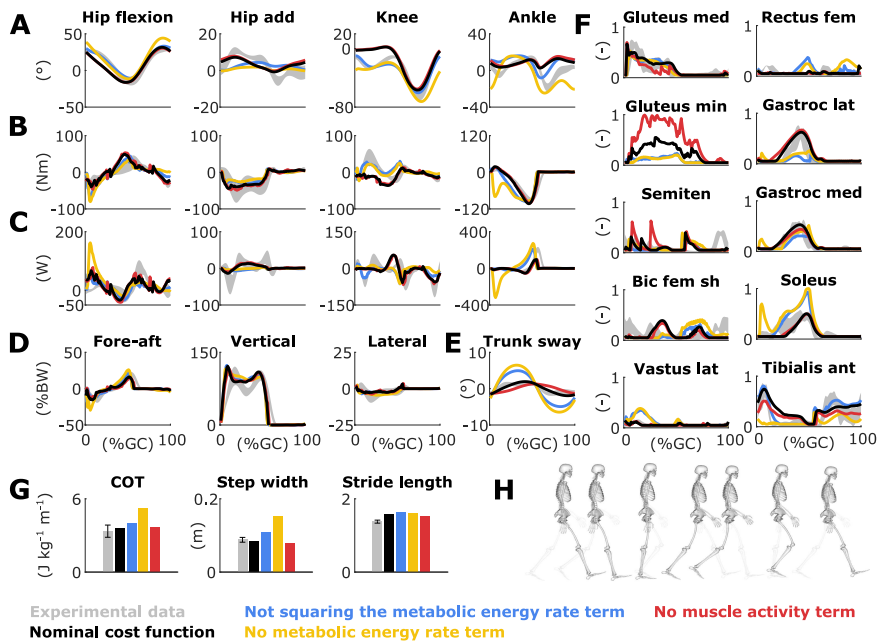


Figure 6.1: Simulated walking gaits with nominal and alternative cost functions. (A) Joint angles (add: adduction). The nominal cost function predicted an extended knee during mid-stance and limited ankle plantarflexion at push-off. Not squaring or removing the metabolic energy rate term from the cost function increased knee flexion but also trunk sway (E) and step width (G). (B) Joint torques. An extended knee resulted in small knee torques but limited ankle plantarflexion did not result in reduced ankle torques. (C) Joint powers. Limited ankle plantarflexion resulted in reduced ankle powers. (D) Ground reaction forces (BW: body weight; GC: gait cycle). (E) Trunk sway (i.e., trunk rotation in frontal plane). (F) Muscle activations (med: medius; min: minimus; semiten: semitendinosus; bic: biceps; fem: femoris; sh: short head; lat: lateralis; ant: anterior). Removing the muscle activity term from the cost function resulted in unrealistically high muscle activations. The experimental electromyography data (gray curves) was normalized to peak nominal activations (black curves). (G) Metabolic cost of transport (COT), step width, and stride length. The nominal COT matched experimental data [36]. (H) Resultant walking pattern with nominal cost function (Movie 1). Experimental data is shown as mean \pm two standard deviations.

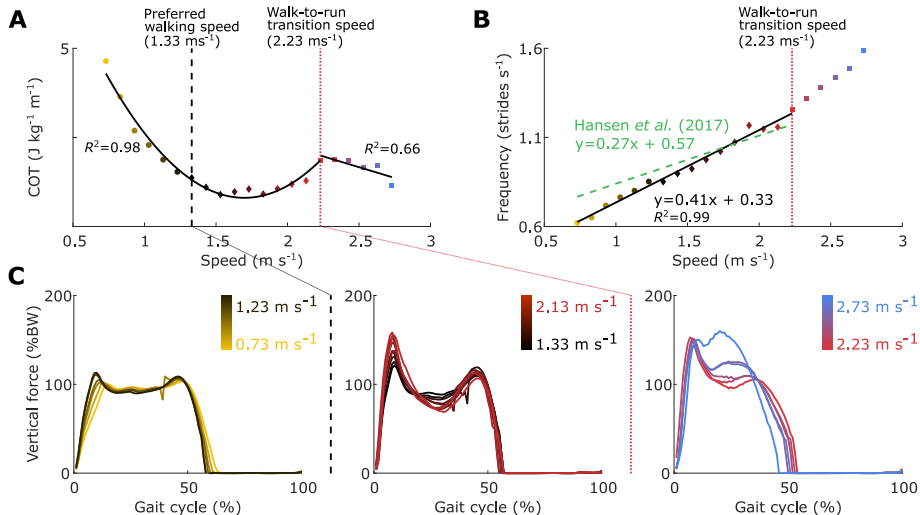


Figure 6.2: Alterations in gait features with speed. (A) Quadratic and linear regressions (black curves) based on simulation results (colored markers) between metabolic cost of transport (COT) and speed for walking (0.73 to 2.23 m s^{-1} ; $R^2 = 0.98$) and running (2.23 to 2.73 m s^{-1} ; $R^2 = 0.66$), respectively. (B) Linear regression (black curve) based on simulation results from walking (colored markers) between stride frequency and speed ($R^2 = 0.99$). The regression line is compared with the one obtained from experimental data [213]. (C) Vertical ground reaction forces (BW: body weight) at walking speeds less than the preferred walking speed of 1.33 m s^{-1} (left), at walking speeds greater than the preferred walking speed (middle), and at running speeds (right). Each colored curve represents a simulation result for a different gait speed.

mid-stance than torques of the unaffected leg (Figure 6.4; Movie 7). The COT was similar to the nominal COT, as expected for physically fit amputees [217].

The sensitivity analyses showed that different metabolic energy models resulted in qualitatively similar walking patterns, although we observed some differences in hip, knee, and ankle angles caused by differences in the muscle lengthening heat rate component of the metabolic cost (Figure C.2 and Table C.2 in Appendix C; Movie 8). Increasing the lower bound on muscle activations from 0.05 to 0.1 resulted in larger knee flexion angles, knee torques, and vasti activity during stance but also in a larger COT ($5.10 \text{ J kg}^{-1} \text{ m}^{-1}$). Lower bounds larger than 0.1 resulted in non-human-like gaits (Figure C.3 in Appendix C). The geometry of foot-ground contact and the mesh density had little influence on

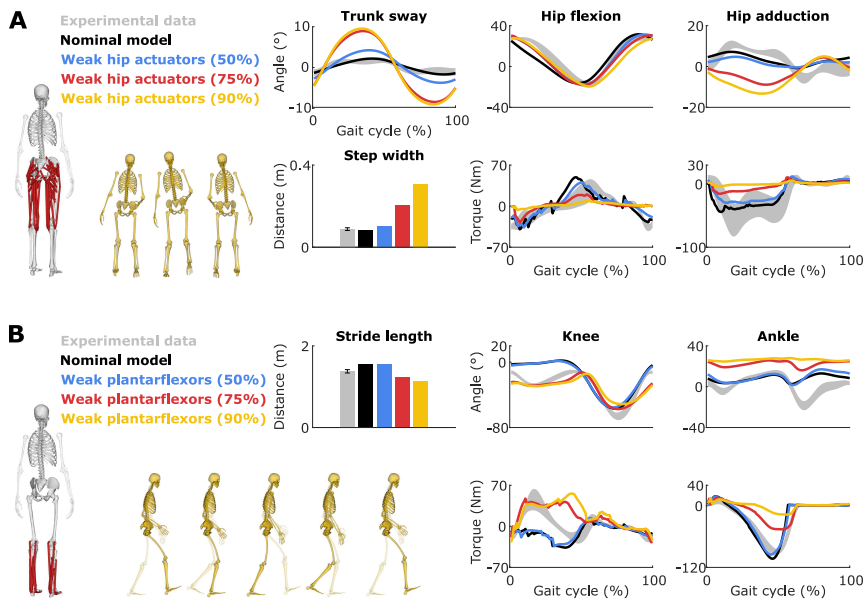


Figure 6.3: **Effect of muscle weakness on walking pattern.** (A) Hip muscle weakness. Reducing hip muscle strength by 50, 75, and 90% resulted in increased trunk sway and step width, and decreased hip torques. (B) Ankle plantarflexor weakness. Reducing ankle plantarflexor strength by 50, 75, and 90% resulted in increased knee flexion and ankle dorsiflexion, and decreased stride lengths that reduced ankle torques. Experimental data of the healthy subject is shown as mean \pm two standard deviations. The simulations minimized the nominal cost function at the subject's preferred walking speed (1.33 m s^{-1}).

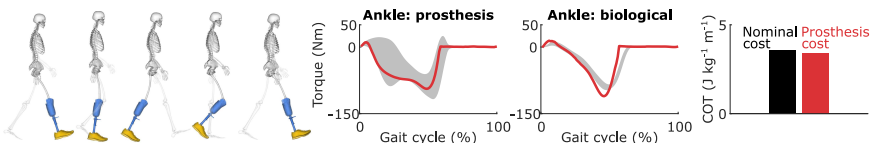


Figure 6.4: **Simulated walking gait of an amputee with a transtibial passive prosthesis.** Simulated ankle torques (red curves) matched the average ankle torques of six transtibial amputees [216]. The metabolic cost of transport (COT) for healthy and amputee walking was similar. Experimental data (gray envelopes) is shown as mean \pm two standard deviations. The simulations minimized the nominal cost function at an imposed speed of 1.33 m s^{-1} . The prosthesis geometry is for visualization only.

the simulations (Figures C.4-C.6 in Appendix C). Finally, increasing model's peak mechanical power reduced the transition speed to 2.13 m s^{-1} (Figure C.1 in Appendix C).

Discussion

We developed a computational efficient framework for predictive simulations of 3D human gaits that allowed us to explore a broad range of control strategies and conditions. Our simulations showed that healthy and pathological gaits can emerge from the same underlying control strategy, thereby providing further support for observations based on experimental protocols [218] and conceptual models that did not account for the large redundancy in the musculoskeletal system [33]. In addition, we showed that predictive simulations based on complex 3D musculoskeletal models can capture healthy and pathological human gait mechanics and energetics, a first prerequisite for the use of our models and simulation framework for clinical outcome predictions.

Our framework generated 3D muscle-driven simulations in only 36 minutes on average, which is more than 20 times faster than existing simulations with similarly complex or simpler models (i.e., between 13 and 60 hours) [36, 25, 37]. Note that fair comparison of computational efficiency with published simulations is difficult as none of these studies solved the exact same problems. Further, prior studies might not have prioritized computational efficiency. Our use of direct collocation, implicit differential equations, and algorithmic differentiation likely explains the superior computational efficiency of our framework but a comparison with alternative methods is required to further our insight into how each of these components contributed. We also made several assumptions that may have contributed to the rapid convergence of our simulations but that may not always hold. First, imposing symmetry allows simulating only half a gait cycle but is not valid, for example, in impaired gait. Optimizing for a complete gait cycle results in a higher computational time (e.g., prosthesis simulation in Table C.3 in Appendix C). Second, fixing the moving knee flexion axis increases computational speed but might not be valid when studying knee pathologies. Third, using an implicit formulation of activations dynamics eliminates muscle excitations from the optimization problems and, therefore, we used activations instead of excitations to evaluate motor unit recruitment in the metabolic energy model. Similarly, our implicit approach to impose activation dynamics does not allow us to directly formulate constraints on excitations (e.g., imposing that excitations are driven by muscle reflexes).

Our cost function (i.e., control strategy) included both metabolic energy rate and muscle activity, which was important to predict physiological walking. Although human walking is often assumed to result from minimizing only energy consumption [33, 34, 35, 36, 37], including squared muscle activity might be important for minimizing signal-dependent motor noise since muscle activity is believed to directly affect motor noise [219, 220]. Our cost function also included a joint acceleration term that was important to obtain convergence. Minimizing joint accelerations or jerks (i.e., rate of change of joint accelerations) to obtain smooth movements also resulted in good predictions of planar reaching movements [221, 222]. However, observed reaching movements were predicted equally well when minimizing uncertainty due to sensorimotor noise [220]. Therefore, it remains unclear whether smoothness of the gait patterns is part of the control strategy or emerges from non-modeled neuro-musculoskeletal features (e.g., robustness against perturbations or soft tissue damping). Minimizing only squared muscle activations led to exaggerated trunk sway and step width (Figure 6.1). Hence, the observation based on 2D models that minimizing muscle activity rather than COT better predicts running kinematics [41] and preferred walking speed in elderly [40] might not hold for simulations based on 3D models.

Our simulations produced walking gaits at low speeds and running gaits at high speeds. Nevertheless, the simulated walk-to-run transition speed (2.23 m s^{-1}) was slightly greater than reported values (1.89 to 2.16 m s^{-1} [223]) and most running gaits presented a longer stance phase than expected (close to 50% of the gait cycle), suggesting that our cost function may not capture all goals during running. Other strategies such as reducing maximum dorsiflexor moment [223] or locomotor variability, and avoiding instabilities [224] have been suggested to trigger the walk-to-run transition. Increasing the model's muscle mechanical power reduced the transition speed to 2.13 m s^{-1} . This is in agreement with the delayed walk-to-run transition observed in young children that has been attributed to reduced peak mechanical power compared to adults [225]. We might have obtained a similar decrease by reducing the cost of peak mechanical power over mechanical work [225] or by increasing muscle power through increased muscle volumes.

Our simulations produced realistic gaits at different gait speeds, with muscle strength deficits, and with lower leg prosthesis use based on the same control strategy. Hence, a range of healthy and pathological human gaits emerged from the multi-objective cost function that was identified by judging the realism of a simulated gait pattern at self-selected speed only. Yet this observation does not imply that the proposed cost function represents the underlying physiological

control mechanisms that drive locomotion. Although omitting any term in our cost function resulted in less realistic patterns, it is possible that a different set of weight factors or alternative cost functions containing criteria proposed in the literature but not considered in this study (e.g., head stability [226] and angular momentum regulation [227]) will result in equally or more realistic gaits. Especially since many of the proposed criteria are related through system dynamics.

Despite the absence of reflexes and other motor control pathways, our simulations captured the prominent features of human gait. This may be because preferred gait patterns are dictated in part by musculoskeletal mechanics and not only by a control strategy. This would explain why we obtained human-like walking patterns with different cost functions and is in line with observations based on passive walkers that natural dynamics may largely govern locomotion [228]. Second, in a healthy nervous system, different control pathways might interact in a way that optimizes a task-level goal. Our cost function might therefore capture the result of distributed pathways within the central nervous system without explicitly describing these pathways. Such optimization is less likely in the presence of pathologies of the central nervous system, such as spasticity, in which reflex loops are dysregulated. Third, reflexes and other feedback pathways might be especially important to move in a noisy world (i.e., to reject disturbances) but we did not model any noise. This omission might explain the lack of hamstrings activity at terminal swing (Semiten in Figure 6.1), which has been reported to be reflex-driven [182]. We expect our predictions to be more accurate if we model known control loops [24], especially in the presence of pathologies or in noisy environments. Alternatively, our framework could be used to test the effect of hypothesized control pathways on human locomotion.

Combining our simulation workflow with experimental studies will advance our understanding of criteria driving gait selection and improve the accuracy of our predictions. The hypothesis that the COT is optimized during gait has been extensively tested both by observing natural behavior and by manipulating the relation between COT and gait pattern (e.g., [19]). Our simulations suggested that minimizing metabolic rate alone does not result in realistic gaits and pointed to other performance criteria that can be experimentally tested. For example, passive joint torques could be manipulated through braces, whereas manipulating muscle activations or joint accelerations will be more challenging. Our simulations elicited the potential role of the musculoskeletal mechanics, which could also be manipulated experimentally for example by locking degrees of freedom, reducing the base of support (cfr., [229]), or adding mass to certain segments. These experiments could be combined with approaches based on

inverse optimal control to automate the search for a walking control strategy. To realize the potential of our framework for optimal treatment design, experimental work is also needed to investigate how the control strategy changes in case of motor control impairments.

We have demonstrated the ability of our simulations to reproduce key features of healthy and pathological human locomotion. Nevertheless, our simulations deviated from measured data in two notable ways. First, our predicted knee flexion during mid-stance was limited, resulting in small knee torques (Figure 6.1). Other predictive studies have reported limited knee flexion during mid-stance and argued that the cause is the lack of stability requirements [39, 51]. Similar to these studies, we did not model any stability requirements and included both muscle activity and metabolic rate in the cost function, which might explain why reducing knee torques and, therefore, knee extensor activity was optimal. Co-contraction has been suggested to play a stabilizing role during walking. We found that imposing co-contraction resulted in a more flexed knee during stance at the cost of a higher COT. Future work should investigate more physiologically-inspired approaches to account for stability, such as feedback control through spinal reflexes [24]. Alternatively, we could explicitly model and minimize the uncertainty on the simulated movement due to perturbations using approaches from the domain of robust optimal control [230] although such approaches induce significant computational costs. Second, our simulations produced less ankle plantarflexion at push-off (Figure 6.1). The absence of a metatarsophalangeal (MTP) joint might explain reduced plantarflexion, as similar ankle kinematics have been observed experimentally when limiting the range of motion of the MTP joint [203]. The simplistic trunk model might have contributed further to the aforementioned differences between simulated and measured walking patterns. By contrast, the foot-ground contact geometry had little influence on the simulated walking pattern. Our evaluation of the simulated patterns was qualitative rather than quantitative as we found it hard to capture the realism of a gait pattern in a few numbers. Although depending on subjective interpretation, a comprehensive comparison of simulated and measured trajectories along with the animated movements allowed us to judge the realism of our simulations.

Different gaits locally optimize the nominal cost function. We used a discretization scheme with a predefined number of mesh intervals and a gradient-based method to solve the optimization problems. Gradient-based methods find a local optimum, as opposed to the global optimum, and might hence be sensitive to the initial guess. Our simulations based on the nominal cost function at the preferred walking speed converged to similar results whether using an

initial guess derived from walking data or a quasi-random initial guess (Figure C.6 in Appendix C), whereas previous studies required initial guesses derived from computationally expensive data-tracking simulations [36, 37]. In addition, using a finer mesh led to similar results (Figure C.6 in Appendix C). However, we obtained a different gait pattern when using an initial guess derived from running data (Figure C.6 in Appendix C). The optimal cost and COT of this gait were much larger than those resulting from the two other initial guesses, suggesting different local optima. This is not surprising, since humans adopt a range of different gait patterns at a given speed depending on the context. For example, it has been shown that humans do not always adopt a walking pattern that minimizes energy consumption but prefers such option when instructed to self-explore different patterns [19]. Local optima might hence characterize a model describing human locomotion. How to model the context-dependent selection of a local optimum remains, however, an open question.

Overall, our physics-based computational framework holds the potential to greatly expedite advances in understanding human locomotion. In particular, we expect our efficient simulations, when combined with patient-specific neuro-musculoskeletal models, to enable optimal design of treatments aiming to restore gait function by allowing *in silico* assessment of the effect of changes in the neuro-musculoskeletal system on the gait pattern. Currently, treatment of gait impairments resulting from interactions between motor control and musculoskeletal deficits, such as in cerebral palsy, is often unsuccessful [7]. Optimal treatment design might hence have a large impact on patients' quality of life. Yet the availability of models and methods characterizing these patient-specific deficits is still limited and should be the focus of future research. Further, the design of experimental protocols to collect data required to personalize these models will be particularly important as such protocols should be comprehensive enough to allow for accurate modeling while accounting for practical limitations in clinical contexts. We also envision numerous applications beyond personalized medicine. Our framework can be used to design assistive devices, to simulate gaits of extant and extinct species, to optimize performance in sports by designing equipment and training programs, or to synthesize realistic movements in animations.

Acknowledgments

We thank H. Geyer and S. Song for insightful discussions on predictive simulations; M. Afschrift and T. Van Wouwe for data collection; L. Ting, M. Daley, P. Bishop, A. Lai, H. Kainz, M. Afschrift for editorial suggestions;

and W. Aerts for providing the prosthesis model. This work was supported by the Research Foundation Flanders (FWO) under PhD grant (1S35416N) and travel grant (V441717N) to AF, and research project grant (G079216N) to FDG, and by the NIH under grant (P2C HD065690) to the National Center for Simulation in Rehabilitation Research (NCSRR). CLD received a Stanford Bio-X Graduate Fellowship. JG has benefited from KU Leuven-BOF PFV/10/002 Center of Excellence: Optimization in Engineering (OPTEC) and from Flanders Make ICON (DriveTrainCodesign).

Data availability

The data and scripts required for reproducing the results are available at <https://simtk.org/projects/3dpredictsim>. The movies are available upon request.

Chapter 7

Study 5: Physics-based predictive simulations to explore the differential effects of motor control and musculoskeletal deficits on gait dysfunction in cerebral palsy: a retrospective case study

Submitted as:

Falisse A., Pitto L., Kainz H., Wesseling M., Van Rossom S., Hoang H., Papageorgiou E., Bar-On L., Hallemans A., Desloovere K., Molenaers G., Van Campenhout A., De Groote F., Jonkers I. *Physics-based predictive simulations to explore the differential effects of motor control and musculoskeletal deficits on gait dysfunction in cerebral palsy: a retrospective case study.* Frontiers in Human Neuroscience.

Abstract

Model-based simulations of walking have the theoretical potential to support clinical decision making by predicting the functional outcome of treatments in terms of walking performance. Yet before using such simulations in clinical practice, their ability to identify the main treatment targets in specific patients needs to be demonstrated. In this study, we generated predictive simulations of walking with a medical imaging based neuro-musculoskeletal model of a child with cerebral palsy presenting crouch gait. We explored the influence of altered muscle-tendon properties, reduced neuromuscular control complexity, and spasticity on gait function in terms of joint kinematics, kinetics, muscle activity, and metabolic cost of transport. We modeled altered muscle-tendon properties by personalizing Hill-type muscle-tendon parameters based on data collected during functional movements, simpler neuromuscular control by reducing the number of independent muscle synergies, and spasticity through delayed muscle activity feedback from muscle force and force rate. Our simulations revealed that, in the presence of aberrant musculoskeletal geometries, altered muscle-tendon properties rather than reduced neuromuscular control complexity and spasticity were the primary cause of the crouch gait pattern observed for this child, which is in agreement with the clinical examination. These results suggest that muscle-tendon properties should be the primary target of interventions aiming to restore a more upright gait pattern for this child. This suggestion is in line with the gait analysis following muscle-tendon property and bone deformity corrections. The ability of our simulations to distinguish the contribution of different impairments on walking performance opens the door for identifying targeted treatment strategies with the aim of designing optimized interventions for neuro-musculoskeletal disorders.

Introduction

Cerebral palsy (CP) is the most common cause of motor disability amongst children, affecting 2 to 3 per 1000 live births in Europe [1]. CP is caused by a non-progressive lesion in the immature brain that may induce inabilities to selectively control muscles, spasticity, and weakness. These deficits undermine walking performance and, over time, lead to secondary impairments, such as bone deformities and muscle contracture, that may further deteriorate walking abilities [2]. Numerous treatments target these impairments with the aim of improving walking performance, such as single-event multi-level orthopedic surgeries (SEMLS) to correct multiple bone and muscle impairments in a single intervention [5]. Yet walking involves complex interactions between the

musculoskeletal and motor control systems, which are both impaired in CP. Hence, the treatment outcome does not only depend on the success of the intervention in terms of musculoskeletal remediation but also on the remaining motor control [6]. As a result, over the last decades, only modest, unpredictable, and stagnant treatment outcomes have been documented for children with CP [10]. For example, SEMLS have been reported to improve walking performance in only 25 to 43% of the patients [7, 8] and to lead to clinically meaningful improvements over natural progression in only 37% of the cases [9]. Computer models that can predict the functional outcome of treatments on walking performance have the potential to improve this success rate by allowing clinicians to optimize the clinical decision making (e.g., by discriminating the effects of musculoskeletal restoration due to surgical interventions to those from tone reduction and physical therapy targeting motor control impairments). However, predictive simulations are not yet applied in clinical practice, in part due to computational and modeling challenges.

Predictive simulations generate novel movements based on a mathematical model of the neuro-musculoskeletal system without relying on experimental data. Typically, these simulations consist in identifying muscle excitations that follow a certain control strategy and drive the musculoskeletal model to achieve a movement-related goal (e.g., moving forward at a given speed). For such simulations to be valuable in predicting the functional outcome of treatments on walking performance, they should be based on models that are complex enough to describe the musculoskeletal structures and motor control processes underlying walking that may be impaired and thus affected by treatment. Yet these complex models are computationally expensive in predictive simulations [35, 36, 25, 37] and, therefore, their ability to predict the variety of gaits encountered under different conditions (e.g., healthy and pathological gaits) has been only scarcely explored in the literature. We recently developed a simulation framework to generate rapid (i.e., about 30 minutes of computational time) predictive simulations of gait with complex models [231]. Further, we demonstrated the ability of our framework to predict the mechanics and energetics of a broad range of gaits, suggesting that our models and simulations were sufficiently generalizable for use in clinical applications. Nevertheless, the ability of our simulations to identify the main treatment targets in specific patients remains untested. Specifically, for children with CP, simulations should allow distinguishing the effects of musculoskeletal versus motor control impairments on walking performance to be able to help clinicians optimize treatments.

Predicting the effects of impairments on walking performance in children with

CP requires that the neuro-musculoskeletal model captures these impairments. In this work, we focus on two types of impairments: motor control impairments that include spasticity and non-selective muscle control, and musculoskeletal impairments that include bone deformities and altered muscle-tendon properties.

Spasticity has been described as a velocity-dependent increase in tonic stretch reflex responses resulting from hyper-excitability of the stretch reflex [58]. Following such description, models have been developed to describe the measured response in muscle activity (i.e., electromyography (EMG)) to passive stretches based on feedback from muscle velocity [100]. However, we previously showed that a model based on feedback from muscle force and force rate better explains the response of spastic hamstrings and gastrocnemii than length- and velocity-based models [232]. Further, we found that a force-based model could predict muscle activity in agreement with pathological EMG during gait. While spasticity manifests during passive stretches, its influence during gait remains unclear [95]. Incorporating spasticity models in predictive simulations would allow evaluating the impact of spasticity on gait performance, providing insights into the role of spasticity during gait. Further, modeling spasticity is a prerequisite for simulating the effects of treatments aiming to reduce spasticity, such as botulinum toxin-A (BTX) injections.

The inability to selectively control muscles has been described through muscle synergies [59], which are independent groups of muscles activated in a fixed ratio by a single input signal. Children with CP have been shown to use fewer synergies (i.e., a simpler neuromuscular control strategy) than typically developing (TD) individuals during walking [61] as well as to use synergies exhibiting a greater stride-to-stride variability [62]. However, assessing the relationship between simpler neuromuscular control and impaired gait is difficult. For example, Shuman *et al.* [94] showed that treatments such as BTX injections, selective dorsal rhizotomy, and SEMLS minimally affected synergies despite changing the walking patterns. Predictive simulations have the potential to relate synergy complexity to impaired walking abilities, which might help designing specific treatments (e.g., physical therapy protocols) targeting impaired selective motor control.

Bone deformities and resultant altered muscle path trajectories make the use of generic musculoskeletal models linearly-scaled to the subjects' anthropometry inappropriate for clinical analyses in children with CP. A well established approach to capture these aberrant geometries is through the use of models created from Magnetic Resonance Imaging (MRI) [73, 74, 75]. Such models have been shown to improve, for example, the accuracy of moment arm estimation in

children with CP [76]. Besides geometries, the muscle-tendon properties are also altered in these children (e.g., smaller muscle volumes and shorter fiber lengths as compared to TD individuals) [84, 233, 82, 81, 83]. This makes the use of Hill-type muscle-tendon models with generic (i.e., anthropometry-based) parameters unsuited for clinical studies. Indeed, such parameters may not reflect altered muscle force generating capacities and, therefore, result in unrepresentative simulations. To capture the impact of altered muscle-tendon properties on walking performance, the muscle-tendon parameters should be personalized. Different approaches have been proposed for such purpose, including methods based on angle-torque relationships from functional movements [90, 168].

Predictive simulations have the potential to shed light upon the influence of altered musculoskeletal properties, impaired selective motor control, and spasticity on walking performance by evaluating the isolated effects of these impairments. Yet only few predictive analyses have used simulations for such purpose. Recent modeling work showed that a musculoskeletal model could reproduce an unimpaired walking pattern with five synergies but not with two synergies similar to those seen after neurological injury, suggesting that impaired control affects walking performance [103]. Another predictive analysis explored the effects of aging on walking performance by adjusting skeletal and neuromuscular parameters and reported a predominant contribution of loss in muscle strength and mass to reduced energy efficiency [40]. Both studies, however, relied on simple two-dimensional (2D) models, neglecting motor control mechanisms in the frontal plane. To the authors' knowledge, no study has yet attempted to relate patients' clinical examination reports to the outcome of predictive simulations evaluating the effects of musculoskeletal and motor control impairments on walking performance based on three-dimensional (3D) subject-specific models.

The purpose of this study was to evaluate the ability of our predictive simulation platform to differentiate the effects of musculoskeletal and motor control impairments on the impaired walking pattern (i.e., crouch gait) of a specific child with CP. To this aim, we evaluated the effect of these impairments on gait patterns predicted by performance optimization (Figure 7.1A). We first investigated the influence of using personalized rather than generic muscle-tendon parameters, thereby assessing the contribution of the child's altered muscle-tendon properties to the crouch gait pattern. We then evaluated the impact of imposing a number of synergies lower than typically reported for unimpaired individuals, thereby testing how reducing neuromuscular control complexity affects walking performance. We finally investigated the effect of spasticity modeled based on muscle force and force rate feedback. In all cases,

we used a MRI-based musculoskeletal model of the child to take the aberrant geometries into account. We found that altered muscle-tendon properties rather than control impairments alone caused a crouch gait pattern. As an additional analysis, we investigated whether the child's impairments impede a walking pattern similar to TD walking or rather make such a walking pattern less optimal. To this aim, we extended the performance criterion of the predictive simulations with a tracking term that penalized deviations from a TD walking pattern. We found that the musculoskeletal impairments did not prevent an upright walking pattern resembling TD walking but that upright walking was less optimal than walking in crouch.

Methods

The overall process to evaluate the effects of impairments on walking performance through predictive simulations is outlined in Figure 7.1B. The following sections provide details of this process.

Experimental data

We collected data from one child with diplegic CP (age: 10-15 years; height: 125-150 cm; mass: 30-40 kg). The data collection was approved by the Ethics Committee at UZ Leuven (Belgium) and written informed consent was obtained from the child's parents. The child was instrumented with retro-reflective skin mounted markers whose 3D trajectories were recorded (100 Hz) using a motion capture system (Vicon, Oxford, UK) during overground walking at self-selected speed. Ground reaction forces were recorded (1000 Hz) using force plates (AMTI, Watertown, USA). EMG was recorded (2000 Hz) using a telemetric Zerowire system (Cometa, Milan, Italy) from eight muscles of each leg (rectus femoris, biceps femoris short head, semitendinosus, tibialis anterior, gastrocnemius lateralis, vastus lateralis, soleus, and gluteus medius). EMG from the rectus femoris and vastus lateralis was of poor quality and excluded from the analysis.

On the same day as the gait analysis, spasticity of the right medial hamstrings and gastrocnemii was assessed using an instrumented passive spasticity assessment (IPSA; described in detail in [109]). Hamstrings and gastrocnemii were passively stretched by moving knee and ankle, respectively, one at a time from a predefined position throughout the full range of motion (ROM). The stretches were performed at slow and fast velocities. EMG was collected

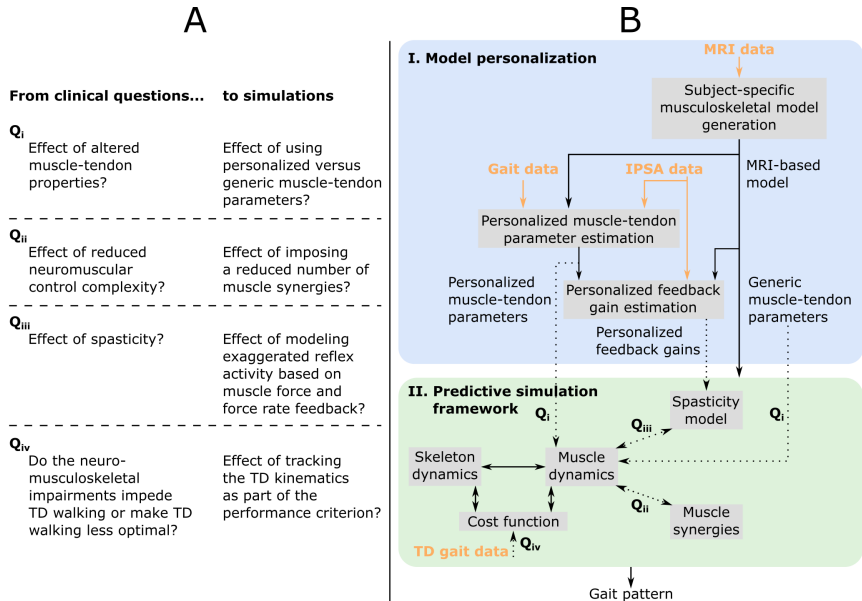


Figure 7.1: Overview of (A) clinical questions and corresponding simulations, and (B) methodology. MRI images are used to generate a musculoskeletal model of the child with subject-specific geometries. This MRI-based model as well as experimental data collected during walking and instrumented passive spasticity assessments (IPSA) are inputs to optimization procedures providing personalized estimates of Hill-type muscle-tendon parameters characterizing altered muscle-tendon properties and personalized feedback gains characterizing spasticity. The framework for predictive simulations generates gait patterns by optimizing a cost function, describing a walking-related performance criterion, subject to the muscle and skeleton dynamics of the MRI-based musculoskeletal model. We investigated the effects of impairments on predicted gait patterns (dotted arrows): Q_i we evaluated the effect of altered versus unaltered muscle-tendon properties by using personalized versus generic muscle-tendon parameters in the muscle dynamics; Q_{ii} we assessed the influence of reducing the neuromuscular control complexity by imposing a reduced number of muscle synergies; Q_{iii} we explored the impact of spasticity on walking performance. Details on how we modeled these impairments are described in the methods. As an additional analysis, Q_{iv}, we evaluated how well the model was able to reproduce the gait pattern of a typically developing (TD) child by adding a term in the cost function penalizing deviations between predicted gait pattern and measured gait data of a TD child. All these analyses can be combined as well as performed in isolation. Details are provided in section “model-based analyses”.

from four muscles (semitendinosus, gastrocnemius lateralis, rectus femoris, and tibialis anterior) using the same system and electrode placement as used for gait analysis. The motion of the distal and proximal segments were tracked using two inertial measurement units (Analog Devices, ADIS16354). The forces applied to the segment were measured using a hand-held six degrees of freedom (DOFs) load-cell (ATI Industrial Motion, mini45). The position of the load-cell relative to the joint axis was manually measured by the examiner.

Muscle strength, selectivity, and ROM were evaluated (Table 7.1) with a standardized clinical examination protocol [110]. The child had close to normal ROM at the hip and ankle but bilateral knee extension deficits, bilateral spasticity in most muscles, good strength in most muscles although slight deficits in hip extensors, knee extensors, and hip abductors, and good to perfect selectivity in most muscles. MRI images were collected for the hip region (i.e., pelvis and femur according to the protocol described in [111]). The child was classified at a level II in the Gross Motor Function Classification System (GMFCS).

We processed the experimental gait and IPSA data, used as input for the estimation of muscle-tendon parameters and feedback gains (Figure 7.1; details below), with OpenSim 3.3 [112] using the MRI-based model described below.

Subject-specific musculoskeletal model generation

A 3D musculoskeletal model with subject-specific geometries was created from MRI images [74, 75, 111]. Bones of the lower limbs and pelvis were segmented using Mimics (Materialize, Leuven, Belgium). Anatomical reference frames, joint axes, and muscle origin and insertion points were defined using a previously developed workflow [234]. The model consisted of 21 DOFs (six between the pelvis and the ground; three at each hip joint; one at each knee, ankle, and subtalar joint; and three at the lumbar joint), 86 muscles actuating the lower limbs (43 per leg), three ideal torque actuators at the lumbar joint, and four contact spheres per foot [63, 112]. We added passive torques to the joints of the lower limbs and the trunk to model the role of the ligaments and other passive structures [35]. These passive torques varied exponentially with joint positions and linearly with joint velocities.

We used Raasch's model [29, 52] to describe muscle excitation-activation coupling (muscle activation dynamics) and a Hill-type muscle-tendon model [27, 53] to describe muscle-tendon interaction and the dependence of muscle force on fiber

	ROM		Spasticity	
	Left	Right	Left	Right
Hip flexion	145°	140°	Hip flexion MAS	2 2
Hip extension	-10°	-10°	Hip add (Knee 0°) MAS	1.5 1.5
Hip abd (Knee 0°)	25°	25°	Hip add (Knee 90°) MAS	0 0
Hip abd (Knee 90°)	45°	45°	Hamstrings MAS	1.5 1
Hip add	0°	0°	Hamstrings Tard	-70° /
Hip int rotation (prone)	60°	70°	DuncanEly MAS	1.5 1.5
Hip ext rotation (prone)	25°	25°	Soleus MAS	0 0
Hip int rotation (supine)	25°	30°	Soleus Tard	/ /
Hip ext rotation (supine)	55°	50°	Gastrocnemius MAS	1.5 1.5
Knee flexion	120°	120°	Gastrocnemius Tard	0° 5°
Knee extension	-20°	-15°	Tibialis Post MAS	0 0
Knee spontaneous position	-30°	-25°	Clonus	0 0
Popliteal angle Unilateral	-70°	-65°		
Popliteal angle Bilateral	-65°	-60°		
Ankle dorsi (Knee 90°)	20°	25°		
Ankle dorsi (Knee 0°)	15°	15°		
Ankle plantarflexion	35°	35°	Femoral anteversion	35° 35°
Ankle inversion	40°	45°	Tibia-femoral angle	25° 25°
Ankle eversion	10°	10°	Bimalleor angle	40° 40°
	Selectivity		Strength	
	Left	Right	Left	Right
Hip flexion	2	2	Hip flexion	4 4
Hip extension	1.5	1.5	Hip extension	3 3
Hip abd	1.5	1.5	Hip abd	3+ 3+
Hip add	2	2	Hip add	4 4
Knee flexion	1.5	1.5	Knee flexion	4 3+
Knee extension	1	1.5	Knee extension	3+ 3+
Ankle dorsi (Knee 90°)	1.5	1.5	Ankle dorsi (Knee 90°)	4 4
Ankle dorsi (Knee 0°)	1.5	1.5	Ankle dorsi (Knee 0°)	4 4
Ankle plantarflexion	1.5	1.5	Ankle plantarflexion	4 3+
Ankle inversion	1.5	1.5	Ankle inversion	4 4
Ankle eversion	2	1.5	Ankle eversion	4 4

Table 7.1: **Clinical examination.** ROM is range of motion. Spasticity, MAS is for Modified Ashworth Scale: 1 is low, 1+ is medium, and 2 is high spastic involvement; Tard is for Tardieu test. Strength: 3 is medium and 4 is good strength; strength from 3 indicates ability to move against gravity. Selectivity: 1 is medium, 1.5 is good, and 2 is perfect selective control. Clinically meaningful deviations from unimpaired individuals are in bold. Add is adduction; abd is abduction; dorsi is dorsiflexion.

length and velocity (muscle contraction dynamics). We modeled skeletal motion with Newtonian rigid body dynamics and smooth approximations of compliant Hunt-Crossley foot-ground contacts [112, 119, 190, 231]. We calibrated the Hunt-Crossley contact parameters (transverse plane locations and contact sphere radii) through muscle-driven tracking simulations of the child's experimental walking data as described in previous work [231]. To increase computational speed, we defined muscle-tendon lengths, velocities, and moment arms as a polynomial function of joint positions and velocities [127, 231].

Personalized muscle-tendon parameter estimation

The force-length-velocity relationships describing the force generating capacity of the Hill-type muscle-tendon model are dimensionless and can be scaled to a specific muscle through five muscle-tendon parameters: the maximal isometric force F_m^{\max} , the optimal fiber length l_m^{opt} , the tendon slack length l_t^s , the optimal pennation angle α_m^{opt} , and the maximal fiber contraction velocity v_m^{\max} (assigned to ten times l_m^{opt}). In this study, we used generic and personalized parameters when generating predictive simulations of walking (Figure 7.1).

The generic parameters were derived by linearly scaling the parameters of a generic musculoskeletal model [63] to the child's anthropometry. The linear scaling was only performed for the optimal fiber lengths and tendon slack lengths. The maximal isometric muscle forces were scaled based on body mass M [100]:

$$F_{m,\text{subject}}^{\max} = F_{m,\text{gait2392}}^{\max} \left(\frac{M_{\text{subject}}}{M_{\text{gait2392}}} \right)^{(2/3)}, \quad (7.1)$$

where gait2392 refers to the OpenSim gait2392 model [63, 112].

The personalized parameters reflect the muscle force generating capacity of the subject. Only optimal fiber lengths and tendon slack lengths were personalized as gait simulations have been shown to be the most sensitive to these two parameters [106]. The personalization process was based on an extension of an optimal control approach to solve the muscle redundancy problem while accounting for muscle dynamics [53, 168]. Solving the muscle redundancy problem identifies muscle excitations that reproduce joint torques underlying a given movement while minimizing a performance criterion (e.g., muscle effort). We augmented this formulation in different ways. First, we added optimal fiber lengths and tendon slack lengths as optimization variables. Second, we

introduced a term in the cost function minimizing the difference between muscle activations and scaled EMG signals where scale factors were included as optimization variables. Third, we assumed that muscles operate around their optimal fiber lengths, and that maximal and minimal fiber lengths across movements should hence be larger and smaller, respectively, than their optimal fiber lengths. Fourth, we assumed that resistance encountered when evaluating the ROM during the clinical examination may be, at least in part, attributed to passive muscle forces. Hence, we included a term in the cost function minimizing the difference between fiber lengths at these extreme positions of the ROM and reference fiber lengths generating large passive forces. Finally, we minimized optimal fiber lengths, assuming that children with CP have short fibers [84]. The problem thus consisted in identifying muscle excitations and parameters that minimized a multi-objective cost function:

$$J_{\text{estimation}} = \int_{t_0}^{t_f} \left(\underbrace{w_1 \|a\|_2^2}_{\text{Muscle effort}} + \underbrace{w_2 \|a - \text{EMG}\|_2^2}_{\text{EMG deviation}} + \underbrace{w_3 \|l_m^{\max} - l_{\text{ref}}^{\max}\|_2^2}_{\text{Passive forces in extreme positions}} \right. \\ \left. + \underbrace{w_4 \|l_m^{\text{opt}}\|_1}_{\text{Short fibers}} + \underbrace{w_5 \|a_r\|_2^2}_{\text{Reserve actuators}} \right) dt, \quad (7.2)$$

where t_0 and t_f are initial and final times, a are muscle activations, l_m^{\max} and $l_{\text{ref}}^{\max} = 1.5$ are simulated and reference fiber lengths, respectively, at the extreme positions of the ROM, a_r are reserve actuators, w_{1-5} are weight factors, and t is time. This cost function was subject to constraints enforcing muscle dynamics, that resultant muscle forces should reproduce joint torques calculated from inverse dynamics, that fiber lengths should cross their optimal fiber lengths during the movement, and that the difference between activations and EMG should not be larger than 0.1. Reserve actuators are non-physiological ideal actuators added to muscle-generated torques to ensure that joint torques from inverse dynamics can be reproduced. The weights were manually adjusted to the following: $w_1 = 10 \times 10^{-4}$, $w_2 = 30 \times 10^{-4}$, $w_3 = 3550 \times 10^{-4}$, $w_4 = 1010 \times 10^{-4}$, and $w_5 = 5400 \times 10^{-4}$. These weights primarily penalized the use of reserve actuators and encouraged the generation of passive forces in the extreme positions of the ROM. We solved this problem while simultaneously considering data from four gait trials of each leg and six passive stretches (IPSA measurements) of the right hamstrings, rectus femoris, and gastrocnemii at slow

and fast velocities (one stretch per muscle per speed). Data from 14 trials (gait and passive trials combined) was thus included. Data from passive stretches of left leg muscles was not available. Hence, we imposed that corresponding parameters of both legs could not differ by more than 5%. The parameters were allowed to vary between 50 and 200% of the generic values.

Spasticity model - Personalized feedback gain estimation

We modeled spasticity through delayed feedback from muscle-tendon force and its first time derivative (i.e., force rate) [232]. The model relates sensory information s (i.e., muscle force and force rate) to feedback muscle activations a_s through a first order differential equation:

$$\tau \frac{da_s}{dt} = \begin{cases} -a_s, & s \leq T_s \\ -a_s + g_s(s - T_s), & s > T_s \end{cases} \quad (7.3)$$

where T_s is a feedback threshold, g_s is a feedback gain, and $\tau_s = 30$ ms is a time delay.

We determined the threshold for force feedback as the value 20 ms before the EMG onset [132] and used a zero threshold for force rate feedback. We identified the personalized feedback gains that minimized the difference between EMG and feedback muscle activations during fast passive stretches (IPSA measurements). We performed such optimization for the right medial hamstrings (i.e., biceps femoris long head, semitendinosus, and semimembranosus) and for the right gastrocnemii (i.e., gastrocnemius lateralis and medialis). We used semitendinosus EMG to drive the three hamstrings and gastrocnemius lateralis EMG to drive both gastrocnemii. We normalized EMG using scale factors identified when estimating the personalized muscle-tendon parameters. We described the optimization process in detail in previous work [232]. We incorporated the spasticity model with personalized feedback gains in our framework for predictive simulations (Figure 7.1). Since we only had IPSA measurement for the right leg, we used feedback gains and thresholds identified with right leg data for left leg muscles. Gait EMG data and spasticity, as clinically assessed (Table 7.1), were comparable for both legs.

Muscle synergies

We modeled the reduced neuromuscular control complexity through muscle synergies. These synergies consisted of two matrices: a $N_{\text{syn}} \times N_f$ matrix H , where N_{syn} is the number of synergies and N_f is the number of frames, containing synergy activations and a $N_m \times N_{\text{syn}}$ matrix W , where N_m is the number of muscles, containing weights that determine the contribution of each muscle in each synergy. Individual muscle activations were composed from synergies as follows:

$$a = W \times H, \quad (7.4)$$

where a has dimensions $N_m \times N_f$. Importantly, we did not impose subject-specific synergies when generating predictive simulations (Figure 7.1). Instead, we modeled the effect of reducing the neuromuscular control complexity by limiting the number of synergies per leg to four or three, thereby limiting the selection of independent muscle activations. This represents a reduction of the neuromuscular control complexity under the assumption that five synergies describe healthy human locomotion [59].

Problem formulation

We predicted gait patterns by optimizing a gait-related cost function, independent of experimental data, based on the MRI-based musculoskeletal model described above. In addition to optimizing performance, we imposed average gait speed and periodicity of the gait pattern. We optimized for a full gait cycle to account for asymmetry of CP gait. We solved the resultant optimal control problem via direct collocation. The problem formulation and computational choices are detailed in previous work [231].

The cost function represents the goal of the motor task. We modeled this task-level goal as a weighted sum of gait-related performance criteria including metabolic energy rate, muscle fatigue, joint accelerations, passive joint torques, and trunk actuator excitations:

$$J_{\text{prediction}} = \int_0^{t_f} \frac{1}{d} \left(\underbrace{w_1 \|\dot{E}\|_2^2}_{\text{Metabolic energy rate}} + \underbrace{w_2 \|a\|_{10}^{10}}_{\text{Muscle fatigue}} + \underbrace{w_3 \|u_{dv}\|_2^2}_{\text{Joint accelerations}} \right. \\ \left. + \underbrace{w_4 \|T_p\|_2^2}_{\text{Passive torques}} + \underbrace{w_5 \|e_t\|_2^2}_{\text{Trunk excitations}} \right) dt, \quad (7.5)$$

where t_f is unknown gait cycle duration, d is distance traveled by the pelvis in the forward direction, \dot{E} are metabolic energy rates, a are muscle activations, \ddot{q} are joint accelerations, T_p are passive joint torques, e_t are excitations of the trunk torque actuators, w_{1-5} are weight factors, and t is time. We modeled metabolic energy rate using a smooth approximation of the phenomenological model described by Bhargava *et al.* [130]. This metabolic model requires parameters for fiber type composition and muscle specific tension, which we obtained from the literature [131]. We manually adjusted the weight factors until we found a set of weights that predicted human-like walking: $w_1 = (25/86/\text{body mass}) \times 10^{-2}$, $w_2 = 25/86 \times 10^2$, $w_3 = 50/21$, $w_4 = 10/15 \times 10^2$, and $w_5 = 1/3 \times 10^{-1}$. We added several path constraints enforcing a prescribed average gait speed corresponding to the child's average gait speed ($d/t_f = 1 \text{ m s}^{-1}$), imposing periodic states over the complete gait cycle (except for the pelvis forward position), and preventing inter-penetration of body segments.

Model-based analyses

We investigated the differential effects of altered muscle-tendon properties, reduced neuromuscular control complexity, and spasticity on gait patterns predicted with the MRI-based musculoskeletal model (Figure 7.1). In particular, we compared predicted joint kinematics and kinetics, muscle activity, and stride lengths to their experimental counterparts. We also evaluated how impairments affected the metabolic cost of transport (COT), defined as metabolic energy consumed per unit distance traveled.

First, we tested the influence of altered versus unaltered muscle-tendon properties by using personalized versus generic muscle-tendon parameters in the

muscle dynamics (Q_i in Figure 7.1). In this initial analysis, we did not include spasticity, nor imposed synergies.

Second, we assessed the impact of reducing the neuromuscular control complexity by imposing fixed numbers of synergies (Q_{ii} in Figure 7.1). To assess the effect of reducing the number of synergies, we compared the synergy activations resulting from simulations with three and four synergies using the coefficient of determination R^2 and the synergy weights using Pearson's coefficient of correlation r . We generated simulations with both sets of muscle-tendon parameters to explore the effect of synergies in isolation as well as in combination with altered muscle-tendon properties.

Finally, we evaluated the effect of spasticity in the three medial hamstrings and two gastrocnemii of both legs (Q_{iii} in Figure 7.1). We modeled muscle activations as the sum of reflex muscle activations determined based on the personalized spasticity model and feedforward muscle activations:

$$a_{\text{sum}} = a_{ff} + a_{F_t} + a_{dF_t}, \quad (7.6)$$

where a_{ff} are feedforward muscle activations, and a_{F_t} and a_{dF_t} are muscle activations from muscle force and force rate feedback, respectively. We only tested the effect of spasticity based on the model with personalized muscle-tendon parameters, since these parameters were used to estimate the feedback gains. We tested the effect of spasticity in combination with selective control (i.e., no synergy constraints) as well as with a reduced number of muscle synergies.

As an additional analysis, we investigated whether the child adopted an impaired crouch gait pattern because of neuro-mechanical constraints or because it was more optimal (Q_{iv} in Figure 7.1). To this aim, we added a term in the cost function that penalized deviations from measured kinematics of a TD child:

$$J_{\text{tracking}} = \int_0^{t_f} \left(\underbrace{w_6 \|q - \hat{q}\|_2^2}_{\text{TD kinematics deviation}} \right) dt, \quad (7.7)$$

where \hat{q} are measured joint positions of a TD child and $w_6 = 100/20$ is a weight factor. We generated these simulations with personalized parameters as well as with and without synergies. We did not include spasticity in this analysis since

it had little influence on the walking pattern in the simulations described above.

We formulated our problems in MATLAB using CasADI [56], applied direct collocation using a third order Radau quadrature collocation scheme with 150 mesh intervals per gait cycle, and solved the resulting nonlinear programming problems with the solver IPOPT [122]. We applied algorithmic differentiation to compute derivatives [231]. We started each optimization from multiple initial guesses and selected the result with the lowest optimal cost. Initial guesses for joint variables were based on experimental data. Specifically, for all simulations, we used two initial guesses derived from experimental kinematics of the CP and the TD child. For simulations accounting for synergies, we added initial guesses derived from simulated kinematics with the lowest optimal costs produced without synergies and with more synergies (e.g., with three synergies, initial guesses were derived from the best kinematic solutions with four synergies and without synergies). For simulations accounting for spasticity, we added initial guesses derived from simulated kinematics with the lowest optimal costs produced without spasticity. In all cases, initial guesses for muscle, trunk, and synergy variables were constant across time and not informed by experimental data. Initial guesses for synergy weights were constant across muscles and independent of experimental data.

Results

Gait analysis

The child walked with a pronounced crouch gait pattern characterized by bilateral knee extension deficits with reduced knee ROM during swing, a lack of right ankle dorsiflexion at the end of swing, excessive left ankle dorsiflexion, excessive and deficient right and left hip adduction, respectively, and excessive bilateral hip internal rotation (Figures 7.2 and D.1 in Appendix D; Movies 1-2).

Influence of the muscle-tendon parameters

Using personalized versus generic muscle-tendon parameters resulted in a crouch (i.e., excessive knee flexion) versus a more upright gait pattern (Figures 7.2 and D.1 in Appendix D; Movies 3-4). Personalized optimal fiber lengths and tendon slack lengths were generally smaller and larger, respectively, than their generic counterparts (Tables D.1-D.2). The use of personalized parameters resulted in decreased deviations (smaller root mean square error (RMSE)) between

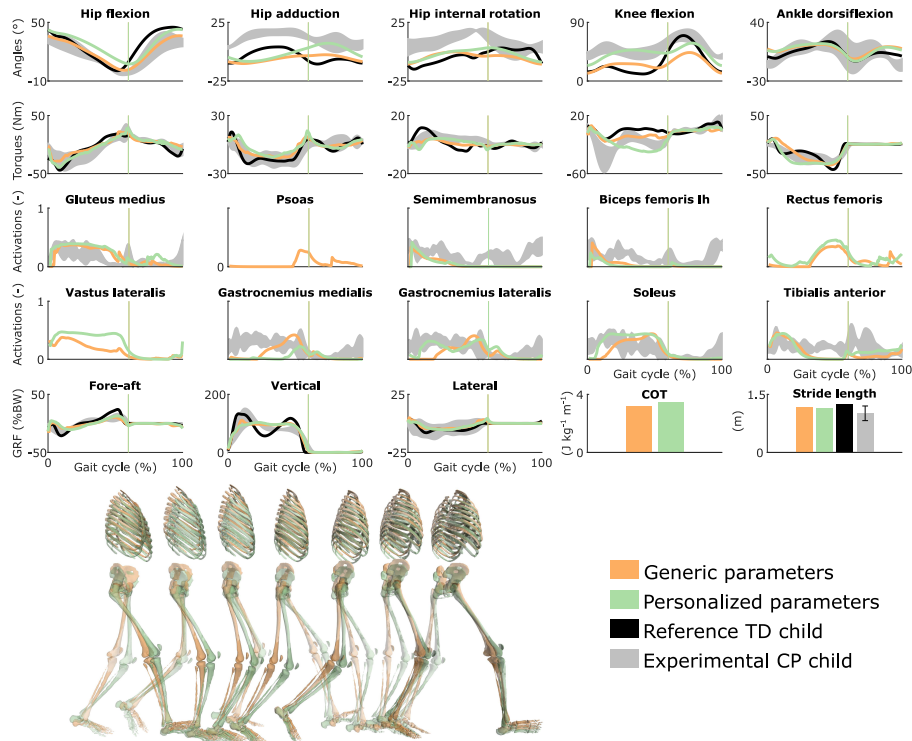


Figure 7.2: Influence of the muscle-tendon parameters on the predicted walking gaits. Variables from the right leg are shown over a complete gait cycle; left leg variables are shown in Figure D.1 in Appendix D. Vertical lines indicate the transition from stance to swing. Experimental data is shown as mean \pm two standard deviations. Experimental EMG data was normalized to peak activations. GRF is for ground reaction forces; BW is for body weight; COT is for metabolic cost of transport; lh is for long head. Gait snapshots cover a gait cycle starting at right heel strike; left leg segments are more transparent.

measured and predicted knee angles (RMSE of 17° and 11° for the left and right leg, respectively) as compared to the use of generic parameters (RMSE of 43° and 25°). The gastrocnemius lateralis and soleus (ankle plantarflexors) were activated earlier in stance with the crouch gait, as observed in the child's EMG. The vasti (knee extensors) activity was also increased during stance when the model walked in crouch. The COT was higher with the personalized parameters (crouch gait; $3.45 \text{ J kg}^{-1}\text{m}^{-1}$) than with the generic parameters (more upright gait; $3.18 \text{ J kg}^{-1}\text{m}^{-1}$). Predicted stride lengths were larger than the average stride length of the child but were within two standard deviations.

Influence of the synergies with generic muscle-tendon parameters

Reducing the number of synergies in combination with generic muscle-tendon parameters did not induce the amount of crouch that was experimentally measured in the child, although it altered muscle coordination and increased COT (Figures 7.3 and D.2 in Appendix D; Movie 5). The right knee flexion angles increased during stance with the reduction of the neuromuscular control complexity but were still smaller than experimentally measured. This was accompanied with increased rectus femoris (knee extensor) activity. The synergies had a limited effect on the left leg that had a straight knee pattern during stance. The COT increased with the reduction of the neuromuscular control complexity (3.58 and $3.90 \text{ J kg}^{-1}\text{m}^{-1}$ with four and three synergies, respectively). The synergies had little effect on the predicted stride lengths that were larger than the child's average stride length but were within two standard deviations. The synergies of the three-synergy case were similar to the first three synergies of the four-synergy case (average R^2 and r over three common synergy activations and weight vectors, respectively, of both legs: 0.84 ± 0.19 and 0.83 ± 0.10). The additional synergy in the four-synergy case was activated in early stance and at the transition between stance and swing, and mainly consisted of hip adductors.

Influence of the synergies with personalized muscle-tendon parameters

Reducing the number of synergies in combination with personalized muscle-tendon parameters had a minor effect on gait kinematics but altered muscle coordination and increased COT (Figures 7.4 and D.3 in Appendix D; Movie 6). Specifically, synergies only had a slight effect on the kinematics during the swing phase of the right leg but affected the activation pattern of certain

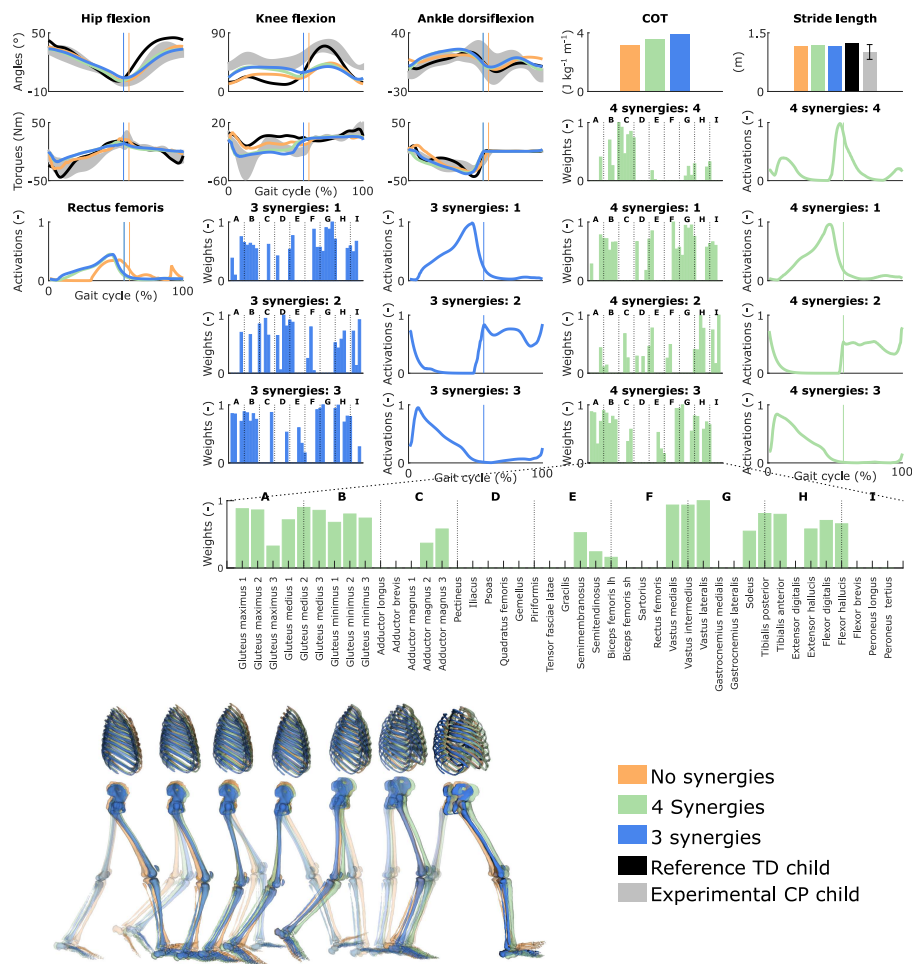


Figure 7.3: **Influence of the synergies on walking gaits predicted with the generic muscle-tendon parameters.** Variables from the right leg are shown over a complete gait cycle; left leg variables are shown in Figure D.2 in Appendix D. Vertical lines (solid) indicate the transition from stance to swing. Panels of synergy weights are divided into sections (A-I) to relate bars to muscle names provided in the bottom bar plot, which is an expanded version of the plot of weights with title 4 synergies: 3. Lh and sh are for long and short head, respectively. Weights were normalized to one. Experimental data is shown as mean \pm two standard deviations. Gait snapshots cover a gait cycle starting at right heel strike; left leg segments are more transparent.

muscles (e.g., gastrocnemius medialis and lateralis). The COT increased with the reduction of the neuromuscular control complexity (3.94 and $4.09 \text{ J kg}^{-1}\text{m}^{-1}$ with four and three synergies, respectively). Stride lengths slightly decreased with synergies but remained larger than the child's average stride length. The synergies of the three-synergy case were similar to the first three synergies of the four-synergy case (average R^2 and r : 0.85 ± 0.05 and 0.87 ± 0.09 , respectively). The additional synergy in the four-synergy case was activated in early stance and at the transition between stance and swing, and mainly consisted of the gemellus, piriformis, tibialis posterior, and several ankle plantarflexors.

Influence of spasticity

Spasticity had a limited effect on muscle coordination and almost no influence on gait kinematics (Figures 7.5 and D.4 in Appendix D; Movie 7). Specifically, spastic activity was predicted in the medial hamstrings in early stance but this had, overall, a minor effect on the total (i.e., combined spastic and non-spastic contributions) medial hamstrings activity when compared to simulations without spasticity. Bursts of spastic activity were also observed in early swing. Medial hamstrings activity contributes to knee flexion but since similar (timing and magnitude) activity profiles were predicted with and without spasticity, there was no difference in predicted knee flexion angles. A constant low spastic contribution was predicted for the gastrocnemius lateralis during stance, whereas a minor contribution was predicted for the gastrocnemius medialis during stance and at the transition between stance and swing. Spasticity hence does not explain the lack of right ankle dorsiflexion (i.e., increased plantarflexion) observed at the end of swing in experimental data. Similar observations hold with and without synergies. The COT increased when incorporating spasticity (3.75 and $4.18 \text{ J kg}^{-1}\text{m}^{-1}$ with zero and four synergies, respectively).

Influence of tracking the kinematics of a TD child

Tracking the TD kinematics while using personalized muscle-tendon parameters produced an upright gait pattern when not incorporating synergies, but decreased the overall gait performance (Figures 7.6 and D.5 in Appendix D; Movie 8). Specifically, the simulated gait had a similar COT ($3.46 \text{ J kg}^{-1}\text{m}^{-1}$) as the crouch gait pattern predicted without such tracking term but the contribution of most terms in the cost function increased, suggesting that walking upright is not prevented by mechanical constraints (i.e., aberrant musculoskeletal geometries and altered muscle-tendon properties) but is less optimal, due to these mechanical constraints, than walking in crouch for

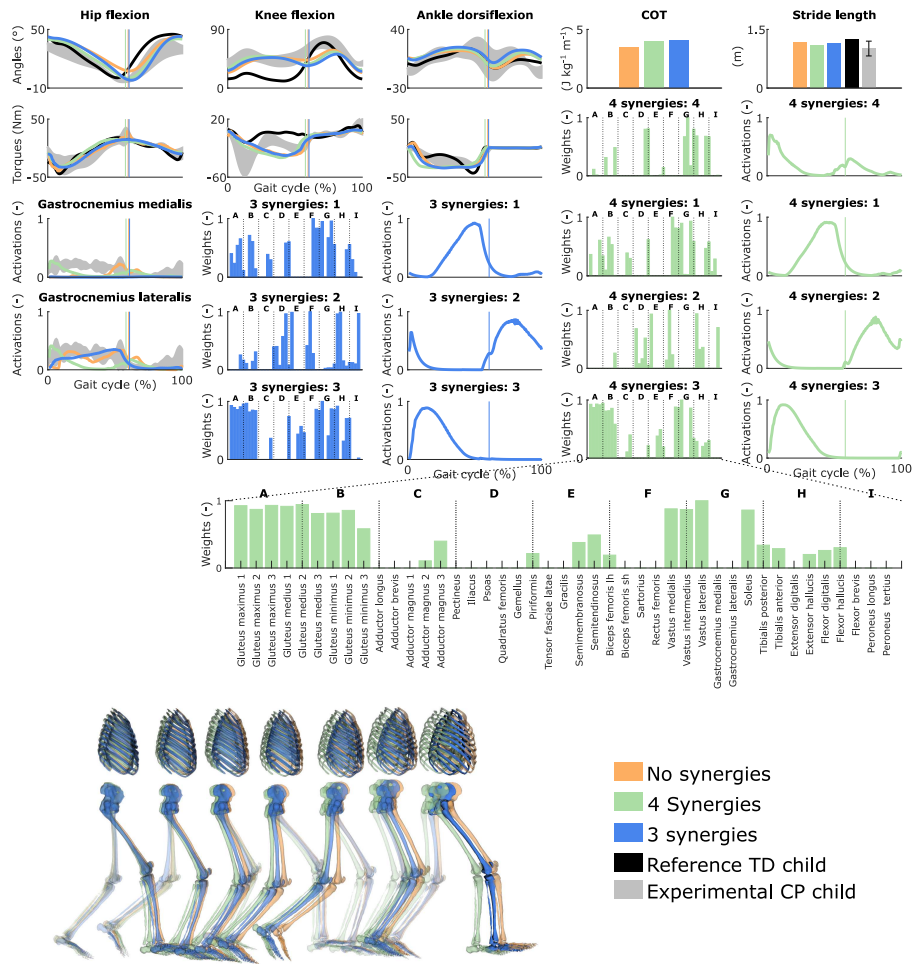


Figure 7.4: Influence of the synergies on walking gaits predicted with the personalized muscle-tendon parameters. Variables from the right leg are shown over a complete gait cycle; left leg variables are shown in Figure D.3 in Appendix D. Vertical lines (solid) indicate the transition from stance to swing. Panels of synergy weights are divided into sections (A-I) to relate bars to muscle names provided in the bottom bar plot, which is an expanded version of the plot of weights with title 4 synergies: 3. Lh and sh are for long and short head, respectively. Weights were normalized to one. Experimental data is shown as mean \pm two standard deviations. Experimental EMG data was normalized to peak activations. Gait snapshots cover a gait cycle starting at right heel strike; left leg segments are more transparent.

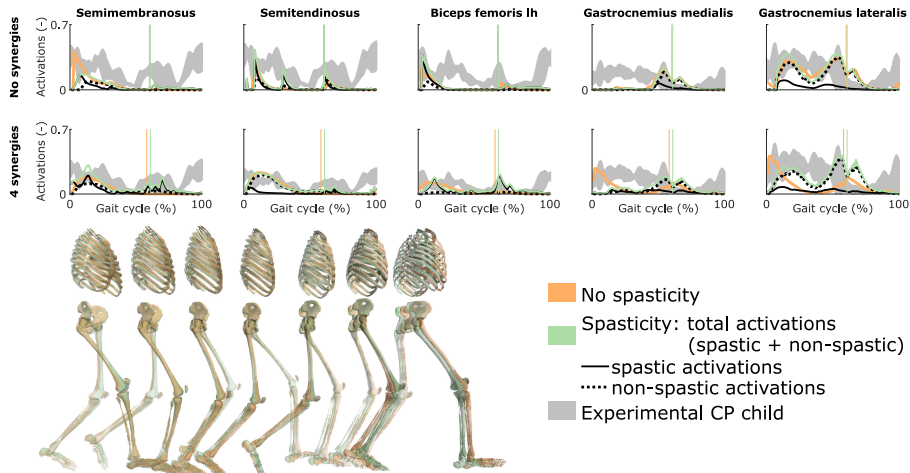


Figure 7.5: Influence of spasticity on the predicted muscle activity. Activations from right leg muscles only are shown over a complete gait cycle; left leg activations are shown in Figure D.4 in Appendix D. When accounting for spasticity, total activations (green) combine spastic (solid black) and non-spastic (dotted black) activations. Vertical lines indicate the transition from stance to swing. Experimental data is shown as mean \pm two standard deviations. Experimental EMG data was normalized to peak activations. Lh is for long head. Gait snapshots cover a gait cycle starting at right heel strike; left leg segments are more transparent; the snapshots are for the case with no synergies.

this child. The contribution of the muscle fatigue term increased by 29%, in part driven by higher activations of the glutei. The contribution of the joint acceleration, metabolic energy rate, and passive joint torque terms increased by 15%, 15%, and 36%, respectively, when walking upright. Similarly, passive muscle forces increased when walking upright for the iliacus and psoas (hip flexors), and biceps femoris short head (knee flexor). Knee flexion increased when adding synergies but did not reach the angle that was experimentally measured in the child (Figure D.6 in Appendix D). Nevertheless, this suggests that reduced neuromuscular control complexity may contribute to crouch gait. The gastrocnemius lateralis and soleus (ankle plantarflexors) were also activated earlier during stance with synergies. Imposing synergies increased the COT (4.12 and $4.05 \text{ J kg}^{-1}\text{m}^{-1}$ with four and three synergies, respectively).

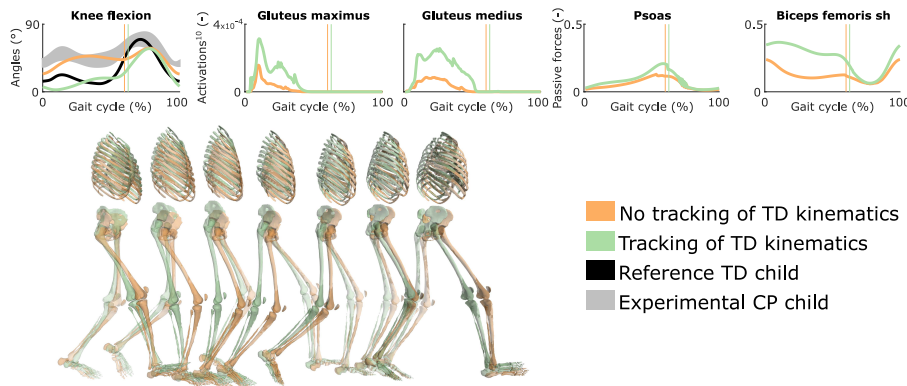


Figure 7.6: Influence of tracking the TD kinematics on predicted walking gaits. Variables from the right leg are shown over a complete gait cycle; left leg variables are shown in Figure D.5 in Appendix D. Vertical lines indicate the transition from stance to swing. Experimental data is shown as mean \pm two standard deviations. Muscle fatigue is modeled by activations at the tenth power. Passive muscle forces are normalized by maximal isometric muscle forces. Sh is for short head. Gait snapshots cover a gait cycle starting at right heel strike; left leg segments are more transparent. The influence of synergies on predicted walking gaits is depicted in Figure D.6 in Appendix D.

Discussion

We demonstrated the ability of predictive simulations to explore the differential effects of musculoskeletal and motor control impairments on the gait pattern of a child with CP. In this specific case, aberrant musculoskeletal geometries combined with altered muscle-tendon properties explained the key gait deviation of the child, namely the crouch gait pattern. Accounting for aberrant geometries alone (i.e., MRI-based model with generic muscle-tendon parameters) did not result in a crouch gait pattern. Despite altered muscle-tendon properties and aberrant geometries, the model could still adopt a more upright gait pattern (TD kinematics tracking). Yet such pattern was less optimal as it induced higher muscle fatigue compared to the crouch gait pattern. These simulations thus suggest that adopting an upright gait pattern for this child might produce an early onset of fatigue, which might explain in part why the child walks in crouch. Importantly, not only fatigue, but also joint accelerations, passive joint torques, and metabolic energy rates increased with an upright gait pattern, likely contributing to the selection of a crouch gait pattern.

Decreasing the neuromuscular control complexity through a reduced number of synergies had a lower effect on the simulated gait patterns than muscular deficits as evaluated when comparing simulated gait patterns obtained with personalized and generic muscle-tendon parameters. Nevertheless, the synergies resulted in increased knee flexion in several simulations, indicating that impaired selective motor control may contribute to gait deficits as suggested in prior simulation studies [103]. In this study, we imposed the number of synergies but not the synergy structure (synergy weights and activations were optimization variables and not informed by experimental data). We thus explored the effect of reducing the neuromuscular control complexity but not the impact of imposing the child's experimental synergies. We expect this impact to be limited for this child since he had a good selectivity. Nevertheless, further work should consider such investigation.

Our predictive simulations generated both movement patterns and the underlying synergies. Only imposing the number of synergies resulted in synergies that presented common features with those reported in the literature, such as one synergy activated during early stance and composed by the glutei and vasti, and one synergy activated during late stance consisting of the glutei, ankle plantarflexors, and iliacus [60]. This suggests that synergy structures might emerge from mechanical constraints and performance optimization during walking. Future research should explore this hypothesis based on a larger population.

Decreasing the number of synergies resulted in a larger COT, as may be expected with a higher level of co-activations. This finding has been hypothesized in previous studies [235, 103] but not tested explicitly. It is indeed difficult to dissociate the influence of the neuromuscular control complexity on the COT through experiments or based on measured data, since many other factors (e.g., spasticity [236] and weakness [70]) might also play a role. Overall, our predictive simulations allow exploring the effects of isolated impairments on gait energetics, which was not possible through analyses based on measured data.

Spasticity had a minor influence on the predicted gait kinematics, suggesting a low impact of spasticity on gait performance for this child. This hypothesis is in agreement with several studies reporting a lack of correlation between spasticity as diagnosed during passive movements and determinants of gait [161, 162, 163]. However, it would be premature to draw such conclusion based on this single case study. First, spasticity was only taken into account for the medial hamstrings and gastrocnemii, whereas the rectus femoris and several hip flexors and adductors were also reported to be spastic (Table 7.1). Including

these other muscles may have an influence on walking performance. Second, experimental data from the spasticity assessment was only collected for the right leg, whereas bilateral spasticity was reported (Table 7.1). We optimized the feedback parameters using that data but used the resulting parameters for both legs, which might affect our predictions. Third, we used feedback parameters optimized from passive stretches to predict spasticity (i.e., reflex activity) during gait, assuming no reflex modulation. This assumption is in line with the decreased reflex modulation reported for patients with spasticity [176, 175, 174, 95]. Yet further research is needed to ensure that the same model is valid in passive and active conditions. Note that the current model does not distinguish between concentric and eccentric contractions, whereas spasticity is presumably only manifest upon muscle stretch. Finally, the optimized feedback gains depend on EMG that was normalized using scale factors optimized during the muscle-tendon parameter estimation. However, these factors may not truly reflect the magnitude of the spastic responses, which may result in an under- or over-estimation of the predicted spastic activity during gait. In previous work [232], we showed that predicted spastic responses of the gastrocnemii were in agreement with large EMG signals observed in early stance in subjects landing on their toes. In this study, the child had a flat foot landing and we did not observe such EMG rise, therefore suggesting that the effect of spasticity of the gastrocnemii during gait might be limited for this child. Interestingly, our model captured this phenomenon as it did not predict large spastic activity in early stance.

Our analysis suggests that muscle-tendon properties rather than selective motor control and spasticity should be the target of interventions aiming to restore an upright posture for this child. This suggestion is in line with the surgical report and one-year post-operative gait analysis. Specifically, the child underwent SEMLS consisting of bilateral rectus femoris transfer, distal femur extension and derotation osteotomy, tibia derotation, and patella distalization that successfully addressed the knee extension deficits and restored the upright gait pattern. The intervention also included bilateral BTX injections in the psoas (hip flexor) and gracilis (hip flexor, adductor, and knee flexor) to reduce spasticity. However, BTX injections are unlikely to have had an effect one year post-treatment [3], suggesting a limited contribution of reduced psoas and gracilis spasticity on restored knee extension. Note that our study did not investigate the sensitivity of the predicted walking patterns to bone misalignment as we considered the same aberrant geometries for all analyses. Studying the effect of bone deformities on the gait pattern should be considered in future work.

Our simulations with personalized muscle-tendon parameters captured salient

features of the child's walking pattern. Nevertheless, they deviated from measured data in different ways. In particular, our model did not adopt the observed flat foot landing. Such pattern might have different underlying roots. On the one hand, it might be an ankle strategy to add functional limb length and compensate for the knee extension deficits. Our simulations did not predict such compensation strategy but also lacked knee flexion in early stance as compared to measured data (Figure 7.2). Increased knee flexion might strengthen the need for ankle compensation, causing the model to adopt a flat foot landing. On the other hand, it might be due to contracture of the plantarflexors [237, 238] although this hypothesis is less likely for this child who had a normal ROM in terms of plantarflexion.

Other factors might have contributed to the deviations between predicted and measured movements. First, the musculoskeletal model had generic rather than subject-specific (i.e., MRI-based) geometries for feet and tibias. Since the child later underwent a surgery that included bilateral tibia derotation, these generic geometries might have contributed to the gait deviations. Second, the clinical examination indicated that the child's trunk was leaning forward. This is likely a compensation strategy, since no fixed lordosis was reported. However, our model had a very simple trunk representation (i.e., one joint with three DOFs), limiting the emergence of compensation strategies. How to model the trunk to capture such compensations remains an open question. Third, our control strategy likely did not capture all complex control mechanisms that might be at play during gait. For instance, we did not consider in our cost function criteria such as head stability [226] and pain that might contribute to gait control. Further, we designed our cost function based on previous work with a healthy adult but the same performance criterion might not hold for children with CP. Nevertheless, our cost function predicted, as expected, a crouch gait pattern with personalized parameters and a more upright gait pattern with generic parameters, suggesting that it captured at least part of the child's control strategy. Finally, the personalized muscle-tendon parameters might not accurately capture the effect of the child's altered muscle-tendon properties. In previous work [168], we underlined the importance of incorporating experimental data from multiple functional movements when calibrating muscle-tendon parameters in order to obtain valid parameter estimates (i.e., representative of the subject). In this study, the available experimental data was limited to walking trials and passive stretches from one leg. Hence, it is likely that some parameters were calibrated to fit the experimental data but did not truly reflect the force-generating capacities of the child. When used in conditions different from the experiments, these parameters may hence result in non-representative force predictions. A challenge for upcoming research will be the design of experimental protocols to collect experimental data that contains sufficient information for providing valid muscle-

tendon parameter estimates while accounting for physiological limitations of impaired individuals and practical limitations of clinical contexts. It is also worth noting that our parameter estimation procedure only adjusted optimal fiber lengths and tendon slack lengths, whereas other parameters may need to be personalized, such as maximal isometric muscle forces, tendon compliance, or maximal muscle contraction velocities. The muscle force-length-velocity relationships might also be altered in children with CP due to their longer sarcomere lengths. Overall, further tuning of the neuro-musculoskeletal model and validation of the simulation framework outcome with a large population are necessary for augmenting the representativeness of the simulations.

Conclusion

This study suggests that predictive simulations are able to identify the main treatment targets for specific patients. In particular, our results showed that, in the presence of aberrant musculoskeletal geometries, altered muscle-tendon properties rather than reduced neuromuscular control complexity and spasticity were the primary driver of the impaired crouch gait pattern observed for the child with CP of this study. Based on this observation, we would recommend altered muscle-tendon properties to be the primary target of clinical interventions aiming to restore a more upright posture, which is in line with the surgical report and one-year post-operative gait analysis. Validation of our simulation workflow through analysis of many more cases is, however, necessary to build confidence in the simulation outcomes. Overall, these results open the door for predicting the functional outcome of treatments on walking performance by allowing *in silico* assessment of the effect of changes in the neuro-musculoskeletal system on the gait pattern.

Acknowledgments

This work was supported by the IWT-TBM grant SimCP (140184). AF also received a PhD grant (1S35416N) from the Research Foundation Flanders (FWO). HK received a H2020-MSCA individual fellowship (796120). LBO received a postdoctoral grant (12R4215N) from the Research Foundation Flanders (FWO) and a grant (016.186.144) from the Netherlands Organisation for Scientific Research (NWO).

Data availability

The data and scripts required for reproducing the results are available at <https://simtk.org/projects/predictcpgait>. The movies are available upon request.

Chapter 8

General discussion

Overall, this dissertation contributed to the development of a framework for personalized musculoskeletal modeling and predictive simulation that allows studying human movement in healthy and pathological population such as in children with CP.

The central hypothesis of this work was that predictive simulations can be exploited to explore the differential effects of motor control and mechanical deficits on the walking abilities of children with CP. We formulated three objectives to investigate this hypothesis. The first objective was to develop methods and models to characterize the mechanical (study 1) and motor control (study 2) deficits of children with CP. The second objective was to develop methods to generate computationally efficient predictive simulations of movement (study 3). The third objective was to exploit predictive simulations to i) evaluate candidate walking control strategies in healthy and impaired individuals (study 4) and ii) explore the differential effects of motor control and mechanical deficits on the walking pattern of a child with CP (study 5).

The general discussion consists of three parts. First, we summarize the different studies and present their specific conclusions. Second, we discuss their conclusions from a more general perspective. Finally, we discuss their limitations and provide avenues for future research.

Specific conclusions

Objective 1: Develop methods and models to characterize the mechanical and motor control deficits of children with CP.

The parameters of the Hill-type muscle-tendon model describe the force generating capacities of the muscle-tendon unit. Subject-specific parameters allow reflecting the effect of altered muscle-tendon properties and are important for accurate simulations. Methods have been developed to provide such subject-specific estimates but were mostly based either on scaling from anthropometric dimensions, which is not appropriate for children with CP, or either on computationally expensive numerical tools, which limits a broad applicability. In study 1, we developed a computationally efficient approach to provide subject-specific estimates of optimal fiber lengths and tendon slack lengths based on experimental torque-angle relationships from functional movements. In addition, we investigated which functional movements contained the data necessary to obtain valid (i.e., representative) estimates of parameters for the knee actuators of healthy adults.

Hypothesis study 1: A computationally efficient approach based on optimal control can identify subject-specific muscle-tendon parameters that improve the accuracy of movement simulations as compared to generic (i.e., linearly-scaled from anthropometric dimensions) parameters.

We first collected experimental data from eight healthy adults during six functional movements: gait, squat, stair ascent and descent, sit-to-stand-to-sit, and squat jump. We then developed an optimal control formulation to identify subject-specific muscle-tendon parameters that minimized the difference between joint torques generated from EMG-driven musculoskeletal models and joint torques calculated from inverse dynamics. Finally, we evaluated the ability of knee actuator parameters estimated based on a set of calibration movements to predict knee joint torques of movements not included in the estimation phase (i.e., validation movements). We performed this evaluation for all possible sets of calibration movements to identify which sets contained sufficient information for a valid parameter estimation.

Our results confirmed our hypothesis: subject-specific muscle-tendon parameters improved the accuracy of knee joint torque simulations over generic parameters, thereby underlining the importance of subject-specific parameters for accurate simulations. Our estimations showed that subject-specific parameters differed

more from their generic counterpart for the knee flexors than for the knee extensors, suggesting that subject-specific estimation of knee flexor parameters should be prioritized. The optimal control formulation we proposed was computationally more efficient than existing methods in the literature. This computational benefit likely results from the use of efficient numerical tools including direct collocation, implicit differential equations, and algorithmic differentiation. These tools are typically more efficient than algorithms such as simulated annealing previously used for similar purposes [108]. Our identifiability study showed that only a few sets of calibration movements contained the information required to estimate parameters needed to generate accurate simulations for validation movements, underlining the importance of an appropriate selection of experimental data to obtain valid muscle-tendon parameters. Specifically, for estimating parameters of the knee actuators in healthy adults, information from gait and sit-to-stand-to-sit was essential among the tested movements.

Spasticity is a common neural impairment in children with CP that is characterized by exaggerated muscle reflex activity in response to muscle spindle firing. Spindle proprioceptive receptors are widely thought to encode information about muscle length and velocity changes [97, 98], which supports modeling spasticity based on feedback from muscle length and velocity [100]. Nevertheless, recent experimental findings suggest that spindle firing might be more directly related to muscle force and force rate rather than to muscle length and velocity [99]. In study 2, we developed and evaluated three models of spasticity based on delayed feedback from sensory information. The first model relied on feedback from muscle length and velocity, the second model relied on feedback from muscle length, velocity, and acceleration, and the third model relied on feedback from muscle force and force rate.

Hypothesis study 2: A spasticity model based on feedback from muscle force and force rate better explains the spastic response of hamstrings and gastrocnemii during passive stretches and gait than models based on feedback from muscle length, velocity, and acceleration.

We first collected data from six children with CP during instrumented spasticity assessments of the hamstrings and gastrocnemii. These assessments consist in passively stretching the muscles at different velocities while collecting biomechanical information such as joint kinematics, torques, and EMG. We then developed an optimal control formulation to identify subject-specific feedback gains that minimized the difference between feedback muscle activity and EMG measured during the passive stretches. We performed this optimization for

the three spasticity models separately. Finally, we applied gait data to the calibrated models to predict spastic contributions during gait and we compared our predictions to EMG.

As hypothesized, a spasticity model combining delayed feedback from muscle force and force rate better explained the response of spastic hamstrings and gastrocnemii during passive stretches than models based on delayed feedback from muscle length, velocity, and acceleration. In addition, the force-based model predicted muscle activity during gait that was in agreement with hamstrings and gastrocnemii EMG. Specifically, the force-based model predicted the abnormal peak in gastrocnemii activity observed in early stance in the subset of children who landed on their forefoot instead of on their heel. Our results hence suggest that force encoding in muscle spindles in combination with altered feedback parameters underlie spastic activation of muscles during passive stretches and gait. This suggestion corroborates the conclusions of a recent experimental study showing that spindle firing, measured *in vivo* during passive muscle stretches, is uniquely related to muscle force and force rate but not to muscle length and velocity [99]. This observation is in line with older *in vitro* studies that related peaks in muscle spindle firing rates to muscle force transients at stretch onset [159, 160]. Fiber length and velocity are related to muscle force through the muscle force-length-velocity properties but this relationship is nonlinear. Hence, muscle length and velocity offer a good proxy for muscle force and force rate to describe the exaggerated reflex activity under conditions where this nonlinearity is limited (e.g., on the ascending limb of the force-length relationship and the most linear parts of the force-velocity relationship) but not in all conditions.

Modeling spasticity based on muscle force and force rate allowed us to directly relate measures of spasticity in passive muscles to muscle activity during gait, suggesting that spasticity plays a role in impeding gait performance in spastic CP. Yet this hypothesis is still a matter of debate in the literature (see [95] for a review) and should be confirmed. For instance, incorporating the force-based spasticity model in predictive gait simulations may allow us to shed further light upon the role of spasticity during gait (study 5). Overall, the proposed force-based model has the potential to contribute to our understanding of movement impairments due to spasticity.

Objective 2: Develop methods to generate computationally efficient predictive simulations of movement.

Predictive simulations of human movement can be formulated as optimal control problems that minimize an objective function subject to constraints describing the musculoskeletal dynamics. Yet these problems are challenging to solve because of the stiffness and nonlinearity of the equations describing muscle and skeleton dynamics. Further, combining predictive simulations with complex musculoskeletal models results in large and computationally expensive problems. In study 3, we developed a computationally efficient framework to generate predictive simulations of human movement with complex 3D musculoskeletal models. Key to this efficiency is the use of advanced numerical methods including direct collocation, implicit differential equations, and algorithmic differentiation. Specifically, as part of study 3, we evaluated the benefits of using algorithmic differentiation instead of finite differences to compute derivatives when performing optimal control simulations of walking.

Hypothesis study 3: Algorithmic differentiation improves the computational efficiency of optimal control simulations of movement as compared to finite differences.

We first enabled the use of algorithmic differentiation in OpenSim, the software for modeling and simulation used in this dissertation [112]. Then, we developed an interface between OpenSim and CasADi, a tool for nonlinear optimization and algorithmic differentiation [56]. Finally, through this interface, we generated optimal control predictive and tracking simulations of walking using both algorithmic differentiation and finite differences.

As hypothesized, algorithmic differentiation drastically improved the computational efficiency of optimal control simulations as compared to finite differences. We showed that this computational benefit primarily results from the ability of algorithmic differentiation to evaluate function derivatives through its reverse mode. This mode or algorithm is beneficial when a function has many more inputs than outputs as the number of function evaluations required to evaluate the function derivatives is then proportional to the number of outputs. The objective function has many inputs but only one output. Computing its gradient, as required during the optimization, is thus performed in only one reverse sweep using algorithmic differentiation. By contrast, finite differences require many more function evaluations as they need to evaluate the sensitivity of the objective function to all its inputs to compute its gradient.

Algorithmic differentiation has been underused in biomechanics, likely since widely used software such as OpenSim did not leverage tools for algorithmic differentiation. In this study, we filled this gap and provided tools that should be beneficial for the biomechanics community. Overall, the combination of algorithmic differentiation with other efficient numerical tools such as direct collocation and implicit differential equations allows overcoming the computational roadblocks that have long limited the use of optimal control simulations for biomechanical applications.

Objective 3: Exploit predictive simulations to i) evaluate candidate walking control strategies in healthy and impaired individuals and ii) explore the differential effects of motor control and mechanical deficits on the walking pattern of a child with CP.

Under the assumption of optimal performance during human movement, the performance criterion determines the control strategy of the motor task. Yet it remains unclear what such criterion would be for human gait. Experimental studies [18, 19] suggested that energy considerations underlie gait selection, which has driven simulation studies to use energy-based criteria in predictive simulations [35, 33, 34, 36, 25]. However, other studies also proposed criteria centered on muscle activity, used as surrogates for muscle effort and fatigue, for gait control [39, 41, 40]. Human locomotion might also be governed by multiple performance criteria [41, 208] but the effect of combining different criteria in the cost function on the predicted gait pattern has not been widely explored with complex 3D models, likely due to the associated computational costs.

It is also unclear whether a single task-level performance criterion can explain the range of gaits adopted by healthy and impaired individuals in different contexts (e.g., healthy and amputee walking). This knowledge is, nevertheless, important in the perspective of optimal treatment design as it would inform whether similar performance criteria can be used for predicting the effect of treatments on walking performance and for predicting healthy human walking. Findings from experimental studies [218] and simulation studies with simple models [33] suggest that similar control strategies govern human locomotion.

In study 4, we exploited the computational efficiency of our predictive simulations with complex 3D musculoskeletal models to identify a performance

criterion that could accurately produce healthy human walking. We then evaluated whether the identified criterion could predict the mechanics and energetics of a broad range of gaits encountered in diverse conditions, such as gaits at different speeds, with muscle strength deficits, and with a lower leg prosthesis.

Hypothesis study 4: A broad range of healthy and pathological human gaits can emerge from optimizing the same control strategy.

We found that a performance criterion based on metabolic energy rate, muscle activity, and joint accelerations produced a human-like walking gait. Omitting any of these terms resulted in less physiologically-realistic patterns characterized by kinematic or muscular compensation non-observed experimentally, thereby supporting the hypothesis that the high-level control strategy, modeled through the performance criterion, driving human gait should include multiple optimality criteria [208]. Minimizing metabolic energy rate is commonly used in predictive simulation studies [35, 33, 34, 36]. Nevertheless, unless combined with a criterion based on muscle activity, the predicted muscle activations were unrealistically high. Minimizing squared muscle activity might be important for minimizing signal-dependent motor noise [219, 220] and has also been suggested to underlie human locomotion based on results generated with 2D models [39, 41, 40]. Yet minimizing squared muscle activity alone produced unrealistic patterns in the frontal plane, which suggests that observations from simulations based on 2D models might not hold for simulations based on 3D models. We found that the joint acceleration term was important for convergence of the optimization algorithm. Whether this term is part of the human gait control strategy remains, nonetheless, an open question. It is worth mentioning that other criteria might contribute to human gait control but have not been considered in this study (e.g., head stability [226]). Further, different criteria or constraints might apply under different contexts (e.g., pain or mood) and explain some of the observed gait variability [239].

Our results confirmed our hypothesis as we showed that a variety of healthy and pathological gaits emerged from optimizing the same control strategy, providing support for observations based on experimental protocols [218] and simple models with few DOFs and without muscles that did not account for the large redundancy in the musculoskeletal system [33]. To our knowledge, no studies had yet tested such hypothesis with complex 3D musculoskeletal models. This is an important finding as it suggests that our simulation framework and neuromusculoskeletal model are generalizable enough for use in different contexts such as to study healthy and pathological gait, which is a first step towards their

use for clinical applications. Interestingly, our simulations captured the salient features of human gaits while based on a simple control strategy that neglected known control mechanisms such as spinal reflexes. We hypothesized that a possible reason for such simple controller to provide human-like gait is that not only the control strategy but also, and possibly in large part, the musculoskeletal mechanics may dictate the preferred human gaits. This hypothesis is in line with observations based on passive-dynamics-based robots suggesting that natural dynamics may largely govern locomotion [228]. We expect spinal reflexes to be particularly important for robustness against uncertainties (e.g., motor noise or unstable terrains), which have been neglected in this work.

Before using model-based simulations for optimal treatment design, the ability of such simulations to identify the main treatment targets in specific patients needs to be demonstrated. In study 5, we tested this ability by generating predictive simulations for a child with CP and by comparing the simulation outcomes with the child's clinical examination and treatment reports. We explored the contribution of altered muscle-tendon properties, reduced neuromuscular control complexity, and spasticity to the impaired child's walking pattern while using a MRI-based musculoskeletal model. Since the child's clinical analysis reported a crouch gait pattern, we expected our predictive simulations to produce such pattern when incorporating the subject's impairments into the neuro-musculoskeletal model. Furthermore, the child's clinical examination reported close to normal range of motion at the hip and ankle but bilateral knee extension deficits, bilateral spasticity, and good muscle strength and selective control. Hence, we expected altered muscle-tendon properties and spasticity rather than reduced neuromuscular control complexity to be the main drivers of the crouch gait pattern.

Hypothesis study 5: Accounting for altered muscle-tendon properties and spasticity produces a crouch gait pattern resembling the observed pattern of the child.

We characterized the subject's altered muscle-tendon properties by personalizing the Hill-type muscle-tendon parameters following an approach based on study 1. We modeled spasticity through delayed muscle activity feedback from muscle force and force rate as described in study 2, and represented reduced neuromuscular control complexity through muscle synergies. We generated predictive simulations using the framework developed in study 3 and used a control strategy inspired from the one identified in study 4.

Our simulations showed that, in the presence of aberrant geometries, altered muscle-tendon properties were the primary driver of the crouch gait pattern observed for this child, which is in line with the surgical report and one-year post-operative gait analysis. Specifically, the simulations, relying on a MRI-based musculoskeletal model, predicted a crouch gait pattern with personalized parameters but a more upright, unimpaired-like pattern with generic parameters. Reducing the complexity of the neuromuscular control had a smaller influence on walking performance than using personalized parameters and did not produce a crouch pattern when combined with generic parameters. This suggests that a reduced neuromuscular control complexity is not driving the child to walk in crouch, as was expected from the clinical examination that reported good muscle selectivity. In contrast with our hypothesis, our simulations suggested that spasticity of the hamstrings and gastrocnemii, as assessed during passive stretches, had almost no influence on walking performance. This observation is in line with a series of studies reporting a lack of correlation between spasticity as diagnosed during passive motions and determinants of gait [161, 162, 163]. Yet it would be premature to draw conclusions based on the analysis of a single case. On the one hand, spasticity might have little effect for that subject but a larger influence for other individuals. On the other hand, we limited our analysis to two spastic muscle groups (medial hamstrings and gastrocnemii) for which we had data, whereas other muscles (rectus femoris and several hip flexors and adductors) were reported to be spastic. Further, our spasticity model calibrated based on passive measurements might be inaccurate for gait but also prone to calibration errors due to measurement and data processing inaccuracies (e.g., EMG processing). Expanding this analysis to a larger population may provide more insight into the impact of spasticity on walking performance.

Overall, we showed that our simulation framework and model were suitable to identify the main treatment targets for a specific child with CP. Indeed, the framework generated an impaired gait pattern resembling the child's experimental data when incorporating the child's impairments into the neuromusculoskeletal model and allowed identifying which impairments had the most influence on gait performance. Validation of these results is, nevertheless, necessary before using our simulation framework and model in clinical practice (see section about future work).

General discussion and conclusions

Efficient computational methods allow exploring the neuro-mechanics of human movement in diverse contexts.

In the studies of this dissertation, we used advanced computational methods to solve a series of optimal control problems applied to the neuro-mechanical system. Some of these problems had already been investigated, to some extent, in the literature. For instance, previous research had developed methods to estimate subject-specific muscle-tendon parameters [90, 91], to model spasticity [100], or to generate predictive simulations of movement [35, 39, 43, 36, 25, 37]. However, our use of efficient computational methods allowed us to expand this research to more complex models, describing the neuro-mechanical structures of the human body with more details, and to a broader spectrum of conditions. For example, in study 4, we showed that the computational time required to generate predictive simulations of walking was about 20 times faster with our framework than in published work although we used a musculoskeletal model at least as complex. This allowed us to explore a variety of conditions such as gaits at different speeds, with strength deficits, with a lower leg prosthesis, and, in study 5, with impairments characteristic of children with CP.

The efficient computational methods we used mainly consisted of direct collocation methods, implicit formulations of the muscle and skeleton dynamics, and algorithmic differentiation. These methods have been previously applied to biomechanical problems [52, 39, 55, 44, 53, 54, 46, 37] but, to the best of our knowledge, they have never been used together for optimal control predictive simulations. The unique feature of our simulation framework is thus this combination of efficient tools that allowed the generation of rapid simulations. Importantly, the modeling flexibility of our framework allowed us to exploit these efficient simulations for various purposes. For example, we used our framework to study gait in healthy individuals, in children with CP by incorporating features such as spasticity and synergies, and in amputees by replacing part of the leg with a passive transtibial prosthesis. This demonstrates the suitability and versatility of our approach to multiple scenarios. Finally, although our studies were limited to studying human locomotion, we envision numerous other applications for our simulation framework such as supporting the design of assistive devices, simulating gaits of extant and extinct species, or optimizing performance in sports by designing equipment and training programs.

Predictive simulations with complex 3D musculoskeletal models provide insight into gait control in healthy individuals and children with CP.

Predictive simulations provide an elegant approach to decipher the neuro-mechanical principles underlying human locomotion. Specifically, as opposed to inverse and tracking simulations that rely on measured data, predictive simulations account for the complex interactions between neural and mechanical systems by generating novel movements. Hence, studies based on predictive simulations allow bridging the gap between inverse biomechanical studies that ignore the neural control of the musculoskeletal system and motor control studies that neglect the inherent contribution of the musculoskeletal mechanics to the control of movement. In this dissertation, we illustrated the importance of taking both neural and mechanical systems into account. On the one hand, we highlighted the impact of the neural system by describing how the use of different cost functions affected the resultant gait patterns. On the other hand, we demonstrated the influence of the musculoskeletal system by showing how altering muscle-tendon properties produced different simulations.

Our predictive simulations supported the hypothesis that gait is governed by multiple performance criteria [208] and that those criteria are consistent across gait conditions. This finding motivated us to apply a performance criterion identified for a healthy adult (study 4) to a child with CP (study 5). This is a strong assumption that should be validated. However, the gait pattern predicted for the child with CP, when accounting for personalized muscle-tendon parameters, resembled the crouch gait pattern experimentally observed, providing support for our assumption. How to validate the identified multi-objective cost function, consisting of terms including metabolic energy rate, muscle activity, and joint accelerations, remains an open question that should ideally be addressed through experiments. For example, Selinger *et al.* [19] tested the hypothesis of minimal metabolic energy expenditure during gait by using exoskeletons to shift the subjects' energetically optimal gait patterns to abnormal gaits. They showed that the subjects adapted their gait patterns to converge to these new energetic optima, providing support for control strategies based on minimal energy expenditure. Importantly, our predictive studies were exploratory in nature and we did not aim to identify a strategy unifying gait control in healthy individuals and children with CP. It is possible that alternative cost functions containing criteria proposed in literature but not considered in our studies (e.g., head stability [226] and angular momentum regulation [227]) will result in equally or more realistic gaits.

Our simulations emphasized the importance of using 3D rather than 2D musculoskeletal models for studying the neuro-mechanics of human gait. The use of 3D models increases the computational complexity but we found that altered neuro-musculoskeletal features may have an effect on the frontal plane. For example, we showed in study 4 that hip muscle strength deficits led the model to use hip circumduction to compensate for its weakness, a compensation strategy in the frontal place. We also found that a cost function minimizing only squared muscle activity produced exaggerated trunk sway and step width. Such finding would not be possible with 2D simulations, which may thus mislead the conclusions. We therefore recommend the use of 3D musculoskeletal models in neuro-mechanical analyses of human gait, certainly in clinical contexts, since 2D models may not account for important control mechanisms.

Our studies assumed optimal human performance, which allowed us to formulate predictive simulations of movement as optimal control problems. While this assumption is common in the field [39, 41, 47, 48, 51], it does not rule out the existence of other control mechanisms that have been neglected in our work. Geyer and Song have demonstrated through multiple studies the ability of a neuromuscular controller primarily based on spinal reflexes to generate human-like locomotion. Specifically, they showed that this controller was able to produce diverse 2D and 3D human locomotion behaviors [24, 25], was robust against a series of gait perturbations [50], and was suitable to investigate the effects of aging on walking performance [40]. Beyond simulation, versions of this neuromuscular controller have also been successful for the control of prostheses [240, 241] and exoskeletons [242]. These results suggest that motor control may, at least in part, be encoded in muscle-reflex-based neural circuits for some muscles. Despite the absence of such reflexes in the control scheme, our simulations captured the salient features of gait. A possible explanation is that our cost function captured the result of distributed pathways within the central nervous system without explicitly describing these pathways. In other words, spinal reflexes might also be tuned to optimize human performance [25, 40]. As briefly introduced above, we anticipate reflexes to be particularly important in noisy environments due to their intrinsic abilities to reject disturbances, which can have both internal (e.g., motor noise) and external (e.g., unstable terrain) sources. Accounting for such disturbances might underline the need for incorporating reflexes in the control scheme and, therefore, emphasize the limitations of a control strategy based on pure optimal performance.

Another hypothesis of control is centered around the role of CPGs in the neural circuitry responsible for human locomotion [243]. CPGs provide feedforward inputs to drive the model forward but neglect interactions with the environment,

which contrasts with a theory based on spinal reflexes that primarily relies on interactions with the environment to drive the model forward [25]. Although widely accepted for controlling locomotion in vertebrates, the existence of CPGs for locomotion in humans remains unclear (see [16] for a review). An interesting control model framed by Dzeladini *et al.* [26] is the use of CPGs as a feedforward component of a muscle-reflex-based controller. The proposed model was inspired from the work of Kuo [244] who suggested to view CPGs as observers of feedback control rather than unique generators of commands. Dzeladini *et al.* [26] showed that such combined model was able to modulate gait speed while preserving the robustness to perturbation characteristic of muscle reflexes. Although this dissertation was framed on the hypothesis of optimal performance only, the aforementioned control models could be incorporated within our simulation framework. For instance, we could integrate spinal reflexes as part of the control mechanisms in the same way as we incorporated spasticity, since we modeled spasticity based on feedback from muscle states or in other words based on muscle reflexes. Similarly, we could integrate CPGs within the neuro-musculoskeletal model.

Combining personalized modeling with predictive simulation provides a unique approach to study the effect of neuro-musculoskeletal features on locomotion.

In this dissertation, we have developed methods and models that let us explore the effects of specific neuro-musculoskeletal features on human gait through (predictive) simulations. In particular, in multiple occasions, our studies investigated how altering parameters of the Hill-type muscle-tendon model affected gait simulations. For example, we showed how subject-specific optimal fiber lengths and tendon slack lengths improved the simulations of knee joint torques in healthy adults over generic parameters, how impaired gait patterns emerged when decreasing the maximal isometric muscle forces of several muscle groups, how the maximal muscle contraction velocities affected the walk-to-run transition speed, or how personalized and generic parameters produced different gait patterns. The ability to dissociate the differential effects of altering these parameters opens new perspectives for modeling impairments and treatments. For example, with our simulation framework, we could explore the effect of strengthening muscles and alleviating contractures by increasing maximal isometric muscle forces and optimal fiber lengths, respectively. On the other hand, these results also underline the sensitivity of gait simulations to the Hill-type muscle-tendon parameters. Reliable simulations thus require representative parameters, which cannot be computed through simple linear scaling based on anthropometric dimensions. In study 1, we proposed a method

to estimate subject-specific parameters that we exploited in studies 2 and 5. Yet we also showed how sensitive the parameter estimation can be to the available experimental data. Specifically, we found in study 1 that utilizing data from diverse but specific functional movements was essential to provide valid estimates of parameters for a set of muscles. In study 5, we did not have data from such diversity of movements and we estimated parameters of many more muscles, which suggests that the optimized parameters might have overfitted the available data. This might result in inaccurate simulations, thereby unreliable for clinical applications. This underlines a real challenge for future work, namely designing experimental protocols that are comprehensive enough to allow for accurate modeling while accounting for the practical limitations inherent in clinical contexts. Ideally, these protocols should include collection of MRI images to represent bony deformities and altered muscle-tendon path trajectories, motion capture data (marker trajectories, EMG, and ground reaction forces) from a variety of functional movements to estimate muscle-tendon parameters, instrumented spasticity assessments to estimate pathological feedback gains, and data from standardized clinical examination protocol such as muscle strength, selectivity, and range of motion. Including data from ultrasound images in the muscle-tendon parameter estimation may result in a more accurate parameter identification. Such comprehensive data collection is practically difficult but likely necessary to guarantee a certain level of confidence in the simulation results.

Not only the musculoskeletal properties but also the neural features are expected to influence human locomotion. In particular, motor control impairments characteristic of children with CP, such as a lack of selective motor control and spasticity, are thought to affect walking performance [103]. Our predictive simulations allowed us to shed some light upon the individual effects of these two impairments on the gait pattern of a child with CP. Such simulations based on MRI-based 3D musculoskeletal models had, to the best of our knowledge, never been performed in published work. We cannot draw strong conclusions based on the single case study included in this work but our study emphasizes the potential of our simulation framework to advance our understanding of how subject-specific musculoskeletal and motor control deficits affect the locomotion of specific patients.

Limitations and future work

In this dissertation, we developed methods and models to improve model-based predictions of walking in children with CP. In addition, we applied these tools to gain insight into gait control and the effect of motor control and mechanical deficits on human locomotion. Our methods, models, and findings are, nonetheless, subject to limitations, thereby requiring future research.

Gradient-based optimization algorithms involve local minima.

The use of gradient-based optimization algorithms such as IPOPT [122] to solve optimal control problems is subject to local minima. In our studies, to increase the likelihood of finding good enough local minima (i.e., local minima that are close to the global minima), we started each optimization problem with multiple initial guesses and selected the solution with the lowest optimal cost. Nevertheless, this only mitigates the risk of reporting solutions that are not good enough local minima. An approach to reduce the risk of local minima is to make the optimal control problems more convex through the use of different optimization variables. For example, in study 1, we used the affine transformation of muscle-tendon parameters proposed by Van Campen *et al.* [89] when estimating optimal fiber lengths and tendon slack lengths. Similar transformations may also be beneficial to improve the convergence of the problems. In study 3, we underlined the poor performance (higher computational time and larger number of iterations to converge to an optimal solution) of using an exact compared to an approximated Hessian of the Lagrangian when generating predictive simulations of walking. We found that this poor performance was due to the magnitude of regularization needed to satisfy the requirements of the optimization algorithm when using an exact Hessian of the Lagrangian. Convexification, for example through variable transformation, of the nonconvex optimal control problems is thus expected to improve performance, as illustrated by De Groote *et al.* [52] for solving the muscle redundancy problem. Future work aiming to improve computational efficiency may consider such convexification of the problems underlying predictive simulations of movement.

Our predictive simulations showed that different human-like gait patterns could be produced when solving the same problem with different initial guesses, suggesting different local minima. This is not surprising, since humans adopt a range of gait patterns depending on the context. For example, it has been shown using experimental protocols with exoskeletons that humans do not always adopt a walking pattern that minimizes energy consumption but prefer such option

when instructed to self-explore diverse patterns [19]. Local optima might hence characterize a model describing human locomotion. A limitation of our studies is that we only selected solutions that had the lowest optimal costs, whereas, in practice, the selection of the solution might be dependent on the context. In other words, local minima might represent a series of compensation strategies and humans might not always select the most efficient strategy. Considering only the solution that corresponds to the lowest cost hence potentially discards valuable information. How to model the context-dependent selection of a specific walking pattern remains, however, an open question.

Multi-objective cost functions involve subjective selections of performance criteria and weight factors.

Across all studies, we used multi-objective cost functions formulated as weighted sums of performance criteria. While the selection of several performance criteria (e.g., metabolic energy rate, muscle activity, and passive joint torques) was supported by physiology and previous studies, the incorporation of others (e.g., joint accelerations) was the result of trial and error. We also used such heuristic to set the relative weightings of the different terms in the cost function. This approach, however, limits the explorable solution space and implies subjective decisions, which may result in inaccurate or incomplete conclusions. Furthermore, it is a time consuming process that restricts the ability to comprehensively explore the role of many performance criteria in the control of human locomotion. Consequently, our search was limited to only several criteria and sets of weight factors. In future work, more advanced or systematic approaches should be considered for identifying relevant performance criteria and for finding the corresponding weightings.

As a proof of concept, we tested an approach based on inverse optimal control that consists in identifying weight factors that reproduce a given reference trajectory (e.g., an experimental walking pattern). This approach preserves the predictive property of the simulations, since no tracking terms are included in the cost function, but allows an optimal tuning of the weights. We demonstrated the suitability of this approach to retrieve weight factors that had been used to generate a reference trajectory with a simple 2D musculoskeletal model. However, our preliminary tests with more complex 3D musculoskeletal models proved to be computationally very expensive. Further research is thus necessary for enabling such upscaling in model complexity. Yet we believe that versions of this approach may result in predictions closer to experimental data and may emphasize the role of certain criteria in gait control.

In study 5, we used a multi-objective cost function whose terms were similar to the ones identified in study 4. However, since we scaled the optimization variables, to ensure that they were in the same order of magnitude [129], based on their bounds and since the bounds differed in between studies, we had to re-identify weight factors in study 5 and did not use the ones from study 4. Hence, this makes difficult a proper comparison of weightings between both studies and does not allow investigating whether the same set of weight factors holds across subjects. In future studies, we recommend using a more generic scaling approach and to ensure that terms in the cost function are dimensionless to enable a meaningful comparison and interpretation of weight factors across studies and subjects.

Modeling choices and assumptions limit representativeness.

As highlighted across our studies, gait simulations are sensitive to a series of features, including muscle-tendon parameters and motor control models. Yet other features may play a role in human locomotion but have not been considered in our models, limiting their representativeness. Among these features are information from sensory systems as well as noise and uncertainties.

The sensory systems consist of the vestibular, visual, and somatosensory systems, which provide information about the state of the musculoskeletal system. Accounting for the effect of these systems may improve the representativeness of our models. For example, previous work integrated head acceleration as part of the multi-objective cost function designed for predictive simulations of walking [49]. They hypothesized that minimizing such term would reflect the desire for stabilization of the vestibular and visual systems during locomotion [245]. In our model, we could limit trunk sway and thus head acceleration by playing with the trade-off between metabolic energy rate and muscle activity but it is likely that minimizing head acceleration might have led to similar results. This illustrates the difficulty to distinguish cause-effect relationships that have a physiological meaning or that are the results of modeling and simulation artifacts. The somatosensory system consists of numerous receptors, such as muscle spindles, Golgi tendon organs, and other mechanoreceptors, that provide the central nervous system with sensory information. This information has been largely ignored in our studies, except for modeling spasticity, although it might be highly important for, among others, balance control [246]. Accounting for sensory information has thus the potential to improve the realism of our simulations. Yet incorporating such features also increases the computational complexity of the models, which might not be desirable. Overall, it is important to find a trade-off between model accuracy and efficiency, a trade-off that

should be based on the research or clinical question. For example, modeling the effect of treatments on patients with sensory deficits (e.g., vestibular loss) may require incorporating vestibular information into the neuro-musculoskeletal model, whereas conceptual models (e.g., spring-mass models [204]) may be sufficient for exploring fundamental principles of gait mechanics.

Our models did not account for any type of uncertainties (e.g., motor noise, sensory noise, unstable terrains), which likely explains some of the consistent deviations we observed between our predictive simulations and measured data. For example, previous predictive studies [39, 51] related the lack of knee flexion during mid-stance, also present in our simulations, to the lack of stability requirements in the model. Integrating uncertainties in the model might therefore induce more stable strategies, which might lead to increased knee flexion during mid-stance. One approach for such integration is through the use of robust optimal control that extends the optimal control framework we used in this dissertation to also consider uncertainties in the dynamics and cost function. Houska *et al.* [230] proposed a robust optimal control formulation that conceptually consists in limiting the propagation of uncertainties modeled through the state co-variance matrix. This formulation has the advantage of being compatible with the computational tools we used for our simulations. Nevertheless, accounting for this state co-variance matrix also drastically increases the problem size, limiting a direct applicability for our already large optimal control problems. Robust optimal control is an area for further research that should be considered for modeling human locomotion.

An interesting approach to generate simulations robust against uncertainties would be to combine robust optimal control with models of the feedback pathways existing in the spinal and supraspinal structures. Such approach would allow us to compute feedback gains that are optimal and robust against uncertainties, while improving the representativeness of the models. As introduced above, applying robust optimal control and relying on increasingly complex models would, nonetheless, likely come at the expense of the computational efficiency.

An alternative to robust optimal control for generating simulations that are robust against uncertainties is (deep) reinforcement learning. Reinforcement learning has been used to compute robust control policies capturing human movement. Typically, in such approach, the control policy is modeled through a neural network that is trained based on reference data. For example, to generate predictive simulations of gait, the neural network could be trained to generate muscle excitations driving the musculoskeletal model to reproduce measured gait

patterns [247]. The training process is, as optimal control, based on optimization methods. Yet reinforcement learning often relies on stochastic optimization methods, whereas optimal control is commonly based on deterministic methods. By considering uncertainties in the system, stochastic methods allow computing robust control policies but, as a side effect, are often computational expensive. Promising work has recently been achieved using deep reinforcement learning for human movement simulation. In particular, Lee *et al.* used such approach to train neural networks, which took between 12 and 36 hours of computational time, that generated predictive simulations of a variety of conditions, such as healthy and pathological gaits, dancing, and jumping, based on a highly complex model actuated by more than 300 muscles [248]. They also demonstrated the potential of their approach for simulating surgery outcome by predicting the impact of different surgeries on the walking pattern. These results suggest that deep reinforcement learning should be considered in future research aiming to predict the functional outcome of treatments on walking performance.

A series of other factors may further contribute to the heterogeneity of human gait, including ligaments, viscous tissues, and tendon compliance, but have been modeled using generic parameters in our studies. Improving the representativeness of the models will require personalizing these parameters in future work. As discussed for the muscle-tendon parameters, such personalization will require collecting experimental data containing sufficient information for valid estimation and extrapolation to new conditions.

Model-based predictions of treatment outcomes require validation.

The methods and models developed across our studies improved model-based predictions of walking in children with CP. The natural upcoming step for this work is to validate these developments to pave the way for model-based predictions of treatment outcomes. This validation step should guarantee generalizability and representativeness of our simulation framework and models. Generalizability implies that the methods and models can be successfully applied to a heterogeneous group of children with CP. Specifically, the parameter estimation procedure should allow identifying subject-specific muscle-tendon parameters for children with different disorders (e.g., weakness of different muscle groups), the spasticity model should allow describing the spastic response of muscle groups not analyzed in our studies (e.g., rectus femoris and psoas), and the predictive simulations should allow producing a variety of impaired gait patterns (e.g., different levels of crouch and stiff knee gaits). Representativeness implies that the models and simulations can capture subject-specific gait

deficiencies in enough details to consider subject-specific treatment options. Such validation will require performing numerous analyses of case studies with children with CP presenting different impairments and levels of involvement. The validation analyses should also include pre- and post-intervention case studies to ensure that simulations can accurately capture the effect of treatments. Overall, such validation is challenging and will not happen overnight but we believe that it is technically feasible based, among others, on the developments and insights from the studies of this dissertation.

Conclusions

Using computer models for predicting the functional outcome of treatments has been something of a holy grail in the field of computational biomechanics over the last decades. Anderson and Pandy were among the first to generate fully predictive simulations of walking using detailed musculoskeletal models and to promote their upcoming use for optimizing treatment design [35]. Two decades later and despite their recognized potential, predictive simulations are still largely underused in research contexts, let alone clinical practice. However, a lot of progress has been achieved, scaling down computational costs and increasing physiological resemblance. And while the journey is still long, I believe the developments of this dissertation have contributed to advancing a step closer to see this holy grail materialize.

Appendix A

Study 1: supplementary material

Methods

Muscle-tendon dynamics

The muscle-tendon (MT-) dynamics, comprising activation and contraction dynamics, were described by two nonlinear first order differential equations that relate the control, muscle excitation e , to the states, neural excitation r and normalized muscle fiber length \tilde{l}_m . Using the terminology of Buchanan *et al.* [91], activation dynamics were modeled in two steps. The first step defined the transformation from muscle excitation e , indirectly measured through EMG, to neural excitation r using a first-order differential equation based on Thelen [249, 28]. A hyperbolic tangent function was used to smoothly transition between activation and deactivation, providing continuous derivatives required for gradient-based optimization [53]:

$$f = 0.5 \tanh(b(e - r)), \quad (\text{A.1})$$

$$\frac{dr}{dt} = \left[\frac{1}{\tau_a (0.5 + 1.5r)} (f + 0.5) + \frac{0.5 + 1.5r}{\tau_d} (-f + 0.5) \right] (e - r), \quad (\text{A.2})$$

where $\tau_a = 15$ ms and $\tau_d = 60$ ms are the activation and deactivation time constants respectively. The second step defined the transformation from neural

excitation r to muscle activation a through the EMG-to-activation relationship [91, 90]:

$$a = \frac{e^{Ar} - 1}{e^A - 1}, \quad (\text{A.3})$$

where A is a nonlinear shape factor ($A = 0$ indicates a linear relationship). Contraction dynamics were described by the Hill model [27] that defines the MT-unit as a tendon of length l_t in series with a pennate muscle of length l_m and pennation angle α (see Figure 3.1). The tendon was modeled as a nonlinear spring:

$$F_t = F_m^{\max} f_t(\tilde{l}_t) \quad (\text{A.4})$$

where F_t is the tendon force, $\tilde{l}_t = l_t/l_t^s$ is the normalized tendon length, and f_t is the tendon force-length characteristic. The muscle was modeled as a contractile element (CE) in parallel with a passive element (PE):

$$F_m = F_m^{\max} [a f_{act}(\tilde{l}_m) f_v(\tilde{v}_m) + f_{pas}(\tilde{l}_m)], \quad (\text{A.5})$$

where F_m is the muscle force, $\tilde{l}_m = l_m/l_m^{\text{opt,var}}$ with $l_m^{\text{opt,var}}$ the variable optimal muscle fiber length (defined in A.9) is the normalized muscle fiber length, $\tilde{v}_m = v_m/v_m^{\max}$ with $v_m^{\max} = 10l_m^{\text{opt,var}}$ is the normalized muscle fiber velocity [27], and f_{act} , f_{pas} , and f_v are respectively the active muscle force-length, passive muscle force-length, and muscle force-velocity characteristics. All MT-force characteristics are at least second order continuous for compatibility with the interior point numerical optimization solver that uses second-order derivative information (for more details and mathematical expressions, see supplementary materials of De Groote *et al.* [53]). The interaction between muscle and tendon was described by:

$$l_{mt} = l_t + l_m \cos \alpha, \quad (\text{A.6})$$

$$l_m \sin \alpha = l_m^{\text{opt,var}} \sin \alpha_m^{\text{opt}}, \quad (\text{A.7})$$

$$F_t = F_m \cos \alpha, \quad (\text{A.8})$$

where l_{mt} is the MT-length. Huijing *et al.* [250] reported that optimal muscle fiber length increases as muscle activation decreases. This muscle property was shown to increase the joint moment predictions [90] and was modeled by using a variable optimal muscle fiber length defined by [90]:

$$l_m^{\text{opt, var}} = l_m^{\text{opt}} (\gamma (1 - \alpha)), \quad (\text{A.9})$$

where $\gamma = 15\%$ is the percentage change in optimal muscle fiber length. Equations (A.4-A.9) determine the five unknowns F_t , F_m , l_t , l_m , α , given the inputs a and l_{mt} . The dynamic nature of the Hill model results from the muscle fiber velocity dependence of (A.5).

Definition of physiologically feasible combinations of MT-parameters

The search space of the optimal estimation problem was restricted to physiologically feasible combinations $[l_m^{\text{opt}}, l_t^s]$ defined based on a three-step procedure [89]. First, for each knee actuator ($j = 1, \dots, 8$), $l_{m,j}^{\text{opt}}$ and $l_{t,j}^s$ were constrained within $\pm 50\%$ of their nominal values (i.e. values from linearly scaled models). The intervals were then discretized into sets of 11 nodes, each separated by 10%, resulting in 121 possible discrete parameter combinations per knee actuator (grid, Figure A.1). Second, for each possible discrete parameter combination, the normalized muscle fiber length $\tilde{l}_{m,j}$ was computed based on the Hill model. This computation was performed considering a muscle activation of 0.8 and for the two extreme MT-lengths (maximal and minimal $l_{mt,j}$) encountered across the set of dynamic motions. Discrete parameter combinations resulting in $\tilde{l}_{m,j}$ within the muscle operating range [27]:

$$0.4 < \tilde{l}_{m,j} < 1.6, \quad (\text{A.10})$$

for both extreme MT-lengths were selected (gray and black circles, Figure A.1). Third, for each selected discrete parameter combination, the normalized muscle fiber length for the body in the anatomical position at rest $\tilde{l}_{m,j}^0$ was computed based on the Hill model. This computation was performed considering a muscle activation of 0.1 and for the MT-length obtained when the body is in the anatomical position. Discrete parameter combinations resulting in $\tilde{l}_{m,j}^0$ within an interval around the reference normalized muscle fiber length $\tilde{l}_{m,j}^{0,\text{ref}}$:

$$\Delta_1 \tilde{l}_{m,j}^{0,\text{ref}} < \tilde{l}_{m,j}^0 < \Delta_2 \tilde{l}_{m,j}^{0,\text{ref}} \quad (\text{A.11})$$

were defined as physiologically feasible parameter combinations (black circles, Figure A.1). Reference values were obtained from a cadaver study [251].

$\Delta_1 = 0.5$ and $\Delta_2 = 2.5$ were chosen to allow for inter-subject and inter-muscle variabilities on $\tilde{l}_{m,j}^{0,\text{ref}}$ and measurement errors on $\tilde{l}_{m,j}^0$.

First-order regressions were then established between transformed physiologically feasible combinations $1/l_{m,j}^{\text{opt}}$ and $l_{t,j}^s/l_{m,j}^{\text{opt}}$ (Figure A.2). The deviation of the transformed physiologically feasible combinations from the first-order regression line was small and quantified by δ_j :

$$\frac{1}{l_{m,j}^{\text{opt}}} - C_{1,j} \frac{l_{t,j}^s}{l_{m,j}^{\text{opt}}} - C_{2,j} = \delta_j, \quad (\text{A.12})$$

where $C_{1,j}$ and $C_{2,j}$ are the regression coefficients. The ratio $l_{t,j}^s/l_{m,j}^{\text{opt}}$ and the parameter δ_j were used as static parameters in the optimal estimation problem instead of $l_{t,j}^s$ and $l_{m,j}^{\text{opt}}$. This parameter transformation was performed to improve the numerical condition of the problem [89].

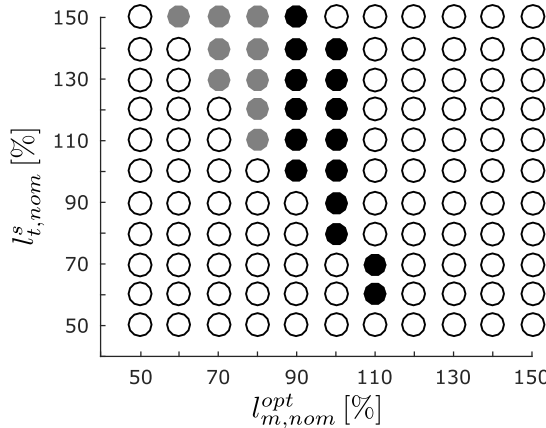


Figure A.1: Representative example of physiologically feasible combinations $[l_m^{\text{opt}}, l_t^s]$ for one knee actuator. The grid represents the combinations $[l_m^{\text{opt}}, l_t^s]$ discretized in sets of 11 nodes, each separated by 10%, around the nominal values. The gray and black circles represent the discrete parameter combinations resulting in normalized muscle fiber lengths l_m^{opt} within the muscle operating range. The black circles represent the discrete parameter combinations that additionally result in normalized fiber lengths in the anatomical position at rest l_m^0 within an interval around the reference normalized muscle fiber length. Physiologically feasible combinations $[l_m^{\text{opt}}, l_t^s]$ are restricted to black circles.

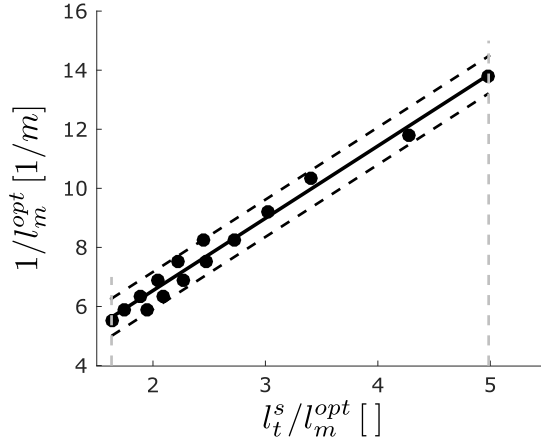


Figure A.2: Representative example of the first-order regression established between transformed physiologically feasible combinations l_t^s / l_m^{opt} and $1 / l_m^{opt}$ for one knee actuator (parameter combinations from Figure A.1). The black line represents the first-order regression line, the black dashed lines represent the maximal deviation from the regression line (i.e. the physiological bounds on δ) and the gray dashed lines represent the physiological bounds on l_t^s / l_m^{opt} .

Definition of initial guesses of static parameters

The optimal estimation problem was solved using two initial guesses of static parameters to decrease the probability of finding local optima as a consequence of using a gradient-based method. The solution resulting in the smallest value of the cost functional was then selected. For each knee actuator, the interval $\left[\left(l_{t,j}^s / l_{m,j}^{opt} \right)^{\min}, \left(l_{t,j}^s / l_{m,j}^{opt} \right)^{\max} \right]$ was discretized into five nodes being equally separated. For each node, the corresponding combination $[l_{m,j}^{opt}, l_{t,j}^s]$ was computed using $\delta_j = 0$ (A.12) and was used to simulate the EMG-driven model-based (EDM-) moments. MT-models with rigid tendons were used for the simulations to avoid time-consuming integration of the dynamic equations. Rigid tendons have constant length ($l_t = l_t^s$). Under this assumption, l_m and v_m are thus completely determined by l_{mt} and v_{mt} (A.6), enabling algebraic solution of equations (A.4-A.9). Note that v_{mt} is the first-order derivative of l_{mt} . The first initial guess of static parameters was based on the combination $[l_{m,j}^{opt}, l_{t,j}^s]$ resulting in the smallest RMSE between ID- and EDM-moments. This first initial guess was considered as a hot start for the optimal estimation problem. The second initial guess was arbitrary and corresponded to the

third node for all knee actuators. This second initial guess did not require any additional computations. The initial guesses of static parameters were compared by expressing the ratio of the initial MT-parameters corresponding to the hot start to the initial MT-parameters corresponding to the arbitrary guess. Initial MT-parameters were obtained from the static parameters using the parameter transformation defined in (A.12). This comparison is presented in Table A.1.

Influence of the initial guess of static parameters

The influence of the initial guess of static parameters on the cost functional was evaluated by computing, for each suitable calibration set and dataset, the ratio of the cost function value obtained from the hot start to the cost function value obtained from the arbitrary guess. Average and standard deviation were thereafter calculated over all seven suitable calibration sets and 11 datasets. The influence of the initial guess of static parameters on the MT-parameter estimates and the moment simulations (via the metrics R^2 and RMSE) was similarly evaluated.

Implementation algorithm of Modenese *et al.*

The subject-specific MT-parameters estimated in this study were compared to those computed using the anthropometry-based nonlinear scaling algorithm proposed by Modenese *et al.* [86]. This algorithm is available at https://simtk.org/home/opt_muscle_par and its implementation requires: i) a reference model, ii) a target model, iii) the ranges of motion of the joint angles, and iv) the number of evaluation points per coordinate. In the implementation, the generic OpenSim gait2392 model was used as reference model and the linearly scaled model as target model. The ranges of motion for the joint angles were computed based on the available dynamic motions (Table A.2). Note that although only knee actuators were considered in this study, several knee actuators are bi-articular and therefore the three joints spanned by the knee actuators were to be included. Finally, 10 evaluation points per coordinate were used as convergence was obtained from 10 evaluation points. In more details, convergence was assessed by calculating the percentages of variations of the parameter values of the knee muscles using n and $n - 1$ evaluation points per coordinate (for $n = 6, \dots, 15$) (the reader is referred to [86] for more details about the convergence assessment). For all subjects, variations were smaller than 2% for $n \geq 10$ suggesting convergence. Note that in this convergence assessment, the abduction/adduction and internal/external rotation degrees of freedom of the knee were locked when estimating the MT-parameters. This was needed

to limit the computational time (estimating the MT-parameters of the knee muscles of one leg required about 14 hours and 3 minutes when including and excluding, respectively, those two degrees of freedom) and only small variations ($< 3\%$) were observed between these two cases using 10 evaluation points per coordinate. MT-parameters reported in the manuscript were estimated while including the two degrees of freedom.

	BFLH	GL	GM	RF	SM	VI	VL	VM
	Mean	Mean	Mean	Mean	Mean	Mean	Mean	Mean
	\pm	\pm	\pm	\pm	\pm	\pm	\pm	\pm
	std	std	std	std	std	std	std	std
	[%]	[%]	[%]	[%]	[%]	[%]	[%]	[%]
Tendon slack length	77.0 \pm 10.8	94.5 \pm 6.3	93.4 \pm 6.4	103.8 \pm 7.4	88.2 \pm 3.9	93.3 \pm 30.3	111.7 \pm 19.3	103.4 \pm 28.5
Optimal fiber length	159.3 \pm 31.6	128.8 \pm 33.4	143.6 \pm 44.7	87.6 \pm 31.0	146.5 \pm 19.6	105.6 \pm 30.4	85.4 \pm 23.0	97.0 \pm 33.4

Table A.1: **Comparison initial guesses of MT-parameters.** Ratios hot start to arbitrary guess for the initial tendon slack lengths and the optimal muscle fiber lengths. Ratios are averaged over all seven suitable calibration sets and 11 datasets (mean and standard deviation).

		Hip			Knee			Ankle
DOF		Flex ⁺ / Ext	Add ⁺ / Abd	Int ⁺ /Ext Rot	Flex/ Ext ⁺	Add ⁺ / Abd	Int ⁺ /Ext Rot	Plan/ Dors ⁺
ROM	Min	-24°	-24°	-24°	-112°	-7°	-12°	-48°
	Max	103°	14°	18°	5°	14°	20°	41°

Table A.2: **Considered range of motion.** The ⁺ indicates for which motion the angle is defined positive (e.g. knee extension corresponds to positive angles). Flex/ext: flexion/extension; add/abd: adduction/abduction; int/ext rot: internal/external rotation; plan/dors: plantar/dorsi flexion.

Results

Influence of the initial guess of static parameters

The values of the cost function obtained from both initial guesses of static parameters were, on average, similar but showed variability over calibration

sets and datasets (average ratio hot start to arbitrary guess $101.12 \pm 5.45\%$ over all seven suitable calibration sets and 11 datasets). The influence of the initial guess on the MT-parameter estimates was, on average, very limited but showed variability over calibration sets and datasets. In particular, larger variabilities were observed for the tendon slack length of the BFLH and for the optimal muscle fiber lengths (Table A.3). Overall, the initial guess had a small impact on the moment simulations (average ratios hot start to arbitrary guess $100.49 \pm 7.80\%$ and $100.25 \pm 6.85\%$ over all seven suitable calibration sets and 11 datasets for R^2 and RMSE respectively).

Comparison between subject-specific, reference, linearly scaled and nonlinearly scaled MT-parameters

Table A.4 and Table A.5 respectively give the subject-specific (i.e. estimated from the suitable calibration sets) l_t^s and l_m^{opt} expressed as percentage of the reference (i.e. estimated from all motions) l_t^s and l_m^{opt} (Ratio 1), the linearly scaled l_t^s and l_m^{opt} (Ratio 2) and the nonlinearly scaled l_t^s and l_m^{opt} (Ratio 3). Average subject-specific and reference MT-parameters are comparable. The largest deviations for l_t^s and l_m^{opt} were observed for the BFLH and the RF respectively (ratios $104.5 \pm 15.1\%$ and $106.3 \pm 38.6\%$). Compared to linearly scaled MT-parameters, subject-specific l_t^s of the flexors were smaller (ratio $82.1 \pm 10.2\%$), subject-specific l_m^{opt} of the flexors were larger (ratio $143.0 \pm 25.8\%$) and subject-specific l_t^s and l_m^{opt} of the extensors were relatively comparable. Larger variabilities were observed for l_m^{opt} and in particular for RF (ratio $100.5 \pm 40.7\%$). Compared to nonlinearly scaled MT-parameters, subject-specific l_t^s of the flexors were smaller (ratio $81.7 \pm 11.0\%$), subject-specific l_m^{opt} of the flexors were larger (ratio $150.7 \pm 31.6\%$) and subject-specific l_t^s and l_m^{opt} of the extensors were relatively comparable. Larger variabilities were observed for l_m^{opt} and in particular for RF (ratio $106.0 \pm 40.5\%$). Linearly and nonlinearly scaled MT-parameters were thus comparable to subject-specific MT-parameters for the extensors, in particular the vasti, but not for the flexors. All ratios are averaged over all seven suitable calibration sets and 11 datasets.

	BFLH	GL	GM	RF	SM	VI	VL	VM
	Mean							
	±	±	±	±	±	±	±	±
	std							
	[%]	[%]	[%]	[%]	[%]	[%]	[%]	[%]
Tendon slack length	102.3	99.7	99.8	101.2	100.4	101.3	99.8	100.2
	±	±	±	±	±	±	±	±
	12.7	4.2	3.4	5.5	4.4	6.5	4.0	5.5
Optimal fiber length	100.0	103.0	104.6	98.7	101.7	102.1	101.2	101.9
	±	±	±	±	±	±	±	±
	16.3	18.1	21.0	27.2	16.6	12.0	10.4	11.7

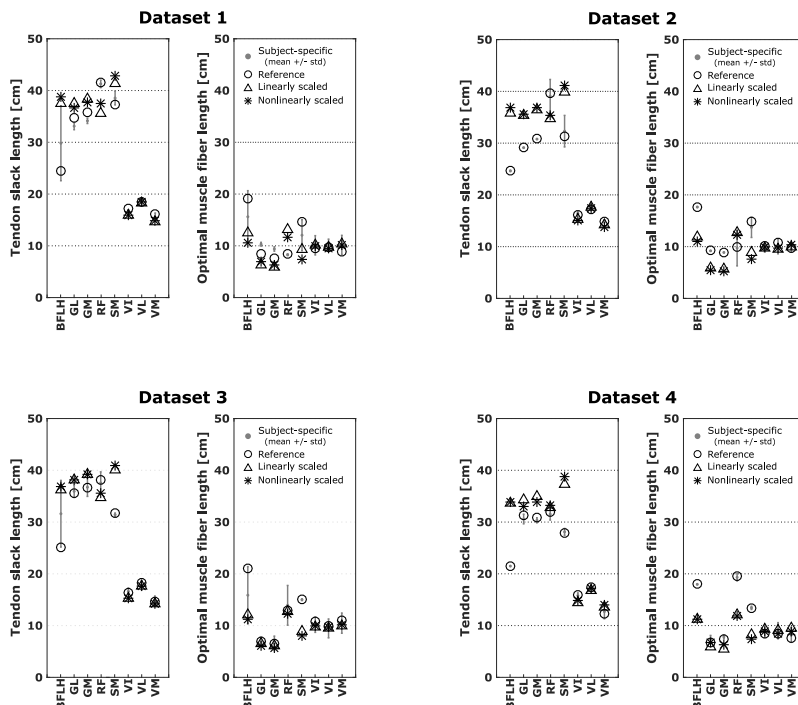
Table A.3: **Comparison MT-parameters estimated from both initial guesses of static parameters.** Ratios hot start to arbitrary guess for the tendon slack length and the optimal muscle fiber length estimates. Ratios are averaged over all seven suitable calibration sets and 11 datasets (mean and standard deviation).

	Tendon slack length							
	Flexors				Extensors			
	BFLH	GL	GM	RF	SM	VI	VL	VM
	Mean	Mean	Mean	Mean	Mean	Mean	Mean	Mean
	± std	± std	± std	± std	± std	± std	± std	± std
	[%]	[%]	[%]	[%]	[%]	[%]	[%]	[%]
Ratio 1	104.5	100	99.5	100.9	100.3	99.9	99.1	99.8
	± 15.1	± 3.7	± 3.2	± 5.4	± 9.8	± 4.0	± 3.5	± 5.2
Ratio 2	71.5	88.2	88.3	80.6	107.8	105.2	101.5	102.8
	± 11.0	± 5.3	± 5.0	± 7.1	± 9.6	± 3.9	± 3.5	± 7.3
Ratio 3	69.8	89.3	89.3	78.2	104.7	105.2	101.3	102.6
	± 10.9	± 5.6	± 5.0	± 6.8	± 8.9	± 4.0	± 3.8	± 7.5

Table A.4: **Comparison tendon slack lengths.** Subject-specific tendon slack length expressed as a percentage of the reference tendon slack length (Ratio 1), the linearly scaled tendon slack length (Ratio 2) and the nonlinearly scaled tendon slack length (Ratio 3). Ratios are averaged over all seven suitable calibration sets and 11 datasets (mean and standard deviation).

	Optimal muscle fiber length							
	Flexors				Extensors			
	BFLH	GL	GM	RF	SM	VI	VL	VM
Mean	Mean	Mean	Mean	Mean	Mean	Mean	Mean	Mean
± std	± std	± std	± std	± std	± std	± std	± std	± std
[%]	[%]	[%]	[%]	[%]	[%]	[%]	[%]	[%]
Ratio 1	95.8 ± 13.8	102.4 ± 12.0	103.7 ± 12.4	95.3 ± 13.0	106.3 ± 38.6	101.7 ± 11.5	101.2 ± 11.7	103.6 ± 12.8
Ratio 2	144.7 ± 22.2	135.0 ± 27.9	140.8 ± 28.1	151.5 ± 21.9	100.5 ± 40.7	96.4 ± 9.7	98.4 ± 12.0	91.1 ± 11.7
Ratio 3	157.7 ± 24.9	132.1 ± 29.1	136.9 ± 28.1	176.2 ± 22.8	106.0 ± 40.5	96.3 ± 9.8	99.1 ± 12.7	91.4 ± 12.2

Table A.5: **Comparison optimal muscle fiber lengths.** Subject-specific optimal muscle fiber length expressed as a percentage of the reference optimal muscle fiber length (Ratio 1), the linearly scaled optimal muscle fiber length (Ratio 2) and the nonlinearly scaled optimal muscle fiber length (Ratio 3). Ratios are averaged over all seven suitable calibration sets and 11 datasets (mean and standard deviation).



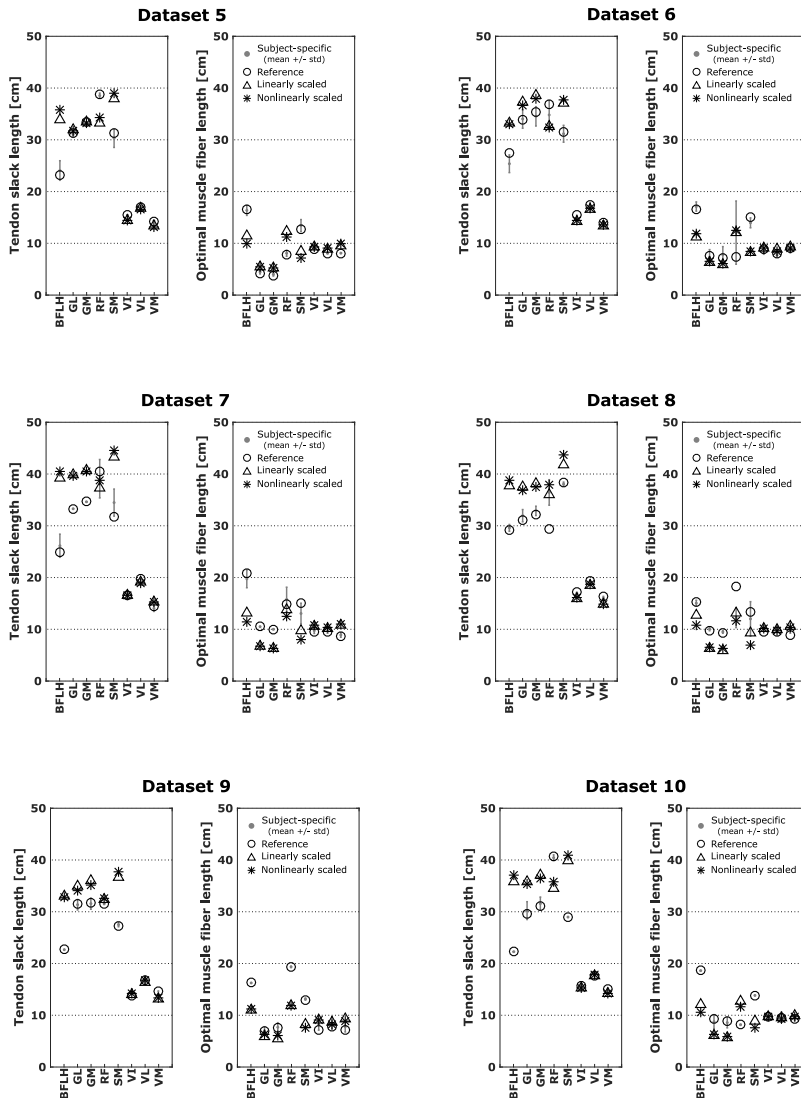


Figure A.3: Comparison between subject-specific MT-parameters averaged over all seven suitable calibration sets (gray, standard deviation), reference MT-parameters (circles), linearly scaled MT-parameters (triangles) and nonlinearly scaled MT-parameters (stars). Results are given for the datasets 1-10 individually (results of dataset 11 are presented in the manuscript (Figure 3.4)).

Appendix B

Study 2: supplementary material

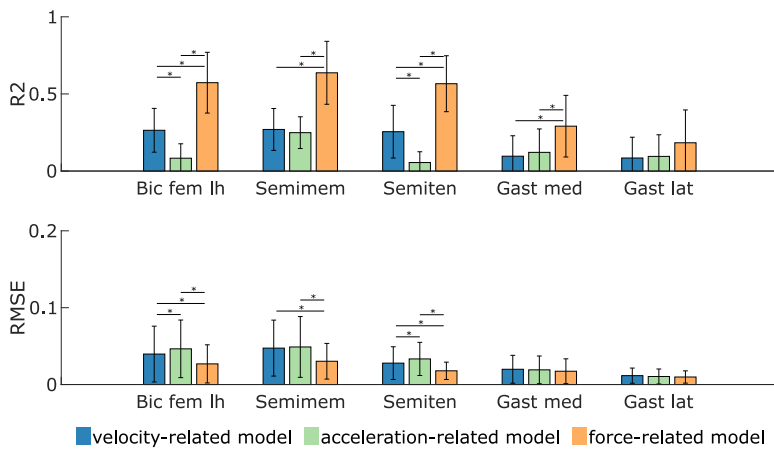


Figure B.1: Fits (R^2 and RMSE) between EMG and simulated muscle excitation during passive stretches at medium velocity. Muscle excitation is estimated based on the three spasticity models (velocity-, acceleration-, and force-related). A larger R^2 /smaller RMSE value represents a better fit. The statistical significance level was set to 0.05. Results are averaged over eight and 12 values for the hamstrings (biceps femoris long head (Bic fem lh), semimembranosus (Semimem), and semitendinosus (Semiten)) and gastrocnemii (gastrocnemius medialis (Gast med) and lateralis (Gast lat)), respectively.

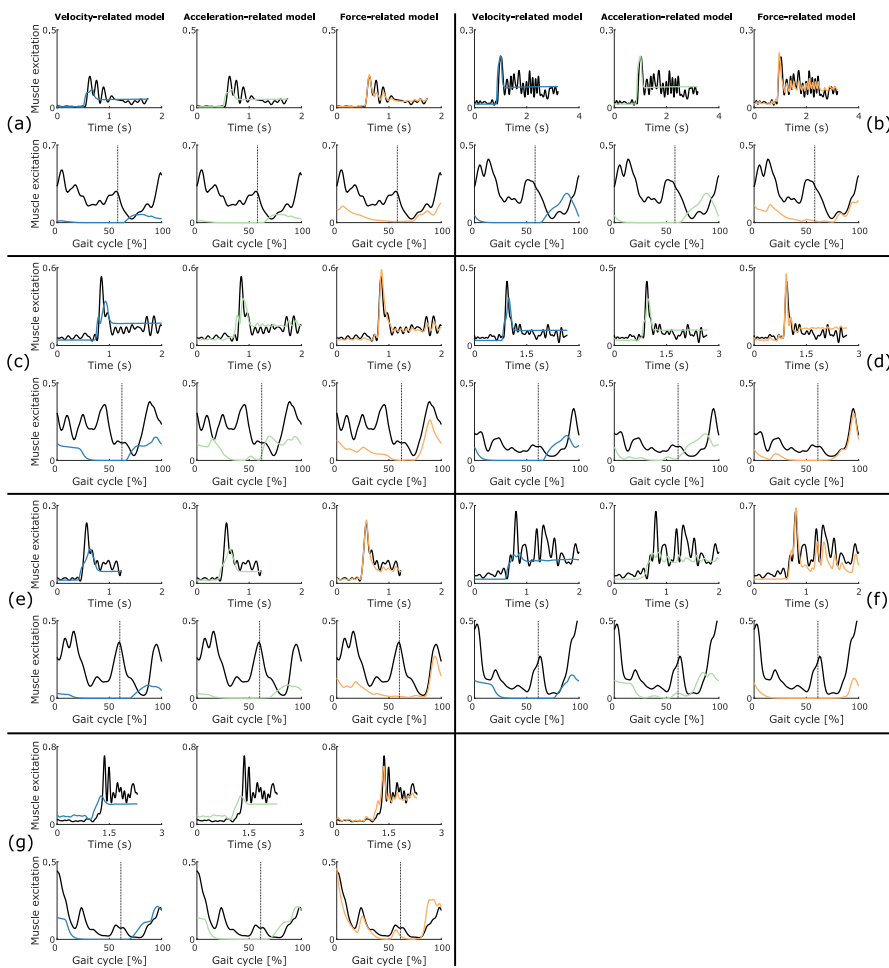


Figure B.2: EMG compared to sensory feedback of the semimembranosus (hamstrings). The EMG (thick black lines) and sensory feedback (colored lines) are shown for one trial of a fast passive stretch motion (top) and a gait motion (bottom). The velocity-related model combines muscle fiber length and velocity feedback. The acceleration-related model combines muscle fiber length, velocity, and acceleration feedback. The force-related model combines muscle force and dF/dt feedback. The three models also include a baseline activation during the fast passive stretch motion (top). The vertical lines indicate the transition from stance to swing. Each box (a-g) represents a different case.

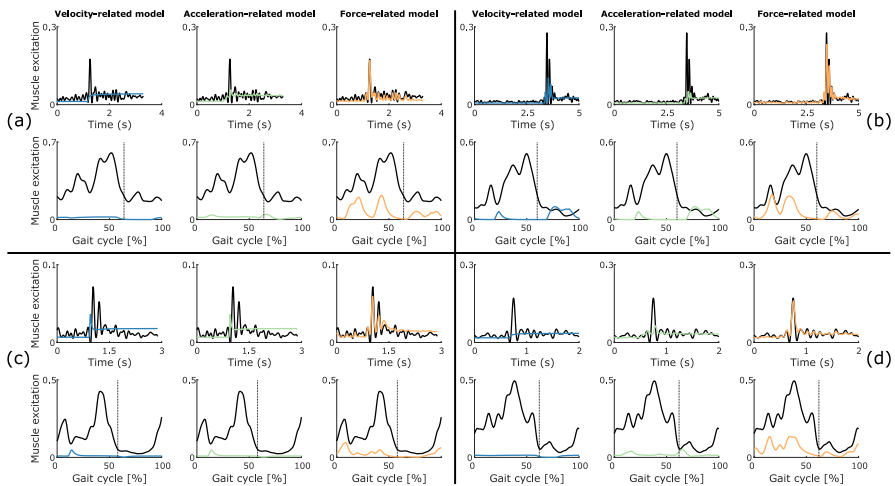


Figure B.3: EMG compared to sensory feedback of the gastrocnemius medialis (gastrocnemii). The EMG (thick black lines) and sensory feedback (colored lines) are shown for one trial of a fast passive stretch motion (top) and a gait motion (bottom). The velocity-related model combines muscle fiber length and velocity feedback. The acceleration-related model combines muscle fiber length, velocity, and acceleration feedback. The force-related model combines muscle force and dF/dt feedback. The three models also include a baseline activation during the fast passive stretch motion (top). The vertical lines indicate the transition from stance to swing. Each box (a-d) represents a different case. In all cases, the CP children landed on their heel.

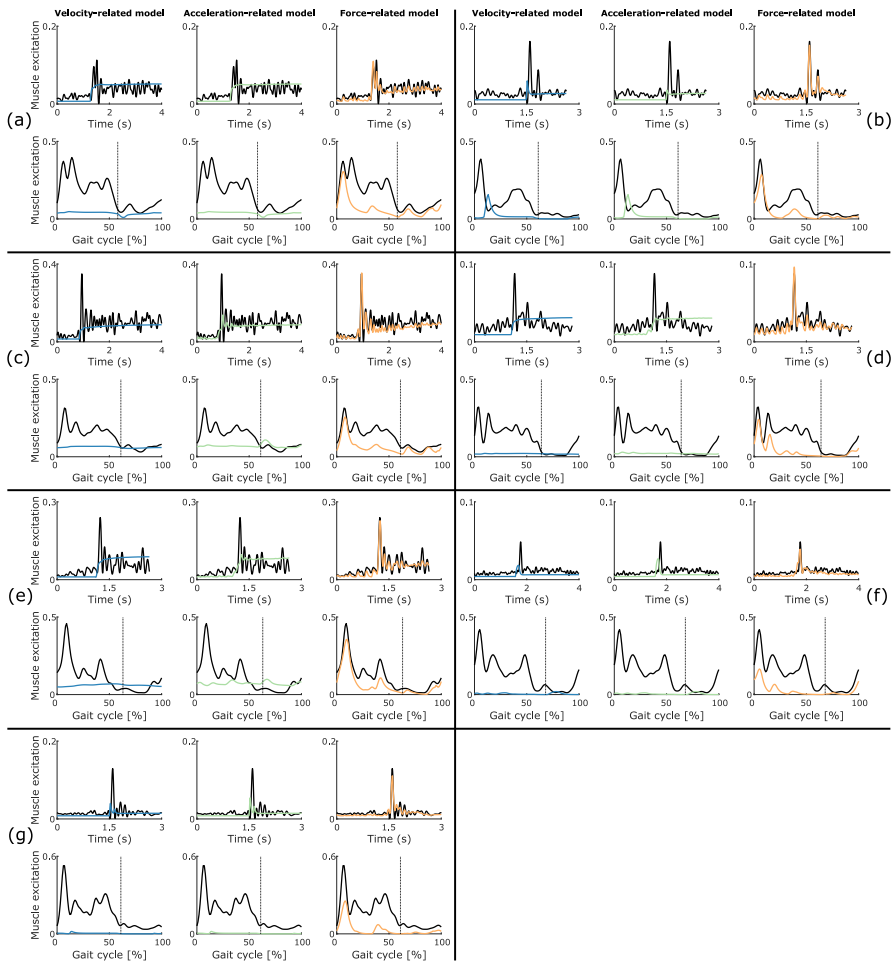


Figure B.4: EMG compared to sensory feedback of the gastrocnemius medialis (gastrocnemii). The EMG (thick black lines) and sensory feedback (colored lines) are shown for one trial of a fast passive stretch motion (top) and a gait motion (bottom). The velocity-related model combines muscle fiber length and velocity feedback. The acceleration-related model combines muscle fiber length, velocity, and acceleration feedback. The force-related model combines muscle force and dF/dt feedback. The three models also include a baseline activation during the fast passive stretch motion (top). The vertical lines indicate the transition from stance to swing. Each box (a-g) represents a different case. In all cases, the CP children landed on their forefoot and we therefore observe a large abnormal peak in activity at initial contact.

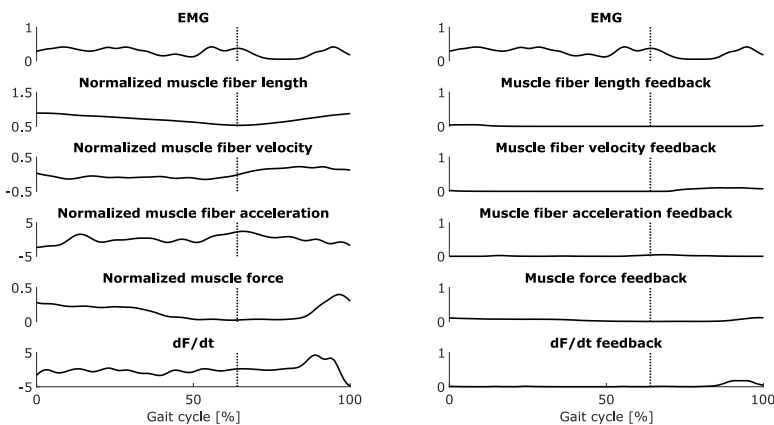


Figure B.5: **EMG, sensory information, and sensory feedback of the semimembranosus (hamstrings) during a gait trial.** The EMG (top), normalized sensory information (left), and corresponding sensory feedback (right) are shown for one gait trial for the semimembranosus (hamstrings) of one CP child (corresponding to Figure 4.4). The vertical lines indicate the transition from stance to swing. Normalized muscle fiber acceleration is the first time derivative of normalized muscle fiber velocity. dF/dt is the first time derivative of normalized muscle force.

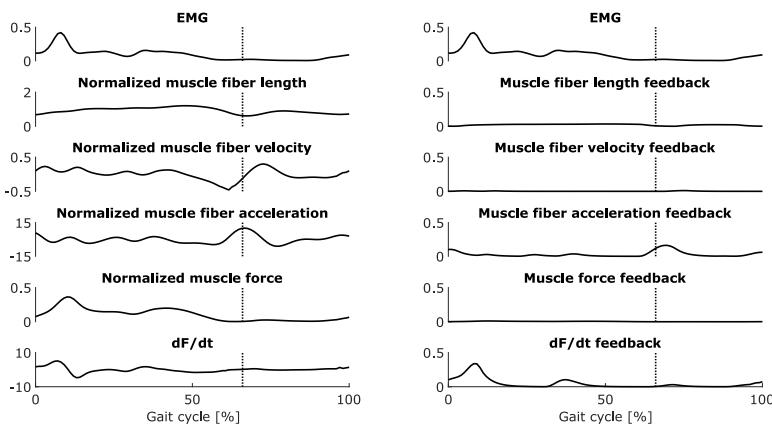


Figure B.6: EMG, sensory information, and sensory feedback of the gastrocnemius medialis (gastrocnemii) during a gait trial. The EMG (top), normalized sensory information (left), and corresponding sensory feedback (right) are shown for one gait trial for the gastrocnemius medialis (gastrocnemii) of one CP child (corresponding to Figure 4.6). The vertical lines indicate the transition from stance to swing. Normalized muscle fiber acceleration is the first time derivative of normalized muscle fiber velocity. dF/dt is the first time derivative of normalized muscle force.

Appendix C

Study 4: supplementary material

Experimental data

The subject (female; age: 35 years; height: 170 cm; mass: 62 kg) was instrumented with 45 retro-reflective skin-mounted markers. Three-dimensional marker coordinates were recorded (100 Hz) using a ten-camera motion capture system (Vicon, Oxford, UK). Ground reaction forces and electromyography (EMG) data were recorded (1000 Hz) using two force plates (AMTI, Watertown, USA) and a wireless EMG acquisition system (Cometa Mini Wave, Milano, Italy), respectively. Ground reaction forces were low-pass filtered (6 Hz) using a second-order dual-pass Butterworth filter. EMG data was collected from 14 muscles (peroneus brevis and longus, tibialis anterior, gastrocnemius lateralis and medialis, soleus, vastus lateralis and medialis, adductor longus, rectus femoris, tensor fascia latae, gluteus medius, hamstrings lateralis and medialis) and was processed by band-pass filtering (20-400 Hz), full-wave rectification, and low-pass filtering (10 Hz) using a second-order dual-pass Butterworth filter.

Smooth approximations

We performed smooth approximations of the contact and metabolic energy models to allow having twice continuously differentiable models, which are required when using gradient-based optimization [51]. We performed smooth

approximations of conditional *if statements* using hyperbolic tangent functions. For example, the following *if statement*:

$$y = \begin{cases} 0, & x < d \\ a, & x \geq d \end{cases} \quad (\text{C.1})$$

can be approximated by:

$$f = 0.5 + 0.5 \tanh(b(x - d)), \quad (\text{C.2})$$

$$y = af, \quad (\text{C.3})$$

where b is a parameter that determines the smoothness of the transition.

Optimal control problem formulation

We applied direct collocation to solve the optimal control problems underlying the predictive simulations. We sought to find the states, controls, and static (i.e., time-independent) parameters that minimized a cost function subject to dynamic and path constraints.

Optimization variables

States: $x(t)$	Controls: $u(t)$	Static parameter
Muscle activations a Tendon forces F_t Arm activations a_{arms} Joint positions q Joint velocities v	Derivatives of a : u_{da} Derivatives of F_t : u_{dF_t} Arm excitations e_{arms} Derivatives of v (accelerations): u_{dv}	Half gait cycle duration t_f

Cost function

We used multi-objective cost functions describing trade-offs between walking-related performance criteria:

$$J = \frac{1}{d} \int_0^{t_f} \left(\underbrace{w_1 \|\dot{E}\|_2^2}_{\text{Metabolic energy rate}} + \underbrace{w_2 \|a\|_2^2}_{\text{Muscle activity}} + \underbrace{w_3 \|u_{dv,lt}\|_2^2}_{\text{Joint accelerations}} + \underbrace{w_4 \|T_p\|_2^2}_{\text{Passive torques}} + \underbrace{w_5 \|e_{\text{arms}}\|_2^2}_{\text{Arm excitations}} \right) dt, \quad (\text{C.4})$$

where d is distance traveled by the pelvis in the forward direction, \dot{E} is metabolic energy rate (details in Chapter 6), $u_{dv,lt}$ are joint accelerations of the lower limbs and trunk, T_p are passive joint torques, t is time, and w_{1-5} are weight factors. To avoid singular arcs, situations for which controls are not uniquely defined by the optimality conditions [129], we also appended a penalty function J_p with the remaining controls to the cost function:

$$J_p = \frac{1}{d} \int_0^{t_f} w_u \left(\|u_{da}\|_2^2 + \|u_{dF_t}\|_2^2 + \|u_{dv,\text{arms}}\|_2^2 \right) dt, \quad (\text{C.5})$$

where $w_u = 0.001$ weights the penalty function against the other terms in the cost function and $u_{dv,\text{arms}}$ are joint accelerations of the arms.

Dynamic constraints

Due to the implicit formulation of muscle and skeleton dynamics, the dynamic equations were the following:

$$\frac{da}{dt} = s_{da} u_{da}, \quad (\text{C.6})$$

$$\frac{dF_t}{dt} = s_{dF_t} u_{dF_t}, \quad (\text{C.7})$$

$$\frac{dq}{dt} = v, \quad (\text{C.8})$$

$$\frac{dv}{dt} = u_{dv}, \quad (\text{C.9})$$

$$\frac{da_{\text{arms}}}{dt} = \frac{(e_{\text{arms}} - a_{\text{arms}})}{\tau}, \quad (\text{C.10})$$

where $s_{da} = 100$ and $s_{dF_t} = 100$ are scale factors, and $\tau = 35$ ms is a time constant. Equations C.6-C.9 correspond to the differential equations for muscle activation, contraction, and skeleton dynamics. Equation C.10 explicitly describes the dynamics of the torque actuators that move the arms and corresponds to a first order approximation of a time delay.

Path constraints

The first set of path constraints defined the implicit muscle (equations C.11-C.13) and skeleton dynamics (equation C.14):

$$0 \leq s_{da} u_{da} + \frac{a}{\tau_d}, \quad (\text{C.11})$$

$$s_{da} u_{da} + \frac{a}{\tau_a} \leq \frac{1}{\tau_a}, \quad (\text{C.12})$$

$$f_c(a, F_t, u_{dF_t}) = 0, \quad (\text{C.13})$$

$$T = f_s(q, v, u_{dv}), \quad (\text{C.14})$$

where $\tau_a = 15$ ms and $\tau_d = 60$ ms are muscle activation and deactivation time constants, $f_c(\cdot)$ describes the muscle contraction dynamics according to a Hill-type muscle model [53], and $f_s(\cdot)$ computes net joint torques T according to the skeleton dynamics.

Additional path constraints imposed null pelvis residuals T_{pelvis} (i.e., dynamic consistency; equation C.15), that the lower limb and trunk net joint torques equal the sum of muscle, passive, and damping torques (equation C.16), and that the arm net joint torques equal the sum of the actuator and damping torques (equation C.17):

$$T_{\text{pelvis}} = 0, \quad (\text{C.15})$$

$$T_{lt} = \sum_{m=1}^M MA_m F_{t,m} + T_p - Bv_{lt}, \quad (\text{C.16})$$

$$T_{\text{arms}} = a_{\text{arms}} s_{\text{arms}} - Bv_{\text{arms}}, \quad (\text{C.17})$$

where T_{lt} are torques of the lower limbs and trunk, MA_m is moment arm of muscle m , $B = 0.1$ is a damping factor, T_{arms} are torques of the arms, and $s_{\text{arms}} = 150$ is a scale factor. We imposed left-right symmetry so that we only needed to simulate half a gait cycle. To this aim, we prescribed the relation (i.e., equal or opposite) between the states at the start and end of half a gait cycle (except for the pelvis position in the forward direction). We imposed an average gait speed of $d/t_f = v_{\text{avg}}$, where $v_{\text{avg}} = 1.33 \text{ m s}^{-1}$ was used (subject's preferred walking speed). Finally, to prevent interpenetration of body segments, we imposed minimal distances in the transverse plane between the calcaneus origins (9 cm), between the ipsilateral femur and hand origins (18 cm), and between the tibia origins (11 cm). These distances were informed by experimental data.

Bounds

Joint states and controls (q , v , and u_{dv}) were bounded such that they allowed the generation of healthy and pathological gait patterns. We first used a spline approximation of the experimental walking joint positions \hat{q} to estimate \hat{v} and \hat{u}_{dv} . We then computed the minimum (\hat{q}_{\min} , \hat{v}_{\min} , and $\hat{u}_{dv,\min}$), maximum (\hat{q}_{\max} , \hat{v}_{\max} , and $\hat{u}_{dv,\max}$) and range (\hat{q}_r , \hat{v}_r , and $\hat{u}_{dv,r}$) for each of these variables over the gait cycle. Joint states and controls were then bounded as follows:

$$\hat{q}_{\min} - 2\hat{q}_r \leq q \leq \hat{q}_{\max} + 2\hat{q}_r, \quad (\text{C.18})$$

$$\hat{v}_{\min} - 3\hat{v}_r \leq v \leq \hat{v}_{\max} + 3\hat{v}_r, \quad (\text{C.19})$$

$$\hat{u}_{dv,\min} - 3\hat{u}_{dv,r} \leq u_{dv} \leq \hat{u}_{dv,\max} + 3\hat{u}_{dv,r}. \quad (\text{C.20})$$

We manually set the bounds of the pelvis translations:

$$0 \leq q_{\text{pelvis for}} \leq 2, \quad (\text{C.21})$$

$$0.75 \leq q_{\text{pelvis up}} \leq 1.1, \quad (\text{C.22})$$

$$-0.1 \leq q_{\text{pelvis lat}} \leq 0.1, \quad (\text{C.23})$$

where for is forward, up is upward, and lat is lateral. The values are in meters. The bounds of several arm joint angles were also manually set to prevent interpenetration of body segments:

$$0 \leq q_{\text{elbow}}, \quad (\text{C.24})$$

$$q_{\text{shoulder add}} \leq \hat{q}_{\text{shoulder add,max}}, \quad (\text{C.25})$$

$$q_{\text{shoulder rot}} \leq \hat{q}_{\text{shoulder rot,max}}, \quad (\text{C.26})$$

where add is adduction and rot is rotation. Muscle states and controls (a , F_t , u_{da} , u_{dF_t}) were bounded as follows:

$$0.05 \leq a \leq 1, \quad (\text{C.27})$$

$$0 \leq F_t \leq 5, \quad (\text{C.28})$$

$$-\frac{\tau_d}{100} \leq u_{da} \leq \frac{\tau_a}{100}, \quad (\text{C.29})$$

$$-1 \leq u_{dF_t} \leq 1, \quad (\text{C.30})$$

and arm actuator states and controls (a_{arms} and e_{arms}) were bounded between -1 and 1. We set the lower bound on muscle activations to 0.05 to account for a baseline activation. Since we use an implicit formulation of contraction dynamics, the lower bound is allowed to be 0 but a baseline activation is more physiological.

For the simulations at speeds greater than the preferred walking speed, we adjusted the lower bound of the pelvis pitch and shoulder flexion angles, and the upper bound of the pelvis forward velocity to allow for the generation of running motions:

$$-20^\circ \leq q_{\text{pelvis pitch}}, \quad (\text{C.31})$$

$$-50^\circ \leq q_{\text{pelvis flex}}, \quad (\text{C.32})$$

$$\dot{q}_{\text{pelvis for}} \leq 4 \text{ m s}^{-1}, \quad (\text{C.33})$$

where flex is flexion.

Scaling

To improve the numerical condition of the problem, we scaled the optimization variables so that they had the same order of magnitude [129]. In particular, we scaled joint states and controls, and tendon forces such that their lower and upper bounds were between -1 and 1. To this aim, we used as scale factors the maximum of the absolute value of the lower and upper bounds. Other muscle and arm states and controls were not further scaled, since their lower and upper bounds were already between -1 and 1. Further, as recommended in the literature [129], we scaled the dynamic constraints using the same scale factors as used to scale the states.

Initial guesses

We used two initial guesses (Table C.1) for all simulations at the preferred walking speed (1.33 m s^{-1}) and selected the result with the lowest optimal cost. One initial guess (data-informed) relied on experimental data from walking trials for the joint states and controls. The other initial guess (quasi-random) did not rely on any data and described an unrealistic motion. We used the quasi-random initial guess to demonstrate the robustness of our simulations against the initial guess. For the simulations at different speeds, we used five initial guesses (Table C.1) and selected the result with the lowest optimal cost. We used more initial guesses for this analysis since we did not have experimental

data at each intermediate speed. In all cases, the initial guesses for the muscle states and controls, arm states and controls, and final time were constant across time.

Transcription and solver

We transcribed each optimal control problem into a nonlinear programming problem (NLP) using a third order Radau quadrature collocation scheme with 50 mesh intervals per half gait cycle. We used the interior-point solver IPOPT [122] with the linear algebra package MUMPS [124], using first order derivative information, a limited-memory quasi-Newton method (L-BFGS) to approximate the Hessian of the Lagrangian, and a NLP relative error tolerance of 1×10^{-4} with a maximum of 10,000 iterations. We formulated each optimal control problem in MATLAB (The Mathworks Inc., USA) using CasADi, a tool for nonlinear optimization and algorithmic differentiation [56].

Tracking simulations

We calibrated the contact models while performing muscle-driven tracking simulations of the subject's experimental walking data. We formulated the tracking simulations via direct collocation in the same way as the predictive simulations but we added the transverse plane locations and radii of the contact spheres as optimization variables (static parameters) and used a different cost function:

$$J = \int_{t_i}^{t_f} \left(w_1 \|q - \hat{q}\|_2^2 + w_2 \|GRF - G\hat{R}F\|_2^2 + w_3 \|GRT - G\hat{R}T\|_2^2 + w_4 \|T - \hat{T}\|_2^2 + w_5 \|a\|_2^2 \right) dt, \quad (\text{C.34})$$

where t_i and t_f are known initial and final times (t_f was not an optimization variable in this case), \hat{q} are experimental joint positions (except for the upward pelvis position to account for uncertainties in the vertical location of the contact geometries in the foot) obtained from inverse kinematics, $G\hat{R}F$ are experimental ground reaction forces, $G\hat{R}T$ are experimental ground reaction torques expressed in the ground frame, and \hat{T} are experimental net joint torques (except for the pelvis torques that are imposed to be tracked, through path constraints, for

dynamic consistency between the tracking simulation and the experimental results from inverse dynamics) obtained from inverse dynamics. We allowed the contact sphere locations and the radii to vary by 25 mm and 50% from their original values [46], respectively. We manually tuned the values of the weight factors, following a heuristic approach, until we found a cost function that well reproduced all experimental data.

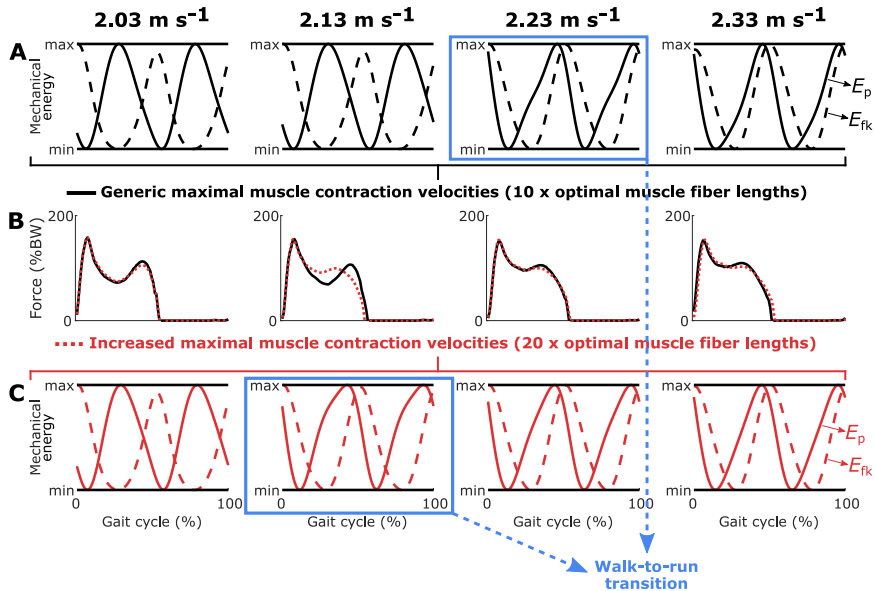


Figure C.1: Mechanical energy and simulated vertical ground reaction forces around walk-to-run transition speed with and without increased muscle mechanical power. (A) Simulated mechanical energy (gravitational potential energy E_p and forward kinetic energy E_{fk}) at different speeds with generic maximal muscle contraction velocities. From 2.23 m s^{-1} onwards, E_p and E_{fk} are in phase (maxima occurring close in time), indicating a transition from walking to running [210]. (B) Corresponding simulated vertical ground reaction forces (Force; BW: body weight). Increasing the maximum muscle mechanical power by doubling the maximal muscle contraction velocities had a large influence on the simulated force at 2.13 m s^{-1} . (C) Simulated mechanical energy at different speeds with increased maximal muscle contraction velocities. Increasing the maximum muscle mechanical power reduced the walk-to-run transition speed from 2.23 m s^{-1} to 2.13 m s^{-1} . This shift is in agreement with experiments reporting a delayed walk-to-run transition in children due to reduced peak mechanical power as compared to adults [225]. The simulations minimized the nominal cost function.

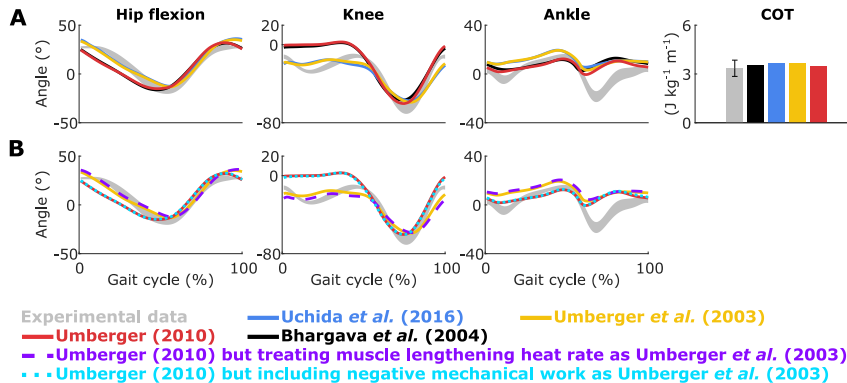


Figure C.2: Simulated walking gaits with different metabolic energy models. (A) The models presented by Uchida *et al.* (2016) and Umberger *et al.* (2003) predicted different hip flexion, knee, and ankle angles than the models presented by Bhargava *et al.* (2004) and Umberger (2010). These differences had little influence on the metabolic cost of transport (COT) computed using the model presented by Bhargava *et al.* (2004) based on the simulated states in a post-processing step. Note that there are larger differences in the COT computed with the different metabolic energy models based on the same states. The main differences between the models are the treatment of negative mechanical work and muscle lengthening heat rate (Table C.2). **(B)** Treating the muscle lengthening heat rate in Umberger (2010) as in Umberger *et al.* (2003) explained most of the differences between both models. By contrast, including negative mechanical work in Umberger (2010) as in Umberger *et al.* (2003) had little influence on the results. Experimental data is shown as mean \pm two standard deviations. The simulations minimized the nominal cost function (except for the use of different metabolic energy models) at the preferred walking speed (1.33 m s^{-1}).

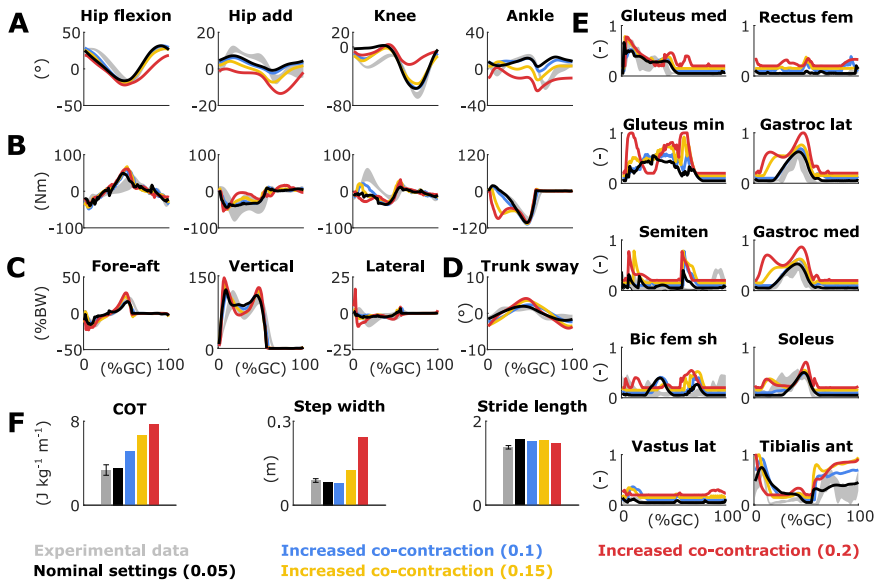


Figure C.3: Simulated walking gaits with increased co-contraction. Simulating co-contraction by increasing the lower bounds on muscle activations from 0.05 to 0.1 resulted in larger knee flexion during stance associated with larger knee torques, vasti activity, but also COT ($5.10 \text{ J kg}^{-1} \text{ m}^{-1}$). Enforcing more co-contraction (lower bounds on muscle activations equal to 0.15 and 0.2) affected the kinematics, resulting in non-human-like gaits with high COT and muscle activity. Experimental data is shown as mean \pm two standard deviations. The experimental electromyography data (gray curves) was normalized to peak nominal activations (black curves; med: medius; min: minimus; semiten: semitendinosus; bic: biceps; fem: femoris; sh: short head; lat: lateralis; gastroc: gastrocnemius; ant: anterior). GRF: ground reaction forces; BW: body weight; GC: gait cycle; add: adduction.

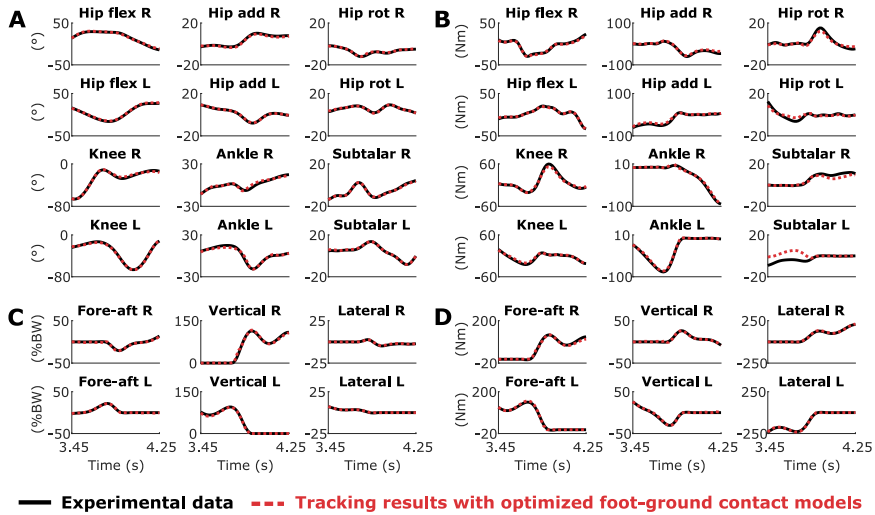


Figure C.4: Tracking simulations with optimized foot-ground contact models. The musculoskeletal model with optimized contact models (optimized contact sphere locations and radii) accurately reproduced experimental (A) joint angles (flex: flexion; add: adduction; rot: rotation; R: right; L: left), (B) joint torques, (C) ground reaction forces (BW: body weight), and (D) ground reaction torques. Ground reaction forces and torques are expressed in the ground frame. This indicates that the musculoskeletal model is sufficiently complex to reproduce experimental walking data.

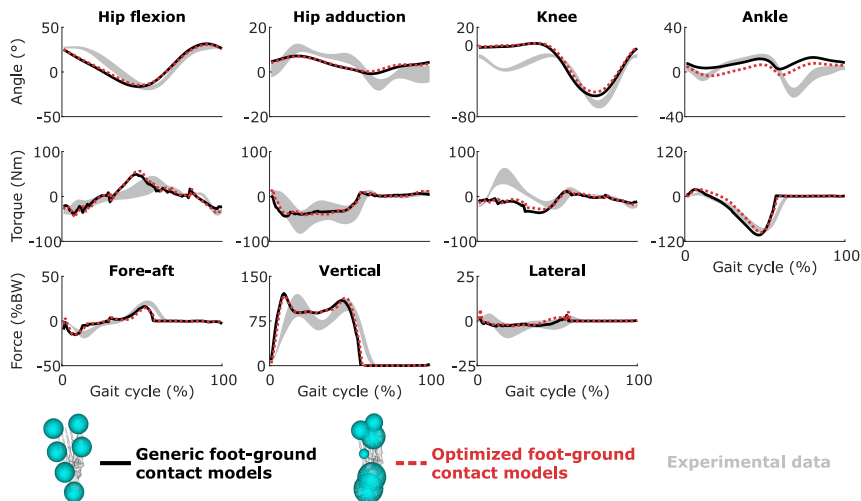


Figure C.5: Simulated walking gait with optimized foot-ground contact models. Despite large differences in contact geometry, the use of optimized contact models instead of generic models from the literature [46] had little influence on the predicted gait pattern (Force: ground reaction force; BW: body weight), except for a small offset in the ankle angle. This suggests a low sensitivity of the results to the contact models. The foot diagrams depict a down-up view of the configuration of the contact spheres of the right foot. Experimental data is shown as mean \pm two standard deviations. The simulations minimized the nominal cost function at the preferred walking speed (1.33 m s^{-1}).

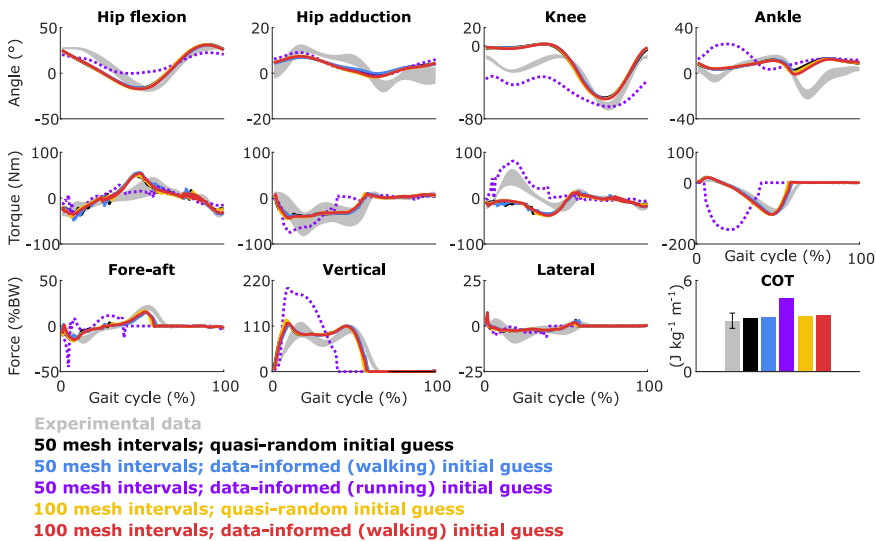


Figure C.6: Simulated walking gaits with data-informed (walking and running) and quasi-random initial guesses, and with finer mesh. Varying the initial guess (between data-informed (walking) and quasi-random) and increasing the number of mesh intervals (from 50 to 100) had, overall, little influence on the predicted gait patterns (Force: ground reaction force; BW: body weight; COT: metabolic cost of transport). The four curves nearly coincide. By contrast, using the initial guess derived from running data led to the prediction of a different gait pattern. Yet that simulation had a much larger optimal cost than the simulations resulting from the two other initial guesses with 50 meshes, meaning that the optimal control problems converged to different local optima. Similar to humans, the model can hence adopt different gaits at the same speed. The quasi-random initial guess resulted in a lower optimal cost with both meshes as compared to the data-informed initial guesses. A finer mesh resulted in smoother control and state trajectories as can be appreciated when looking at the hip flexion torques. Computational times increased when increasing the number of mesh intervals from 50 (25, 21, and 53 minutes with the quasi-random, data-informed (walking), and data-informed (running) initial guesses, respectively) to 100 (62 and 69 minutes with the quasi-random and data-informed initial guesses, respectively). Experimental data is shown as mean \pm two standard deviations. The simulations minimized the nominal cost function at the preferred walking speed (1.33 m s^{-1}).

States x / Controls u		Joints		u		Muscles and Arms		Time
Static parameters p	q	x	v	u_{adv}	a, F_t, a_{arms}	u_{da}, u_{dF_t}	e_{arms}	$\frac{p}{t_f}$
Preferred walking speed	Data-informed (walking)	\hat{q}_{walk}		Spline-based derivatives of \hat{q}_{walk}	0.1	0.01	0.1	0.6
	Quasi-random	0 except $q_{\text{pelvis}} = f_q(v_{\text{avg}}, t_f)$ $q_{\text{pelvis up}} = \text{standing}$	$v_{\text{pelvis for}} = v_{\text{avg}}$	0 except $v_{\text{pelvis for}} = v_{\text{avg}}$	0.1	0.01	0.1	0.6
	Data-informed (walking)	\hat{q}_{walk}		Spline-based derivatives of \hat{q}_{walk}	0.1	0.01	0.1	$f_t(v_{\text{avg}})$
	Data-informed (running)	\hat{q}_{run}		Spline-based derivatives of \hat{q}_{run}	0.1	0.01	0.1	$f_t(v_{\text{avg}})$
	Quasi-random	0 except $q_{\text{pelvis}} = f_q(v_{\text{avg}}, t_f)$ $q_{\text{pelvis up}} = \text{standing}$	$v_{\text{pelvis for}} = v_{\text{avg}}$	0 except $v_{\text{pelvis for}} = v_{\text{avg}}$	0.1	0.01	0.1	$f_t(v_{\text{avg}})$
	Full optimal solution (OS) at closest speed		OS at closest speed					
Different speeds	Partial optimal solution (OS) at closest speed		OS at closest speed (q_{opt})	Spline-based derivatives of q_{opt}	0.1	0.01	0.1	OS at closest speed

Table C.1: Initial guesses. Details for each initial guess. \hat{q}_{walk} and \hat{q}_{run} refer to the walking and running joint positions, respectively, averaged across experimental trials, pelvis for and pelvis up refer to the forward and upward pelvis translations, respectively, $f_q(v_{\text{avg}}, t_f)$ describes a linear displacement as a function of speed v_{avg} and time t_f , standing refers to the upright standing posture and $f_t(v_{\text{avg}})$ is an expression for t_f as a function of v_{avg} (t_f from 0.70 to 0.35 s by increments of -0.018 s associated with imposed speed v_{avg} from 0.73 to 2.73 m s^{-1} by increments of 0.1 m s^{-1}). For the initial guesses based on the full and partial optimal solutions at closest speed, we started from the preferred walking speed (1.33 m s^{-1}) for which we selected the result with the lowest optimal cost from the data-informed (walking and running) and quasi-random initial guesses. For the remaining speeds, optimal results at the closest speed used to generate the initial guess were obtained using the same approach for determining the initial guess.

Metabolic energy model	Negative mechanical work	Muscle lengthening heat rate	Motor unit recruitment model
Bhargava <i>et al.</i> (2004)	Excluded	$f_B(\cdot)$	Included
Umberger <i>et al.</i> (2003)	Included	$f_U(\cdot)$	Excluded
Umberger (2010)	Excluded	$\frac{3}{40}f_U(\cdot)$	Excluded
Uchida <i>et al.</i> (2016)	Included	$f_U(\cdot)$	Included

Table C.2: Metabolic energy model properties. Main differences between metabolic energy models. The models of Umberger *et al.* (2003), Umberger (2010), and Uchida *et al.* (2016) are the same except in their treatment of negative mechanical work, muscle lengthening heat rate, and motor unit recruitment. The functions $f_B(\cdot)$ and $f_U(\cdot)$ describe the muscle lengthening heat rate for the models of Bhargava *et al.* (2004) and Umberger *et al.* (2003), respectively. In Umberger (2010), $f_U(\cdot)$ is scaled down with respect to Umberger *et al.* (2003) to compensate for the exclusion of negative mechanical work.

N_m	Speed	Case	N_s	CPU time mean(std)
50	Preferred walking speed	Nominal cost function	2	23 (2)
		No metabolic energy rate term	2	29 (7)
		No muscle activity term	2	38 (2)
		No squaring metabolic energy rate term	2	31 (2)
		No passive joint torque term	2	25 (3)
		Lower weight on joint accelerations	2	51 (10)
		Muscle strength deficits	*6	30 (5)
		Weak ankle plantarflexors	*6	32 (5)
		Sensitivity analyses	Metabolic energy models	44 (11)
		Co-contraction	*6	35 (19)
		Contact models	2	26 (3)
		Nominal cost function: from 0.73 to 2.73 m s ⁻¹	\$99	35 (14)
		Increased maximal muscle contraction velocities: from 1.33 to 2.23 m s ⁻¹	¶52	35 (17)
100	Preferred walking speed	Nominal cost function	2	65 (6)
		Passive transtibial prosthesis	2	77 (40)
				Total: 36(15) IPOPT: 25(11) NLP: 10(4)

Table C.3: **Computational (CPU) times.** Details for the 197 simulations. N_m and N_s are for number of mesh intervals and simulations, respectively. *6 results from simulations with three levels of weakness (50, 75, and 90%) or co-contraction (0.1, 0.15, and 0.2) with two initial guesses. \$99 results from simulations at 20 different speeds (from 0.73 to 2.73 m s⁻¹ by increments of 0.1 m s⁻¹ except for the preferred walking speed) with five initial guesses plus the preferred walking speed with the data-informed (running) initial guess minus two simulations that we excluded (no optimal solution). The simulations at the preferred walking speed with the data-informed (walking) and quasi-random initial guesses are counted in the nominal cost function case (first row). ¶52 results from simulations at 10 different speeds with increased maximal muscle contraction velocities (from 1.43 to 2.33 m s⁻¹ by increments of 0.1 m s⁻¹) with five initial guesses plus the preferred walking speed with the data-informed (walking and running) and quasi-random initial guesses minus one simulation that we excluded (no optimal solution). In the last row, we distinguish the time spent in IPOPT and to evaluate the NLP functions from the total time.

Appendix D

Study 5: supplementary material

	Glu max 1		Glu max 2		Glu max 3		Glu med 1		Glu med 2	
Generic Person	L	R	L	R	L	R	L	R	L	R
	13.35	13.44	12.93	12.95	12.85	12.72	6.23	6.11	10.36	10.34
Generic Person	6.67	6.72	6.47	6.47	7.99	7.61	3.11	3.05	5.18	5.45
	Glu med 3		Glu min 1		Glu min 2		Glu min 3		Add long	
Generic Person	L	R	L	R	L	R	L	R	L	R
	6.82	6.76	6.80	6.99	6.81	6.93	3.66	3.62	13.01	12.40
Generic Person	3.55	3.38	4.56	4.80	3.73	3.93	2.05	1.95	6.51	6.20
	Add brev		Add mag 1		Add mag 2		Add mag 3		Pectineus	
Generic Person	L	R	L	R	L	R	L	R	L	R
	13.93	13.08	9.10	8.29	11.67	11.19	12.63	13.13	16.06	14.41
Generic Person	8.68	8.27	7.55	7.19	5.88	5.60	6.63	6.56	10.04	9.57
	Iliacus		Psoas		Quad fem		Gemellus		Piri	
Generic Person	L	R	L	R	L	R	L	R	L	R
	10.35	10.06	9.50	9.35	3.71	3.72	1.67	1.57	2.28	2.31
Generic Person	5.17	5.03	4.75	4.68	4.16	3.96	1.90	1.81	1.21	1.15
	TFL		Gracilis		Semimem		Semiten		Bic fem lh	
Generic Person	L	R	L	R	L	R	L	R	L	R
	8.81	8.88	33.36	33.23	7.48	7.50	18.32	18.42	10.05	10.08
Generic Person	9.28	8.84	16.68	16.61	7.88	7.75	10.26	10.80	10.03	10.48
	Bic fem sh		Sartorius		Rectus fem		Vas med		Vas int	
Generic Person	L	R	L	R	L	R	L	R	L	R
	13.54	14.08	56.42	56.73	7.74	7.73	8.09	8.02	7.66	7.59
Generic Person	7.39	7.04	38.74	36.89	8.16	8.59	4.93	4.70	4.76	4.73
	Vas lat		Gas med		Gas lat		Soleus		Tib post	
Generic Person	L	R	L	R	L	R	L	R	L	R
	7.49	7.43	3.86	3.89	5.56	5.58	2.62	2.64	2.72	2.74
Generic Person	6.50	6.23	3.26	3.43	3.21	3.38	1.93	2.03	1.44	1.37
	Tib ant		Ext dig		Ext hal		Flex dig		Flex hal	
Generic Person	L	R	L	R	L	R	L	R	L	R
	8.45	8.52	8.83	8.84	9.51	9.54	2.90	2.91	3.64	3.65
Generic Person	4.22	4.26	4.64	4.42	5.01	4.77	1.53	1.45	1.92	1.83
	Per brev		Per long		Per tert					
Generic Person	L	R	L	R	L	R				
	4.15	4.23	4.26	4.28	6.32	6.50				
Generic Person	2.19	2.12	2.24	2.14	3.35	3.25				

Table D.1: **Generic and personalized optimal fiber lengths (cm).** L and R are for left and right, respectively. Person: personalized; Glu: gluteus; max: maximus; med: medius; min: minimus; add: adductor; long: longus; brev: brevis; mag: magnus; quad: quadratus; fem: femoris; piri: piriformis; TFL: tensor fasciae latae; semimem: semimembranosus; semiten: semitendinosus; bic: biceps; fem: femoris; lh: long head; sh: short head; vas: vastus; med: medialis; int: intermedius; lat: lateralis; gas: gastrocnemius; tib: tibialis; post: posterior; ant: anterior; ext: extensor; dig: digitalis; hal: hallucis; flex: flexor; per: peroneus; tert: tertius.

	Glu max 1		Glu max 2		Glu max 3		Glu med 1		Glu med 2	
Generic Person	L	R	L	R	L	R	L	R	L	R
	11.75	11.83	11.17	11.18	10.18	10.07	9.08	8.90	4.54	4.53
	11.34	11.93	12.01	11.92	13.23	13.51	9.94	10.46	8.35	8.79
	Glu med 3		Glu min 1		Glu min 2		Glu min 3		Add long	
Generic Person	L	R	L	R	L	R	L	R	L	R
	5.60	5.55	1.6	1.64	3.16	3.22	4.92	4.85	10.42	9.93
	8.47	8.48	3.12	3.29	6.11	6.43	7.06	6.88	11.85	11.29
	Add brev		Add mag 1		Add mag 2		Add mag 3		Pectineus	
Generic Person	L	R	L	R	L	R	L	R	L	R
	1.36	1.28	6.27	5.72	12.54	12.03	25.07	26.06	0.12	0.11
	2.69	2.56	4.81	4.58	13.12	12.50	27.07	25.78	0.23	0.22
	Iliacus		Psoas		Quad fem		Gemellus		Piri	
Generic Person	L	R	L	R	L	R	L	R	L	R
	9.31	9.05	10.33	10.16	1.65	1.66	2.71	2.55	9.29	9.40
	13.49	13.39	15.19	14.93	1.37	1.30	3.47	3.30	10.40	10.85
	TFL		Gracilis		Semimem		Semiten		Bic fem lh	
Generic Person	L	R	L	R	L	R	L	R	L	R
	39.41	39.73	13.27	13.22	33.56	33.64	23.88	24.01	31.45	31.53
	37.94	36.14	20.25	20.21	30.10	31.68	30.11	31.69	28.75	30.26
	Bic fem sh		Sartorius		Rectus fem		Vas med		Vas int	
Generic Person	L	R	L	R	L	R	L	R	L	R
	7.83	8.14	3.90	3.92	31.88	31.85	11.46	11.36	11.97	11.87
	10.38	10.93	7.80	7.42	28.93	29.40	14.25	14.95	14.30	15.05
	Vas lat		Gas med		Gas lat		Soleus		Tib post	
Generic Person	L	R	L	R	L	R	L	R	L	R
	14.01	13.88	34.99	35.23	33.44	33.56	23.41	23.61	27.22	27.35
	14.13	14.87	33.23	34.59	33.38	34.48	23.53	23.52	29.27	29.16
	Tib ant		Ext dig		Ext hal		Flex dig		Flex hal	
Generic Person	L	R	L	R	L	R	L	R	L	R
	19.23	19.39	29.86	29.91	26.12	26.21	34.07	34.18	32.18	32.3
	20.40	21.48	30.93	31.75	27.67	28.43	35.60	35.49	34.12	33.87
	Per brev		Per long		Per tert					
Generic Person	L	R	L	R	L	R				
	13.37	13.63	30.01	30.11	8.00	8.23				
	15.09	15.88	31.25	31.40	9.66	10.17				

Table D.2: **Generic and personalized tendon slack lengths (cm).** L and R are for left and right, respectively. Person: personalized; Glu: gluteus; max: maximus; med: medius; min: minimus; add: adductor; long: longus; brev: brevis; mag: magnus; quad: quadratus; fem: femoris; piri: piriformis; TFL: tensor fasciae latae; semimem: semimembranosus; semiten: semitendinosus; bic: biceps; fem: femoris; lh: long head; sh: short head; vas: vastus; med: medialis; int: intermedius; lat: lateralis; gas: gastrocnemius; tib: tibialis; post: posterior; ant: anterior; ext: extensor; dig: digitalis; hal: hallucis; flex: flexor; per: peroneus; tert: tertius.

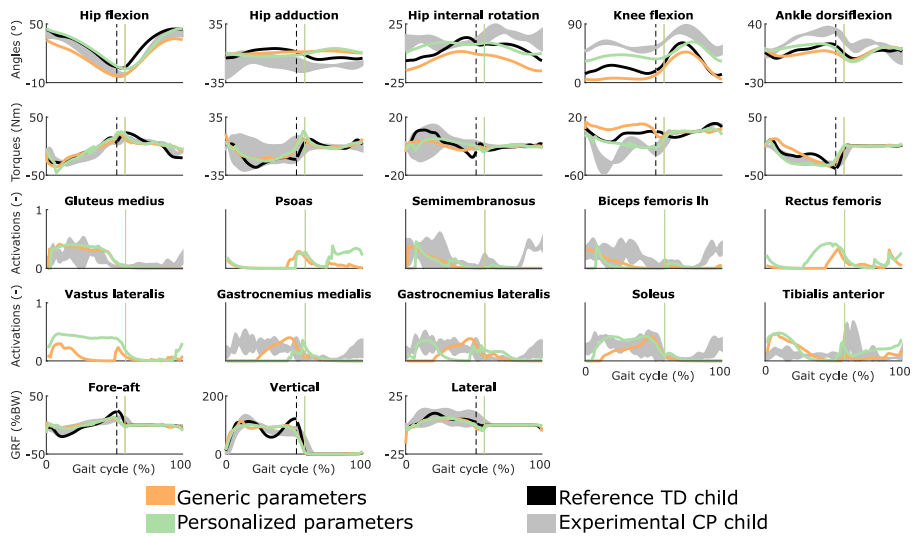


Figure D.1: Influence of the muscle-tendon parameters on the predicted walking gaits. Variables from the left leg are shown over a complete gait cycle; right leg variables are shown in Figure 7.2. Solid vertical lines indicate the transition from stance to swing. Experimental data is shown as mean \pm two standard deviations. Experimental EMG data was normalized to peak activations. Reference TD child data was available for a single gait cycle starting at right heel strike; left leg data was thus reconstructed from that gait cycle but is discontinuous as indicated by the dashed vertical lines. GRF is for ground reaction forces; BW is for body weight; COT is for metabolic cost of transport; lh is for long head.

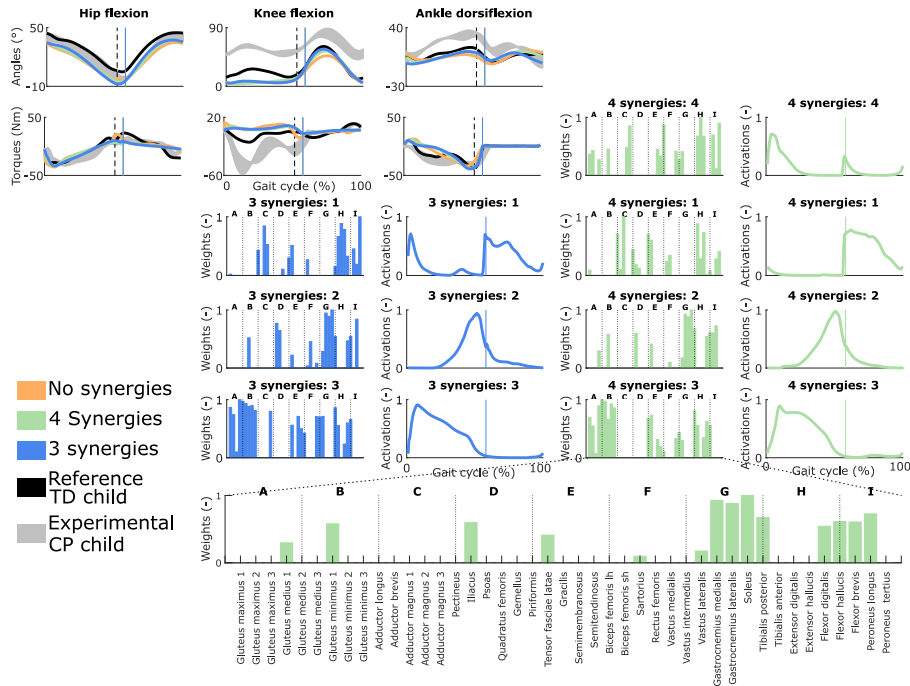


Figure D.2: Influence of the synergies on walking gaits predicted with the generic muscle-tendon parameters. Variables from the left leg are shown over a complete gait cycle; right leg variables are shown in Figure 7.3. Vertical lines (solid) indicate the transition from stance to swing. Panels of synergy weights are divided into sections (A-I) to relate bars to muscle names provided in the bottom bar plot, which is an expanded version of the plot of weights with title 4 synergies: 3. Lh and sh are for long and short head, respectively. Weights were normalized to one. Experimental data is shown as mean \pm two standard deviations. Reference TD child data was available for a single gait cycle starting at right heel strike; left leg data was thus reconstructed from that gait cycle but is discontinuous as indicated by the dashed vertical lines.

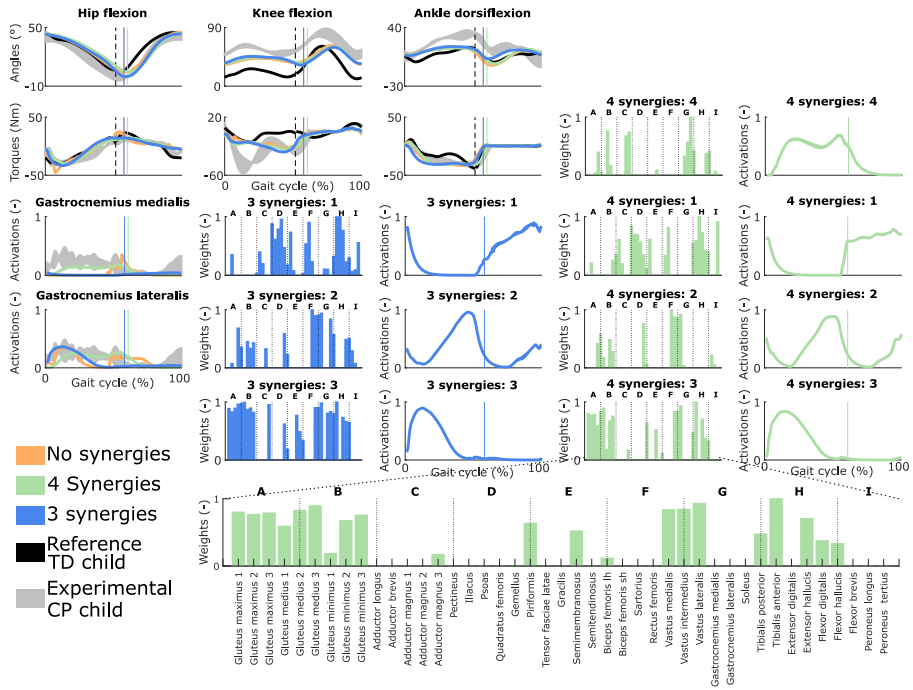


Figure D.3: Influence of the synergies on walking gaits predicted with the personalized muscle-tendon parameters. Variables from the left leg are shown over a complete gait cycle; right leg variables are shown in Figure 7.4. Vertical lines (solid) indicate the transition from stance to swing. Panels of synergy weights are divided into sections (A-I) to relate bars to muscle names provided in the bottom bar plot, which is an expanded version of the plot of weights with title 4 synergies: 3. Lh and sh are for long and short head, respectively. Weights were normalized to one. Experimental data is shown as mean \pm two standard deviations. Experimental EMG data was normalized to peak activations. Reference TD child data was available for a single gait cycle starting at right heel strike; left leg data was thus reconstructed from that gait cycle but is discontinuous as indicated by the dashed vertical lines.

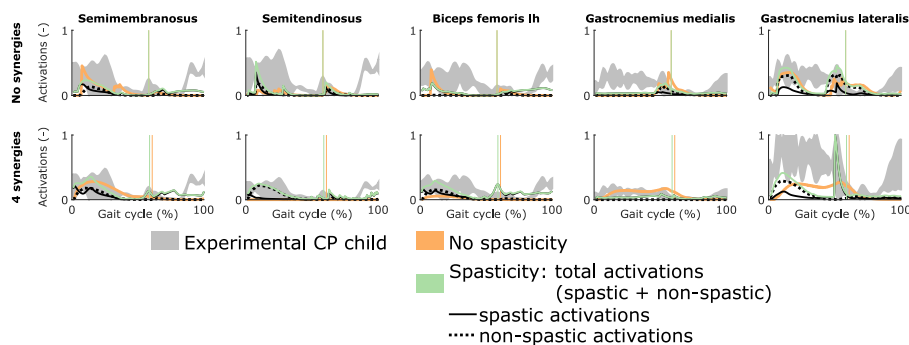


Figure D.4: Influence of spasticity on the predicted muscle activity. Activations from left leg muscles only are shown over a complete gait cycle; right leg activations are shown in Figure 7.5. When accounting for spasticity, total activations (green) combine spastic (solid black) and non-spastic (dotted black) activations. Vertical lines indicate the transition from stance to swing. Experimental data is shown as mean \pm two standard deviations. Experimental EMG data was normalized to peak activations. Lh is for long head.

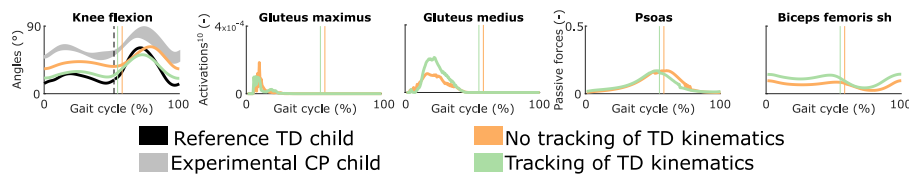


Figure D.5: Influence of tracking the TD kinematics on predicted walking gaits. Variables from the left leg are shown over a complete gait cycle; right leg variables are shown in Figure 7.6. Vertical lines indicate the transition from stance to swing. Experimental data is shown as mean \pm two standard deviations. Muscle fatigue is modeled by activations at the tenth power. Passive muscle forces are normalized by maximal isometric muscle forces. Sh is for short head.

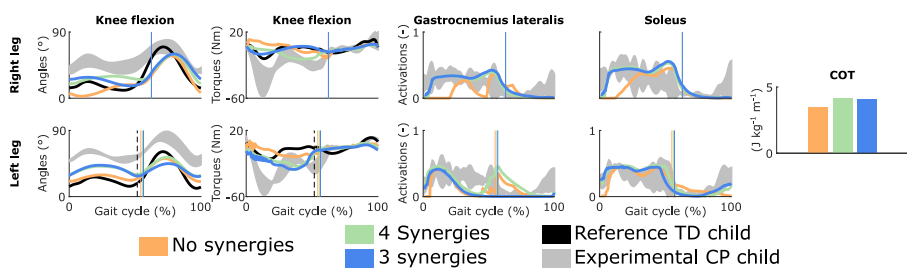


Figure D.6: Influence of the synergies on walking gaits predicted with the personalized muscle-tendon parameters while tracking the TD kinematics. Solid vertical lines indicate the transition from stance to swing. Experimental data is shown as mean \pm two standard deviations. Experimental EMG data was normalized to peak activations. Reference TD child data was available for a single gait cycle starting at right heel strike; left leg data was thus reconstructed from that gait cycle but is discontinuous as indicated by the dashed vertical lines.

Appendix E

OpenSim versus Human Body Model: A comparison study for the lower limbs during gait

Published as:

Falisse A., Van Rossum S., Gijsbers J., Steenbrink F., van Basten B.J.H., Jonkers I., van den Bogert A.J., De Groot F. *OpenSim versus Human Body Model: a comparison study for the lower limbs during gait*, (2018). Journal of Applied Biomechanics, **34**(6): 496-502.

Abstract

Musculoskeletal modeling and simulations have become popular tools for analyzing human movements. However, end-users are often not aware of underlying modeling and computational assumptions. This study investigates how these assumptions affect biomechanical gait analysis outcomes performed with Human Body Model and the OpenSim gait2392 model. We compared joint kinematics, kinetics, and muscle forces resulting from processing data from seven healthy adults with both models. Although outcome variables had similar patterns, there were statistically significant differences in joint kinematics (maximal difference: 9.8 ± 1.5 degrees in sagittal plane hip rotation), kinetics (maximal difference: 0.36 ± 0.10 N·m/kg in sagittal plane hip moment), and muscle forces (maximal difference: 8.51 ± 1.80 N/kg for psoas). These differences might be explained by differences in hip and knee joint center locations up to 2.4 ± 0.5 and 1.9 ± 0.2 cm in the postero-anterior and infero-superior directions, respectively, and by the offset in pelvic reference frames of about 10 degrees around the medio-lateral axis. Model choice may not influence the conclusions in clinical settings where the focus is on interpreting deviations from reference data but will affect the conclusions of mechanical analyses where the goal is to obtain accurate estimates of kinematics and loading.

Introduction

Musculoskeletal models for biomechanical simulations have become increasingly popular to analyze human movement. In addition to joint kinematics and kinetics, musculoskeletal models enable researchers and clinicians to assess other biomechanical variables such as muscle lengths and forces. Different software systems were developed for modeling and analyzing human movement (e.g. AnyBody [252], OpenSim [112], and Human Body Model [127]) and there is an increasingly large body of literature reporting analyses of motion based on these software systems. OpenSim offers several musculoskeletal models with varying complexity (e.g. number of muscles and kinematic degrees of freedom (DOFs)), therefore giving users multiple choices for their study. Roelker *et al.* [253] recently provided valuable information about which OpenSim model to use for studying gait by investigating the effects of using different models on joint kinematics, kinetics, and muscle function. They reported that differences between models were mainly due to different coordinate system definitions and muscle parameters and concluded that the gait2392 model is sufficiently complex to study gait in healthy adults. When interpreting differences in results obtained with different software systems, the added challenge is that

discrepancies might result from differences between data processing workflows besides differences between models. To our knowledge, no studies have assessed differences in joint kinematics, kinetics and muscle forces induced by the use of different models in different software systems. In this study, we compared the clinically-oriented Human Body Model with the research-oriented OpenSim gait2392 model [63]. The goals of this comparison were (1) to evaluate how the model and computational choices influence joint kinematics, kinetics, and muscle forces resulting from processing the same experimental gait data and (2) to relate the outcome differences to the underlying modeling and computational assumptions.

Methods

Seven healthy adults (three females and four males, age: 30.7 ± 6.1 years, height: 176.7 ± 7.1 cm, and weight: 69.4 ± 6.4 kg) gave informed consent to participate in the study approved by the Ethics Committee at UZ Leuven (Belgium). Each subject was instrumented with 22 retro-reflective skin-mounted markers, corresponding to the Human Body Model marker set excluding arms, head, and torso [127]. Three-dimensional marker coordinates were recorded (100 Hz) using a ten-camera motion capture system (Vicon, Oxford, UK). Ground reaction forces were recorded (1000 Hz) using two force plates (AMTI, Watertown, USA). The subjects were instructed to walk at self-selected speed.

The experimental data were processed with OpenSim 3.3 using the gait2392 model, later referred to as OpenSim model, and with the Gait Offline Analysis Tool 3.3 (Motekforce Link B.V., Amsterdam, The Netherlands) that integrates Human Body Model. The metatarsophalangeal joints of the OpenSim model were locked so that both models had 21 similar DOFs actuated by 43 muscles per leg. Marker information from a standing calibration trial was used to scale the OpenSim model to the subjects' anthropometry using OpenSim's Scale tool (see Tables E.4-E.5 in Supplementary Material for the marker pairs used to scale the segments' dimensions and for the marker weights used to fit the model's pose to the standing calibration pose, respectively) and to initialize a new model in Human Body Model [127].

The processing pipeline with both systems consisted of inverse kinematics, kinematic filtering, inverse dynamics, and static optimization. The same weighted least squares problem (see Table E.6 in Supplementary Material for the marker weights) was solved with both systems during inverse kinematics. Details

about the different optimization algorithms can be found in Supplementary Material. The resulting root mean square (RMS) and maximum marker errors between modeled and measured marker positions were compared using a Wilcoxon signed rank statistical analysis. Since OpenSim's effective dual-pass filter cutoff frequency is lower than the user-specified cutoff frequency [254], a scaling factor was applied to match Human Body Model's effective 6 Hz cutoff frequency when filtering the kinematics and the ground reaction forces (more details in Supplementary Material). Human Body Model is real-time and induces a 37 ms time delay when filtering the kinematics [127]. This delay was corrected when comparing the results.

Different static optimization formulations are available in both systems. Human Body Model enables scaling muscle activity by muscle volume in the objective function (default setting) [255, 127] whereas OpenSim enables considering the muscles as ideal force generators or constraining them by their force-length-velocity properties (more details in Supplementary Material) [27, 256]. All formulations were tested to investigate their impact on the muscle force estimation. Similar optimization problems are solved in OpenSim and Human Body Model when the muscles are considered as ideal force generators and when muscle activity is not scaled by muscle volume. However, OpenSim enables the use of reserve actuators whereas Human Body Model does not use upper bounds on muscle activations to guarantee the feasibility of the optimization problem and both systems use different optimization algorithms (more details in Supplementary Material). Both models use identical values for maximal isometric muscle forces to relate muscle activations to muscle forces but there are small differences in moment arms. Human Body Model uses polynomial functions of the joint angles whereas OpenSim uses muscle-tendon paths (line segments between muscle points defined in segmental reference frames) to compute moment arms [127]. Human Body Model's polynomials are defined such that the moment arms computed based on these polynomials match the OpenSim moment arms within 2 mm for the generic model. Moment arms do not depend on subject size in Human Body Model but are influenced by scaling in OpenSim.

Since the number of gait trials with valid force plate contacts was unevenly divided among subjects, we selected one representative trial for each leg of each subject based on the kinematic errors. We considered each leg apart to increase the size of the dataset. Asymmetry between both legs may exist [257], contributing to the variability in our data. The representative trial was the trial with the RMS inverse kinematic marker error that best matched the error averaged over all trials [258]. This resulted in 14 trials (stride duration: 1.05

± 0.06 s) that were used for further analysis. Joint kinematics, kinetics, and muscle forces were time-normalized to the gait cycle duration and averaged over the 14 representative trials. Biomechanical outcomes resulting from the different models and static optimization formulations were analyzed using non-parametric paired t-tests with the one-dimensional statistical parametric mapping package SPM1D [259, 260]. The level of significance was set to $p < .05$.

To evaluate joint center location differences between models, we calculated the transformations between corresponding segment reference frames that best mapped the OpenSim model markers to the corresponding Human Body Model markers in a least squares sense. We then used these transformations to express the OpenSim model joint centers in the corresponding Human Body Model reference frames and computed the distance between joint centers of both models. To evaluate pelvic reference frame differences, we similarly calculated the transformation between pelvic reference frames and expressed the difference in orientation in Euler angles (sequence of rotation axes: medio-lateral, infero-superior, postero-anterior).

Results

Differences in joint kinematics were found when processing the same experimental gait data with the OpenSim model and with Human Body Model. Joint kinematics showed similar patterns but statistically differed for all DOFs (maximal statistical differences: 9.8 ± 1.5 degrees, 5.5 ± 1.0 degrees, 8.5 ± 3.6 degrees, 5.0 ± 1.0 degrees, 6.5 ± 1.5 degrees, and 15.6 ± 6.2 degrees for the sagittal hip, frontal hip, transversal hip, sagittal knee, sagittal ankle, and subtalar rotations, respectively) during large intervals ranging from 33% (sagittal ankle rotation) to 100% (sagittal hip rotation) of the gait cycle. An offset in sagittal hip rotation (flexion/extension) was observed (Figure E.1). After scaling in OpenSim, RMS marker error (1.2 ± 0.1 cm) and maximal marker error (2.2 ± 0.2 cm) of the markers corresponding to anatomical landmarks were close to OpenSim's recommendations [261] (smaller than 1 and 2 cm, respectively) and had a low sensitivity to user inputs (marker pairs and weights used for scaling) (see Table E.7 in Supplementary Material). RMS and maximum marker errors after inverse kinematics were statistically smaller ($p < .001$) with Human Body Model (0.5 ± 0.1 and 1.1 ± 0.3 cm, respectively) than with the OpenSim model (0.7 ± 0.1 and 1.6 ± 0.4 cm, respectively). Marker errors met OpenSim's best practices [261] (RMS marker error smaller than 2 cm and maximum marker error smaller than 2-4 cm) for both models and had a low sensitivity to user inputs (marker pairs and weights used for scaling and marker weights used for

inverse kinematics) in OpenSim (see Table E.8 in Supplementary Material).

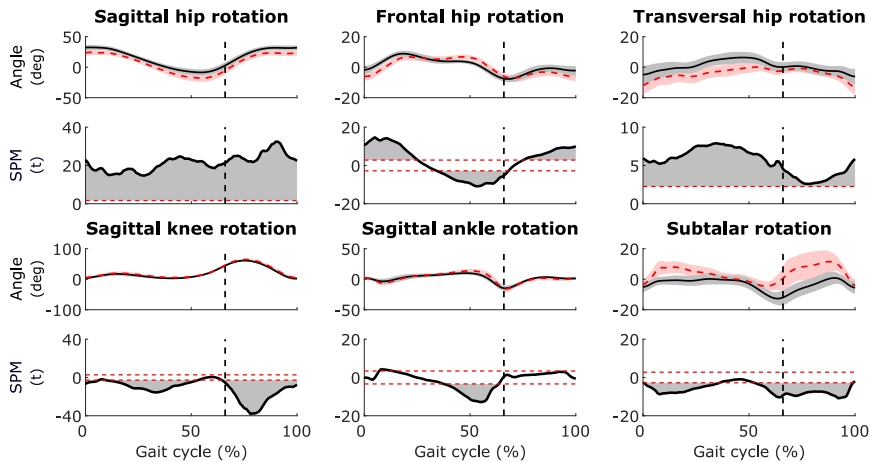


Figure E.1: [First and third row] Comparison of joint kinematics calculated with the OpenSim model (dashed red) and Human Body Model (black). [Second and fourth row] Results from the statistical analysis using non-parametric paired t-tests in SPM1D. Gray shaded areas above and below the red dashed lines indicate significant differences. The vertical black dashed line indicates the transition from stance to swing.

Differences in joint kinetics were found between the OpenSim model and Human Body Model. Joint moments showed similar patterns but statistically differed during several intervals of the gait cycle for all DOFs (maximal statistical differences: $0.36 \pm 0.10 \text{ N}\cdot\text{m}/\text{kg}$, $0.21 \pm 0.03 \text{ N}\cdot\text{m}/\text{kg}$, $0.09 \pm 0.02 \text{ N}\cdot\text{m}/\text{kg}$, $0.18 \pm 0.04 \text{ N}\cdot\text{m}/\text{kg}$, $0.18 \pm 0.03 \text{ N}\cdot\text{m}/\text{kg}$, and $0.25 \pm 0.11 \text{ N}\cdot\text{m}/\text{kg}$ for the sagittal hip, frontal hip, transversal hip, sagittal knee, sagittal ankle, and subtalar moments, respectively) (Figure E.2).

Differences in muscle forces were found between the OpenSim model and Human Body Model. Muscle forces computed using similar static optimization formulations showed similar patterns but statistically differed during several intervals of the gait cycle for most muscles (Figure E.3 and Figures E.4-E.7 in Supplementary Material). The largest statistical differences were observed for the psoas ($8.51 \pm 1.80 \text{ N}/\text{kg}$), soleus ($8.11 \pm 1.30 \text{ N}/\text{kg}$), and peroneus longus ($6.50 \pm 2.59 \text{ N}/\text{kg}$). Maximum absolute reserve actuators were smaller than $4.0e-4 \text{ N}\cdot\text{m}/\text{kg}$ in OpenSim, which met the requirements advocated by Hicks *et al.* [262]. In Human Body Model, muscle activations exceeded one (maximum

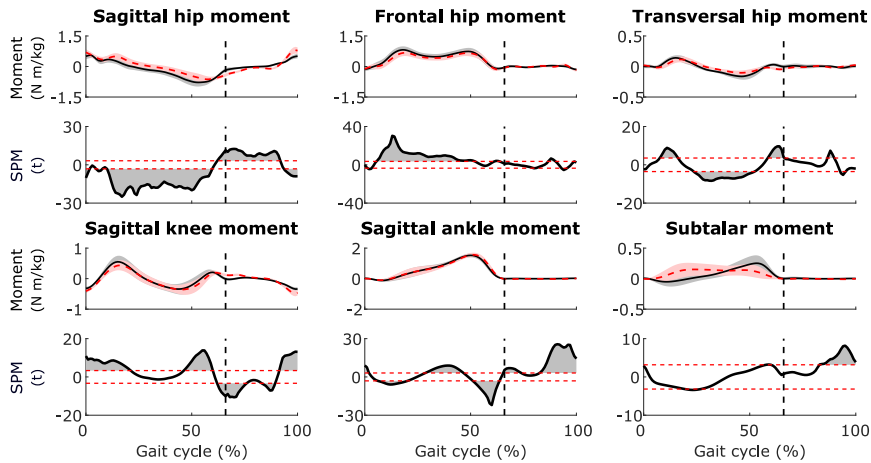


Figure E.2: [First and third row] Comparison of joint kinematics calculated with the OpenSim model (dashed red) and Human Body Model (black). [Second and fourth row] Results from the statistical analysis using non-parametric paired t-tests in SPM1D. Gray shaded areas above and below the red dashed lines indicate significant differences. The vertical black dashed line indicates the transition from stance to swing.

1.1) for the psoas in four out of 14 trials during small intervals of the gait cycle (<5%). Differences in modeling muscle function and performance criteria had an effect on the estimated muscle forces. Constraining the muscles by their force-length-velocity properties in OpenSim induced statistical differences for most muscles (Figures E.8-E.11 in Supplementary Material) although, overall, the impact was relatively limited. The soleus, tibialis posterior, and medial gastrocnemius showed the largest statistical differences (4.27 ± 1.28 N/kg, 3.84 ± 2.76 N/kg, and 3.73 ± 1.21 N/kg, respectively). Scaling muscle activity by muscle volume in the Human Body Model static optimization objective function had a more pronounced influence as the contribution of smaller muscles increased at the expense of larger muscle (Figures E.12-E.15 in Supplementary Material). In particular, we observed a statistical decrease in force for large muscles including the psoas, gluteus maximus 2 (medial part), and soleus (maximal statistical differences: 6.01 ± 0.85 N/kg, 3.00 ± 0.48 N/kg, and 2.40 ± 0.73 N/kg, respectively) and a statistical increase in force for small muscles including the piriformis, gluteus minimus 3 (posterior part), and tensor fasciae latae (maximal statistical differences: 3.35 ± 0.58 N/kg, 2.10 ± 0.40 N/kg, and 1.48 ± 0.31 N/kg, respectively).

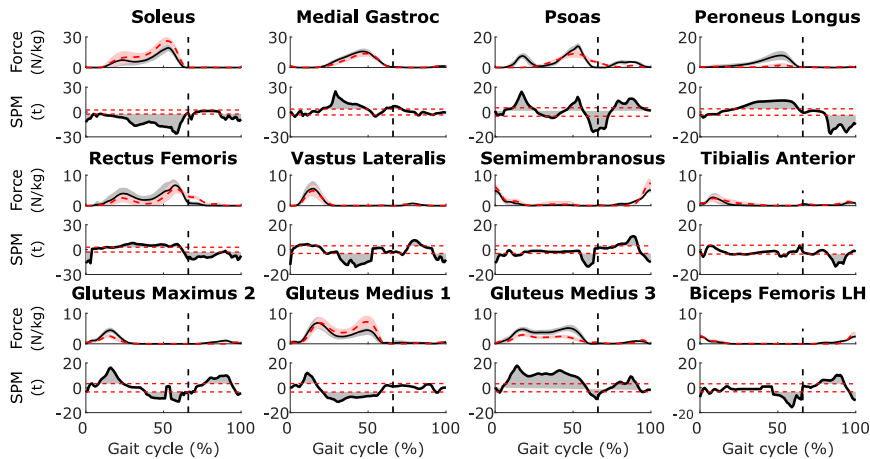


Figure E.3: [First, third, and fifth row] Comparison of muscle forces estimated with the OpenSim model (dashed red) and Human Body Model (black). Muscle forces estimated without taking force-length-velocity properties into account (OpenSim) and without scaling muscle activity by muscle volume in the static optimization objective function (Human Body Model). [Second, fourth, and sixth row] Results from the statistical analysis using non-parametric paired t-tests in SPM1D. Gray shaded areas above and below the red dashed lines indicate significant differences. The vertical black dashed line indicates the transition from stance to swing. See Figures E.4-E.7 in Supplementary Material for other muscles.

Definitions of reference frames and joint centers differed between the OpenSim model and Human Body Model. First, the pelvic reference frames had different orientations as calculated through the Euler angles (Table E.1). The largest difference was on average 10.2 degrees about the medio-lateral axis. Second, the hip joint centers had different locations (Table E.2). In particular, the hip joint center was on average 2.4 cm more anterior in Human Body Model as compared to the OpenSim model. Third, the tibia origins, defining the position of the knee joint centers, had different locations in both models (Table E.3). In particular, the tibia origin was on average 1.9 cm more superior in the OpenSim model as compared to Human Body Model. Finally, the subtalar axis was defined differently in both models. The subtalar axes in Human Body Model and in the OpenSim model are inclined by 42 and 37 degrees, respectively, from the transversal plane and deviate medially by -23 and -9 degrees, respectively, from the sagittal plane [263].

Rotation axes	Subjects							mean \pm std
	1	2	3	4	5	6	7	
Medio-lateral	10.1	10.3	10.5	10.8	9.2	9.3	11.1	10.2 \pm 0.7
Infero-superior	-1.1	0.8	0.1	-0.3	1.0	-0.4	-2.3	-0.3 \pm 1.1
Postero-anterior	-0.6	-1.0	1.3	-0.3	0.2	-1.4	-0.2	-0.3 \pm 0.9

Table E.1: Differences in pelvic reference frame orientation between **OpenSim model** and **Human Body Model** evaluated through Euler angles (degree). The Euler angles describe the orientation of the pelvic reference frame of the OpenSim model with respect to the pelvic reference frame of Human Body Model (sequence of rotation axes: medio-lateral, infero-superior, postero-anterior).

Axes	Subjects							mean \pm std
	1	2	3	4	5	6	7	
Postero-anterior	2.2	2.3	2.5	1.9	2.9	2.7	2.5	2.4 \pm 0.3
Infero-superior	1.2	1.6	1.0	0.6	1.4	1.7	2.8	1.5 \pm 0.7
Medio-lateral	1.0	0.7	1.3	0.9	0.8	0.8	1.5	1.0 \pm 0.3

Table E.2: Differences (cm) in right hip joint center location between **OpenSim model** and **Human Body Model**. The differences are between the location of Human Body Model right hip joint center and the location of the OpenSim model right hip joint center expressed in Human Body Model pelvic reference frame. Positive results indicate a more anterior/superior/lateral location in Human Body Model as compared to the OpenSim model.

Axes	Subjects							mean \pm std
	1	2	3	4	5	6	7	
Postero-anterior	0.1	0.3	0.4	0.2	0.3	0.2	0.5	0.3 \pm 0.1
Infero-superior	-2.3	-1.8	-2.2	-1.7	-1.9	-2.0	-1.8	-1.9 \pm 0.2
Medio-lateral	1.5	0.6	0.6	1.0	0.1	1.4	0.7	0.9 \pm 0.5

Table E.3: Differences (cm) in right tibia coordinate frame origin location between **OpenSim model** and **Human Body Model**. The differences are between the location of Human Body Model right tibia coordinate frame origin and the origin of the OpenSim model right tibia coordinate frame expressed in Human Body Model femur reference frame. Positive results indicate a more anterior/superior/lateral location in Human Body Model as compared to the OpenSim model.

Discussion

The primary goals of this study were to compare the OpenSim gait2392 model with Human Body Model based on joint kinematics, kinetics, and muscle forces calculated during gait for healthy adults and to relate the outcome differences to the modeling and computational assumptions. Overall, outcome variables had similar patterns across models but they statistically differed in large intervals of the gait cycle.

OpenSim and Human Body Model generate different kinematic models. In particular, we observed large differences in hip and knee joint center locations. Human Body Model estimates the hip joint center locations based on pelvic width and depth using Harrington equations [264]. In OpenSim, the hip joint center locations are scaled with the pelvis. In this study, the hip joint center locations from the generic OpenSim model were scaled in the medio-lateral direction with pelvic width and in the infero-superior and postero-anterior directions with pelvic depth. Kainz *et al.* [265] found that Harrington equations are more accurate than other regression equations but suggest the use of functional methods, such as geometric sphere fitting methods [266, 267], in people with sufficient active hip range of motion, as the subjects in this study. More accurate methods to define subject-specific kinematic models [268] have not been integrated in existing software and are not widely adopted. The OpenSim model and Human Body Model also rely on different joint axis definitions. First, in Human Body Model, the subtalar axis is defined based on the average subtalar joint from Isman and Inman [269] whereas the OpenSim model subtalar axis is derived from Inman [270] and is in the experimental range of values (20 to 68 and -47 to -4 degrees for the horizontal inclination and medial deviation, respectively) obtained from cadaver measurements [269]. Second, the OpenSim model uses a moving knee flexion axis [271] to account for the translation of the tibiofemoral joint in the sagittal plane whereas Human Body Model uses a fixed axis. Finally, there is a large offset between the pelvic reference frames (rotation about the medio-lateral axis) in both models. It is worth mentioning that Roelker *et al.* also reported differences in pelvic neutral position definition between different OpenSim models [253]. This suggests, along with the findings of this study, that this modeling feature is highly variable across existing musculoskeletal models. The differences in pelvic reference frame orientation cause the observed offset in sagittal hip rotation. In combination with the different hip joint center locations, the different pelvic reference frames also explain the different hip rotations in the frontal and transversal planes. The different hip and knee joint center locations and subtalar axis definitions can explain the differences in knee and subtalar rotations. We expect the computational choices (e.g. optimization

algorithms and stopping criteria) related to the approaches used for solving inverse kinematics in OpenSim and Human Body Model to have contributed to a lesser extent to the differences in kinematic results than the joint definition differences. Given that OpenSim and Human Body Model use the same initial guesses for the optimization algorithms and that Human Body Model allows a relatively long computational time to solve the inverse kinematic optimization problem, we do not think that convergence to different local optimal or not achieving convergence contributed to the observed differences in kinematics.

The filter used to process the inverse kinematic results has a different order in OpenSim (third order) and in Human Body Model (second order). The users have no access to this computational feature, nor through the graphical user interfaces (GUI) of both software systems, nor through to the application programming interface (API) of OpenSim. We therefore choose to present results obtained with the built-in filters since we expect that most users will perform their entire data processing with either OpenSim or Human Body Model. However, we evaluated the impact of using a second order filter versus a third order filter by processing the OpenSim inverse kinematic results of one trial outside the OpenSim platform before performing inverse dynamics and static optimization. The largest differences in joint moments and muscle forces were 0.06 Nm/kg for the sagittal hip moment and 0.46 N/kg for the rectus femoris, respectively. As a general limitation of this study, due to the limited flexibility of the Human Body Model and OpenSim platforms, we were unable to investigate the influence of each individual modeling and computational choice on the results. As a result, we could only outline important differences in underlying modeling and data processing assumptions without quantifying their relative contributions.

Joint kinematic differences directly affect the joint moments. Other factors also play a role such as different inertial properties [272] and different joint definitions. The different joint definitions will result in different locations and orientations of the joint centers and axes in space after inverse kinematics, and hence the forces and moments applied in the joints to counteract the ground reaction forces and gravity will differ. In particular, we have studied the sensitivity of the joint moments to the knee flexion axis (moving versus fixed) in OpenSim and observed statistical differences (maximal statistical difference: 0.05 ± 0.01 N·m/kg for the knee) (Figure E.16 in Supplementary Material).

Differences in muscle forces result from differences in joint kinematics and kinetics as well as from differences in moment arms. These differences in moment arms are due to the different computation of moment arms in both

models, to the different joint kinematics that are inputs to this computation, and to the influence of the subject size that is taken into account in OpenSim but not in Human Body Model. Differences in joint kinematics between the OpenSim model and Human Body Model induced differences in moment arms up to 1.5 cm (quadratus femoris for hip flexion). Differences in moment arms between the smallest (height: 169 cm) and the tallest (height: 190 cm) subjects were up to 0.9 cm (gluteus maximus 3 (posterior part) for hip flexion) in the anatomical position. In Human Body Model, psoas muscle activations exceeded one suggesting an unrealistic muscle force distribution. It was more optimal to activate the psoas above one than increasing the contribution of another muscle (e.g. rectus femoris). Muscle activations exceeding one were dependent on the static optimization objective function. In more detail, piriformis muscle activations exceeded one (maximum 1.1) for two out of 14 trials during small intervals of the gait cycle (<7%) when scaling muscle activity by muscle volume in the static optimization objective function. This underlines the importance of the criterion used to solve the muscle redundancy problem. However, it is to be mentioned that muscle activations will also depend on the muscle-tendon parameters, which appear in the objective function. We expect that more representative muscle-tendon parameters will result in muscle activations smaller than one during gait for both objective functions. Overall, activations larger than one are not physiological and should be identified as a limitation of the model. Finally, no experimental muscle activations (electromyography) were available to further validate the static optimization results, which is a limitation of this study.

Modeling assumptions affect the estimation of muscle forces. In particular, the sensitivity of the results to the choice of the objective function was underlined by the differences observed in estimated muscle forces when scaling muscle activity by muscle volume in the static optimization objective function in Human Body Model. Constraining the muscles by their force-length-velocity properties in OpenSim had less influence on the estimated muscle forces. However, this constraint might be more important for faster motions for which muscle properties and dynamics play a more important role [53, 47]. Finally, for various reasons, we expect different optimization algorithms and stopping criteria in OpenSim and Human Body Model to have a limited influence on the static optimization results. First, we have studied the sensitivity of the results to the stopping criteria in OpenSim and found that muscle activations differed at most by 1e-4 (biceps femoris short head) when changing the convergence criterion (from 1e-4 to 1e-5) and the maximum number of iterations (from 100 to 10,000). Second, Human Body Model allows a relatively long computational time to solve the static optimization problem, limiting the risks of sub-optimal solutions. Third, the static optimization problem is a quadratic programming problem

(i.e. local optima are global optima) and the initial guesses will therefore not affect the results.

OpenSim and Human Body Model were designed with different applications and target users in mind. Human Body Model is real-time and aimed towards clinicians with no particular technical skills. It relies on a pre-defined muscle model which may not be suitable when subject-specificity is required [273, 168]. OpenSim is open-source, enables subject-specific modeling, and is more aimed towards researchers with technical background. Its standard workflow is offline although an OpenSim-based real-time system was recently developed to compute inverse kinematics and inverse dynamics for lower-limb applications [274]. Finally, Human Body Model does not require user inputs to create a model and is therefore robust against user errors. In contrast, OpenSim provides the users with more flexibility in the scaling and inverse kinematic setups. However, the user choices can have an influence on the results (see Table E.8 in Supplementary Material).

We found differences in joint kinematics, kinetics, and muscle forces resulting from processing the same experimental gait data from healthy adults using the OpenSim model and Human Body Model. Both models are similar in many aspects but differ in the definitions of the kinematic model (joint center and axis definitions) and we expect these differences to be the main causes for the outcome differences. Since different computational choices resulted in different muscle forces, continued efforts for validating models and methods are required [262, 275]. Depending on the aim, differences in biomechanical variables between models and software systems may be more or less important. In clinical analyses, focus is on interpreting deviations from reference data. Processing reference and patient data with the same model and software system is hence in general sufficient to deal with model and computational uncertainties. We compared standard deviations of joint kinematics and kinetics between the OpenSim model and Human Body Model as well as which trials deviated more than one standard deviation from the mean (see Table E.9 in Supplementary Material). Since we observed similar results, we expect similar interpretations when comparing reference and patient data based on either the OpenSim model or Human Body Model. In contrast, as described by Roelker *et al.* [253], processing reference and patient data with different models and software systems may result in incorrect interpretations if discrepancies between models and software systems are not taken into account. In mechanical analyses, the goal is to obtain accurate estimates of kinematics and loading and, therefore, discrepancies between models or computational choices may lead to different conclusions. In such cases, musculoskeletal models should be used with care.

Similarly, differences in biomechanical variables are important when comparing results from studies in the literature that were obtained with different models and software systems. Differences that are smaller than the differences reported in this study cannot be attributed to differences in the movement execution.

Based on the results of this study, we recommend researchers aiming to compare their results with results from other simulation studies to pay special attention to the definition of the pelvic reference frame, the hip and knee joint centers, and the static optimization cost function. Since it is currently unknown which cost function provides the 'best' approximation of the human control strategy, computed muscle activations should be interpreted carefully and, whenever possible, compared to experimentally measured muscle activations. Muscle forces are the main determinants of lower limb contact forces during walking. The large differences in muscle forces might therefore influence the evaluation of joint loading. We previously found differences in knee joint loading of about 8 N/kg between healthy individuals and patients with severe osteoarthritis [276]. Similar differences might be caused by the differences in magnitudes of the muscle forces we report here. However, all muscles spanning a joint determine joint loading and therefore additional model comparison is needed to evaluate the effect of model choice on joint loading. Nevertheless, we advise researchers to be aware of the effect of modeling choices on computed muscle forces when evaluating joint loading. Overall, in model-based biomechanical analyses, users should be conscious of the modeling and computational assumptions and their influence on the biomechanical variables.

Acknowledgments

Research funded by a PhD grant (1S35416N) from the Research Foundation Flanders (FWO).

Supplementary Material

Scaling

Tables E.4 and E.5 respectively give the marker pairs and weights that were used during scaling in OpenSim. When scaling the pelvis uniformly, the scaling applied to the pelvis in the postero-anterior and infero-superior directions is the same as the scaling applied in the medio-lateral direction (i.e. based on the marker pair R ASIS and L ASIS defining pelvic width). We have investigated the sensitivity of the scaling RMS marker error, scaling maximum marker error, and inverse kinematic results to the scaling setup in OpenSim. In particular, we have compared three scaling setups. The first setup scaled the pelvis uniformly and used the set of marker weights S_1 (Table E.5). The second setup scaled the pelvis non-uniformly and used the set of marker weights S_1 . The third setup scaled the pelvis non-uniformly and used the set of marker weights S_2 (Table E.5). The results presented in this study are based on a non-uniform scaling of the pelvis and the set of marker weights S_1 (second setup). The results of the sensitivity analyses are presented in Tables E.7 and E.8.

Filtering

OpenSim uses a third-order zero-phase forward and reverse low-pass Butterworth filter to process the joint kinematics. Since this filter is applied twice (forward and reverse), the frequency response is squared compared to the response of a single-pass filter such as the Human Body Model real-time filter. To compensate for the dual pass and use a similar cutoff frequency in both filters, the cutoff frequency used in OpenSim was scaled with a factor given by Winter [254]:

$$w = \left(\sqrt{2} - 1 \right)^{1/2n}, \quad (\text{E.1})$$

where n is the order of the filter. To match the 6 Hz cutoff frequency used in the Human Body Model real-time filter to process the joint kinematics, we therefore selected a $6.9494 = 6/0.8634$ Hz cutoff frequency in OpenSim where 0.8634 is the scaling factor obtained from equation E.1 with $n = 3$.

Human Body Model also processes the ground reaction forces using the same real-time filter. This step is not part of the standard OpenSim data processing pipeline and was therefore performed manually using a second-order zero-phase forward and reverse low-pass Butterworth filter. The order of the filter was

chosen to match the one used in Human Body Model and a $7.4790 = 6/0.8022$ Hz cutoff frequency (where 0.8022 is the scaling factor obtained from equation E.1 with $n = 2$) was selected to compensate for the dual-pass. The ground reaction forces were therefore processed in a similar way with both models / software systems.

Inverse kinematics

Table E.6 gives the marker weights used during inverse kinematics in OpenSim and Human Body Model. We have investigated the sensitivity of the inverse kinematic results to the set of marker weights in OpenSim. In particular, we have compared two sets of marker weights (S_a and S_b in Table E.6). The first set of marker weights (S_a) was used to generate the results of this study. The results of the sensitivity analysis are presented in Table E.8.

OpenSim solves the inverse kinematic problem using a general quadratic programming solver, with a convergence criterion of 1e-4 and a limit of 1000 iterations per frame. For unconstrained problems with bounded coordinates, the LBFGS method [277] is used as optimization algorithm. Human Body Model solves the inverse kinematic problem using the Levenberg-Marquardt algorithm [278] with a limit of 99 iterations and 0.99 s per frame, and a tolerance level of 1e-4. These stopping criteria are for non-real time, using the Gait Offline Analysis Tool. Both algorithms use as initial guess the model in the default position for the first frame and then, for each frame, the solution from the previous frame.

Static optimization

A static optimization problem was solved to estimate the muscle forces [256]. Different formulations of the optimization problem are available in both systems.

In Human Body Model, two objective functions J_1 (equation E.2) and J_2 (equation E.3) can be selected. They differ by a scaling factor introduced in J_2 that weights the squared normalized muscle forces by the muscle volume. The mathematical expressions of these objective functions are given by:

$$J_1 = \sum_{i=1}^m \left(\frac{F_i}{F_{\max,i}} \right)^2 \quad (\text{E.2})$$

where m is the number of muscles, i is the muscle index, F is the muscle force, and F_{\max} is the maximal isometric muscle force, and:

$$J_2 = \sum_{i=1}^m V_i \left(\frac{F_i}{F_{\max,i}} \right)^2 \quad (\text{E.3})$$

where V is proportional to muscle volume ($V = l^{\text{opt}} F_{\max}$ where l^{opt} is the optimal muscle fiber length).

In OpenSim, the muscles can be considered as ideal force generators or constrained by their force-length-velocity properties [27]. The objective function J_3 used in OpenSim is given by:

$$J_3 = \sum_{i=1}^m (a_i)^2 \quad (\text{E.4})$$

where a is the muscle activation.

When considering the muscles as ideal force generators (by not taking into account force-length-velocity properties of muscle), J_3 equals J_1 since $a = F/F_{\max}$, and the formulation of the static optimization problem is therefore similar in OpenSim and Human Body Model. The comparison of the muscle forces estimated based on this formulation in OpenSim and Human Body Model is presented in Figures E.4-E.7. The impact of the force-length-velocity properties on the muscle forces estimated in OpenSim is presented in Figures E.8-E.11. Finally, the impact of the muscle volume scaling (equation E.3) on the muscle forces estimated in Human Body Model is presented in Figures E.11-E.15. Note that the tendon is assumed to be rigid in static optimization.

OpenSim solves the static optimization problem using the interior-point algorithm IPOPT [122], with a converge criterion of 1e-4 and a limit of 100 iterations per frame. Human Body Model solves the static optimization problem using a recurrent neural network [279], simulated numerically with the forward Euler method [127], with a limit of 10,000 iterations and 0.05 s per frame, and a tolerance level of 1e-2. These stopping criteria are for non-real time, using the Gait Offline Analysis Tool.

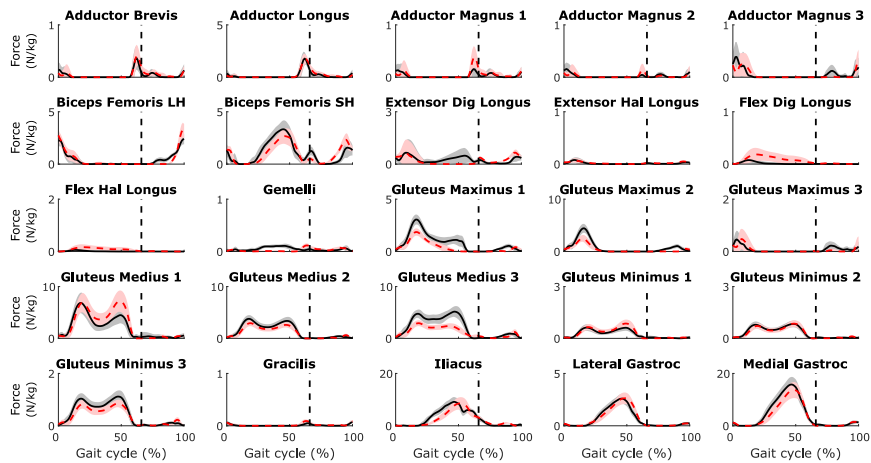


Figure E.4: Comparison of muscle forces estimated with the OpenSim gait2392 model (dashed red) and Human Body Model (black). Muscle forces estimated considering the muscles as ideal force generators (OpenSim) and without scaling the static optimization objective function by muscle volume (Human Body Model). The vertical black dashed line indicates the transition from stance to swing - Part 1

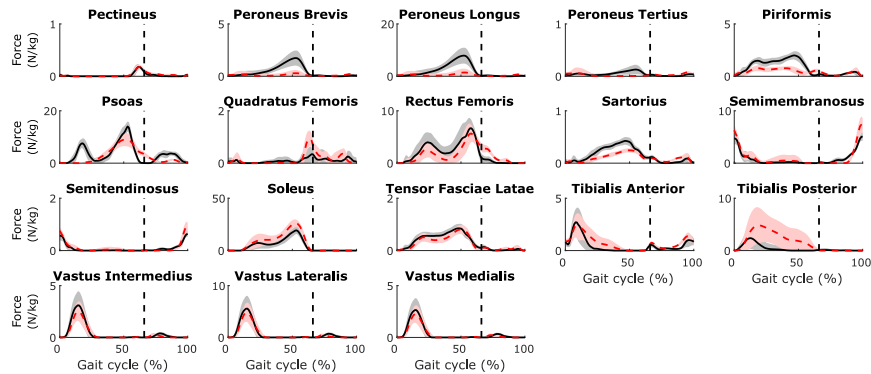


Figure E.5: Comparison of muscle forces estimated with the OpenSim gait2392 model (dashed red) and Human Body Model (black). Muscle forces estimated considering the muscles as ideal force generators (OpenSim) and without scaling the static optimization objective function by muscle volume (Human Body Model). The vertical black dashed line indicates the transition from stance to swing – Part 2

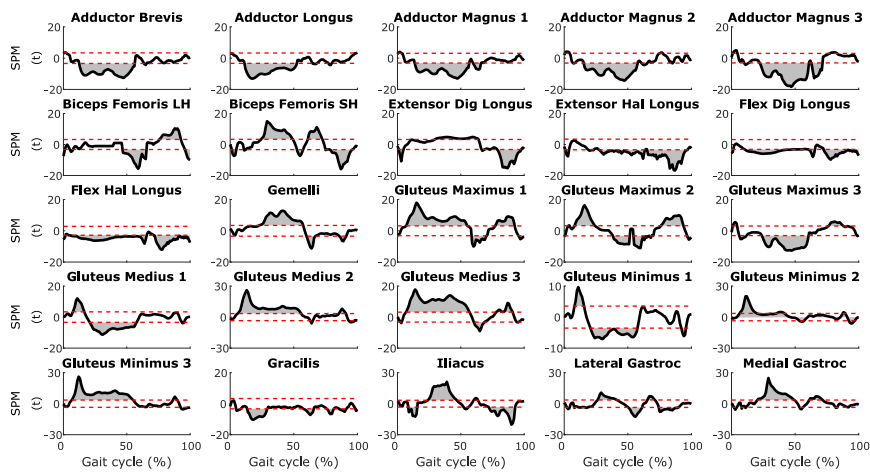


Figure E.6: Results from the statistical analysis comparing muscle forces estimated with the OpenSim gait2392 model and Human Body Model (see Figure E.4) using non-parametric paired t-tests in SPM1D. Gray shaded areas above and below the red dashed lines indicate significant differences – Part 1

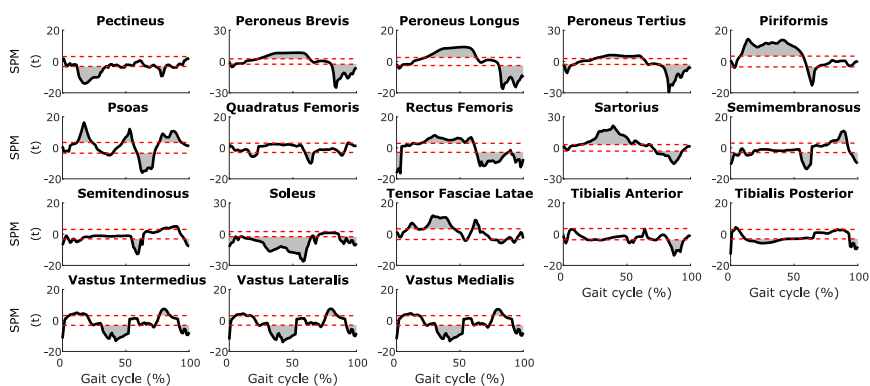


Figure E.7: Results from the statistical analysis comparing muscle forces estimated with the OpenSim gait2392 model and Human Body Model (see Figure E.5) using non-parametric paired t-tests in SPM1D. Gray shaded areas above and below the red dashed lines indicate significant differences - Part 2

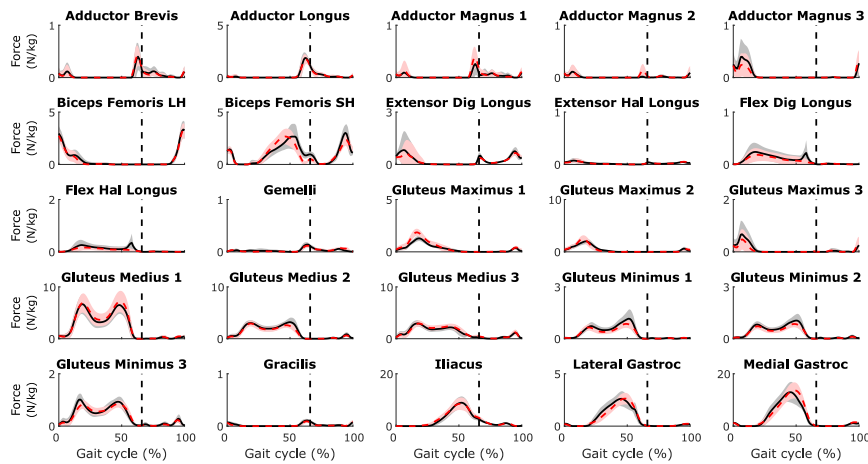


Figure E.8: Comparison of muscle forces estimated with the OpenSim gait2392 model considering the muscles as ideal force generators (dashed red) or taking the force-length-velocity properties into account (black). The vertical black dashed line indicates the transition from stance to swing - Part 1

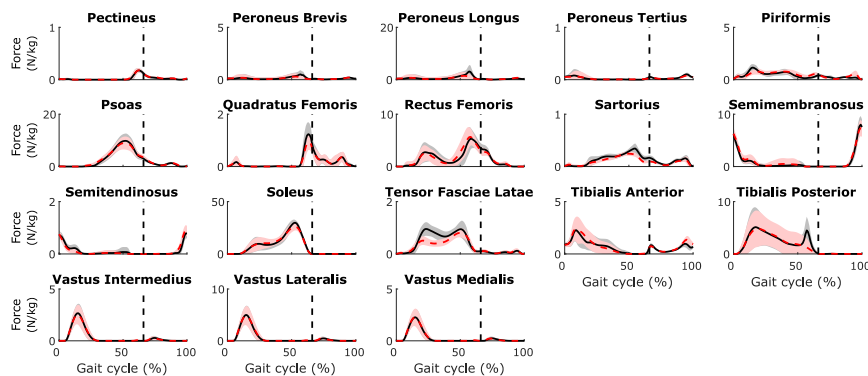


Figure E.9: Comparison of muscle forces estimated with the OpenSim gait2392 model considering the muscles as ideal force generators (dashed red) or taking the force-length-velocity properties into account (black). The vertical black dashed line indicates the transition from stance to swing - Part 2

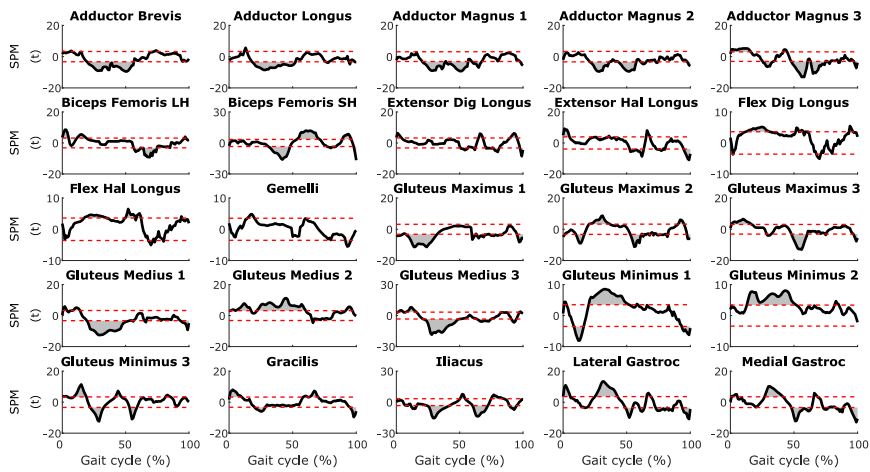


Figure E.10: Results from the statistical analysis comparing muscle forces estimated with the OpenSim gait2392 model considering the muscles as ideal force generators or taking the force-length-velocity properties into account (see Figure E.8) using non-parametric paired t-tests in SPM1D. Gray shaded areas above and below the red dashed lines indicate significant differences - Part 1

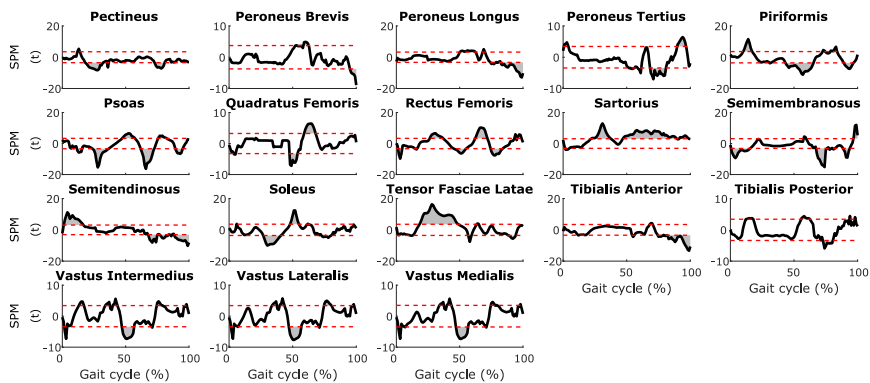


Figure E.11: Results from the statistical analysis comparing muscle forces estimated with the OpenSim gait2392 model considering the muscles as ideal force generators or taking the force-length-velocity properties into account (see Figure E.9) using non-parametric paired t-tests in SPM1D. Gray shaded areas above and below the red dashed lines indicate significant differences - Part 2

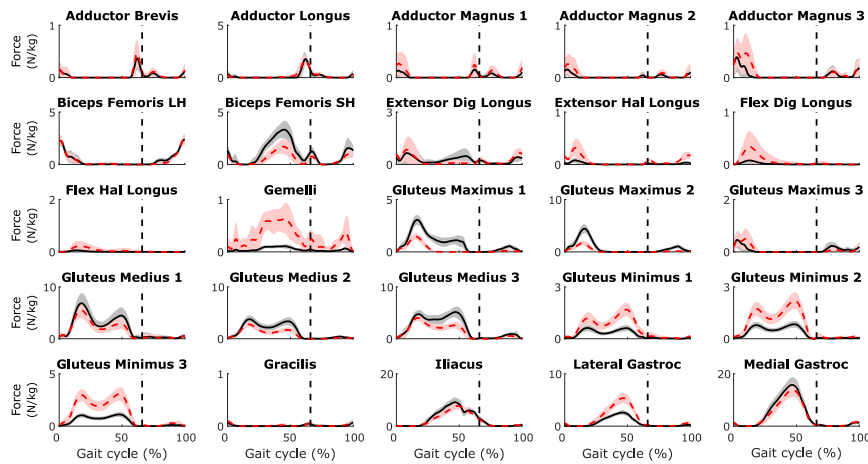


Figure E.12: Comparison of muscle forces estimated in Human Body Model with (dashed red) and without (black) scaling the static optimization objective function by muscle volume. The vertical black dashed line indicates the transition from stance to swing - Part 1

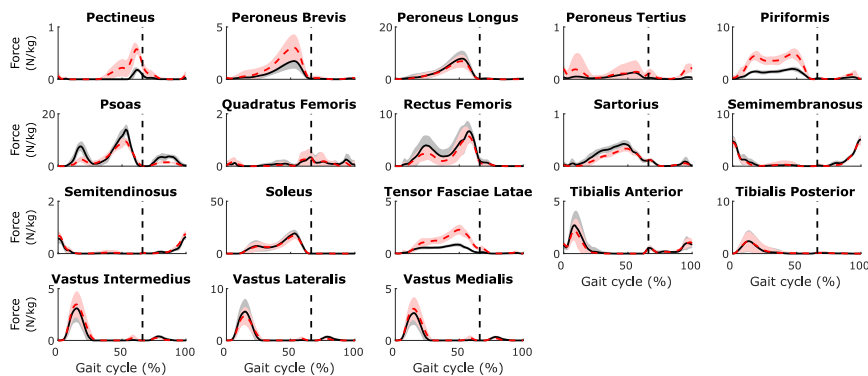


Figure E.13: Comparison of muscle forces estimated in Human Body Model with (dashed red) and without (black) scaling the static optimization objective function by muscle volume. The vertical black dashed line indicates the transition from stance to swing - Part 2

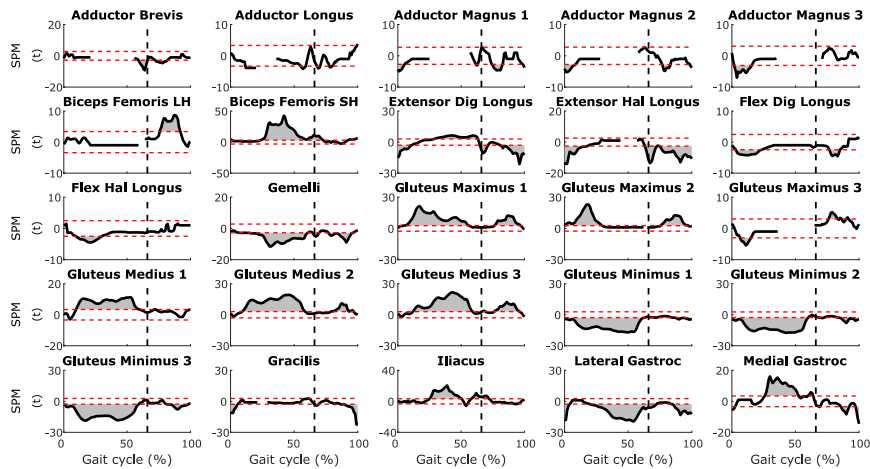


Figure E.14: Results from the statistical analysis comparing muscle forces estimated in Human Body Model with and without scaling the static optimization objective function by muscle volume (see Figure E.12) using non-parametric paired t-tests in SPM1D. Gray shaded areas above and below the red dashed lines indicate significant differences. Parts without t waveforms were excluded from the analysis since there was no variance - Part 1

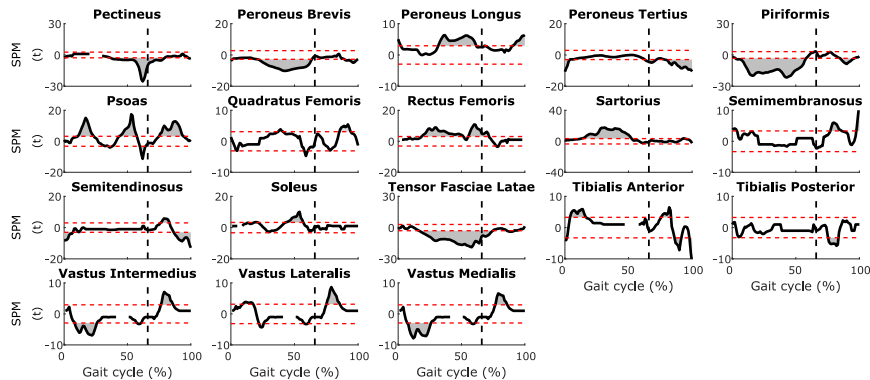


Figure E.15: Results from the statistical analysis comparing muscle forces estimated in Human Body Model with and without scaling the static optimization objective function by muscle volume (see Figure E.13) using non-parametric paired t-tests in SPM1D. Gray shaded areas above and below the red dashed lines indicate significant differences. Parts without t waveforms were excluded from the analysis since there was no variance - Part 2

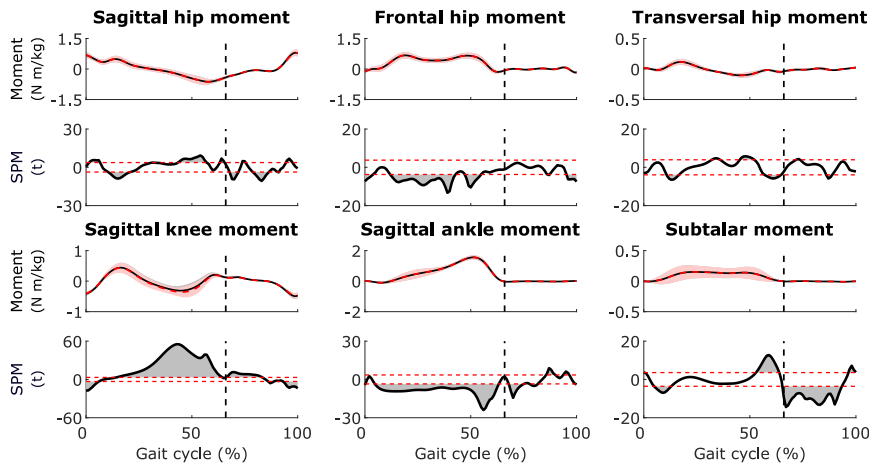


Figure E.16: [First and third row] Comparison of joint kinetics calculated in OpenSim with a moving (dashed red) or a fixed (black) knee flexion axis. [Second and fourth row] Results from the statistical analysis using non-parametric paired t-tests in SPM1D. Gray shaded areas above and below the red dashed lines indicate significant differences. The vertical black dashed line indicates the transition from stance to swing.

Body	Marker Pair 1	Marker Pair 2	Marker Pair 3	Marker Pair 4
Pelvis (med-lat)	R-ASIS/L-ASIS			
Pelvis (pos-ant)	R-ASIS/R-PSIS	L-ASIS/L-PSIS		
Pelvis (inf-sup)	R-ASIS/R-PSIS	L-ASIS/L-PSIS		
Femur	R-ASIS/R-MEK	L-ASIS/L-MEK	R-ASIS/R-LEK	L-ASIS/L-LEK
Tibia	R-MEK/R-MM	L-MEK/L-MM	R-LEK/R-LM	L-LEK/L-LM
Foot	R-HEE/R-MT2	L-HEE/L-MT2		

Table E.4: **Marker pairs used during scaling in OpenSim.** Med is for medial, lat is for lateral, pos is for posterior, ant is for anterior, inf is for inferior, sup is for superior, R-L are for Right-Left, ASIS is for anterior superior iliac spine, PSIS is for posterior superior iliac spine, MEK is for medial epicondyle of the knee, LEK is for lateral epicondyle of the knee, MM is for medial malleolus, LM is for lateral malleolus, HEE is for heel, and MT2 is for second meta tarsal.

Marker	Weight		Marker	Weight		Marker	Weight	
	<i>S</i> ₁	<i>S</i> ₂		<i>S</i> ₁	<i>S</i> ₂		<i>S</i> ₁	<i>S</i> ₂
R-L-ASIS	25	10	R-L-PSIS	15	10	R-L-LTHI	1	1
R-L-LEK	15	10	R-L-MEK	15	10	R-L-LSHA	1	1
R-L-LM	15	10	R-L-MM	15	10	R-L-HEE	10	10
R-L-MT5	1	1	R-L-MT2	4	10			

Table E.5: **Marker weights used during scaling in OpenSim.** S_1 and S_2 refer to two different sets of marker weights. S_1 was used to generate the results presented in this study. R-L are for Right-Left, ASIS is for anterior superior iliac spine, PSIS is for posterior superior iliac spine, LTHI is for lateral thigh, LEK is for lateral epicondyle of the knee, MEK is for medial epicondyle of the knee, LSHA is for lateral shank, LM is for lateral malleolus, MM is for medial malleolus, HEE is for heel, MT5 is for fifth meta tarsal, and MT2 is for second meta tarsal.

Marker	Weight		Marker	Weight		Marker	Weight	
	<i>S</i> _a	<i>S</i> _b		<i>S</i> _a	<i>S</i> _b		<i>S</i> _a	<i>S</i> _b
R-L-ASIS	1	3	R-L-PSIS	1	2.2	R-L-LTHI	1	1
R-L-LEK	1	2	R-L-MEK	0	1	R-L-LSHA	1	1
R-L-LM	1	1	R-L-MM	0	1	R-L-HEE	1	1.2
R-L-MT5	1	1	R-L-MT2	1	1.2			

Table E.6: **Marker weights used during inverse kinematics in OpenSim and Human Body Model (S_a only).** S_a and S_b refer to two different sets of marker weights. S_a was used to generate the results presented in this study. R-L are for Right-Left, ASIS is for anterior superior iliac spine, PSIS is for posterior superior iliac spine, LTHI is for lateral thigh, LEK is for lateral epicondyle of the knee, MEK is for medial epicondyle of the knee, LSHA is for lateral shank, LM is for lateral malleolus, MM is for medial malleolus, HEE is for heel, MT5 is for fifth meta tarsal, and MT2 is for second meta tarsal.

Metric	Scaling setup	Subjects							mean \pm std
		1	2	3	4	5	6	7	
RMS marker error (cm)	A	3.0	2.8	2.5	1.8	2.4	3.4	3.3	2.7 ± 0.5
	B	3.0	1.7*	1.4*	1.0*	1.4*	1.7*	2.2*	1.6 ± 0.4 *
	C	1.4*	2.6	2.5	1.8	2.3	3.2	2.7	2.6 ± 0.4
Max. marker error (cm)	A	1.4*	1.3*	1.4*	1.0*	1.2*	1.2*	1.2*	1.2 ± 0.2 *
	B	3.0	2.6	2.4	1.8	2.3	3.2	2.7	2.6 ± 0.4
	C	1.4*	1.3*	1.3*	0.9*	1.2*	1.2*	1.2*	1.2 ± 0.2 *
Max. marker error (cm)	A	6.9	6.3	6.7	5.2	7.3	8.0	8.2	6.9 ± 1.0
	B	2.2*	3.1*	2.4*	2.1*	2.5*	2.9*	4.9*	2.9 ± 1.0 *
	C	7.2	6.7	7.0	5.2	7.7	8.3	7.4	7.1 ± 1.0
Max. marker error (cm)	A	2.1*	2.6*	2.4*	2.1*	2.3*	1.9*	2.1*	2.2 ± 0.2 *
	B	7.3	6.5	6.7	5.2	7.4	8.2	7.4	7.0 ± 0.9
	C	2.1*	2.7*	2.4*	2.0*	2.4*	1.9*	1.9*	2.2 ± 0.3 *
Marker error (marker)	A	R-LTHI	R-LTHI	R-LTHI	R-LTHI	R-LTHI	R-LSHA	R-LSHA	
		R-LEK*	L-PSIS*	R-MT5*	R-MT5*	L-PSIS*	L-PSIS*	L-PSIS*	
	B	R-LTHI	R-LTHI	R-LTHI	R-LTHI	R-LTHI	L-LTHI	L-LTHI	
		R-LEK*	R-LEK*	R-MT5*	R-MT5*	R-MT5*	R-LM*	R-LM*	
	R-LTHI	R-LTHI	R-LTHI	R-LTHI	R-LTHI	R-LTHI	L-LTHI	L-LTHI	
		R-LEK*	R-LEK*	R-MT5*	R-MT5*	R-MT5*	R-PSIS*	R-PSIS*	
	C	R-LEK*	R-LEK*	R-LEK*	R-LEK*	R-LEK*	R-MT5*	R-MT5*	
		R-LEK*	R-LEK*	R-LEK*	R-LEK*	R-LEK*	R-LM*	R-LM*	
		R-LEK*	R-LEK*	R-LEK*	R-LEK*	R-LEK*	L-PSIS*	L-PSIS*	

Table E.7: Root mean square (RMS) marker error (cm) and maximum marker error (cm) during scaling in OpenSim. Scaling setup A scales the pelvis uniformly and uses the set of markers S_1 (see table E.5). Scaling setup B scales the pelvis non-uniformly and uses the set of markers S_2 (see table E.5). For the maximum marker error, the corresponding marker is reported: R-L are for Right-Left, LTHI is for lateral thigh, LSHA is for lateral shank, LEK is for lateral epicondyle of the knee, PSIS is for posterior superior iliac spine, MT5 is for fifth meta tarsal, and LM is for lateral malleolus. * indicates results excluding non-bony landmark markers (i.e. R-L LTHI and R-L LSHA). Scaling setup B was used to generate the results presented in this study.

Degree of freedom	Setups being compared			
	A vs B	A vs C	B vs C	B vs D
Sagittal plane hip	2.0 ± 1.4	1.7 ± 1.2	1.8 ± 2.0	0.5 ± 0.3
Frontal plane hip	0.4 ± 0.3	0.5 ± 0.4	0.4 ± 0.4	0.7 ± 0.4
Transversal plane hip	0.6 ± 0.6	0.9 ± 0.6	0.5 ± 0.4	0.3 ± 0.2
Sagittal plane knee	0.8 ± 0.6	1.0 ± 0.5	0.4 ± 0.5	0.3 ± 0.2
Sagittal plane ankle	1.0 ± 1.0	2.1 ± 1.4	1.4 ± 1.2	0.4 ± 0.3
Subtalar	1.4 ± 1.3	1.8 ± 1.8	2.1 ± 1.8	0.4 ± 0.3

Table E.8: **Absolute difference (degrees) in joint kinematics averaged over the gait cycle and the 14 representative trials between different setups.** Setup A scales the pelvis uniformly, uses the set of markers S_1 (see Table E.5) for scaling, and uses the set of markers S_a (see Table E.6) for inverse kinematics. Setup B scales the pelvis non-uniformly, uses the set of markers S_1 (see Table E.5) for scaling, and uses the set markers S_a (see Table E.6) for inverse kinematics. Setup C scales the pelvis non-uniformly, uses the set of markers S_2 (see Table E.5) for scaling, and uses the set of markers S_a (see Table E.6) for inverse kinematics. Setup D scales the pelvis non-uniformly, uses the set of markers S_1 (see Table E.5) for scaling, and uses the set of markers S_b (see Table E.6) for inverse kinematics. Setup B was used to generate the results presented in this study. The largest effect of the scaling setup was 2.1 degrees for the ankle and subtalar joints (A vs C and B vs C, respectively). The largest effect of the inverse kinematic setup was 0.7 degrees for the frontal plane hip joint (B vs D).

Degree of freedom	Joint kinematics		Joint kinetics	
	Human Body Model	OpenSim	Human Body Model	OpenSim
Sagittal plane hip	4.4	4.9	0.13	0.13
Frontal plane hip	2.2	2.3	0.13	0.12
Transversal plane hip	4.0	3.9	0.04	0.03
Sagittal plane knee	4.3	3.9	0.13	0.12
Sagittal plane ankle	3.3	3.6	0.14	0.14
Subtalar	3.9	5.5	0.07	0.07

Table E.9: **Root mean square (RMS) standard deviation of the joint kinematics (degrees) and the joint kinematics (N·m/kg).**

Acknowledgments

After about five years of work, time has come to hand in my thesis. I am grateful to many people for their contribution to my work but, first of all, I would like to acknowledge the generous support of the Research Foundation Flanders (FWO) that made my research in Leuven and abroad possible.

I had the chance to collaborate with two fantastic supervisors whose personalities and skills greatly complement each other. Ilse, I have enjoyed your guidance and got inspired by your vision. Despite your busy agenda, you made time for discussing when needed and our talks always gave me new motivation to go ahead. I am grateful for your trust, for having let me carry out my research abroad without much control. I am impressed by how you managed to get the lab where it is now: delivering high-quality research while maintaining a great atmosphere of friendliness. I hope it stays as it is in the future. Friedl, you have been the architect behind my projects, shaping my way of conducting scientific research. I am deeply grateful for the amount of knowledge I have gained from you over the years. I will remember your inexhaustible passion for biomechanics, your attention to detail, and your ability to master so many different aspects of our field. I hope many others will have the chance to enjoy the friendly and successful collaboration I have had with you. I also would like to acknowledge the positive and constructive feedback I have received from my jury members Kaat Desloovere, Goele Pipeleers, Joris De Schutter, and Auke Ijspeert. They certainly contributed to improve the quality of my thesis.

I would like to thank the many colleagues and friends I have had in the group over the years. Naming all of them is a challenge I will not take on. It has been great working with you, doing tons of sport, having fun at conferences, and traveling across the world. I have a collection of fantastic memories from those years spent in the lab. A special thanks to the SimCP team for the nice project we worked on together.

I am particularly grateful to a couple of people who deeply contributed to my research and without whom this dissertation would have been much different. Chris, meeting you during my first visit at Stanford has given a different shape to my PhD. I think Gil and I did not measure the size of the project we started at that time but, in the end, it has been terrific to work together. You made me feel knowledgeable and achieve things I never would have thought of. Thanks a bunch. Joris, I am glad I got a chance to meet you. You figured out what I needed for my project in a few minutes and made everything work so smoothly. I have rarely met people as sharp as both of you. Thanks for having made my project so much more interesting.

I have been lucky to be a visiting scholar at Stanford in two occasions and I would like to thank all of those, in particular the OpenSim staff, who made those stays possible. Thanks Gil as well for having been such a nice partner in this adventure. Researching at Stanford was fascinating and among the highlights of my PhD. Leaving the Californian sun for Pittsburgh has been quite a move, but I very much enjoyed the stimulating research environment I discovered at Carnegie Mellon. I am very grateful to Hartmut and Seungmoon for having hosted me in the Robotics Institute for these few months. Those stays abroad will remain great memories.

I would like to thank very much my parents and siblings. They have always been a great source of inspiration and support. To all my friends, thanks for being there to do everything but research.

Finally, Florence, thank you for your continued support over the years, for your encouragements to take on new challenges, and for pushing me to fully live each opportunity.

Scientific acknowledgments, personal contribution, conflict of interest statement, and appositions

The author would like to acknowledge the contribution of all co-authors to the individual papers. In particular, the author thanks Sam Van Rossum for collecting and processing experimental data in study 1, Lynn Bar-On for collecting and processing experimental data in study 2, Christopher L. Dembia, Joris Gillis, and Gil Serrancolí for contributing to the development of the simulation framework exploited in studies 3-5, Gil Serrancolí for developing the pendulum simulations in study 3, Maarten Afschrift and Tom Van Wouwe for collecting experimental data used in studies 3-4, all members of the SimCP consortium for collecting experimental data and creating the MRI-based musculoskeletal model in study 5, and all co-authors for providing feedback on paper drafts prior to submission. Furthermore, I would like to thank Ilse Jonkers and Friedl De Groot for their valuable feedback and edits of the thesis.

The author, Antoine Falisse, carried out all investigations performed in the different studies and wrote all chapters of this dissertation. He shares a first co-authorship with Gil Serrancolí for the third study.

Neither the author, nor any of the co-authors have any conflict of interest.

Appositions:

- Hypothesis-driven analysis should be prioritized over post-hoc analysis.
- Sharing code and datasets that enable reproducing published results should be a pre-requisite for publication.
- Incentives for peer-reviewing should be offered to accelerate the dissemination of research results and maintain a high scientific quality.

Curriculum vitae

Antoine received a B.S. degree in Engineering Science (2012, UC Louvain, Belgium) and a M.Sc. in Biomedical Engineering (2014, UC Louvain, Belgium). He started his PhD training in 2015 as part of the SimCP project (IWT-TBM) aiming to develop a simulation framework to predict gait performance following orthopedic interventions in children with cerebral palsy. In 2016, he secured a four-year FWO-SB fellowship on the topic of his dissertation. In 2017 and 2019, Antoine was a visiting research scholar for five weeks in the National Center for Simulation in Rehabilitation Research (NCSRR) at Stanford University where he worked in close collaboration with developers of the OpenSim software. In 2017-2018, Antoine was a visiting PhD student for a six-month period in the Robotics Institute at Carnegie Mellon University in Professor Geyer's lab where he gained expertise in predictive simulations of human movement. He received a FWO grant for a long-stay abroad for that research stay. In 2019, Antoine received the Andrzej Komor New Investigator Award at the XVII International Symposium on Computer Simulation in Biomechanics (Canmore, Canada) as well as the David Winter Young Investigator Award at the XXVII Congress of the International Society of Biomechanics (Calgary, Canada).

Antoine was a board member of the PhD society of the KU Leuven as well as the PhD student representative of the Faculty of Movement and Rehabilitation Sciences in different boards of the doctoral school. Antoine helped in supervising several master students in Biomedical Engineering. He also led, in several occasions, the practical sessions of a course on scientific programming for the research master in Human Movement Sciences as well as the practical sessions in the second year biomechanics course of undergraduate students in Rehabilitation Sciences and Physical Education.

List of publications

Articles in internationally reviewed academic journals

- **Falisse A.**, Serrancolí G., Dembia C.L., Gillis J., De Groote F. *Algorithmic differentiation improves the computational efficiency of OpenSim-based trajectory optimization of human movement*, (2019). PLoS ONE, **14**(10): e0217730. DOI: 10.1371/journal.pone.0217730.
- **Falisse A.**, Serrancolí G., Dembia C.L., Gillis J., Jonkers I., De Groote F. *Rapid predictive simulations with complex musculoskeletal models suggest that diverse healthy and pathological human gaits can emerge from similar control strategies*, (2019). Journal of the Royal Society Interface, **16**(157): 20190402. DOI: 10.1098/rsif.2019.0402.
- Pitto L., Kainz H., **Falisse A.**, Wesseling M., Van Rossum S., Hoang H., Papageorgiou E., Hallemans A., Desloovere K., Molenaers G., Van Campenhout A., De Groote F., Jonkers I. *SimCP: a simulation platform to predict gait performance following orthopedic intervention in children with Cerebral Palsy*, (2019). Frontiers in Neurorobotics, **13**: 54. DOI: 10.3389/fnbot.2019.00054.
- Serrancolí G., **Falisse A.**, Dembia C.L., Vantilt J., Tanghe K., Lefever D., Jonkers I., De Schutter J., De Groote F. *Subject-exoskeleton contact model calibration leads to accurate interaction force predictions*, (2019). IEEE Transactions on Neural System and Rehabilitation Engineering, **27**(8): 1597-1605. DOI: 10.1109/TNSRE.2019.2924536.
- **Falisse A.**, Bar-On L., Desloovere K., Jonkers I., De Groote F. *A spasticity model based on feedback from muscle force explains muscle activity during passive stretches and gait in children with cerebral palsy*, (2018). PLoS ONE, **13**(12): e0208811. DOI: 10.1371/journal.pone.0208811.
- **Falisse A.**, Van Rossum S., Gijsbers J., Steenbrink F., van Basten B.J.H., Jonkers I., van den Bogert A.J., De Groote F. *OpenSim versus Human Body Model: a comparison study for the lower limbs during gait*, (2018). Journal of Applied Biomechanics, **34**(6): 496-502. DOI: 10.1123/jab.2017-0156.
- Kainz H., Goudriaan M., **Falisse A.**, Huenaerts C., Desloovere K., De Groote F., Jonkers I. *The influence of maximum isometric muscle force scaling on estimated muscle forces from musculoskeletal models of children with cerebral palsy*, (2018). Gait & Posture, **65**: 213-220. DOI: 10.1016/j.gaitpost.2018.07.172.

- **Falisse A.**, Van Rossum S., Jonkers I., De Groote F. *EMG-driven optimal estimation of subject-specific Hill model muscle-tendon parameters of the knee joint actuators*, (2017). IEEE Transactions on Biomedical Engineering, **64**(9): 2253-2262. DOI: 10.1109/TBME.2016.2630009.

Articles submitted for publication in internationally reviewed academic journals

- **Falisse A.**, Pitto L., Kainz H., Wesseling M., Van Rossum S., Hoang H., Papageorgiou E., Bar-On L., Hallemans A., Desloovere K., Molenaers G., Van Campenhout A., De Groote F., Jonkers I. *Physics-based predictive simulations to explore the differential effects of motor control and musculoskeletal deficits on gait dysfunction in cerebral palsy: a retrospective case study*. Frontiers in Human Neuroscience.

Abstracts and posters presented at international scientific conferences (first author)

- **Falisse A.**, Serrancolí G., Dembia C.L., Gillis J., Jonkers I., De Groote F. *Predicting the mechanics and energetics of a variety of human gaits based on complex musculoskeletal models*, (2019). International Society of Biomechanics. Calgary, Alberta, Canada.
- **Falisse A.**, Serrancolí G., Dembia C.L., Gillis J., Jonkers I., De Groote F. *Direct collocation, implicit differential equations, algorithmic differentiation: A cocktail for rapid predictive simulations of movement based on complex musculoskeletal models*, (2019). Technical Group on Computer Simulation of the International Society of Biomechanics. Canmore, Alberta, Canada.
- **Falisse A.**, Serrancolí G., Dembia C.L., Song S., Gillis J., Jonkers I., De Groote F. *Computationally efficient predictive muscle-driven simulations of 3D walking*, (2018). World Congress of Biomechanics. Dublin, Ireland.
- **Falisse A.**, Serrancolí G., Dembia C.L., Song S., Gillis J., Jonkers I., De Groote F. *Computationally efficient muscle-driven predictive simulations of walking*, (2018). Dynamic Walking. Pensacola, Florida, USA.
- **Falisse A.**, Bar-On L., Desloovere K., Jonkers I., De Groote F. *Simulating muscle spasticity during gait based on passive spasticity assessment*, (2017). International Society of Biomechanics. Brisbane, Queensland, Australia.

- **Falisse A.**, Serrancolí G., Dembia C.L., Gillis J., Jonkers I., De Groote F. *A framework to solve optimal control problems using automatic differentiation of multibody dynamics in OpenSim*, (2017). Technical Group on Computer Simulation of the International Society of Biomechanics. Gold Coast, Queensland, Australia.
- **Falisse A.**, Bar-On L., Desloovere K., Jonkers I., De Groote F. *Subject-specific modeling of muscle hyper-resistance in children with cerebral palsy*, (2016). Neuromechanics. Heidelberg, Germany.
- **Falisse A.**, Bar-On L., Desloovere K., De Groote F., Jonkers I. *Muscle velocity and length feedback can explain muscle activity in spastic hamstrings during and following passive fast-stretch motions*, (2016). Motor Control. Wisła, Poland.
- **Falisse A.**, Van Rossom S., Jonkers I., De Groote F. *Estimation of subject-specific muscle-tendon parameters based on dynamic motions using EMG-driven musculoskeletal model and optimal control approach*, (2015). Technical Group on Computer Simulation of the International Society of Biomechanics. Edinburgh, UK.

Bibliography

- [1] Surveillance of Cerebral Palsy in Europe, “Prevalence and characteristics of children with cerebral palsy in Europe,” *Developmental Medicine & Child Neurology*, vol. 44, no. 9, pp. 633–40, 2002.
- [2] J. R. Gage, M. H. Schwartz, S. E. Koop, and T. F. Novacheck, eds., *The identification and treatment of gait problems in cerebral palsy*. Mac Keith Press, 2nd ed., 2009.
- [3] G. Molenaers, A. van Campenhout, K. Fagard, J. De Cat, and K. Desloovere, “The use of botulinum toxin A in children with cerebral palsy, with a focus on the lower limb,” *Journal of Children’s Orthopaedics*, vol. 4, no. 3, pp. 183–195, 2010.
- [4] P. Steinbok, “Selective dorsal rhizotomy for spastic cerebral palsy: a review,” *Child’s Nervous System*, vol. 23, no. 9, pp. 981–990, 2007.
- [5] J. L. McGinley, F. Dobson, R. Ganeshalingam, B. J. Shore, E. Rutz, and H. K. Graham, “Single-event multilevel surgery for children with cerebral palsy: A systematic review,” *Developmental Medicine & Child Neurology*, vol. 54, no. 2, pp. 117–128, 2012.
- [6] M. H. Schwartz, A. Rozumalski, and K. M. Steele, “Dynamic motor control is associated with treatment outcomes for children with cerebral palsy,” *Developmental Medicine & Child Neurology*, vol. 58, no. 11, pp. 1139–1145, 2016.
- [7] M. C. d. M. Filho, R. Yoshida, W. d. S. Carvalho, H. E. Stein, and N. F. Novo, “Are the recommendations from three-dimensional gait analysis associated with better postoperative outcomes in patients with cerebral palsy?,” *Gait & Posture*, vol. 28, no. 2, pp. 316–322, 2008.
- [8] F. M. Chang, A. J. Seidl, K. Muthusamy, A. K. Meininger, and J. J. Carollo, “Effectiveness of instrumented gait analysis in children

- with cerebral palsy - Comparison of outcomes," *Journal of Pediatric Orthopaedics*, vol. 26, no. 5, pp. 612–616, 2006.
- [9] A. Rajagopal, Ł. Kidziński, A. S. McGlaughlin, J. L. Hicks, S. L. Delp, and M. H. Schwartz, "Estimating the effect size of surgery to improve walking in children with cerebral palsy from retrospective observational clinical data," *Scientific Reports*, vol. 8, no. 1, pp. 1–11, 2018.
 - [10] M. H. Schwartz, "O 046 - A flexible omnibus matching algorithm (FOMA) to support treatment decisions for children with cerebral palsy," *Gait & Posture*, vol. 65, pp. 93–94, 2018.
 - [11] S. Grillner, A. Georgopoulos, and L. Jordan, "Selection and initiation of motor behavior," in *Neurons, networks and motor behavior* (P. Stein, S. Grillner, A. Selverston, and D. Stuart, eds.), MIT Press, 1997.
 - [12] A. H. Cohen and P. Wallen, "The neuronal correlate of locomotion in fish. "Fictive swimming" induced in an in vitro preparation of the lamprey spinal cord," *Experimental Brain Research*, vol. 41, no. 1, pp. 11–18, 1980.
 - [13] K. Minassian, U. S. Hofstoetter, F. Dzeladini, P. A. Guertin, and A. Ijspeert, "The human central pattern generator for locomotion: does it exist and contribute to walking?," *The Neuroscientist*, vol. 23, no. 6, pp. 649–663, 2017.
 - [14] "Lower motor neuron circuits and motor control," in *Neuroscience* (D. Purves, G. Augustine, D. Fitzpatrick, W. Hall, A.-S. LaMantia, J. McNamara, and L. White, eds.), ch. 16, pp. 397–422, Sinauer Associates, 4th ed., 2008.
 - [15] "Locomotion," in *Principles of neural science* (E. Kandel, J. Schwartz, T. Jessel, S. Siegelbaum, and A. Hudspeth, eds.), pp. 812–834, McGraw-Hill, 5th ed., 2013.
 - [16] A. J. Ijspeert, "Locomotion, Vertebrate," in *The Handbook of Brain Theory and Neural Networks* (M. Arbib, ed.), pp. 649–653, MIT Press, 2nd ed., 2003.
 - [17] A. J. Ijspeert, "Central pattern generators for locomotion control in animals and robots: a review," *Neural Networks*, vol. 21, no. 4, pp. 642–653, 2008.
 - [18] J. E. Bertram and A. Ruina, "Multiple walking speed-frequency relations are predicted by constrained optimization," *Journal of Theoretical Biology*, vol. 209, no. 4, pp. 445–453, 2001.

- [19] J. C. Selinger, S. M. O'Connor, J. D. Wong, and J. M. Donelan, "Humans can continuously optimize energetic cost during walking," *Current Biology*, vol. 25, no. 18, pp. 2452–2456, 2015.
- [20] J. Mercier, D. Le Gallais, M. Durand, C. Goudal, J. P. Micallef, and C. Préfau, "Energy expenditure and cardiorespiratory responses at the transition between walking and running," *European Journal of Applied Physiology and Occupational Physiology*, vol. 69, no. 6, pp. 525–529, 1994.
- [21] A. Minetti, L. Ardigo, and F. Saibene, "The transition between walking and running in humans: metabolic and mechanical aspects at different gradients," *Acta Physiologica Scandinavica*, vol. 150, no. 3, pp. 315–323, 1994.
- [22] D. F. Hoyt and C. R. Taylor, "Gait and the energetics of locomotion in horses," *Nature*, vol. 292, no. 5820, pp. 239–240, 1981.
- [23] H. Geyer, A. Seyfarth, and R. Blickhan, "Positive force feedback in bouncing gaits?," *Proceedings of the Royal Society B: Biological Sciences*, vol. 270, no. 1529, pp. 2173–2183, 2003.
- [24] H. Geyer and H. Herr, "A muscle-reflex model that encodes principles of legged mechanics produces human walking dynamics and muscle activities," *IEEE Transactions on Neural Systems and Rehabilitation Engineering*, vol. 18, no. 3, pp. 263–273, 2010.
- [25] S. Song and H. Geyer, "A neural circuitry that emphasizes spinal feedback generates diverse behaviours of human locomotion," *Journal of Physiology*, vol. 593, no. 16, pp. 3493–3511, 2015.
- [26] F. Dzeladini, J. van den Kieboom, and A. Ijspeert, "The contribution of a central pattern generator in a reflex-based neuromuscular model," *Frontiers in Human Neuroscience*, vol. 8, pp. 1–18, 2014.
- [27] F. Zajac, "Muscle and tendon: properties, models, scaling, and application to biomechanics and motor control," *Critical Reviews in Biomedical Engineering*, vol. 17, no. 4, pp. 359–411, 1989.
- [28] J. M. Winters, "An improved muscle-reflex actuator for use in large-scale neuromusculoskeletal models," *Annals of Biomedical Engineering*, vol. 23, no. 4, pp. 359–374, 1995.
- [29] C. C. Raasch, F. E. Zajac, B. Ma, and W. S. Levine, "Muscle coordination of maximum-speed pedaling," *Journal of Biomechanics*, vol. 30, no. 96, pp. 595–602, 1997.

- [30] D. G. Thelen, “Adjustment of muscle mechanics model parameters to simulate dynamic contractions in older adults,” *Journal of Biomechanical Engineering*, vol. 125, no. 1, pp. 70–77, 2003.
- [31] E. M. Arnold, S. R. Hamner, A. Seth, M. Millard, and S. L. Delp, “How muscle fiber lengths and velocities affect muscle force generation as humans walk and run at different speeds,” *The Journal of Experimental Biology*, vol. 216, no. 11, pp. 2150–2160, 2013.
- [32] M. Wesselink, F. De Groote, C. Meyer, K. Corten, J. P. Simon, K. Desloovere, and I. Jonkers, “Gait alterations to effectively reduce hip contact forces,” *Journal of Orthopaedic Research*, vol. 33, no. 7, pp. 1094–1102, 2015.
- [33] M. Srinivasan and A. Ruina, “Computer optimization of a minimal biped model discovers walking and running,” *Nature*, vol. 439, no. 7072, pp. 72–75, 2006.
- [34] L. L. Long III and M. Srinivasan, “Walking, running, and resting under time, distance, and average speed constraints: optimality of walk-run-rest mixtures,” *Journal of the Royal Society Interface*, vol. 10, no. 81, p. 20120980, 2013.
- [35] F. C. Anderson and M. G. Pandy, “Dynamic optimization of human walking,” *Journal of Biomechanical Engineering*, vol. 123, no. 5, pp. 381–390, 2001.
- [36] R. H. Miller, “A comparison of muscle energy models for simulating human walking in three dimensions,” *Journal of Biomechanics*, vol. 47, no. 6, pp. 1373–1381, 2014.
- [37] Y.-C. Lin, J. P. Walter, and M. G. Pandy, “Predictive simulations of neuromuscular coordination and joint-contact loading in human gait,” *Annals of Biomedical Engineering*, vol. 46, no. 8, pp. 1216–1227, 2018.
- [38] R. M. Alexander, “Mechanics of bipedal locomotion,” in *Perspectives in experimental biology* (P. S. Davies, ed.), pp. 493–504, Oxford: Pergamon Press, 1976.
- [39] M. Ackermann and A. J. van den Bogert, “Optimality principles for model-based prediction of human gait,” *Journal of Biomechanics*, vol. 43, no. 6, pp. 1055–1060, 2010.
- [40] S. Song and H. Geyer, “Predictive neuromechanical simulations indicate why walking performance declines with ageing,” *Journal of Physiology*, vol. 596, no. 7, pp. 1199–1210, 2018.

- [41] R. H. Miller, B. R. Umberger, J. Hamill, and G. E. Caldwell, “Evaluation of the minimum energy hypothesis and other potential optimality criteria for human running,” *Proceedings of the Royal Society B: Biological Sciences*, vol. 279, no. 1733, pp. 1498–1505, 2012.
- [42] Y. Xiang, J. S. Arora, and K. Abdel-Malek, “Physics-based modeling and simulation of human walking: A review of optimization-based and other approaches,” *Structural and Multidisciplinary Optimization*, vol. 42, no. 1, pp. 1–23, 2010.
- [43] A. J. van den Bogert, M. Hupperets, H. Schlarb, and B. Krabbe, “Predictive musculoskeletal simulation using optimal control: Effects of added limb mass on energy cost and kinematics of walking and running,” *Proceedings of the Institution of Mechanical Engineers, Part P: Journal of Sports Engineering and Technology*, vol. 226, no. 2, pp. 123–133, 2012.
- [44] A. J. Meyer, I. Eskinazi, J. N. Jackson, A. V. Rao, C. Patten, and B. J. Fregly, “Muscle synergies facilitate computational prediction of subject-specific walking motions,” *Frontiers in Bioengineering and Biotechnology*, vol. 4, p. 77, 2016.
- [45] A. D. Koelewijn and A. J. van den Bogert, “Joint contact forces can be reduced by improving joint moment symmetry in below-knee amputee gait simulations,” *Gait & Posture*, vol. 49, pp. 219–225, 2016.
- [46] Y.-C. Lin and M. G. Pandy, “Three-dimensional data-tracking dynamic optimization simulations of human locomotion generated by direct collocation,” *Journal of Biomechanics*, vol. 59, pp. 1–8, 2017.
- [47] R. Miller, B. Umberger, and G. Caldwell, “Limitations to maximum sprinting speed imposed by muscle mechanical properties,” *Journal of Biomechanics*, vol. 45, no. 6, pp. 1092–1097, 2012.
- [48] R. H. Miller, S. C. E. Brandon, and K. J. Deluzio, “Predicting sagittal plane biomechanics that minimize the axial knee joint contact force during walking,” *Journal of Biomechanical Engineering*, vol. 135, no. 1, p. 011007, 2012.
- [49] T. W. Dorn, J. M. Wang, J. L. Hicks, and S. L. Delp, “Predictive simulation generates human adaptations during loaded and inclined walking,” *PLoS ONE*, vol. 10, no. 4, pp. 1–16, 2015.
- [50] S. Song and H. Geyer, “Evaluation of a neuromechanical walking control model using disturbance experiments,” *Frontiers in Computational Neuroscience*, vol. 11, no. 15, 2017.

- [51] A. D. Koelewijn, E. Dorschky, and A. J. van den Bogert, “A metabolic energy expenditure model with a continuous first derivative and its application to predictive simulations of gait,” *Computer Methods in Biomechanics and Biomedical Engineering*, vol. 21, no. 8, pp. 521–531, 2018.
- [52] F. De Groote, G. Pipeleers, I. Jonkers, B. Demeulenaere, C. Patten, J. Swevers, and J. De Schutter, “A physiology based inverse dynamic analysis of human gait: potential and perspectives,” *Computer Methods in Biomechanics and Biomedical Engineering*, vol. 12, no. 5, pp. 563–574, 2009.
- [53] F. De Groote, A. Kinney, A. Rao, and B. Fregly, “Evaluation of direct collocation optimal control problem formulations for solving the muscle redundancy problem,” *Annals of Biomedical Engineering*, vol. 44, no. 10, pp. 2922–2936, 2016.
- [54] L.-F. Lee and B. R. Umberger, “Generating optimal control simulations of musculoskeletal movement using OpenSim and MATLAB,” *PeerJ*, vol. 4, p. e1638, 2016.
- [55] A. J. van den Bogert, D. Blana, and D. Heinrich, “Implicit methods for efficient musculoskeletal simulation and optimal control,” *Procedia IUTAM*, vol. 2, pp. 297–316, 2011.
- [56] J. A. E. Andersson, J. Gillis, G. Horn, J. B. Rawlings, and M. Diehl, “CasADi : a software framework for nonlinear optimization and optimal control,” *Mathematical Programming Computation*, vol. 11, no. 1, pp. 1–36, 2019.
- [57] P. Rosenbaum, N. Paneth, A. Leviton, M. Goldstein, M. Bax, D. Damiano, B. Dan, and B. Jacobsson, “A report: the definition and classification of cerebral palsy April 2006,” *Developmental Medicine & Child Neurology. Supplement*, vol. 109, pp. 8–14, 2007.
- [58] J. Lance, “Pathophysiology of spasticity and clinical experience with baclofen,” in *Spasticity: Disordered Motor Control* (J. Lance, R. Feldman, R. Young, and W. Koella, eds.), pp. 185–204, Chicago: Year Book Medical, 1980.
- [59] Y. P. Ivanenko, R. E. Poppele, and F. Lacquaniti, “Five basic muscle activation patterns account for muscle activity during human locomotion,” *Journal of Physiology*, vol. 556, no. 1, pp. 267–282, 2004.
- [60] F. De Groote, I. Jonkers, and J. Duysens, “Task constraints and minimization of muscle effort result in a small number of muscle synergies

- during gait," *Frontiers in Computational Neuroscience*, vol. 8, no. 115, pp. 1–11, 2014.
- [61] K. M. Steele, A. Rozumalski, and M. H. Schwartz, "Muscle synergies and complexity of neuromuscular control during gait in cerebral palsy," *Developmental Medicine & Child Neurology*, vol. in press, 2015.
- [62] Y. Kim, T. C. Bulea, and D. L. Damiano, "Children with cerebral palsy have greater stride-to-stride variability of muscle synergies during gait than typically developing children: implications for motor control complexity," *Neurorehabilitation and Neural Repair*, vol. 32, no. 9, pp. 834–844, 2018.
- [63] S. Delp, P. Loan, M. Hoy, F. Zajac, E. Topp, and J. Rosen, "An interactive graphics-based model of the lower extremity to study orthopaedic surgical procedures," *IEEE Transactions on Biomedical Engineering*, vol. 37, no. 8, pp. 757 – 67, 1990.
- [64] J. Hicks, A. Arnold, F. Anderson, M. Schwartz, and S. Delp, "The effect of excessive tibial torsion on the capacity of muscles to extend the hip and knee during single-limb stance," *Gait & Posture*, vol. 26, no. 4, pp. 546–552, 2007.
- [65] J. L. Hicks, M. H. Schwartz, A. S. Arnold, and S. L. Delp, "Crouched postures reduce the capacity of muscles to extend the hip and knee during the single-limb stance phase of gait," *Journal of Biomechanics*, vol. 41, no. 5, pp. 960–967, 2008.
- [66] K. M. Steele, M. M. van der Krog, M. H. Schwartz, and S. L. Delp, "How much muscle strength is required to walk in a crouch gait?," *Journal of Biomechanics*, vol. 45, no. 15, pp. 2564–2569, 2012.
- [67] A. S. Arnold, M. Q. Liu, M. H. Schwartz, S. Öunpuu, and S. L. Delp, "The role of estimating muscle-tendon lengths and velocities of the hamstrings in the evaluation and treatment of crouch gait," *Gait & Posture*, vol. 23, no. 3, pp. 273–281, 2006.
- [68] I. Jonkers, C. Stewart, K. Desloovere, G. Molenaers, and A. Spaepen, "Musculo-tendon length and lengthening velocity of rectus femoris in stiff knee gait," *Gait & Posture*, vol. 23, no. 2, pp. 222–229, 2006.
- [69] J. A. Reinbolt, M. D. Fox, A. S. Arnold, S. Öunpuu, and S. L. Delp, "Importance of preswing rectus femoris activity in stiff-knee gait," *Journal of Biomechanics*, vol. 41, no. 11, pp. 2362–2369, 2008.
- [70] M. M. van der Krog, S. L. Delp, and M. H. Schwartz, "How robust is human gait to muscle weakness?," *Gait & Posture*, vol. 36, no. 1, pp. 113–119, 2012.

- [71] I. Jonkers, C. Stewart, and A. Spaepen, “The study of muscle action during single support and swing phase of gait: clinical relevance of forward simulation techniques,” *Gait & Posture*, vol. 17, no. 2, pp. 97–105, 2003.
- [72] I. Jonkers, C. Stewart, and A. Spaepen, “The complementary role of the plantarflexors, hamstrings and gluteus maximus in the control of stance limb stability during gait,” *Gait & Posture*, vol. 17, no. 3, pp. 264–272, 2003.
- [73] A. S. Arnold, S. S. Blemker, and S. L. Delp, “Evaluation of a deformable musculoskeletal model for estimating muscle-tendon lengths during crouch gait,” *Annals of Biomedical Engineering*, vol. 29, no. 3, pp. 263–274, 2001.
- [74] L. Scheyns, D. Loeckx, A. Spaepen, P. Suetens, and I. Jonkers, “Atlas-based non-rigid image registration to automatically define line-of-action muscle models: A validation study,” *Journal of Biomechanics*, vol. 42, no. 5, pp. 565–572, 2009.
- [75] L. Scheyns, K. Desloovere, A. Spaepen, P. Suetens, and I. Jonkers, “Calculating gait kinematics using MR-based kinematic models,” *Gait & Posture*, vol. 33, no. 2, pp. 158–164, 2011.
- [76] L. Scheyns, K. Desloovere, P. Suetens, and I. Jonkers, “Level of subject-specific detail in musculoskeletal models affects hip moment arm length calculation during gait in pediatric subjects with increased femoral anteversion,” *Journal of Biomechanics*, vol. 44, no. 7, pp. 1346–1353, 2011.
- [77] L. Bosmans, K. Jansen, M. Wesseling, G. Molenaers, L. Scheyns, and I. Jonkers, “The role of altered proximal femoral geometry in impaired pelvis stability and hip control during CP gait: A simulation study,” *Gait & Posture*, vol. 44, pp. 61–67, 2016.
- [78] R. A. Brand, D. R. Pedersen, and J. A. Friederich, “The sensitivity of muscle force predictions to changes in physiologic cross-sectional area,” *Journal of Biomechanics*, vol. 19, no. 8, pp. 589–596, 1986.
- [79] J. A. Friederich and R. A. Brand, “Muscle fiber architecture in the human lower limb,” *Journal of Biomechanics*, vol. 23, no. 1, pp. 91–95, 1990.
- [80] L. R. Smith, K. S. Lee, S. R. Ward, H. G. Chambers, and R. L. Lieber, “Hamstring contractures in children with spastic cerebral palsy result from a stiffer extracellular matrix and increased in vivo sarcomere length,” *The Journal of Physiology*, vol. 589, pp. 2625–2639, 2011.

- [81] L. Barber, T. Hastings-Ison, R. Baker, R. Barrett, and G. Lichtwark, “Medial gastrocnemius muscle volume and fascicle length in children aged 2 to 5 years with cerebral palsy,” *Developmental Medicine and Child Neurology*, vol. 53, pp. 543–548, 2011.
- [82] L. Barber, R. Barrett, and G. Lichtwark, “Passive muscle mechanical properties of the medial gastrocnemius in young adults with spastic cerebral palsy,” *Journal of Biomechanics*, vol. 44, no. 13, pp. 2496–2500, 2011.
- [83] L. Barber, R. Barrett, and G. Lichtwark, “Medial gastrocnemius muscle fascicle active torque-length and Achilles tendon properties in young adults with spastic cerebral palsy,” *Journal of Biomechanics*, vol. 45, no. 15, pp. 2526–2530, 2012.
- [84] R. S. Barrett and G. a. Lichtwark, “Gross muscle morphology and structure in spastic cerebral palsy: a systematic review,” *Developmental Medicine and Child Neurology*, vol. 52, pp. 794–804, 2010.
- [85] C. R. Winby, D. G. Lloyd, and T. B. Kirk, “Evaluation of different analytical methods for subject-specific scaling of musculotendon parameters,” *Journal of Applied Biomechanics*, vol. 41, no. 8, pp. 1682–1688, 2008.
- [86] L. Modenese, E. Ceseracciu, M. Reggiani, and D. G. Lloyd, “Estimation of musculotendon parameters for scaled and subject specific musculoskeletal models using an optimization technique,” *Journal of Biomechanics*, vol. 49, no. 2, pp. 141–148, 2016.
- [87] H. Hatze, “Estimation of myodynamic parameter values from observations on isometrically contracting muscle groups,” *European Journal of Applied Physiology and Occupational Physiology*, vol. 46, no. 4, pp. 325–338, 1981.
- [88] B. Garner and M. Pandy, “Estimation of musculotendon properties in the human upper limb,” *Annals of Biomedical Engineering*, vol. 31, pp. 207–220, 2003.
- [89] A. Van Campen, G. Pipeleers, F. De Groote, I. Jonkers, and J. De Schutter, “A new method for estimating subject-specific muscle-tendon parameters of the knee joint actuators: a simulation study,” *International Journal for Numerical Methods in Biomedical Engineering*, vol. 30, no. 10, pp. 969–987, 2014.
- [90] D. G. Lloyd and T. F. Besier, “An EMG-driven musculoskeletal model to estimate muscle forces and knee joint moments in vivo,” *Journal of Biomechanics*, vol. 36, no. 6, pp. 765–776, 2003.

- [91] T. S. Buchanan, D. G. Lloyd, K. Manal, and T. F. Besier, “Neuromusculoskeletal modeling: estimation of muscle forces and joint moments and movements from measurements of neural command,” *Journal of Applied Biomechanics*, vol. 20, no. 4, pp. 367–395, 2004.
- [92] P. W. Brand, R. B. Beach, and D. E. Thompson, “Relative tension and potential excursion of muscles in the forearm and hand,” *The Journal of Hand Surgery*, vol. 6, no. 3, pp. 209–219, 1981.
- [93] N. Babault, M. Pousson, A. Michaut, Y. Ballay, and J. Van Hoecke, “EMG activity and voluntary activation during knee-extensor concentric torque generation,” *European Journal of Applied Physiology*, vol. 86, no. 6, pp. 541–547, 2002.
- [94] B. R. Shuman, M. Goudriaan, K. Desloovere, M. H. Schwartz, and K. M. Steele, “Muscle synergies demonstrate only minimal changes after treatment in cerebral palsy,” *Journal of NeuroEngineering and Rehabilitation*, vol. 16, no. 46, pp. 1–10, 2019.
- [95] V. Dietz and T. Sinkjaer, “Spastic movement disorder: impaired reflex function and altered muscle mechanics,” *Lancet Neurology*, vol. 6, no. 8, pp. 725–733, 2007.
- [96] L. Bar-On, G. Molenaers, E. Aertbeliën, D. Monari, H. Feys, and K. Desloovere, “The relation between spasticity and muscle behavior during the swing phase of gait in children with cerebral palsy,” *Research in Developmental Disabilities*, vol. 35, no. 12, pp. 3354–3364, 2014.
- [97] P. B. C. Matthews, “The response of de-efferented muscle spindle receptors to stretching at different velocities,” *Journal of Physiology*, vol. 168, no. 3, pp. 660–678, 1963.
- [98] P. B. C. Matthews and R. B. Stein, “The sensitivity of muscle spindle afferents to small sinusoidal changes of length,” *Journal of Physiology*, vol. 200, no. 3, pp. 723–743, 1969.
- [99] K. P. Blum, B. Lamotte D’Incamps, D. Zytnicki, and L. H. Ting, “Force encoding in muscle spindles during stretch of passive muscle,” *PLoS Computational Biology*, vol. 13, no. 9, p. e1005767, 2017.
- [100] M. M. van der Krogt, L. Bar-On, T. Kindt, K. Desloovere, and J. Harlaar, “Neuro-musculoskeletal simulation of instrumented contracture and spasticity assessment in children with cerebral palsy,” *Journal of NeuroEngineering and Rehabilitation*, vol. 13, no. 1, p. 64, 2016.

- [101] R. R. Neptune, D. J. Clark, and S. A. Kautz, “Modular control of human walking: A simulation study,” *Journal of Biomechanics*, vol. 42, no. 9, pp. 1282–1287, 2009.
- [102] M. Sartori, L. Gizzi, D. G. Lloyd, and D. Farina, “A musculoskeletal model of human locomotion driven by a low dimensional set of impulsive excitation primitives,” *Frontiers in Computational Neuroscience*, vol. 7, no. 79, pp. 1–22, 2013.
- [103] N. Mehrabi, M. H. Schwartz, and K. M. Steele, “Can Altered Muscle Synergies Control Unimpaired Gait?,” *Journal of Biomechanics*, vol. 90, pp. 84–91, 2019.
- [104] C. Y. Scovil and J. L. Ronsky, “Sensitivity of a Hill-based muscle model to perturbations in model parameters,” *Journal of Biomechanics*, vol. 39, no. 11, pp. 2055–2063, 2006.
- [105] C. Redl, M. Gfoehler, and M. G. Pandy, “Sensitivity of muscle force estimates to variations in muscle-tendon properties,” *Human Movement Science*, vol. 26, no. 2, pp. 306–319, 2007.
- [106] F. De Groote, A. Van Campen, I. Jonkers, and J. De Schutter, “Sensitivity of dynamic simulations of gait and dynamometer experiments to hill muscle model parameters of knee flexors and extensors,” *Journal of Biomechanics*, vol. 43, no. 10, pp. 1876–1883, 2010.
- [107] D. C. Ackland, Y.-C. Lin, and M. G. Pandy, “Sensitivity of model predictions of muscle function to changes in moment arms and muscle-tendon properties: A Monte-Carlo analysis,” *Journal of Biomechanics*, vol. 45, no. 8, pp. 1463–1471, 2012.
- [108] M. Sartori, M. Reggiani, D. Farina, and D. G. Lloyd, “EMG-driven forward-dynamic estimation of muscle force and joint moment about multiple degrees of freedom in the human lower extremity,” *PLoS ONE*, vol. 7, no. 12, pp. 1–11, 2012.
- [109] L. Bar-On, E. Aertbeliën, H. Wambacq, D. Severijns, K. Lambrecht, B. Dan, C. Huenaerts, H. Bruyninckx, L. Janssens, L. Van Gestel, E. Jaspers, G. Molenaers, and K. Desloovere, “A clinical measurement to quantify spasticity in children with cerebral palsy by integration of multidimensional signals,” *Gait & Posture*, vol. 38, no. 1, pp. 141–147, 2013.
- [110] K. Desloovere, G. Molenaers, H. Feys, C. Huenaerts, B. Callewaert, and P. Van de Walle, “Do dynamic and static clinical measurements correlate with gait analysis parameters in children with cerebral palsy?,” *Gait & Posture*, vol. 24, no. 3, pp. 302–313, 2006.

- [111] L. Bosmans, M. Wesseling, K. Desloovere, G. Molenaers, L. Scheys, and I. Jonkers, "Hip contact force in presence of aberrant bone geometry during normal and pathological gait," *Journal of Orthopaedic Research*, vol. 32, no. 11, pp. 1406–1415, 2014.
- [112] S. Delp, F. Anderson, A. Arnold, P. Loan, A. Habib, C. John, E. Guendelman, and D. Thelen, "OpenSim: open-source software to create and analyze dynamic simulations of movement," *IEEE Transactions on Biomedical Engineering*, vol. 54, no. 11, pp. 1940–1950, 2007.
- [113] M. H. Schwartz and A. Rozumalski, "A new method for estimating joint parameters from motion data," *Journal of Biomechanics*, vol. 38, no. 1, pp. 107–116, 2005.
- [114] S. R. Hamner, A. Seth, and S. L. Delp, "Muscle contributions to propulsion and support during running," *Journal of Biomechanics*, vol. 43, no. 14, pp. 2709–2716, 2010.
- [115] F. De Groote, T. De Laet, I. Jonkers, and J. De Schutter, "Kalman smoothing improves the estimation of joint kinematics and kinetics in marker-based human gait analysis," *Journal of Biomechanics*, vol. 41, no. 16, pp. 3390–3398, 2008.
- [116] D. Limebeer and A. V. Rao, "Faster, higher, and greener: Vehicular optimal control," *IEEE Control Systems Magazine*, vol. 35, no. 2, pp. 36–56, 2015.
- [117] M. Kelly, "An introduction to trajectory optimization: how to do your own direct collocation," *SIAM Review*, vol. 59, no. 4, pp. 849–904, 2017.
- [118] J. Nocedal and S. J. Wright, "Calculating Derivatives," in *Numerical Optimization* (T. V. Mikosch, I. Resnick, S., and S. M. Robinson, eds.), ch. 8, pp. 193–219, Springer-Verlag New York, 2 ed., 2006.
- [119] M. A. Sherman, A. Seth, and S. L. Delp, "Simbody: multibody dynamics for biomedical research," *Procedia IUTAM*, vol. 2, pp. 241–261, 2011.
- [120] J. A. E. Andersson, *A general-purpose software framework for dynamic optimization*. Doctoral thesis, KU Leuven, 2013.
- [121] M. A. Patterson and A. V. Rao, "GPOPS-II : a MATLAB software for solving multiple-phase optimal control problems using hp-adaptive Gaussian quadrature collocation methods and sparse nonlinear programming," *ACM Transactions on Mathematical Software*, vol. 41, no. 1, pp. 1:1–1:37, 2014.

- [122] A. Wächter and L. T. Biegler, “On the implementation of an interior-point filter line-search algorithm for large-scale nonlinear programming,” *Mathematical Programming*, vol. 106, no. 1, pp. 25–57, 2006.
- [123] J. Nocedal and S. J. Wright, “Interior-point methods for nonlinear programming,” in *Numerical Optimization* (T. V. Mikosch, I. Resnick, S., and S. M. Robinson, eds.), ch. 19, pp. 563–597, Springer-Verlag New York, 2 ed., 2006.
- [124] P. R. Amestoy, I. Duff, and J.-Y. L'Excellent, “Multifrontal parallel distributed symmetric and unsymmetric solvers,” *Computer Methods in Applied Mechanics and Engineering*, vol. 184, no. 2-4, pp. 501–520, 2000.
- [125] “HSL. A collection of Fortran codes for large scale scientific computation. <http://www.hsl.rl.ac.uk/>.”
- [126] A. Walther and A. Griewank, “Getting started with ADOL-C,” in *Combinatorial Scientific Computing* (U. Naumann and O. Schenk, eds.), pp. 181–202, Chapman & Hall/CRC Computational Science, 2012.
- [127] A. van den Bogert, T. Geijtenbeek, O. Even-Zohar, F. Steenbrink, and E. Hardin, “A real-time system for biomechanical analysis of human movement and muscle function,” *Medical & Biological Engineering & Computing*, vol. 51, no. 10, pp. 1069–77, 2013.
- [128] M. A. Sherman, A. Seth, and S. L. Delp, “What is a moment arm? Calculating muscle effectiveness in biomechanical models using generalized coordinates,” in *ASME/IIDETC/CIE*, (Portland, Oregon), pp. 1–9, 2013.
- [129] J. T. Betts, “The optimal control problem,” in *Practical Methods for Optimal Control and Estimation Using Nonlinear Programming*, pp. 123–218, Philadelphia: SIAM, 2 ed., 2010.
- [130] L. J. Bhargava, M. G. Pandy, and F. C. Anderson, “A phenomenological model for estimating metabolic energy consumption in muscle contraction,” *Journal of Biomechanics*, vol. 37, no. 1, pp. 81–88, 2004.
- [131] T. K. Uchida, J. L. Hicks, C. L. Dembia, and S. L. Delp, “Stretching your energetic budget: how tendon compliance affects the metabolic cost of running,” *PLoS ONE*, vol. 11, no. 3, p. e0150378, 2016.
- [132] G. Staude and W. Wolf, “Objective motor response onset detection in surface myoelectric signals,” *Medical Engineering and Physics*, vol. 21, no. 6-7, pp. 449–467, 1999.

- [133] M. Klein Horsman, H. Koopman, F. van der Helm, L. Poliacu Prosé, and H. Veeger, “Morphological muscle and joint parameters for musculoskeletal modelling of the lower extremity,” *Clinical Biomechanics*, vol. 22, no. 2, pp. 239–247, 2007.
- [134] E. M. Arnold, S. R. Ward, R. L. Lieber, and S. L. Delp, “A model of the lower limb for analysis of human movement,” *Annals of Biomedical Engineering*, vol. 38, no. 2, pp. 269–279, 2010.
- [135] M. A. King and M. R. Yeadon, “Determining subject-specific torque parameters for use in a torque-driven simulation model of dynamic jumping,” *Journal of Applied Biomechanics*, vol. 18, no. 3, pp. 207–217, 2002.
- [136] B. a. Garner and M. G. Pandy, “Estimation of musculotendon properties in the human upper limb,” *Annals of Biomedical Engineering*, vol. 31, pp. 207–220, 2003.
- [137] M. Wesseling, F. De Groote, C. Meyer, K. Corten, J.-P. Simon, K. Desloovere, and I. Jonkers, “Subject-specific musculoskeletal modelling in patients before and after total hip arthroplasty,” *Computer Methods in Biomechanics and Biomedical Engineering*, vol. 19, no. 15, pp. 1683–1691, 2016.
- [138] S. C. White and D. A. Winter, “Predicting muscle forces in gait from EMG signals and musculotendon kinematics,” *Journal of Electromyography and Kinesiology*, vol. 2, no. 4, pp. 217–231, 1992.
- [139] J. T. Betts, “Parameter estimation,” in *Practical Methods for Optimal Control and Estimation Using Nonlinear Programming*, Advances in Design and Control, pp. 219–245, Philadelphia: SIAM, 2 ed., 2010.
- [140] F. De Groote, B. Demeulenaere, J. Swevers, J. De Schutter, and I. Jonkers, “A physiology-based inverse dynamic analysis of human gait using sequential convex programming: a comparative study,” *Computer Methods in Biomechanics and Biomedical Engineering*, vol. 15, no. 10, pp. 1093–1102, 2012.
- [141] P. Konrad, “The ABC of EMG,” *A practical introduction to kinesiological electromyography*, pp. 1–60, 2005.
- [142] M. J. Weinstein and A. V. Rao, “A source transformation via operator overloading method for the automatic differentiation of mathematical functions in MATLAB,” *ACM Transactions on Mathematical Software*, vol. 42, no. 2, pp. 11:1–11:44, 2016.

- [143] S. L. Delp and F. E. Zajac, "Force- and moment generating capacity of lower-extremity muscles before and after tendon lengthening," *Clinical Orthopaedics and Related Research*, vol. 284, pp. 247–259, 1992.
- [144] J. J. Woods and B. Bigland-Ritchie, "Linear and non-linear surface EMG/force relationships in human muscles. An anatomical/functional argument for the existence of both," *American Journal of Physical Medicine & Rehabilitation*, vol. 62, no. 6, pp. 287–299, 1983.
- [145] J. M. Wakeling, S. S. M. Lee, A. S. Arnold, M. De Boef Miara, and A. A. Biewener, "A muscle's force depends on the recruitment patterns of its fibers," *Annals of Biomedical Engineering*, vol. 40, no. 8, pp. 1708–1720, 2012.
- [146] B. R. Umberger, K. G. M. Gerritsen, and P. E. Martin, "A model of human muscle energy expenditure," *Computer Methods in Biomechanics and Biomedical Engineering*, vol. 6, no. 2, pp. 99–111, 2003.
- [147] V. M. Zatsiorsky and B. I. Prilutsky, *Biomechanics of Skeletal Muscles*. Champaign: Human Kinetics, 2012.
- [148] M. Sartori, D. Farina, and D. G. Lloyd, "Hybrid neuromusculoskeletal modeling to best track joint moments using a balance between muscle excitations derived from electromyograms and optimization," *Journal of Biomechanics*, vol. 47, no. 15, pp. 3613–3621, 2014.
- [149] A. Scholz, M. Sherman, I. Stavness, S. Delp, and A. Kecskeméthy, "A fast multi-obstacle muscle wrapping method using natural geodesic variations," *Multibody System Dynamics*, vol. 36, no. 2, pp. 195–219, 2016.
- [150] R. W. Bohannon and M. B. Smith, "Interrater reliability of a modified Ashworth scale of muscle spasticity," *Physical Therapy*, vol. 67, no. 2, pp. 206–207, 1987.
- [151] R. N. Boyd and H. K. Graham, "Objective measurement of clinical findings in the use of botulinum toxin type A for the management of children with cerebral palsy," *European Journal of Neurology*, vol. 6, no. Suppl. 4, pp. s23–s35, 1999.
- [152] L. M. Mendell, "Modifiability of spinal synapses," *Physiological Reviews*, vol. 64, no. 1, pp. 260–324, 1984.
- [153] J. He, W. R. Norling, and Y. Wang, "A dynamic neuromuscular model for describing the pendulum test of spasticity," *IEEE Transactions on Biomedical Engineering*, vol. 44, no. 3, pp. 175–184, 1997.

- [154] P. Le Cavorzin, S. A. Poudens, F. Chagneau, G. Carrault, H. Allain, and P. Rochcongar, “A comprehensive model of spastic hypertonia derived from the pendulum test of the leg,” *Muscle & Nerve*, vol. 24, no. 12, pp. 1612–1621, 2001.
- [155] J. W. Fee and R. A. Foulds, “Neuromuscular Modeling of Spasticity in Cerebral Palsy,” *IEEE Transactions on Neural Systems and Rehabilitation Engineering*, vol. 12, no. 1, pp. 55–64, 2004.
- [156] Z. Hasan, “A model of spindle afferent response to muscle stretch,” *Journal of Neurophysiology*, vol. 49, no. 4, pp. 989–1006, 1983.
- [157] C.-C. K. Lin and P. E. Crago, “Structural model of the muscle spindle,” *Annals of Biomedical Engineering*, vol. 30, no. 1, pp. 68–83, 2002.
- [158] M. P. Mileusnic, I. E. Brown, N. Lan, and G. E. Loeb, “Mathematical models of proprioceptors. I. Control and transduction in the muscle spindle,” *Journal of Neurophysiology*, vol. 96, no. 4, pp. 1772–1788, 2006.
- [159] D. Lewis and U. Proske, “The effect of muscle length and rate of fusimotor stimulation on the frequency of discharge in primary endings from muscle spindles in the cat,” *Journal of Physiology*, vol. 222, no. 3, pp. 511–535, 1972.
- [160] U. Proske and G. Stuart, “The initial burst of impulses in responses of toad muscle spindles during stretch,” *Journal of Physiology*, vol. 368, no. 1, pp. 1–17, 1985.
- [161] L. Ada, W. Vattanasilp, N. J. O’Dwyer, and J. Crosbie, “Does spasticity contribute to walking dysfunction after stroke?,” *Journal of neurology, neurosurgery, and psychiatry*, vol. 64, no. 5, pp. 628–635, 1998.
- [162] J. Marsden, G. Ramdharry, V. Stevenson, and A. Thompson, “Muscle paresis and passive stiffness: key determinants in limiting function in hereditary and sporadic spastic paraparesis,” *Gait & Posture*, vol. 35, no. 2, pp. 266–271, 2012.
- [163] M. Willerslev-Olsen, J. B. Andersen, T. Sinkjaer, and J. B. Nielsen, “Sensory feedback to ankle plantar flexors is not exaggerated during gait in spastic hemiplegic children with cerebral palsy,” *Journal of Neurophysiology*, vol. 111, no. 4, pp. 746–754, 2014.
- [164] D. L. Damiano, E. Laws, D. V. Carmines, and M. F. Abel, “Relationship of spasticity to knee angular velocity and motion during gait in cerebral palsy,” *Gait & Posture*, vol. 23, no. 1, pp. 1–8, 2006.

- [165] A. Tuzson, K. Granata, and M. Abel, "Spastic velocity threshold constrains functional performance in cerebral palsy," *Archives of Physical Medicine and Rehabilitation*, vol. 84, no. 9, pp. 1363–1368, 2003.
- [166] J. R. Gage, J. Perry, R. R. Hicks, S. Koop, and J. R. Werntz, "Rectus femoris transfer to improve knee function of children with cerebral palsy," *Developmental Medicine & Child Neurology*, vol. 29, pp. 159–166, 1987.
- [167] J. Perry, "Distal rectus femoris transfer," *Developmental Medicine & Child Neurology*, vol. 29, pp. 153–158, 1987.
- [168] A. Falisse, S. Van Rossum, I. Jonkers, and F. De Groote, "EMG-driven optimal estimation of subject-specific Hill model muscle-tendon parameters of the knee joint actuators," *IEEE Transactions on Biomedical Engineering*, vol. 64, no. 9, pp. 2253–2262, 2017.
- [169] J. Hicks, M. Schwartz, and S. Delp, "Modeling and simulation of normal and pathological gait," in *The identification and treatment of gait problems in cerebral palsy* (J. Gage, M. Schwartz, S. Koop, and T. Novacheck, eds.), pp. 285–305, Mac Keith Press, 2nd ed., 2009.
- [170] J. U. Baumann, H. Ruetsch, and K. Schürmann, "Distal hamstring lengthening in cerebral palsy - An evaluation by gait analysis," *International Orthopaedics*, vol. 3, no. 4, pp. 305–309, 1980.
- [171] D. H. Sutherland and J. R. Davids, "Common gait abnormalities of the knee in cerebral palsy," *Clinical Orthopaedics and Related Research*, vol. 288, pp. 139–147, 1993.
- [172] P. Crenna, "Spasticity and 'spastic' gait in children with cerebral palsy," *Neuroscience and Biobehavioral Reviews*, vol. 22, no. 4, pp. 571–578, 1998.
- [173] J. Perry and J. Burnfield, "Normal gait," in *Gait analysis: normal and pathological function*, ch. Knee, pp. 49–162, SLACK Inc, 2nd ed., 2010.
- [174] V. Dietz, "Proprioception and locomotor disorders," *Nature Reviews Neuroscience*, vol. 3, no. 10, pp. 781–790, 2002.
- [175] M. Faist, M. Ertel, W. Berger, and V. Dietz, "Impaired modulation of quadriceps tendon jerk reflex during spastic gait: differences between spinal and cerebral lesions," *Brain*, vol. 122, no. 3, pp. 567–579, 1999.
- [176] T. Sinkjaer, J. B. Andersen, and J. F. Nielsen, "Impaired stretch reflex and joint torque modulation during spastic gait in multiple sclerosis patients," *Journal of Neurology*, vol. 243, no. 8, pp. 566–574, 1996.

- [177] C. Capaday and R. Stein, “Difference in the amplitude of the human soleus H reflex during walking and running,” *Journal of Physiology*, vol. 392, pp. 513–522, 1987.
- [178] P. Crenna and C. Frigo, “Excitability of the soleus H-reflex arc during walking and stepping in man,” *Experimental Brain Research*, vol. 66, no. 1, pp. 49–60, 1987.
- [179] V. Dietz, M. Bischer, M. Faist, and M. Trippel, “Amplitude modulation of the human quadriceps tendon jerk reflex during gait,” *Experimental Brain Research*, vol. 82, no. 1, pp. 211–213, 1990.
- [180] T. Sinkjaer, J. B. Andersen, and B. Larsen, “Soleus stretch reflex modulation during gait in humans,” *Journal of Neurophysiology*, vol. 76, no. 2, pp. 1112–1120, 1996.
- [181] J. B. Nielsen, N. T. Petersen, C. Crone, and T. Sinkjaer, “Stretch reflex regulation in healthy subjects and patients with spasticity,” *Neuromodulation*, vol. 8, no. 1, pp. 49–57, 2005.
- [182] H. Van de Crommert, M. Faist, W. Berger, and J. Duysens, “Biceps femoris tendon jerk reflexes are enhanced at the end of the swing phase in humans,” *Brain Research*, vol. 734, no. 1-2, pp. 341–344, 1996.
- [183] V. G. Macefield, “Discharge rates and discharge variability of muscle spindle afferents in human chronic spinal cord injury,” *Clinical Neurophysiology*, vol. 124, pp. 114–119, 2013.
- [184] R. Wang, P. Herman, Ö. Ekeberg, J. Gäverth, A. Fagergren, and H. Forssberg, “Neural and non-neural related properties in the spastic wrist flexors: An optimization study,” *Medical Engineering and Physics*, vol. 47, pp. 198–209, 2017.
- [185] S. A. Safavynia and L. H. Ting, “Long-latency muscle activity reflects continuous, delayed sensorimotor feedback of task-level and not joint-level error,” *Journal of Neurophysiology*, vol. 110, no. 6, pp. 1278–90, 2013.
- [186] M. J. Grey, N. Mazzaro, J. B. Nielsen, and T. Sinkjaer, “Ankle extensor proprioceptors contribute to the enhancement of the soleus EMG during the stance phase of human walking,” *Canadian Journal of Physiology and Pharmacology*, vol. 82, no. 8-9, pp. 610–616, 2004.
- [187] A. Griewank and A. Walther, *Evaluating derivatives: principles and techniques of algorithmic differentiation*. SIAM, 2 ed., 2008.

- [188] A. H. Gebremedhin, F. Manne, and A. Pothen, “What color is your Jacobian? Graph coloring for computing derivatives,” *SIAM Review*, vol. 47, no. 4, pp. 629–705, 2005.
- [189] “CppAD: A package for differentiation of C++ algorithms. <https://projects.coin-or.org/CppAD/>”
- [190] A. Seth, J. L. Hicks, T. K. Uchida, A. Habib, C. L. Dembia, J. J. Dunne, C. F. Ong, M. S. DeMers, A. Rajagopal, M. Millard, S. R. Hamner, E. M. Arnold, J. R. Yong, S. K. Lakshmikanth, M. A. Sherman, J. P. Ku, and S. L. Delp, “OpenSim: simulating musculoskeletal dynamics and neuromuscular control to study human and animal movement,” *PLoS Computational Biology*, vol. 14, no. 7, p. e1006223, 2018.
- [191] M. Gifthaler, M. Neunert, M. Stäuble, M. Frigerio, C. Semini, and J. Buchli, “Automatic differentiation of rigid body dynamics for optimal control and estimation,” *Advanced Robotics*, vol. 31, no. 22, pp. 1225–1237, 2017.
- [192] Tedrake R. and the Drake Development Team, “Drake: model-based design and verification for robotics. <https://drake.mit.edu/>,” 2019.
- [193] N. Docquier, A. Poncelet, and P. Fisette, “ROBOTRAN: A powerful symbolic generator of multibody models,” *Mechanical Sciences*, vol. 4, no. 1, pp. 199–219, 2013.
- [194] J. Wojtusch, J. Kunz, and O. V. Stryk, “MBSlib-An efficient multibody systems library for kinematics and dynamics simulation, optimization and sensitivity analysis,” *IEEE Robotics and Automation Letters*, vol. 1, no. 2, pp. 954–960, 2016.
- [195] J. Carpentier, G. Saurel, G. Buondonno, J. Mirabel, F. Lamiraux, O. Stasse, and N. Mansard, “The Pinocchio C++ library: A fast and flexible implementation of rigid body dynamics algorithms and their analytical derivatives,” *Proceedings of the 2019 IEEE/SICE International Symposium on System Integration, SII 2019*, pp. 614–619, 2019.
- [196] G. Guennebaud, B. Jacob, and Others, “Eigen v3. <http://eigen.tuxfamily.org/>,” 2010.
- [197] M. Abadi, A. Agarwal, P. Barham, E. Brevdo, Z. Chen, C. Citro, G. S. Corrado, A. Davis, J. Dean, M. Devin, S. Ghemawat, I. Goodfellow, A. Harp, G. Irving, M. Isard, Y. Jia, R. Jozefowicz, L. Kaiser, M. Kudlur, J. Levenberg, D. Mane, R. Monga, S. Moore, D. Murray, C. Olah, M. Schuster, J. Shlens, B. Steiner, I. Sutskever, K. Talwar, P. Tucker, V. Vanhoucke, V. Vasudevan, F. Viegas, O. Vinyals,

- P. Warden, M. Wattenberg, M. Wicke, Y. Yu, and X. Zheng, “TensorFlow: Large-Scale Machine Learning on Heterogeneous Distributed Systems,” *arXiv [Preprint]*. *arXiv:1603.04467*. Available online at: <https://arxiv.org/abs/1603.04467>, 2016.
- [198] The Theano Development Team, R. Al-Rfou, G. Alain, A. Almahairi, C. Angermueller, D. Bahdanau, N. Ballas, F. Bastien, J. Bayer, A. Belikov, A. Belopolsky, Y. Bengio, A. Bergeron, J. Bergstra, V. Bisson, J. B. Snyder, N. Bouchard, N. Boulanger-Lewandowski, X. Bouthillier, A. de Brébisson, O. Breuleux, P.-L. Carrier, K. Cho, J. Chorowski, P. Christiano, T. Cooijmans, M.-A. Côté, M. Côté, A. Courville, Y. N. Dauphin, O. Delalleau, J. Demouth, G. Desjardins, S. Dieleman, L. Dinh, M. Ducoffe, V. Dumoulin, S. E. Kahou, D. Erhan, Z. Fan, O. Firat, M. Germain, X. Glorot, I. Goodfellow, M. Graham, C. Gulcehre, P. Hamel, I. Harlouchet, J.-P. Heng, B. Hidasi, S. Honari, A. Jain, S. Jean, K. Jia, M. Korobov, V. Kulkarni, A. Lamb, P. Lamblin, E. Larsen, C. Laurent, S. Lee, S. Lefrancois, S. Lemieux, N. Léonard, Z. Lin, J. A. Livezey, C. Lorenz, J. Lowin, Q. Ma, P.-A. Manzagol, O. Mastropietro, R. T. McGibbon, R. Memisevic, B. van Merriënboer, V. Michalski, M. Mirza, A. Orlandi, C. Pal, R. Pascanu, M. Pezeshki, C. Raffel, D. Renshaw, M. Rocklin, A. Romero, M. Roth, P. Sadowski, J. Salvatier, F. Savard, J. Schlüter, J. Schulman, G. Schwartz, I. V. Serban, D. Serdyuk, S. Shabanian, É. Simon, S. Spieckermann, S. R. Subramanyam, J. Sygnowski, J. Tanguay, G. van Tulder, J. Turian, S. Urban, P. Vincent, F. Visin, H. de Vries, D. Warde-Farley, D. J. Webb, M. Willson, K. Xu, L. Xue, L. Yao, S. Zhang, and Y. Zhang, “Theano: A Python framework for fast computation of mathematical expressions,” *arXiv [Preprint]* *arXiv:1605.02688* Available online at: <https://arxiv.org/abs/1605.02688>, pp. 1–19, 2016.
- [199] J. Degrave, M. Hermans, J. Dambre, and F. Wyffels, “A differentiable physics engine for deep learning in robotics,” *Frontiers in Neurorobotics*, vol. 13, no. 6, pp. 1–9, 2019.
- [200] J. Nocedal and S. J. Wright, “A regularization procedure,” in *Numerical Optimization* (T. V. Mikosch, I. Resnick, S, and S. M. Robinson, eds.), ch. Appendix B, pp. 635–636, Springer-Verlag New York, 2 ed., 2006.
- [201] P. E. Gill, W. Murray, and M. A. Saunders, “SNOPT: An SQP algorithm for large-scale constrained optimization,” *SIAM Review*, vol. 47, no. 1, pp. 99–131, 2005.
- [202] R. H. Byrd, J. Nocedal, and R. A. Waltz, “KNITRO: an integrated package for nonlinear optimization,” in *Large Scale Nonlinear Optimization*.

- Nonconvex Optimization and Its Applications* (G. Di Pillo and M. Roma, eds.), Boston: Springer, 2006.
- [203] C. Hall and C. J. Nester, “Sagittal plane compensations for artificially induced limitation of the first metatarsophalangeal joint: a preliminary study,” *Journal of the American Podiatric Medical Association*, vol. 94, no. 3, pp. 269–274, 2004.
 - [204] H. Geyer, A. Seyfarth, and R. Blickhan, “Compliant leg behaviour explains basic dynamics of walking and running,” *Proceedings of the Royal Society B: Biological Sciences*, vol. 273, no. 1603, pp. 2861–2867, 2006.
 - [205] A. D. Kuo, “The six determinants of gait and the inverted pendulum analogy: a dynamic walking perspective,” *Human Movement Science*, vol. 26, no. 4, pp. 617–656, 2007.
 - [206] J. M. Donelan, R. Kram, and A. D. Kuo, “Mechanical work for step-to-step transitions is a major determinant of the metabolic cost of human walking,” *The Journal of Experimental Biology*, vol. 205, no. 23, pp. 3717–3727, 2002.
 - [207] A. D. Kuo, J. M. Donelan, and A. Ruina, “Energetic consequences of walking like an inverted pendulum: step-to-step transitions,” *Exercise and sport sciences reviews*, vol. 33, no. 2, pp. 88–97, 2005.
 - [208] Y. Xiang, J. S. Arora, S. Rahmatalla, T. Marler, R. Bhatt, and K. Abdel-Malek, “Human lifting simulation using a multi-objective optimization approach,” *Multibody System Dynamics*, vol. 23, no. 4, pp. 431–451, 2010.
 - [209] A. Falisse, S. Van Rossum, J. Gijsbers, F. Steenbrink, B. J. van Basten, I. Jonkers, A. J. van den Bogert, and F. De Groote, “OpenSim versus Human Body Model: a comparison study for the lower limbs during gait,” *Journal of Applied Biomechanics*, vol. 34, no. 6, pp. 496–502, 2018.
 - [210] D. M. Bramble and D. E. Lieberman, “Endurance running and the evolution of Homo,” *Nature*, vol. 432, no. 7015, pp. 345–352, 2004.
 - [211] E. R. Esposito and R. H. Miller, “Maintenance of muscle strength retains a normal metabolic cost in simulated walking after transtibial limb loss,” *PLoS ONE*, vol. 13, no. 1, p. e0191310, 2018.
 - [212] B. R. Umberger, “Stance and swing phase costs in human walking,” *Journal of the Royal Society Interface*, vol. 7, no. 50, pp. 1329–1340, 2010.
 - [213] E. A. Hansen, L. A. R. Kristensen, A. M. Nielsen, M. Voigt, and P. Madeleine, “The role of stride frequency for walk-to-run transition in humans,” *Scientific Reports*, vol. 7, p. 2010, 2017.

- [214] A. C. Gilliss, R. L. Swanson, D. Janora, and V. Venkataraman, “Use of osteopathic manipulative treatment to manage compensated trendelenburg gait caused by sacroiliac somatic dysfunction,” *The Journal of the American Osteopathic Association*, vol. 110, no. 2, pp. 81–86, 2010.
- [215] L. Segal, S. Sienko Thomas, J. Mazur, and M. Mauterer, “Calcaneal gait in spastic diplegia after heel cord lengthening: a study with gait analysis,” *Journal of Pediatric Orthopaedics*, vol. 9, no. 6, pp. 697–701, 1989.
- [216] R. E. Quesada, J. M. Caputo, and S. H. Collins, “Increasing ankle push-off work with a powered prosthesis does not necessarily reduce metabolic rate for transtibial amputees,” *Journal of Biomechanics*, vol. 49, no. 14, pp. 3452–3459, 2016.
- [217] E. R. Esposito, K. M. Rodriguez, C. A. Ràbago, and J. M. Wilken, “Does unilateral transtibial amputation lead to greater metabolic demand during walking?,” *Journal of Rehabilitation Research and Development*, vol. 51, no. 8, pp. 1287–1296, 2014.
- [218] K. L. Snyder, M. Snaterse, and J. M. Donelan, “Running perturbations reveal general strategies for step frequency selection,” *Journal of Applied Physiology*, vol. 112, no. 8, pp. 1239–1247, 2012.
- [219] E. Todorov and M. I. Jordan, “Optimal feedback control as a theory of motor coordination,” *Nature Neuroscience*, vol. 5, no. 11, pp. 1226–1235, 2002.
- [220] M. Haruno and D. M. Wolpert, “Optimal control of redundant muscles in step-tracking wrist movements,” *Journal of Neurophysiology*, vol. 94, no. 6, pp. 4244–4255, 2005.
- [221] T. Flash and N. Hogan, “The coordination of arm movements: an experimentally confirmed mathematical model,” *The Journal of Neuroscience*, vol. 5, no. 7, pp. 1688–1703, 1985.
- [222] E. Burdet, D. Franklin, and T. Milner, “Motion planning and online control,” in *Human robotics: neuromechanics and motor control*, ch. 9, pp. 185–210, The MIT Press, 2013.
- [223] A. Hreljac, R. T. Imamura, R. F. Escamilla, W. B. Edwards, and T. MacLeod, “The relationship between joint kinetic factors and the walk-run gait transition speed during human locomotion,” *Journal of Applied Biomechanics*, vol. 24, no. 2, pp. 149–157, 2008.
- [224] M. C. Granatosky, C. M. Bryce, J. Hanna, A. Fitzsimons, M. F. Laird, K. Stilson, C. E. Wall, and C. F. Ross, “Inter-stride variability triggers

- gait transitions in mammals and birds," *Proceedings of the Royal Society B: Biological Sciences*, vol. 285, p. 20181766, 2018.
- [225] J. R. Usherwood, T. Y. Hubel, B. J. H. Smith, Z. Self Davies, and G. Sobota, "The scaling or ontogeny of human gait kinetics and walk-run transition: the implications of work vs. peak power minimization," *Journal of Biomechanics*, vol. 81, pp. 12–21, 2018.
- [226] H. B. Menz, S. R. Lord, and R. C. Fitzpatrick, "Acceleration patterns of the head and pelvis when walking on level and irregular surfaces," *Gait & Posture*, vol. 18, no. 1, pp. 35–46, 2003.
- [227] H. Herr and M. Popovic, "Angular momentum in human walking," *The Journal of Experimental Biology*, vol. 211, no. 4, pp. 467–481, 2008.
- [228] S. H. Collins, A. Ruina, R. Tedrake, and M. Wisse, "Efficient bipedal robots based on passive dynamic walkers," *Science*, vol. 307, no. 5712, pp. 1082–1085, 2005.
- [229] M. Vlutters, E. van Asseldonk, and H. van der Kooij, "Reduced center of pressure modulation elicits foot placement adjustments, but no additional trunk motion during anteroposterior-perturbed walking," *Journal of Biomechanics*, vol. 68, pp. 93–98, 2018.
- [230] B. Houska and M. Diehl, "Robustness and stability optimization of power generating kite systems in a periodic pumping mode," *Proceedings of the IEEE International Conference on Control Applications*, pp. 2172–2177, 2010.
- [231] A. Falisse, G. Serrancolí, C. L. Dembia, J. Gillis, I. Jonkers, and F. De Groote, "Rapid predictive simulations with complex musculoskeletal models suggest that diverse healthy and pathological human gaits can emerge from similar control strategies," *Journal of The Royal Society Interface*, vol. 16, no. 157, p. 20190402, 2019.
- [232] A. Falisse, L. Bar-On, K. Desloovere, I. Jonkers, and F. De Groote, "A spasticity model based on feedback from muscle force explains muscle activity during passive stretches and gait in children with cerebral palsy," *PLoS ONE*, vol. 13, no. 12, p. e0208811, 2018.
- [233] L. R. Smith, K. S. Lee, S. R. Ward, H. G. Chambers, and R. L. Lieber, "Hamstring contractures in children with spastic cerebral palsy result from a stiffer extracellular matrix and increased in vivo sarcomere length.," *The Journal of physiology*, vol. 589, pp. 2625–2639, 2011.

- [234] L. Scheyns, A. Van Campenhout, A. Spaepen, P. Suetens, and I. Jonkers, “Personalized MR-based musculoskeletal models compared to rescaled generic models in the presence of increased femoral anteversion: effect on hip moment arm lengths,” *Gait & Posture*, vol. 28, no. 3, pp. 358–365, 2008.
- [235] K. M. Steele, B. R. Shuman, and M. H. Schwartz, “Crouch severity is a poor predictor of elevated oxygen consumption in cerebral palsy,” *Journal of Biomechanics*, vol. 60, pp. 170–174, 2017.
- [236] C. Hemingway, J. McGrogan, and J. M. Freeman, “Energy requirements of spasticity,” *Developmental Medicine & Child Neurology*, vol. 43, no. 04, p. 277, 2001.
- [237] T. A. L. Wren, S. Rethlefsen, and R. M. Kay, “Prevalence of specific gait abnormalities in children with cerebral palsy,” *Journal of Pediatric Orthopaedics*, vol. 25, no. 1, pp. 79–83, 2005.
- [238] M. A. Mathewson, S. R. Ward, H. G. Chambers, and R. L. Lieber, “High resolution muscle measurements provide insights into equinus contractures in patients with cerebral palsy,” *Journal of Orthopaedic Research*, vol. 33, pp. 33–39, 2015.
- [239] C. K. Liu, A. Hertzmann, and Z. Popović, “Learning physics-based motion style with nonlinear inverse optimization,” *ACM Transactions on Graphics*, vol. 24, no. 3, pp. 1071–1081, 2005.
- [240] M. Eilenberg, H. Geyer, and H. Herr, “Control of a powered ankle-foot prosthesis based on a neuromuscular model,” *IEEE Transactions on Neural Systems and Rehabilitation Engineering*, vol. 18, no. 2, pp. 164–173, 2010.
- [241] N. Thatte and H. Geyer, “Toward Balance Recovery With Leg Prostheses Using Neuromuscular Model Control,” *IEEE Transactions on Biomedical Engineering*, vol. 63, no. 5, pp. 904–913, 2016.
- [242] A. R. Wu, F. Dzeladini, T. J. Brug, F. Tamburella, N. L. Tagliamonte, E. H. van Asseldonk, H. van der Kooij, and A. J. Ijspeert, “An adaptive neuromuscular controller for assistive lower-limb exoskeletons: A preliminary study on subjects with spinal cord injury,” *Frontiers in Neurorobotics*, vol. 11, no. 30, pp. 1–14, 2017.
- [243] G. Taga, “A model of the neuro-musculo-skeletal system for anticipatory adjustment of human locomotion during obstacle avoidance,” *Biological Cybernetics*, vol. 78, no. 1, pp. 9–17, 1998.
- [244] A. D. Kuo, “The relative roles of feedforward and feedback in the control of rhythmic movements,” *Motor control*, vol. 6, no. 2, pp. 129–145, 2002.

- [245] T. Pozzo, A. Berthoz, and L. Lefort, “Head stabilization during various locomotor tasks in humans. I. Normal subjects,” *Experimental Brain Research*, vol. 82, no. 1, pp. 97–106, 1990.
- [246] R. J. Peterka, “Sensorimotor integration in human postural control,” *Journal of Neurophysiology*, vol. 88, no. 3, pp. 1097–1118, 2019.
- [247] Ł. Kidziński, S. P. Mohanty, C. Ong, J. L. Hicks, S. F. Carroll, S. Levine, M. Salathé, and S. L. Delp, “Learning to Run challenge: Synthesizing physiologically accurate motion using deep reinforcement learning,” in *The NIPS ’17 Competition: Building Intelligent Systems* (S. Escalera and M. Weimer, eds.), ch. 6, Springer, Cham, the spring ed., 2018.
- [248] S. Lee, M. Park, K. Lee, and J. Lee, “Scalable muscle-actuated human simulation and control,” *ACM Transactions on Graphics*, vol. 38, no. 4, pp. 73:1–73:13, 2019.
- [249] D. G. Thelen, F. C. Anderson, and S. L. Delp, “Generating dynamic simulations of movement using computed muscle control,” *Journal of Biomechanics*, vol. 36, pp. 321–328, 2003.
- [250] P. A. Huijing, “Important experimental factors for skeletal muscle modelling: non-linear changes of muscle length force characteristics as a function of degree of activity,” *European Journal of Morphology*, vol. 34, no. 1, pp. 47–54, 1996.
- [251] S. R. Ward, C. M. Eng, L. H. Smallwood, and R. L. Lieber, “Are current measurements of lower extremity muscle architecture accurate?,” *Clinical Orthopaedics and Related Research*, vol. 467, pp. 1074–1082, 2009.
- [252] M. Damsgaard, J. Rasmussen, S. Christensen, E. Surma, and M. de Zee, “Analysis of musculoskeletal systems in the AnyBody Modeling System,” *Simulation Modelling Practice and Theory*, vol. 14, no. 8, pp. 1100–1111, 2006.
- [253] S. A. Roelker, E. J. Caruthers, R. K. Baker, N. C. Pelz, A. M. Chaudhari, and R. A. Siston, “Interpreting musculoskeletal models and dynamic simulations: causes and effects of differences between models,” *Annals of Biomedical Engineering*, vol. 45, no. 11, pp. 2635–2647, 2017.
- [254] D. Winter, *Biomechanics and motor control of human movement*. Hoboken, New Jersey: John Wiley & Sons, Inc., 4th ed., 2009.
- [255] J. L. Holmberg and A. Klarbring, “Muscle decomposition and recruitment criteria influence muscle force estimates,” *Multibody System Dynamics*, vol. 28, no. 3, pp. 283–289, 2012.

- [256] R. Crowninshield and R. Brand, "A physiologically based criterion of muscle force prediction in locomotion," *Journal of Biomechanics*, vol. 14, no. 11, pp. 793–801, 1981.
- [257] R. L. Lathrop-Lambach, J. L. Asay, S. T. Jamison, X. Pan, L. C. Schmitt, K. Blazek, R. A. Siston, T. P. Andriacchi, and A. M. Chaudhari, "Evidence for joint moment asymmetry in healthy populations during gait," *Gait & Posture*, vol. 40, no. 4, pp. 526–531, 2014.
- [258] P. Dixon, J. Stebbins, T. Theologis, and A. Zavatsky, "Spatio-temporal parameters and lower-limb kinematics of turning gait in typically developing children," *Gait & Posture*, vol. 38, no. 4, pp. 870–875, 2013.
- [259] T. Pataky, M. Robinson, and J. Vanrenterghem, "Vector field statistical analysis of kinematic and force trajectories," *Journal of Biomechanics*, vol. 46, no. 14, pp. 2394–2401, 2013.
- [260] T. E. Nichols and A. P. Holmes, "Nonparametric permutation tests for functional neuroimaging: A primer with examples," *Human Brain Mapping*, vol. 15, no. 1, pp. 1–25, 2002.
- [261] J. L. Hicks, A. Seth, S. R. Hamner, M. S. DeMers, J. S. Higginson, B. A. Knar, A. T. Collins, E. Schrank, and C. Henderson, "Simulation with OpenSim - Best Practices," 2015.
- [262] J. Hicks, T. Uchida, A. Seth, A. Rajagopal, and S. Delp, "Is my model good enough? Best practices for verification and validation of musculoskeletal models and simulations of human movement," *Journal of Biomechanical Engineering*, vol. 137, no. 2, pp. 1–24, 2015.
- [263] S. Delp, *Surgery simulation: a computer graphics system to analyze and design musculoskeletal reconstructions of the lower limb*. PhD thesis, Stanford University, 1990.
- [264] M. Harrington, A. Zavatsky, S. Lawson, Z. Yuan, and T. Theologis, "Prediction of the hip joint centre in adults, children, and patients with cerebral palsy based on magnetic resonance imaging," *Journal of Biomechanics*, vol. 40, no. 3, pp. 595–602, 2007.
- [265] H. Kainz, C. P. Carty, L. Modenese, R. N. Boyd, and D. G. Lloyd, "Estimation of the hip joint centre in human motion analysis: A systematic review," *Clinical Biomechanics*, vol. 30, no. 4, pp. 319–329, 2015.
- [266] S. Piazza, N. Okita, and P. Cavanagh, "Accuracy of the functional method of hip joint center location : effects of limited motion and varied implementation," *Journal of Biomechanics*, vol. 34, no. 7, pp. 967–973, 2001.

- [267] T. Besier, D. Sturnieks, J. Alderson, and D. Lloyd, "Repeatability of gait data using a functional hip joint centre and a mean helical knee axis," *Journal of Biomechanics*, vol. 36, no. 8, pp. 1159–1168, 2003.
- [268] J. Reinbolt, J. Schutte, B. Fregly, B. Koh, R. Haftka, A. George, and K. Mitchell, "Determination of patient-specific multi-joint kinematic models through two-level optimization," *Journal of Biomechanics*, vol. 38, no. 3, pp. 621–626, 2005.
- [269] R. Isman and V. Inman, "Anthropometric Studies of the Human Foot and Ankle," *Foot Ankle*, vol. 11, pp. 97–129, 1969.
- [270] V. Inman, *The joints of the ankle*. Baltimore: Williams & Wilkins, 1976.
- [271] G. Yamaguchi and F. Zajac, "A planar model of the knee joint to characterize the knee extensor mechanism," *Journal of Biomechanics*, vol. 22, no. 1, pp. 1–10, 1989.
- [272] M. Wesseling, F. de Groote, and I. Jonkers, "The effect of perturbing body segment parameters on calculated joint moments and muscle forces during gait," *Journal of Biomechanics*, vol. 47, no. 2, pp. 596–601, 2014.
- [273] B. Fregly, M. Boninger, and D. Reinkensmeyer, "Personalized neuromusculoskeletal modeling to improve treatment of mobility impairments: a perspective from European research sites," *Journal of NeuroEngineering and Rehabilitation*, vol. 9, no. 1, p. 18, 2012.
- [274] C. Pizzolato, M. Reggiani, L. Modenese, and D. Lloyd, "Real-time inverse kinematics and inverse dynamics for lower limb applications using OpenSim," *Computer Methods in Biomechanics and Biomedical Engineering*, vol. 20, no. 4, pp. 436–445, 2017.
- [275] M. Lund, M. de Zee, M. Andersen, and J. Rasmussen, "On validation of multibody musculoskeletal models," *Proceedings of the Institution of Mechanical Engineers, Part H: Journal of Engineering in Medicine*, vol. 226, no. 2, pp. 82–94, 2012.
- [276] S. Meireles, M. Wesseling, C. R. Smith, D. G. Thelen, S. Verschueren, and I. Jonkers, "Medial knee loading is altered in subjects with early osteoarthritis during gait but not during step-up-and-over task," *PLoS ONE*, vol. 12, no. 11, p. e0187583, 2017.
- [277] R. H. Byrd, P. Lu, J. Nocedal, and C. Zhu, "A limited memory algorithm for bound constrained optimization," *Journal of Scientific Computing*, vol. 16, no. 5, pp. 1190–1208, 1995.

- [278] W. Press, S. Teukolsky, W. Vetterling, and B. Flannery, *Numerical Recipes. The art of scientific computing*. Cambridge: Cambridge University Press, 3rd ed., 2007.
- [279] Y. Xia and G. Feng, “An improved neural network for convex quadratic optimization with application to real-time beamforming,” *Neurocomputing*, vol. 64, pp. 359–374, 2005.